

UNIVERSITY OF OKLAHOMA

GRADUATE COLLEGE

NEW STRUCTURAL INSIGHTS OF  
ALKANETHIOL SELF-ASSEMBLED MONOLAYERS ON THE Au(111):  
A MOLECULAR DYNAMICS AND DENSITY FUNCTIONAL THEORY STUDY

A DISSERTATION

SUBMITTED TO THE GRADUATE FACULTY

in partial fulfillment of the requirements for the

Degree of

DOCTOR OF PHILOSOPHY

By

SOUMYA BHATTACHARYA  
Norman, Oklahoma  
2021

NEW STRUCTURAL INSIGHTS OF  
ALKANETHIOL SELF-ASSEMBLED MONOLAYERS ON THE Au(111):  
A MOLECULAR DYNAMICS AND DENSITY FUNCTIONAL THEORY STUDY

A DISSERTATION APPROVED FOR THE HOMER L. DODGE DEPARTMENT OF  
PHYSICS AND ASTRONOMY

BY THE COMMITTEE CONSISTING OF

Dr. Lloyd A. Bumm, Chair

Dr. Liangliang Huang, Co-Chair

Dr. Daniel T. Glatzhofer

Dr. Ian R. Sellers

Dr. Arne Schwettmann

© Copyright by SOUMYA BHATTACHARYA 2021

All Rights Reserved.

TO

MY SON, WIFE, AND FATHER

AND

IN LOVING MEMORY OF MY GRANDMOTHER



## Acknowledgements

I am extremely thankful to my thesis advisor, Dr. Lloyd A. Bumm, for his guidance throughout my research, providing me with deeper physical insights, trusting me with new research endeavors, helping me develop new skills, and supporting me to be an independent thinker.

I am thankful to my current and former research group members for providing me feedback to improve, and discussing different ideas and ways to implement them. I am especially thankful to Mitchell Yothers for helping me with MATLAB scripting and a better understanding of the symmetry and its mathematical description.

I had a wonderful opportunity to collaborate with Drs. Gil Speyer and David K. Ferry from the Arizona State University for our density functional theory simulations. I am thankful for their expertise, guidance, and discussions during our weekly meetings. I also want to thank them for helping me with my job search. I am grateful for our collaboration and meetings with Drs. Liangliang Huang and Guobing Zho from School of Chemical, Biological and Materials Engineering, University of Oklahoma (OU). I am especially thankful to Dr. Liangliang Huang for his valuable guidance throughout the molecular dynamics simulation project.

I thank my committee members, Drs. Daniel T. Glatzhofer, Ian R. Sellers, Liangliang Huang, and Arne Schwettmann, for their constant support and guidance throughout my graduate career.

I would like to thank the Graduate Recruiting and Selection Committee, the Homer L. Dodge Physics and Astronomy department, the Center for Quantum Research and Technology, and the OU College of Arts and Sciences for offering me a chance to prove myself at the University of Oklahoma.

I acknowledge the support from the National Science Foundation (NSF CHE-1710102). Allocation time for molecular dynamics simulations was performed using the Extreme Science and Engineering Discovery Environment (XSEDE) Stampede2 at the Texas Advanced Computing Center through allocation TG-CHE170067 and the OU Supercomputing Center for Education & Research (OSCER) at the University of Oklahoma. Allocation time for density functional theory simulations was performed using the Agave system at Arizona State's Research Computing Center and the OSCER at the University of Oklahoma. I also acknowledge support from Carl. T. Bush and Homer L. Dodge Fellowships, as well as a Robberson Travel Grant. I gratefully acknowledge the support of NVIDIA Corporation with the donation of the Tesla K40 GPU used for this research.

I am grateful to Dr. Eddie A. Baron (Professor, Physics & Astronomy), Gary Bates (Director of Technology Services, CAS IT), Millard B. Latimer II (Sr. Technology Strategist, OU IT), Horst Severini (IT Analyst III, Research Computing (OSCER) and Physics & Astronomy), and Chad E. Cunningham (Manager of the electronics and instrument shops, Physics & Astronomy) for helping me balance my research, work, and family life.

Last, but not least, I thank for the endless support from my wonderful wife, Kirsten L. Bhattacharya and our son, Navid A. Bhattacharya; my father, Samir K. Bhattacharya; my cousins (Nabonita Bhattacharya and Sourav Bhattacharya); my uncle (Siba P. Bhattacharya) and my aunt (Rina Bhattacharya). I would like to thank my best friend, Navid S. Shahabi. I would not be able to do this research without the support from my family and friends.

# Table of Contents

<b>Acknowledgements</b> .....	iv
<b>Table of Contents</b> .....	vi
<b>List of Publications</b> .....	ix
<b>List of Conference Presentations</b> .....	x
<b>List of Figures</b> .....	xi
<b>List of Tables</b> .....	xv
<b>List of Abbreviations</b> .....	xvi
<b>List of Software Used</b> .....	xviii
<b>Abstract</b> .....	xix
<b>Chapter 1: Background and Scope of the Thesis</b> .....	<b>1</b>
1.1 Introduction .....	1
1.2 Nature of the Problem .....	2
<i>1.2.1 Outer Surface</i> .....	4
<i>1.2.2 Molecular Backbone</i> .....	4
<i>1.2.3 Au-S interface</i> .....	14
1.3 Scope of this Thesis.....	17
1.4 References.....	18
<b>Chapter 2: Background for Molecular Dynamics Simulation</b> .....	<b>24</b>
2.1 Introduction .....	24
2.2 Fundamental Principles of Molecular Dynamics .....	25
2.3 Initial Configuration .....	26
2.4 Initial Velocity .....	28
2.5 Total Energy Calculation .....	28
<i>2.5.1 Bonded Interaction Energy</i> .....	29
<i>2.5.2 Non-bonded Interaction Energy</i> .....	32
<i>2.5.3 Force Field Parameters</i> .....	33
2.6 Comparison between United-Atom and All-Atom Model .....	35
2.7 Periodic Boundary Condition.....	36
2.8 Integration Method .....	38
2.9 Ensemble (Nosé–Hoover Thermostat).....	40
2.10 Limitations of Molecular Dynamics .....	41

2.11 References .....	42
<b>Chapter 3: Background for Density Functional Theory Simulation .....</b>	<b>44</b>
3.1 Scope of this Chapter .....	44
3.2 Born-Oppenheimer Approximation .....	44
3.3 Hohenberg-Kohn Theorem.....	45
3.4 Kohn-Sham Formalism .....	48
3.5 Plane Wave Basis.....	51
3.6 Pseudo-wavefunction and Pseudopotential .....	53
3.7 Hamiltonian Matrix Diagonalization .....	55
3.8 Exchange-Correlation Functionals .....	56
3.8.1 Local Density Approximation .....	57
3.8.2 Generalized Gradient Approximation .....	59
3.9 Dispersion Correction to DFT.....	61
3.10 References .....	65
<b>Chapter 4: Exploring the Best Packing of Alkane Chains and its Effect on the Head Groups.....</b>	<b>70</b>
4.1 Scope of this Chapter .....	70
4.2 Determination of the Unique Tilt Direction and Twist Combinations .....	72
4.3 Simulation Method .....	76
4.4 Results and Discussion.....	79
4.5 Conclusions .....	83
4.6 References.....	83
<b>Chapter 5: Chain Packing on Reconstructed Substrate .....</b>	<b>85</b>
5.1 Scope of this Chapter .....	85
5.2 Introduction .....	86
5.3 Interface Models .....	88
5.4 Simulation Details .....	93
5.5 Results and Discussion.....	94
5.5.1 <i>Gauche Fraction and Tilt Angle</i> .....	96
5.5.2 <i>Molecular Height</i> .....	98
5.5.3 <i>Molecular Twist</i> .....	100
5.5.4 <i>Tilt Direction and Thermal Stability</i> .....	103
5.5.5 <i>Basis Offset and Molecular Geometry</i> .....	105

5.6 Conclusions .....	111
5.7 References.....	113
<b>Chapter 6: Effect of Sulfur Hybridization on Methanethiol Adsorption Geometry on Unrelaxed Au(111).....</b>	<b>116</b>
6.1 Scope of this Chapter .....	116
6.2 Introduction .....	116
6.3 Simulation Details .....	119
6.5 Conclusions .....	144
6.6 References.....	145
<b>Chapter 7. Effect of Substrate Relaxation on Thiol Adsorption .....</b>	<b>148</b>
7.1 Scope of this Chapter .....	148
7.2 Introduction .....	149
7.3 Theoretical Methods.....	151
7.4 Results and Discussion.....	156
7.5 Conclusion.....	166
7.6 References.....	166
<b>Chapter 8: Conclusions and Future Outlook.....</b>	<b>170</b>
<b>Appendix A: Running Molecular Dynamics Simulations .....</b>	<b>175</b>
<b>Appendix B: Benchmark for LAMMPS.....</b>	<b>180</b>
<b>Appendix C: Running DFT Simulations using VASP.....</b>	<b>183</b>
<b>Appendix D: MATLAB Script to Generate 109 Unique Tilt Direction and Twist Combinations.....</b>	<b>187</b>
<b>Appendix E: CDD Plots for Azimuthal Angles at High Symmetry Sites and Along Transition Paths.....</b>	<b>191</b>
<b>Appendix F: STM Image Simulation from Molecular Dynamics .....</b>	<b>195</b>
<b>Appendix G: IRRAS Simulation from Molecular Dynamics .....</b>	<b>198</b>

## List of Publications

1. Bhattacharya, S.; Yothers, M. P.; Huang, L.; Bumm, L. A., Interaction of the  $(2\sqrt{3} \times 3)$ rect. Adsorption-Site Basis and Alkyl-Chain Close Packing in Alkanethiol Self-Assembled Monolayers on Au(111): A Molecular Dynamics Study of Alkyl-Chain Conformation. *ACS Omega* **2020**, *5* (23), 13802-13812.
2. Bhattacharya, S.; Speyer, G.; Ferry, D. K.; Bumm, L. A., A Comprehensive Study of the Bridge Site and Substrate Relaxation Asymmetry for Methanethiol Adsorption on Au(111) at Low Coverage. *ACS Omega* **2020**, *5* (33), 20874-20881.
3. Bhattacharya, S.; Speyer, G.; Ferry, D. K.; Bumm, L. A., Effect of Sulfur Hybridization on Methanethiol Adsorption Geometry on Unrelaxed Au(111) – *in preparation for publication*

## List of Conference Presentations

1. Bhattacharya, S.; Speyer, G.; Ferry, D. K.; Bumm, L. A. “Bridge Site Asymmetry for Adsorption of Methanethiol on Au(111): DFT Study of the Adsorption Energy Dependence on the Methyl Orientation at Low Coverage” **ACS Fall 2020 Virtual Meeting & Expo**, San Francisco, CA, 2020 - *Talk*
2. Bhattacharya, S.; Speyer, G.; Ferry, D. K.; Bumm, L. A. “New insights on the Au/S interface of the alkanethiol self-assembled monolayers on Au(111): A DFT study” **64th Oklahoma Pentasectional Meeting of the American Chemical Society**, Norman, OK, 2019 - *Talk*
3. Bhattacharya, S.; Huang, L.; Bumm, L. A. “The packing of the *n*-decanethiol self-assembled monolayers on reconstructed Au(111) substrate: A comparative molecular dynamics study” **63rd Oklahoma Pentasectional Meeting of the American Chemical Society**, Tulsa, OK, 2018 - *Talk*
4. Bhattacharya, S.; Huang, L.; Bumm, L. A. “Local dynamics and disorder of the terminal methyl groups in n-alkanethiol self-assembled monolayers (SAMs) on Au(111): A Molecular Dynamics (MD) study” **62nd Oklahoma Pentasectional Meeting of the American Chemical Society**, Lawton, OK, 2017 - *Talk*
5. Bhattacharya, S.; Huang, L.; Bumm, L. A. “Local dynamics and disorder of the terminal methyl groups in n-alkanethiol self-assembled monolayers (SAMs) on Au(111): A Molecular Dynamics (MD) study” **Physical Electronics Conference**, Fayetteville, AR, 2016 – *Poster*

## List of Figures

Figure 1.1 Three Regions of the Alkanethiol SAM.....	1
Figure 1.2 A Parallel-view Stereo Image Pair of the Molecular Geometry.....	3
Figure 1.3 The $(2\sqrt{3} \times 3)$ rect. Unit Cell on an Unreconstructed Au(111) Surface.....	3
Figure 1.4 Two Possible Superlattice Symmetries for a 1:1 Ratio of the Two Molecule Types in a $(\sqrt{3} \times \sqrt{3})R30^\circ$ Lattice.....	4
Figure 1.5 The Molecular Twist in Two Different Reference Frames.....	6
Figure 1.6 The C–C–C Dihedral Potential Energy and the Corresponding Population of the Dihedral Angle.....	12
Figure 1.7 An Eye-cross Stereo Image Pair of Five Different Bonding Scenarios at the Au-S Interface.....	15
Figure 2.1 Relaxation of <i>n</i> -Decanethiol on the Unrelaxed Au(111) at Different Temperatures ...	26
Figure 2.2 The Bond Stretching Potential Energy for the C-C Bond.....	30
Figure 2.3 The Bond Bending Potential Energy for the C-C-C Bond.....	31
Figure 2.4 Population of the Molecular Twist Predicted by the AA and the UA Models are Compared for the C10 SAM.....	35
Figure 2.5 The Effect of the PBC on the Central Simulation Box Containing Three Particles.....	37
Figure 3.1 Schematic of the DFT Algorithm.....	50
Figure 3.2 The Levels of Approximation for the Long-range Dispersion Energy in the DFT Calculation.....	62
Figure 4.1 Translation Symmetry of the Head Group Lattice.....	70
Figure 4.2 Symmetries Provided by the Trigonal Lattice of the Head Groups.....	72
Figure 4.3 The Temperature Profile During the Entire Simulation.....	76
Figure 4.4 Twist Distribution for the Initial Structure $\{50^\circ, 50^\circ, 50^\circ, 50^\circ; 0^\circ\}$ at Different Temperatures.....	77
Figure 4.5 Grouping Scheme of the 109 Unique Structures Based on the Symmetries.....	79
Figure 4.6 The Average System Energy for the 109 Unique Structures at 4 K for Head-Group Constraints 1 and 2.....	80
Figure 4.7 The Structures with the Best Alkyl Chain Packing for Constraints 1 and 2.....	81
Figure 5.1 An Eye-cross Stereo Image Pair of the SAM Molecular Geometry.....	87
Figure 5.2 The Average Gauche Fraction (%) Compared at 200 K, 250 K, and 300 K.....	96



Figure 5.3 The Spatial Distribution of the Height Difference of the Methyl Interface for the Models at 200 K.....	96
Figure 5.4 The Spatial Distribution of the Height Difference of the Methyl Interface for the Models at 250 K.....	98
Figure 5.5 The Average Height of the Four Basis-Type Methyl-Group C Atoms from the Au(111) Substrate for Each Model at 200 K Separated by Contribution.....	99
Figure 5.6 The Average Height of the Four Basis-Type Methyl-Group C Atoms from the Au(111) Substrate for Each Model at 250 K Separated by Contribution.....	101
Figure 5.7 The Standard Deviation (SD) and the Standard Deviation of the Mean (SDoM) of Molecular Heights for Each Basis Type for the Models.....	103
Figure 5.8 The Spatial Distribution of the Molecular Twist for the Models at 200 K .....	104
Figure 5.9 The Spatial Distribution of the Molecular Twist for the Models at 250 K .....	105
Figure 5.10 Comparison of the SAM Sulfur Adsorption Sites and Alkyl Chain Molecular Geometry for the Models .....	106
Figure 5.11 The RCP View of the SAM Sulfur Adsorption Sites and Alkyl Chain Molecular Geometry for the Head Groups on the Ideal ( $\sqrt{3} \times \sqrt{3}$ )R30° Sites.....	108
Figure 6.1 Geometrical Parameters of an Adsorbed Methanethiol Molecule .....	117
Figure 6.2 The 43 Adsorption Sites Are Shown within the Principle Triangle on the Unreconstructed Au(111) Substrate.....	118
Figure 6.3 Scheme for Relaxing the SCH <sub>3</sub> in Twelve Azimuthal Orientations.....	121
Figure 6.4 Tiling Scheme to Create the Full Surface from Region 1 using the Surface Symmetry .....	123
Figure 6.5 The Energy and Modulation Landscape.....	125
Figure 6.6 The Variation of the Molecular Geometry Corresponding to the Energy Landscape	126
Figure 6.7 Energy Profile Along Four Paths between the High Symmetry Sites Taken from the Energy Landscape.....	128
Figure 6.8 Diagram of the Au(111) Surface in the Simulation.....	128
Figure 6.9 The Au-S DDEC6 Bond Orders for Three S-C Azimuthal Angles at Seven Sites from Bridge to Atop.....	129
Figure 6.10 The Distribution of the Sulfur Electron Lone Pairs for Seven Different Sulfur Atom Locations from the Bridge to the Atop Site with a 0° S-C Bond Azimuthal Angle.....	130
Figure 6.11 The Distribution of the Sulfur Electron Lone Pairs for Fifteen Different Sulfur Atom Locations from One Atop Site to the Other through the Bridge Site with a 90° S-C Bond Azimuthal Angle.....	132

Figure 6.12 The Au-S DDEC6 Bond Orders Versus System Energy for 0°/180° and 90°/270° S-C Azimuthal Angles at Seven Sites from Bridge to Atop .....	133
Figure 6.13 The Au-S DDEC6 Bond Orders for 0° and 180° S-C Azimuthal Angles at Nine Sites Along the Path fcc to Bridge to hcp.....	134
Figure 6.14 The Au-S DDEC6 Bond Orders Versus System Energy for 0° and 180° S-C Azimuthal Angles at Nine Sites Along the Path fcc to Bridge to hcp .....	134
Figure 6.15 The Distribution of the Sulfur Electron Lone Pairs at Nine Sites Along the Path fcc to Bridge to hcp with a 0° S-C Bond Azimuthal Angle.....	135
Figure 6.16 The Distribution of the Sulfur Electron Lone Pairs at Nine Sites Along the Path fcc to Bridge to hcp with a 180° S-C Bond Azimuthal Angle.....	136
Figure 6.17 The Au-S-C and Au-S-Au Bond Angles for 0° and 180° S-C Azimuthal Angles at Nine Sites Along the Path fcc to Bridge to hcp .....	137
Figure 6.18 CDD for 1/4 fcc ( $\varphi = 0^\circ$ ) and 1/4 hcp ( $\varphi = 180^\circ$ ).....	137
Figure 6.19 Nearest-neighbor Au Bond Directions Along the <110> Columns .....	138
Figure 6.20 CDD at the Bridge Site for Four Orientations of the S-C Bond.....	139
Figure 6.21 Variation of the Total System Energy with respect to the Azimuthal Angle of the S-C Bond for Four High Symmetry Sites .....	140
Figure 6.22 The Au-S-C Bond Angles at the Bridge Site for Twelve Different Azimuthal Angles .....	141
Figure 6.23 The Au-S DDEC6 Bond Orders for the Sulfur Atom on the fcc Site for Twelve Different S-C Bond Azimuthal Angles.....	141
Figure 6.24 The Au-S DDEC6 Bond Orders for the Sulfur Atom on the hcp site for Twelve Different S-C Bond Azimuthal Angles.....	141
Figure 6.25 The Au-S DDEC6 Bond Orders for the Sulfur Atom on the Atop Site for Twelve Different S-C Bond Azimuthal Angles.....	142
Figure 6.26 The Au-S DDEC6 Bond Orders for the Sulfur Atom on the Bridge Site for Twelve Different S-C Bond Azimuthal Angles.....	142
Figure 6.27 The Au-S DDEC6 Bond Orders Versus System Energy for the Sulfur Atom on the Bridge Site for Twelve Different S-C Bond Azimuthal Angles.....	143
Figure 6.28 The Distribution of the Sulfur Electron Lone Pairs for the Sulfur Atom on the Bridge Site for Twelve Different S-C Bond Azimuthal Angles.....	144
Figure 7.1 The Top-down View of the Simulation Box Showing the Au(111) Bridge Site Studied with the Adsorbed S Atom.....	148
Figure 7.2 The Energy for Adsorption Sites Along the Transition Path from the fcc 3-fold Hollow Site to the hcp 3-fold Hollow Site for Two Orientations of the S-C Bond.....	149

Figure 7.3 The Thermal Expansion of the Au Lattice Constant .....	151
Figure 7.4 The Equation of State Calculation for Bulk Au with Different Combinations of DFT Functionals .....	154
Figure 7.5 The Au(111) Surface After Relaxation Showing the Displacement Vectors .....	156
Figure 7.6 The Au Atom Displacement for SCH <sub>3</sub> Adsorbed at the Bridge-fcc and the Bridge-hcp Sites .....	160
Figure 7.7 The Au Atom Displacement for SH Adsorbed at the Bridge-fcc and the Bridge-hcp Sites .....	163
Figure A.1 Three Steps to Generate the Initial Structure Used by LAMMPS .....	175
Figure A.2 LAMMPS Batch Script Example for OSCER .....	178
Figure B.1 LAMMPS Benchmarks on Three Different Intel Architectures .....	180
Figure B.2 Distribution of the Total Computational Time (Wall Time) for the Intel Skylake Architecture .....	181
Figure E.1 CDD Side-View Looking along $[\bar{1}\bar{1}2]$ of the Bridge Site for 12 Azimuthal Angles of the S-C Bond .....	191
Figure E.2 CDD at the fcc Hollow Site for Three Azimuthal Angles of the S-C Bond .....	191
Figure E.3 CDD at the hcp Hollow Site for Three Azimuthal Angles of the S-C Bond .....	192
Figure E.4 CDD at the Atop Site for Two Azimuthal Angles of the S-C bond .....	192
Figure E.5 CDD for Seven Sites on the Bridge to Atop Path with $\phi = 0^\circ$ .....	193
Figure E.6 CDD for Nine Sites on the fcc to hcp Path via the Bridge Site for Two Azimuthal Angles of the S-C Bond .....	193
Figure E.7 CDD for Seven Sites along the Paths from a Hollow Site to the Atop Site .....	194
Figure F.1 Schematic Diagram of the Two-Layer Tunnel Junction Model .....	195
Figure F.2 Comparing Simulated and Experimental STM Images .....	196
Figure G.1 The Vibrational Modes for Methyl and Methylene .....	198
Figure G.2 Simulated and Experimental IRRAS Spectra .....	200
Figure G.3 Chain Twist Angle Dependence of the IRRAS Intensities of the C-H Modes .....	201

## List of Tables

Table 2.1. Force Field Parameters for Bond Stretching.....	33
Table 2.2. Force Field Parameters for Bond Bending .....	33
Table 2.3. Fourier Components of the Dihedral Angles.....	34
Table 2.4. Force Field Parameters for Non-Bonded Interactions .....	34
Table 4.1. The Symmetry Group of the Trigonal Lattice Consists of 16 Symmetry Operations ..	73
Table 4.2. Symmetry Operations and the Number of Corresponding Fixed Points for Two Sets of Tilt Directions Used to Calculate the Number of Unique Structures .....	75
Table 5.1. Atomic Structure of the $(2\sqrt{3} \times 3)$ rect. Unit Cell for Ten Au-S Interfacial Models.....	90
Table 5.2. Sulfur and Gold Adatom Coordinates for Ten Au/S Interface Models.....	92
Table 5.3. Comparison of the rms Deviation of the Sulfur Head Groups ( $a_s$ ) and the Alkyl Chain Axes ( $a_c$ ) from the Close-Packed Lattice for Ten Models .....	110
Table 5.4. Comparison Between Simulation and Experimental Results for Different Models...111	
Table 6.1. Summary of the Characteristics for Selected Surface Sites.....	126
Table 7.1. Comparison of the Optimized Au Lattice Constant (Å) for Different DFT Functionals .....	153
Table 7.2. Comparison of the System Energy with respect to Bridge-hcp on Unreconstructed Au .....	158
Table 7.3. Displacement for the Top Two Au Layers from their Unrelaxed Positions.....	159
Table 7.4. Geometric Parameters of the Adsorbate (SCH <sub>3</sub> ) .....	162
Table 7.5. Comparison of the System Energy with respect to SH (S-H, bridge-hcp) on Bulk Au .....	164
Table 7.6. Displacement for the Top Two Au Layers from the Relaxed Bare Au Positions .....	164
Table 7.7. Displacement for the Top Two Au Layers from their Unrelaxed Positions.....	165
Table 7.8. Geometric Parameters of the SH and SCH <sub>3</sub> Adsorbates.....	165
Table G.1. The Vibrational Modes of Alkyl Chains in the C-H Stretching Region.....	200

## List of Abbreviations

AA	all-atom
BO	bond order
C1	methanethiol
C10	<i>n</i> -decanethiol
C18	<i>n</i> -octadecanethiol
CDD	charge density difference
DFT	density functional theory
DoF	degrees of freedom
ELF	electron localization function
EoM	equation of motion
EPM	empirical pseudopotential method
FF	force field
GGA	generalized gradient approximation
GIXRD	grazing incidence X-ray diffraction
HEG	homogeneous electron gas
IRRAS	infrared reflection adsorption spectroscopy
LAMMPS	large-scale atomic/molecular massively parallel simulator
LDA	local density approximation
LEED	low-energy electron diffraction
MD	molecular dynamics
NN	nearest-neighbor
NNN	next-nearest-neighbor
NVT	canonical ensemble
OPLS	optimized potentials for liquid simulations
OPW	orthogonalized plane wave
PAW	projected augmented wave

PBC	periodic boundary condition
PBE	Perdew-Burke-Ernzerhof
PDF	probability density function
RCP	reduced close-packed
rms	root mean square
SAM	self-assembled monolayer
SBO	sum of bond order
SD	standard deviation
SDoM	standard deviation of the mean
SFG	sum frequency generation
SIESTA	Spanish initiative for electronic simulations with thousands of atoms
STM	scanning tunneling microscopy
UA	united-atom
USPP	ultra-soft pseudo-potential
VASP	Vienna ab initio simulation package
vdW	van der Waals
XSW	X-ray standing wave

## **List of Software Used**

LAMMPS (11 August 2017) – Molecular Dynamics Simulation Package

VASP (5.4.4) – Density Functional Theory Simulation Package

VESTA (3.5.7) – Molecular Dynamics and Density Functional Theory Visualization Package

VMD (1.9.3) – Molecular Dynamics and Density Functional Theory Visualization Package

OVITO (3.1.1) – Molecular Dynamics Visualization Package

MATLAB (R2017a through R2021a) – Scripts for Initial Structure Preparation and Post-analysis

## Abstract

Self-assembled monolayers (SAMs) of alkanethiol molecules have been widely studied over the last three decades because of their diverse applications in the biomedical, nanotechnology, surface science, and electronics. It is also regarded as the model system to study the binding of organic molecules on the metal surfaces via thiol functional group. The robustness of the SAM structure combined with the ease of preparation makes it an ideal candidate for both fundamental and applied research.

The structure of the alkanethiol SAMs on the Au(111) substrate is determined by the interplay between the alkyl chain packing and the interaction at the Au-S interface. Although our understanding of the SAM structure has significantly advanced over the last 35 years, an unambiguous atomic description of the Au-S interface and its influence on the chain packing remains elusive. In order to have better control of the SAM structure for different applications, we require a better understanding of the alkanethiol monolayer.

In this work, we use a reductionist approach to determine the preferred head group positions driven by the chain packing, and by the interaction at the Au-S interface, separately. We use molecular dynamics (MD) to study the chain packing of the dense phase saturation coverage decanethiol SAM, and density functional theory (DFT) to study the interaction at the Au-S interface using an isolated methanethiol adsorbate.

Alkane chains prefer a close-packed structure for the efficient interlocking of the methylene groups that minimizes the energy of the system. The molecular plane adjusts its orientation (molecular twist) depending on the spacing and the symmetry of the head groups to achieve a close packing of the chains. We first constrain the head groups at the high symmetry ( $\sqrt{3} \times \sqrt{3}$ )R30° sites



to study the preferred combination of the molecular twists. We use this result as our baseline to study the effect of chain packing on the head group offset from the  $(\sqrt{3} \times \sqrt{3})R30^\circ$  sites.

The position of the head groups also depends on the interaction at the Au-S interface. The preferred sites are determined by the tetrahedral coordination and the  $sp^3$  hybridization of the sulfur head groups. Relaxation and reconstruction (involve adatoms and/or surface vacancies) of the substrate also has significant influence on the preferred adsorption sites. We begin by determining the preferred positions of the head group on the unrelaxed substrate driven by the interaction at the Au-S interface alone. We then use the unrelaxed substrate as our reference to study the effect of substrate relaxation on the head group positions.

To simulate a realistic model of the technologically interesting long-chain dense-phase alkanethiol SAM, we need to combine the effect of the chain packing and the interaction at the Au-S interface. Currently, we do not have a site-dependent force field for the Au-S interface to simulate the SAM structure using MD. On the other hand, the size of the problem is computationally too large for the DFT method. We demonstrated an approach to bridge the computational gap by using the atomic structure at the Au-S interface predicted by the DFT to study the effect on the chain packing. Using our DFT results, we predicted the symmetry of the adsorption site dependent dihedral force fields that can be used in MD to improve the prediction of the SAM structure.

# Chapter 1: Background and Scope of the Thesis

## 1.1 Introduction

Alkanethiol self-assembled monolayers (SAMs) of Au(111) are the most widely studied ordered monolayer systems in the last 35 years<sup>1</sup> because of their potential applications in organic electronics,<sup>2-3</sup> nanotechnology,<sup>4</sup> lithography,<sup>5-6</sup> surface coating for corrosion prevention,<sup>7</sup> chemical sensing,<sup>8</sup> and many others.<sup>9-12</sup> A detailed understanding of the relationship between the properties of the SAM and the underlying structure is desired to fully harness their potential applications. The structure of the SAM is determined by the spontaneous assembly of alkanethiol molecules.

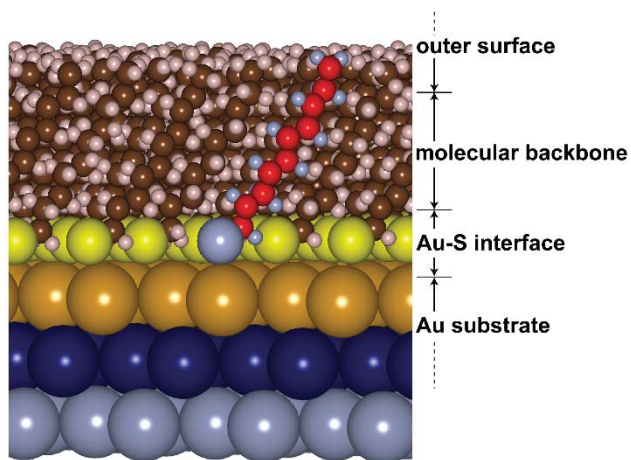


Figure 1.1 Three Regions of the Alkanethiol SAM. The outer surface, the molecular backbone, and the Au-S interface.

The thiol head group of the molecule attaches to the Au substrate via a strong Au-S covalent bond. As the surface density of alkanethiol increases, the interchain van der Waals (vdW) interaction between the alkane chains leads to an ordered 2D crystalline SAM structure. This saturation-coverage dense-phase (one alkanethiol molecule for every three surface

Au atoms) SAM structure can be divided into three regions (Figure 1.1): the outer surface (monolayer-air interface), molecular backbone (alkyl chains), and the Au-S interface at the Au(111) substrate. The structure is controlled by the interplay between the alkyl-chain packing and Au-thiol adsorption interface.<sup>13</sup> The adsorption energy of the monolayer increases with increasing alkyl chain length due to vdW interaction. It is generally accepted that Au(111) undergoes a complex reconstruction, however, there is little consensus on the structure of the Au-S interface beyond its  $(2\sqrt{3} \times 3)\text{rect.}$  symmetry and four molecules per unit cell.

In this thesis, we present an extensive study of chain packing and Au-S interface structure using molecular dynamics (MD) and density functional theory (DFT) simulations. The MD simulation is used to study the packing of decanethiol (C10) molecules in a full-density ensemble of 100 molecules for a simulation time longer than 50 nsec. Whereas the computationally more expensive DFT simulation is used to study the electronic and structural properties of thiol adsorption of an isolated methanethiol (C1) molecule. Our study revealed that the most efficient chain packing offsets the S head groups from the ideal  $(\sqrt{3} \times \sqrt{3})R30^\circ$  positions into a  $(2\sqrt{3} \times 3)$ rect. superlattice overlayer. We also demonstrated for the first time that the structure at the Au-S interface is driven by the hybridization of the sulfur head groups.

## 1.2 Nature of the Problem

In this section we discuss the current understanding of the SAM structure. We begin with the structure at the outer interface and the orientation of the molecular backbone. The Au-S interface is discussed including proposed structures, which are categorized according to the adsorption sites and the number of adatoms and local vacancies per unit cell.

Before delving into discussion of the structure, we first define the key structural parameters of the molecules in the SAM as these are essential for our later discussion. Figure 1.2 shows a diagram of a molecule in a SAM defining the tilt ( $\theta$ ), twist ( $\phi$ ), and tilt direction ( $\chi$ ) for the molecule in the idealized all-trans conformation. The tilt direction is defined with respect to a reference direction,

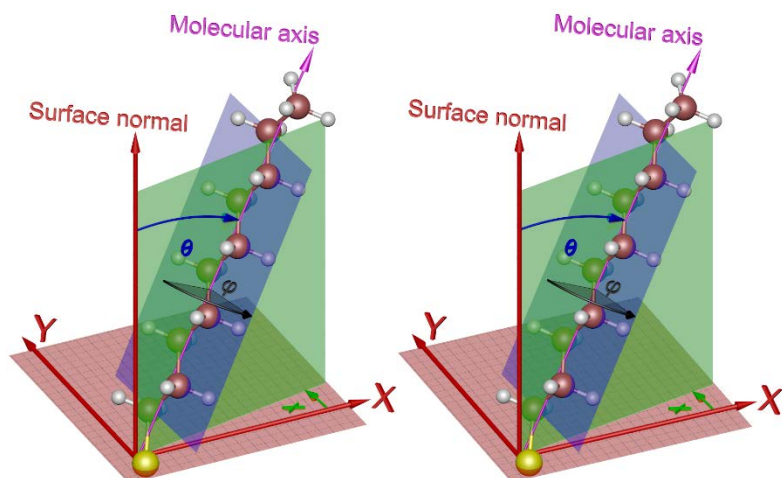


Figure 1.2. A Parallel-view Stereo Image Pair of the Molecular Geometry. In this alkyl-chain centric model, the molecular axis passes through the origin where it intersects the surface. The tilt angle ( $\theta$ ) defined by the angle between the surface normal and the axis of the molecule (molecular axis). The twist of the molecular backbone ( $\phi$ ) is defined by the angle between the tilt plane (green plane) containing the surface normal and the molecular axis and the plane of the alkyl carbon atoms (blue plane). Zero twist angle is defined where these two planes coincide and the bond between the head group and the alpha methylene makes the largest angle with respect to the surface normal ( $\alpha$ -CH<sub>2</sub> is closer to the substrate). A positive increasing twist angle is defined in the counterclockwise direction while looking down the molecular axis toward the surface as is standard for a right-handed coordinate system. The direction of the tilt angle ( $\chi$ ) is the angle between the positive x-axis and the projection of the molecular axis on the plane of the substrate (xy-plane).

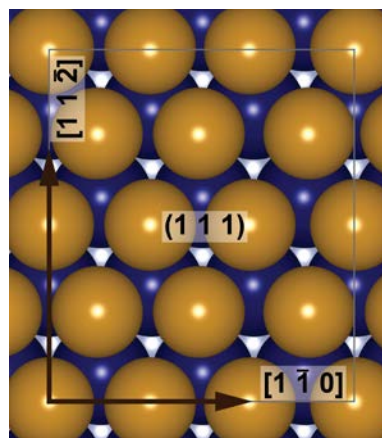


Figure 1.3. The  $(2\sqrt{3} \times 3)$ rect. Unit Cell on an Unreconstructed Au(111) Surface. The six  $\langle 110 \rangle$  directions are symmetry equivalent for the unreconstructed Au(111) and the  $(\sqrt{3} \times \sqrt{3})R30^\circ$  overlayer. The  $(2\sqrt{3} \times 3)$ rect. in general renders all six  $\langle 110 \rangle$  directions inequivalent, depending on the symmetry of the basis.

on the surface (x-axis in Figure 1.2), which is typically the Au $\langle 110 \rangle$  direction and nominally the next-nearest-neighbor (NNN)

direction in the SAM (see Figure 1.3). The molecular axis for an all-trans chain bisects the C-C bonds, Figure 1.2. In general, we define the molecular axis as the best-fit line to the midpoints of the C-C bonds. The twist angle is defined as the rotation of the plane of the carbon atoms around the molecular axis (molecule's long axis) and is right-handed with respect to the axis originating on the surface. The twist angle zero is defined as the angle where the molecular plane and the tilt plane coincide, and the alpha methylene is closest to the surface. These angles are most structurally

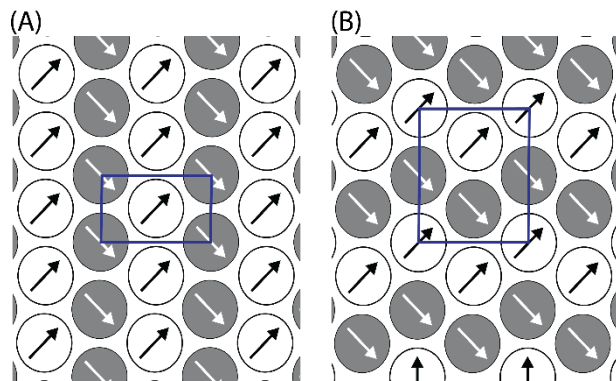


Figure 1.4. Two Possible Superlattice Symmetries for a 1:1 Ratio of the Two Molecule Types in a  $(\sqrt{3} \times \sqrt{3})R30^\circ$  Lattice. (A) 2-molecule basis unit cell  $(\sqrt{3} \times 3)\text{rect.}$  (herringbone), and (B) 4-molecule basis unit cell  $(2\sqrt{3} \times 3)\text{rect.}$  (zig-zag) structures. The arrow within the circles are representing the orientation of the backbone.

descriptive for chains that are close to the all-trans conformation which have a well-defined molecular backbone plane.

### 1.2.1 Outer Surface

The structure of the outer (methyl) interface of alkanethiol SAMs is determined by the packing of the alkane chains and the structure of the Au-S interface. Experimental observations with scanning tunneling

microscopy (STM)<sup>14</sup> and He atom diffraction<sup>15</sup> found the methyl groups form a  $(\sqrt{3} \times \sqrt{3})R30^\circ$ -related close packed structure with a  $(2\sqrt{3} \times 3)\text{rect.}$  four-molecule basis superlattice, commonly called  $c(4 \times 2)$  in the literature.<sup>16</sup> STM typically observes the four symmetry inequivalent molecules as two zig-zag rows (Figure 1.4.B), one row higher than the other, but several other phases of this superlattice structure are also observed.<sup>17-21</sup> The proposed hypotheses attribute the height variation to different twists of the alkyl backbones, the adsorption site, or a combination of these factors.<sup>13, 16, 19</sup> The extent to which these phases are an artifact of the STM imaging conditions or are actually different SAM structures is not yet understood.

### 1.2.2 Molecular Backbone

Within the SAM, the methylene chains organize by the vdW interaction to form a close-packed crystalline structure adopting the all-trans configuration. Infrared reflection absorption spectroscopy (IRRAS)<sup>22-23</sup> shows that the efficient packing of the molecules results in two groups

of molecules with nearly mutually orthogonal backbone twist ( $50^\circ$  and  $132^\circ$ ). The principle experimental measurements of the twist of the alkyl-chain plane ( $\varphi$ ) in SAMs comes from IRRAS. Nuzzo et al.<sup>22, 24</sup> use a single-chain per unit-cell model and report a twist angle of  $55^\circ$ . The most recent study of Laibinis, et al.<sup>2</sup> followed up the previous work using a two-chain per unit-cell model and report twist angles of  $-48^\circ$  and  $+50^\circ$ . We use this latter work for comparison to our simulations. Because a clear and consistent definition of the molecular twist angle is critical for comparison of simulation and experiment, and because the definition of  $\varphi$  (and its zero) in ref. 2 is muddled by the introduction of positive and negative tilt angles, we will discuss the definition in detail for further clarification.<sup>25</sup> We also justify our interpretation of the reported twist angles as  $\varphi = +132^\circ$  and  $+50^\circ$ , based on the inherent symmetries and the discussion in ref. 2.

The molecular geometry of an all-trans alkane chain can be visualized by applying three rotations to the molecule. We begin with the molecule standing straight up on the surface (xy-plane) with the alkyl-chain axis (molecular axis) aligned with the surface normal (z-axis). The alkyl plane is aligned with the xz-plane, with the projection of the S to  $\alpha$ -CH<sub>2</sub> bond vector pointing in the +x-direction. This standing up conformation of the molecule corresponds to zero tilt ( $\theta = 0^\circ$ ) and zero twist ( $\varphi = 0^\circ$ ). Now, rotation of the standing up alkane chain about its molecular axis (z-axis) in the counterclockwise direction (while looking down the molecular axis toward the surface) introduces positive twist. The tilt of a molecule is achieved by rotation of the molecular axis about the y-axis where tilting towards the +x-axis is described as a positive tilt. For tilt direction ( $\chi$ ), the tilted molecule is again rotated around the z-axis (rotation from +x-axis to +y-axis is defined as the positive  $\chi$ ). Stated another way, the angles are defined using the right-handed coordinate convention.

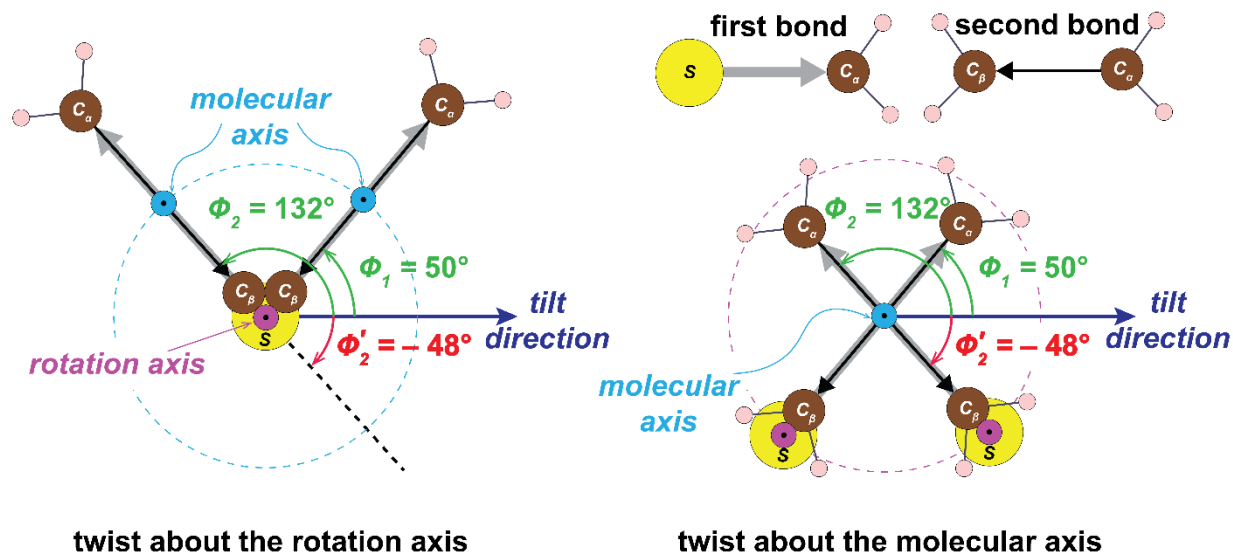


Figure 1.5. The Molecular Twist in Two Different Reference Frames. Left) The view in the frame of the physical rotation, looking down the rotation axis with the sulfur fixed on the surface. The  $\beta$ -CH<sub>2</sub> hydrogens are left out for clarity. Right) The view in the frame of the molecular axis, looking down the chain. Changing the twist causes the molecular axis to precess around the rotation axis. The sulfur to  $\alpha$ -CH<sub>2</sub> vector shown as the thick gray arrow. The  $\alpha$ -CH<sub>2</sub> to  $\beta$ -CH<sub>2</sub> vector is shown as the thin black arrow. The two twist angles from Laibinis et. al. are depicted.<sup>2</sup>

Figure 1.5 shows two views of the molecular twist looking along the physical rotation axis (Figure 1.5, Left) and the molecular axis (Figure 1.5, Right). The twist of a chain is defined by the relative orientation of the carbon plane and the tilt plane, as shown in Figure 1.2. For an all-trans chain in this projection, the twist angle is defined by the angle between the tilt direction and the first bond (S- $\alpha$ CH<sub>2</sub>). With the sulfur fixed on the surface, changing the twist angle causes the molecular axis to precess around the sulfur. These two representations of molecular twist are later used to quantify the offset of the sulfur head group from the ideal  $(\sqrt{3} \times \sqrt{3})R30^\circ$  lattice and deviation of the chain packing from the ideal closed-pack structure. Changing the twist also changes the Au-S-CH<sub>2</sub> bond angle. Twisting a single chain within a SAM would also change its distance to neighboring chains. We depict two twist angles,  $\phi = +132^\circ$  and  $+50^\circ$  (see the discussion below).

For a full understanding of the reported  $\varphi$  values in ref. 2, we need to discuss the basics of the IRRAS measurement and how  $\varphi$  is determined. IRRAS is sensitive to the orientation of the transition dipole of the mode in the monolayer. The component of the transition dipole normal to the metallic substrate (Au(111) in our case) contributes to the IRRAS absorption, while the parallel component to the substrate is strongly suppressed. Consequently, the observed intensity varies with the cosine squared of the angle of the mode with the surface normal. The angle of the mode to the surface normal can be obtained by comparing the intensity in the film to that of a suitable reference phase. Typically, a polycrystalline solid phase alkanethiol or disulfide has been used, which has alkyl chain conformations and molecular environment closely related to that found in SAMs. This approach also relies on the assumption that the transition dipole strength in the SAM is the same as that in the reference phase. This assumption has been shown to work well for the methylene stretching modes, but not so well for the methyl stretching modes,<sup>2, 22, 24</sup> as we will discuss.

The infrared modes used to measure the chain twist are those of the  $d^+$  and  $d^-$  methylene stretching. These two modes and the molecular axis are mutually orthogonal. The  $d^+$  involves the  $\text{CH}_2$  symmetric stretching, where the stretching vibration of the odd and even  $\text{CH}_2$ s are  $180^\circ$  out of phase—antisymmetric in the plane of the chain. The  $d^-$  involves the  $\text{CH}_2$  antisymmetric stretching, where the stretching vibration of the odd and even  $\text{CH}_2$ s are in phase—antisymmetric out of the plane of the chain. For a given tilt angle, the  $d^+$  intensity will be maximum at  $\varphi = 0^\circ$  and  $180^\circ$  and zero at  $90^\circ$  and  $270^\circ$ . The  $d^-$  intensity is offset by  $90^\circ$ , with maxima at  $\varphi = 90^\circ$  and  $270^\circ$  and zeros at  $0^\circ$  and  $180^\circ$ . These properties give the mode intensities  $C_2$  symmetry about the molecular axis ( $\varphi = \varphi + 180^\circ$ ) as well as two mirror planes—the tilt plane ( $\varphi = -\varphi$ ) and the plane perpendicular to the tilt plane containing the molecular axis ( $\varphi = 180^\circ - \varphi$ ). As a result, methylene



modes alone cannot distinguish between symmetry equivalent twists, i.e.  $\varphi = -50^\circ, +50^\circ, +132^\circ$ , and  $-132^\circ$  will have the same  $d^+$  and  $d^-$  intensities.

The three methyl stretching modes have different symmetry with respect to the twist angle and should in principle further constrain the twist angle. The  $r^+$  symmetric stretch is oriented along the  $\text{CH}_2\text{-CH}_3$  bond. The  $r_a^-$  antisymmetric stretch is perpendicular to the  $\text{CH}_2\text{-CH}_3$  bond and in the plane of the alkyl chain. The  $r_b^-$  antisymmetric stretch is perpendicular to the  $\text{CH}_2\text{-CH}_3$  bond and perpendicular to the plane of the alkyl chain. Unlike the symmetry of the methylene modes, the methyl  $r^+$  and  $r_a^-$  modes possess only mirror plane symmetry—the tilt plane ( $\varphi = -\varphi$ ). The  $r_b^-$  mode has the same symmetry as the methylene  $d^-$  mode. The lower symmetry of the methyl modes could further constrain the twist angle within the tilt-plane mirror symmetry. Twist angles in the range  $90^\circ$  to  $270^\circ$  orient the  $\text{CH}_2\text{-CH}_3$  bond more normal to the surface—increasing the intensity of  $r^+$  mode and decreasing the intensity of  $r_a^-$  mode. Whereas, twist angles in the range  $-90^\circ$  to  $+90^\circ$  orient the  $\text{CH}_2\text{-CH}_3$  bond more parallel to the surface—increasing the intensity of  $r_a^-$  mode and decreasing the intensity of  $r^+$  mode. Therefore, these two modes can be used to distinguish twists related by  $C_2$  symmetry about the molecular axis and mirror symmetry about the plane perpendicular to the tilt plane containing the molecular axis. However, the methyl modes are complicated by Fermi resonances and the intensities in the SAM do not correspond as well with the reference phase as do the methylene modes. Since the methyl mode intensities do not correspond well to the reference phase, good fits for  $\text{CH}_2$  and  $\text{CH}_3$  modes could not be achieved by twisting the molecule alone. In addition, the  $r_b^-$  is weaker in the SAM and appears as a shoulder on the stronger  $r_a^-$ , thus not as useful for molecular orientation. Therefore, more interpretation was required.

Given these symmetries, it is perplexing why Laibinis. et al. report  $\varphi = -48^\circ$  and  $+50^\circ$ , which should be practically indistinguishable from the methylene and methyl modes. They use two arguments to guide their interpretation. First, the observed odd-even methyl-mode intensity oscillation. Second, the hypothesis that the surface-S-CH<sub>2</sub> bond orientation and/or torsion angles should be the same for all the molecules. The latter is quite reasonable from the prevailing view at the time, that all the molecules had the same adsorption site, but is not generally the case for the models we consider in our work presented here. Below, we discuss the former line of reasoning.

The intensity of the  $r^+$  mode is observed to be strongest for even-length chains and lower for odd-length chains. The  $r_a^-$  mode displays the opposite odd-even dependence. The conclusion is that the CH<sub>2</sub>-CH<sub>3</sub> bond is more normal to the surface for even than for odd.<sup>26</sup> This supports the hypothesis that the twist angle is in the range  $-90^\circ$  to  $+90^\circ$ . However, their models over predict the magnitude of the oscillation by factor of 2–3 (ref. 2, Figure 5). Nevertheless, they say the two twist angles were restricted to the range of  $-90^\circ$  to  $+90^\circ$  for their fitting. This was argued as satisfying the “methyl surface corrugation” (ref. 2 footnote 43), which we presume to mean the orientation of the methyl groups. This choice of twist angles has the effect of increasing  $r^+$  at the expense of  $r_a^-$ . Reasonable fits of the methyl modes required assuming 45% gauche fraction (defined later) of the C-C-C-CH<sub>3</sub> bond. That equally good fits could have been obtained choosing instead  $\varphi = +132^\circ$  and  $+50^\circ$  seems likely given the data shown in (ref. 2, Figures 8 and 9). Although that choice would make the surface-S-CH<sub>2</sub> bond orientation and/or torsion angles different for the two twist classes. There is also a logical inconsistency in the discussion of the angular difference between the two twist angles. The discussion concludes the difference should be  $82^\circ$ , but the difference between the reported angles is  $98^\circ$ . The choice of  $\varphi = +132^\circ$  and  $+50^\circ$  would satisfy the  $82^\circ$  difference.

The presence of two molecular twists within the unit cell (as opposed to the existence of two phases with different twists) was confirmed from the factor splitting of the scissoring deformation mode of the CH<sub>2</sub> at low temperature observed by IRRAS.<sup>27</sup> Factor splitting also is observed in the orthorhombic phase of crystalline *n*-alkanes, where the all-trans alkane twists adopt the 2-molecule basis herringbone structure (Figure 1.4.A).<sup>28</sup> Drawing analogy with the alkane bulk crystal, a herringbone arrangement of the backbone twists was proposed for the alkanethiol SAMs on Au(111). Although the *n*-alkanethiol SAMs and *n*-alkane crystal share some structural features in common, *viz.* the density of the hydrocarbon chains and two mutually orthogonal twists per unit cell, the SAM has additional constraints imposed by the adsorption sites. As a result, the zig-zag structure (4-molecule basis with two molecules of each twist, Figure 1.4.B) agrees best with the available data<sup>16</sup> rather than the herringbone structure.

In an ordered SAM all the molecules will have the same tilt angle and tilt direction. The tilt angle can be easily understood from the classic description of SAM formation where the sulfur atoms adsorb in  $(\sqrt{3} \times \sqrt{3})R30^\circ$  sites with the alkyl chains initially perpendicular to the surface. The resulting interchain distance is larger than optimal, so the alkyl chains lean over, tilting away from the surface normal, to optimize the interchain vdW interaction. The tilt angle is closely associated with order and the density of the monolayer, with all-trans chains packing most efficiently forming the largest tilt angles and highest volume density. The tilt angle has been measured using optical ellipsometry,<sup>29</sup> diffraction techniques,<sup>30</sup> and IRRAS.<sup>22, 29</sup> Measured values range 25–35°.

The existence of the superlattice and deviation from  $(\sqrt{3} \times \sqrt{3})R30^\circ$  adsorption sites in the  $(2\sqrt{3} \times 3)\text{rect.}$  breaks the simple 2D symmetry of the surface, rendering the six Au<110> directions inequivalent. For the highest symmetry case of unreconstructed Au(111) with a  $(\sqrt{3} \times \sqrt{3})R30^\circ$

overlayer, all the Au<110> directions in the plane are equivalent, therefore all six next nearest neighbor directions are equivalent. By contrast, a  $(2\sqrt{3} \times 3)$ rect. overlayer with a four-molecule basis composed of two groups of conformationally distinct molecules adsorbed in  $(\sqrt{3} \times \sqrt{3})R30^\circ$  sites (e.g. Figure 1.4.B) reduces that symmetry to two different groups of equivalent NNN directions, two in the zig-zag row direction and four at  $60^\circ$  to the zig-zag rows. Addition of complex surface reconstructions within the  $(2\sqrt{3} \times 3)$ rect. unit cell then lead to deviations from  $(\sqrt{3} \times \sqrt{3})R30^\circ$  adsorption sites and/or three or more structurally inequivalent molecules will remove those symmetries resulting in six distinct NNN directions. Thus, the SAM basis may not possess any symmetry beyond  $p1$ .

The alkyl chains are known to be predominantly in the all-trans conformation at room temperature from IRRAS.<sup>22, 27, 31</sup> Both infrared measurements and MD simulations show that the conformational order decreases with decreasing chain length and decreases with increasing temperature. Most of the gauche defects are concentrated near the methyl termini at 300 K but penetrate deeper into the monolayer as the temperature is increased.<sup>32</sup> The deviation from all-trans can be quantified by the gauche fraction.

In the all-trans configuration of the alkyl chain, all the carbon atoms lie on a plane—the molecular plane (Figure 1.2, blue plane). Thermal motion causes the carbon atoms to deviate from the all-trans molecular plane. Excursions of each C–C–C bond dihedral angle ( $\psi$ ) from the trans energy well into the adjacent gauche wells can be quantified by the gauche fraction. The torsion

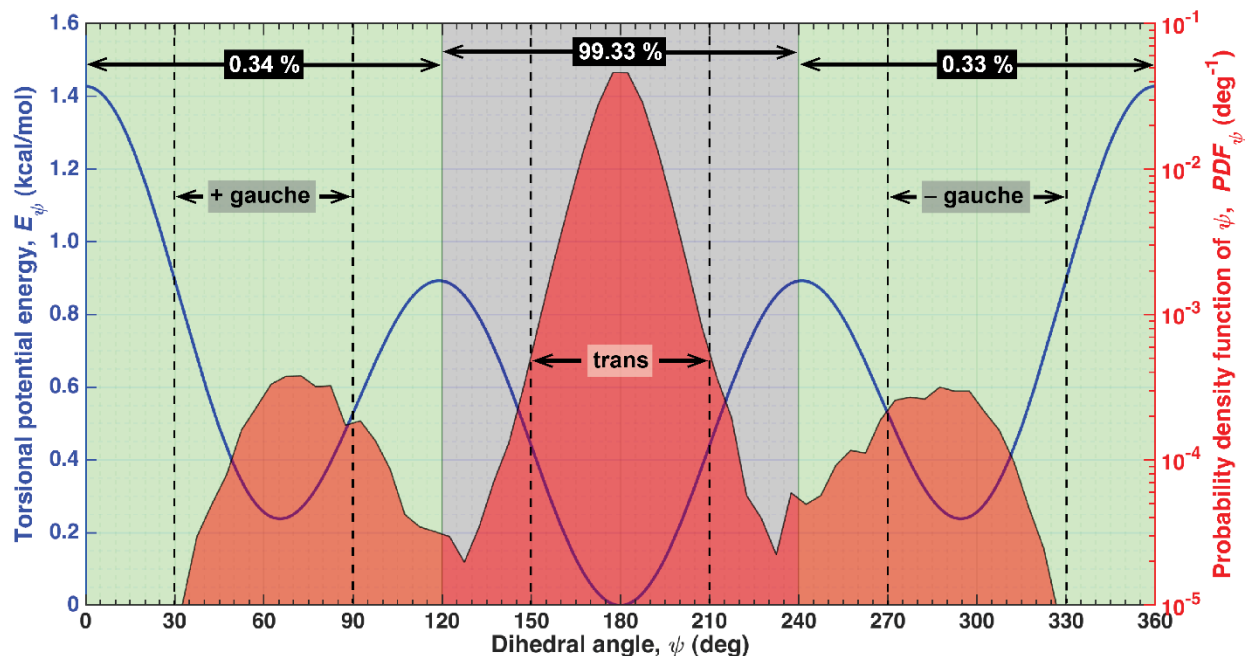


Figure 1.6. The C–C–C–C Dihedral Potential Energy and the Corresponding Population of the Dihedral Angle. The trans and two gauche conformations are noted. On the right y-axis, we plotted the probability density function of the dihedral angle ( $PDF_{\psi}$ ) for model-A at 200 K (see Chapter 5 for model-A). We use semi-log axis for  $PDF_{\psi}$  to better illustrate the gauche population as gauche population is significantly smaller than the trans population.

around the  $C_i-C_{i+1}$  bond is characterized by the  $C_{i-1}-C_i-C_{i+1}-C_{i+2}$  dihedral angle, defined by the angle between the planes containing  $C_{i-1}, C_i, C_{i+1}$  and  $C_i, C_{i+1}, C_{i+2}$  where the anticlockwise rotation of the  $C_{i+1}-C_{i+2}$  bond about the  $C_i-C_j$  bond defines the positive increment of  $\psi$  keeping the  $C_{i-1}-C_i$  bond unchanged. For a C10 molecule the index  $i$  runs from 1 to 8, where  $C_1$  is the alpha carbon and  $C_0$  is the sulfur.

The C-C-C-C dihedral potential ( $E_\psi$ ) is shown in Figure 1.6 (left vertical axis). There is a global energy minimum at  $180^\circ$  (trans, antiperiplanar) and two local minima at  $65^\circ$  and  $295^\circ$  (gauche, synclinal).<sup>33</sup> The C-C-C-C bond conformation is termed trans (all four carbon atoms lie on a plane) when  $150^\circ \leq \psi \leq 210^\circ$  corresponding to the minimum energy configuration of  $\psi$ . Deviation from the trans conformation could result in one of the two gauche conformations namely positive gauche (+gauche) and negative gauche (-gauche) and they are defined as follows: for +gauche,  $30^\circ \leq \psi \leq 90^\circ$  and for -gauche,  $270^\circ \leq \psi \leq 330^\circ$ .<sup>34</sup>

The  $\psi$  probability density function ( $PDF_\psi$ ) for model A at 200 K is overlaid in Figure 1.6 (right vertical axis) showing the distribution of dihedral angles. The semi-log  $PDF_\psi$  plot shows most of the dihedral angles lie in the trans well (99.33 %) with a very small population in the gauche wells (0.67 %), i.e. molecules are predominantly trans in the monolayer. Consistent with previous studies, most of the gauche conformations reside at the surface.<sup>32</sup> The terminal dihedral bonds have a 4.5% gauche fraction, which is 85% of the gauche population in the monolayer. Note the local maxima of the  $PDF_\psi$  for the gauche conformations does not occur at the gauche potential energy minima, but is biased towards the trans conformation side of the wells. This is because the molecules are also subject to C-C-C-H and H-C-C-H dihedral potentials— $PDF_\psi$  is a system property.

For the purpose of characterizing the gauche fraction, dihedral angles  $0-120^\circ$  are counted as +gauche and  $240-360^\circ$ , as -gauche, corresponding to the potential energy wells, shown as two green regions in Figure 1.6. The gauche fraction is calculated as follows:

$$\frac{N_{+gauche} + N_{-gauche}}{N_{total}} \times 100\% .$$

Here  $N_{+gauche}$ ,  $N_{-gauche}$ , and  $N_{total}$  are the population of the dihedral angle in the positive and negative gauche regions and the total population of the C-C-C-C dihedral angle respectively. Such that  $N_{total} = N_{+gauche} + N_{-gauche} + N_{trans}$ .

Conformational defects in the alkyl chains can significantly influence the structure of the monolayer. Disorder in the alkyl chain reduces the volume density because increasing gauche fraction effectively increases the diameter of the chain (becoming shorter and fatter) evolving toward a random coil in the limiting case.<sup>31</sup> Hence, for a fixed surface density of molecules, the fatter the chain becomes, the smaller the tilt angle. For the modest temperatures of interest in our study, the effect of gauche defects is to slightly decrease the tilt angle of the chains.

### ***1.2.3 Au-S interface***

The most poorly understood part of the SAM is the Au-S interface, which is generally accepted to involve a complex reconstruction of the Au(111) surface with Au adatoms and/or Au vacancies. The sulfur adsorption site is also a subject of debate and may involve a combination of different adsorption sites. There is yet no consensus among the experimental measurements beyond the basic symmetry. The simultaneous existence of multiple Au-S interfacial structures would greatly complicate interpretation of experimental measurements that probe areas larger than the typical structural domains (10-20 nm in typical room temperature prepared samples), which is a criticism of the probes most sensitive to the Au-S interface. We now summarize the key issues of the Au-S interface to facilitate discussion.

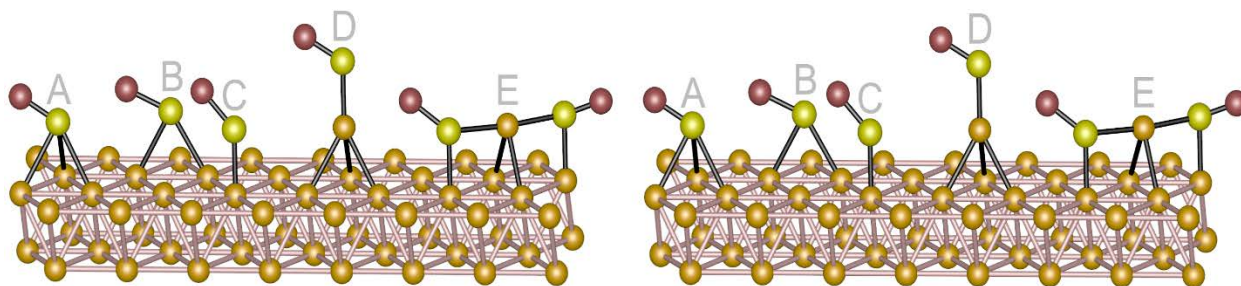


Figure 1.7. An Eye-cross Stereo Image Pair of Five Different Bonding Scenarios at the Au-S Interface. A, B, and C) The S atoms are directly connected to the substrate at hollow, bridge, and atop sites respectively. D) The S atom is attached on top of an Au adatom, which is connected to the substrate at the hollow site. E) The staple motif is composed of a bridge-site Au adatom with two S atoms on the adjacent atop sites.

### 1.2.3.1 Adsorption Sites

The structure of the SAM will be determined by the energetics at the Au-S interface and the bonding to the substrate. Early work assumed the thiol sulfur adsorbed in a 3-fold hollow site by analogy to the known adsorption site for atomic sulfur on Au(111).<sup>35</sup> Subsequent studies with density functional theory (DFT) found the bridge-fcc site to be the most energetically stable adsorption site for the unreconstructed Au(111).<sup>36-41</sup> However, the Au(111) substrate reconstructs upon adsorption, creating new types of adsorption sites.<sup>18, 42-46</sup> Reimers et al. has proposed a strong dispersion character of the bond between the sulfur and the gold atoms, which is best understood as an Au(0)-thiyl species rather than an Au(I)-thiolate species.<sup>47</sup> Experimental techniques to probe the structure of the reconstructed Au-S interface, e.g. STM,<sup>48</sup> GIXRD,<sup>44, 49-51</sup> LEED,<sup>52</sup> XSW,<sup>45, 53</sup> and SFG,<sup>46</sup> in combination with ab initio based modeling<sup>39, 41</sup> have yielded models with a variety of sulfur adsorption sites. For discussion we break these into two groups, adsorption sites where the sulfur adsorbs only to the nominally Au(111) surface atoms and adsorption sites that involve Au adatoms (Figure 1.7) and/or Au vacancies. The most energetically favored adsorption sites for the thiol sulfur on the unreconstructed Au(111) surface are on the bridge site (Figure 1.7.B) and slightly offset from the a-top site (Figure 1.7.C).<sup>54</sup> Participation of Au adatoms increases the array



of possibilities. The simplest sulfur adsorption site is on top of an Au adatom (RS-Au<sub>ad</sub>), which in turn sits in an Au(111) fcc or hcp 3-fold hollow site, (Figure 1.7.D).<sup>52-53, 55</sup> More complex adsorption sites involve bonding to the adatom and the Au(111) surface, the most common is the staple motif (RS-Au<sub>ad</sub>-SR), (Figure 1.7.E).<sup>56-62</sup> The Au adatom in the staple is bonded to the two bridge-site Au surface atoms, with the related thiol sulfur atoms at the adjacent atop sites bonded to the adatom and the substrate atom.<sup>47</sup> The staple can be extended (RS-Au<sub>ad</sub>-SR-Au<sub>ad</sub>-SR) and concatenated into a linear zig-zag chain (across unit cells) or form cyclic structures (within a unit cell).<sup>50, 56, 62</sup> The models examined in this study incorporate a variety of adsorption site combinations.

### *1.2.3.2 Evidence of Reconstruction, Adatoms, and Vacancies*

The unreconstructed Au(111) surface ( $2\sqrt{3} \times 3$ )rect. unit cell contains 12 Au atoms. An integer number of adatoms or vacancies per unit cell correspond to fractional coverages of adatoms and vacancies ( $\theta_{ad}$  and  $\theta_{vac}$ , respectively) in multiples of 1/12 (~0.083). STM studies find two thiols per adatom in circumstances where the sulfur and the Au adatoms can be imaged directly.<sup>48, 63-64</sup> However those are for SAMs of short chain thiols and for low coverage SAMs of long chain thiols where the alkyl chains lay flat on the surface. STM cannot image the sulfur or adatoms in the high coverage phase that is of most interest. Relatively few quantitative measurements of the adatom coverage have been performed and these measure the net coverage ( $\theta_{net} = \theta_{ad} - \theta_{vac}$ ) comparing the bare Au surface to the same surface with a SAM.<sup>65</sup> Studies measuring the coverage of vacancy islands formed during SAM growth find it to be between  $\theta_{net} = 0.04-0.16$ , assuming the vacancy islands result from Au atoms pulled from the Au(111) substrate, after the herringbone reconstruction is lifted.<sup>43, 58, 66-68</sup> In the reverse process, atomic hydrogen was used to gently

remove a SAM leaving the bare Au(111) herringbone reconstruction. The Au atoms released in this process ( $\theta_{\text{net}} = 0.143 \pm 0.033$ ) were measured by STM before and after imaging of the same area.<sup>69</sup> Both of these measurements are consistent with 2 adatoms per unit cell ( $\theta_{\text{ad}} = 0.167$ ) in agreement with the models suggesting 2 RS-Au<sub>ad</sub>-SR species, provided  $\theta_{\text{vac}} = 0$ .<sup>56, 58-59</sup>

The presence of adatoms indicates that surface Au vacancies must also form during SAM growth, as is evident from the Au vacancy islands observed after SAM growth. Although this does not mean the Au vacancies are part of the reconstructed unit cell. Interpreting the vacancy coverage is complicated in studies using samples grown from solution at room temperature, where the SAM structural domains are small (10–20 nm) and coexist with a high density of small vacancy islands. There seems to be ambiguity in the GIXRD experiments whether the measured  $\theta_{\text{vac}}$  is due to vacancies that are part of the reconstruction, vacancy islands, or a combination.<sup>49</sup>

### 1.3 Scope of this Thesis

In this thesis, we focus on two regions of the SAM structure: the molecular backbone and the Au-S interface. Classical MD is used to study the packing of the alkane chains that determines the structure of the backbone. The electronic properties at the Au-S interface are explored using dispersion corrected DFT simulation. The next two chapters (chapter 2 and 3) lay out the foundation for the MD and DFT simulation which we used in the rest of the thesis. A fixed unrelaxed Au(111) substrate is used to study the packing of decanethiol SAM in chapter 4. We constrained the head groups at the ideal ( $\sqrt{3} \times \sqrt{3}$ )R30° sites to determine the structure with the minimum energy. We used this as our reference system. Then we allow in-plane displacement of the head groups which is driven by the close-packed structure of the alkane chains. In chapter 4, we study the relationship between the close-packed structure and the head group offset from the

ideal sites. In the next chapter (chapter 5), we study the chain packing for several proposed reconstructed Au-S interfaces at different simulation temperatures. The Au-S interfaces involve adatoms and/or surface vacancies and are kept fixed throughout the simulation. We compare our simulation with experimental observations at different temperatures. Our results clearly demonstrate the importance of the Au-S interface on the chain packing and hence the overall structure of the SAM. Given the importance of the Au-S interface, we studied the electronic properties of this interface in chapter 6 and 7 with an isolated methanethiol molecule to minimize the interaction between adsorbates. A detailed study of thiol adsorption across unrelaxed Au(111) substrate is presented in the chapter 6. The bonding geometry of methanethiol shows a strong preference for the  $sp^3$  hybridization of the sulfur head group which is also used to explain the staple structure. In chapter 7, we explored the contribution of the surface relaxation on the methanethiol adsorption at the bridge site. Our result shows that the bridge-site asymmetry is enhanced by the relaxation of the surface. In the final chapter (8) of the thesis we highlight the physical insights and their implication on a broader community.

## 1.4 References

1. Nuzzo, R. G.; Allara, D. L., Adsorption of Bifunctional Organic Disulfides on Gold Surfaces. *J. Am. Chem. Soc.* **1983**, *105* (13), 4481-4483.
2. Laibinis, P. E.; Whitesides, G. M.; Allara, D. L.; Tao, Y. T.; Parikh, A. N.; Nuzzo, R. G., Comparison of the Structures and Wetting Properties of Self-Assembled Monolayers of *n*-Alkanethiols on the Coinage Metal Surfaces, Copper, Silver, and Gold. *J. Am. Chem. Soc.* **1991**, *113* (19), 7152-7167.
3. Casalini, S.; Bortolotti, C. A.; Leonardi, F.; Biscarini, F., Self-Assembled Monolayers in Organic Electronics. *Chem. Soc. Rev.* **2017**, *46* (1), 40-71.
4. Love, J. C.; Estroff, L. A.; Kriebel, J. K.; Nuzzo, R. G.; Whitesides, G. M., Self-Assembled Monolayers of Thiolates on Metals as a Form of Nanotechnology. *Chem. Rev.* **2005**, *105* (4), 1103-1170.
5. Tarlov, M. J.; Burgess, D. R. F.; Gillen, G., UV Photopatterning of Alkanethiolate Monolayers Self-Assembled on Gold and Silver. *J. Am. Chem. Soc.* **1993**, *115* (12), 5305-5306.

6. Hartwich, J.; Dreeskornfeld, L.; Heisig, V.; Rahn, S.; Wehmeyer, O.; Kleineberg, U.; Heinzmann, U., STM Writing of Artificial Nanostructures in Ultrathin PMMA and SAM Resists and Subsequent Pattern Transfer in a Mo/Si Multilayer by Reactive Ion Etching. *Appl. Phys. A* **1998**, *66* (1), S685-S688.
7. Magnussen, O. M.; Vogt, M. R.; Scherer, J.; Behm, R. J., Double-Layer Structure, Corrosion and Corrosion Inhibition of Copper in Aqueous Solution. *Appl. Phys. A* **1998**, *66* (1), S447-S451.
8. Fujihira, M.; Tani, Y.; Furugori, M.; Akiba, U.; Okabe, Y., Chemical Force Microscopy of Self-Assembled Monolayers on Sputtered Gold Films Patterned by Phase Separation. *Ultramicroscopy* **2001**, *86* (1), 63-73.
9. Schilardi, P. L.; Azzaroni, O.; Salvarezza, R. C., A Novel Application of Alkanethiol Self-Assembled Monolayers in Nanofabrication: Direct Molding and Replication of Patterned Conducting Masters. *Langmuir* **2001**, *17* (9), 2748-2752.
10. Klutse, C. K.; Mayer, A.; Wittkamper, J.; Cullum, B. M., Applications of Self-Assembled Monolayers in Surface-Enhanced Raman Scattering. *J. Nanotechnol.* **2012**, *2012* (319038), 1-10.
11. Gooding, J. J.; Hibbert, D. B., The Application of Alkanethiol Self-Assembled Monolayers to Enzyme Electrodes. *Trends Anal. Chem.* **1999**, *18* (8), 525-533.
12. Celestin, M.; Krishnan, S.; Bhansali, S.; Stefanakos, E.; Goswami, D. Y., A Review of Self-Assembled Monolayers as Potential Terahertz Frequency Tunnel Diodes. *Nano Res.* **2014**, *7* (5), 589-625.
13. Vericat, C.; Vela, M. E.; Benitez, G.; Carro, P.; Salvarezza, R. C., Self-Assembled Monolayers of Thiols and Dithiols on Gold: New Challenges for a Well-Known System. *Chem. Soc. Rev.* **2010**, *39* (5), 1805-1834.
14. Widrig, C. A.; Alves, C. A.; Porter, M. D., Scanning Tunneling Microscopy of Ethanethiolate and *n*-Octadecanethiolate Monolayers Spontaneously Absorbed at Gold Surfaces. *J. Am. Chem. Soc.* **1991**, *113* (8), 2805-2810.
15. Chidsey, C. E. D.; Liu, G. Y.; Rowntree, P.; Scoles, G., Molecular Order at the Surface of an Organic Monolayer Studied by Low Energy Helium Diffraction. *J. Chem. Phys.* **1989**, *91* (7), 4421-4423.
16. Camillone, N.; Chidsey, C. E. D.; Liu, G.-Y.; Scoles, G., Superlattice Structure at the Surface of a Monolayer of Octadecanethiol Self-Assembled on Au(111). *J. Chem. Phys.* **1993**, *98* (4), 3503-3511.
17. Delamarche, E.; Michel, B.; Gerber, C.; Anselmetti, D.; Guentherodt, H. J.; Wolf, H.; Ringsdorf, H., Real-Space Observation of Nanoscale Molecular Domains in Self-Assembled Monolayers. *Langmuir* **1994**, *10* (9), 2869-2871.
18. Poirier, G. E.; Tarlov, M. J., The c(4×2) Superlattice of *n*-Alkanethiol Monolayers Self-Assembled on Au(111). *Langmuir* **1994**, *10* (9), 2853-2856.
19. Lüsse, B.; Müller-Meskamp, L.; Karthäuser, S.; Waser, R., A New Phase of the c(4 × 2) Superstructure of Alkanethiols Grown by Vapor Phase Deposition on Gold. *Langmuir* **2005**, *21* (12), 5256-5258.

20. Riposan, A.; Liu, G.-Y., Significance of Local Density of States in the Scanning Tunneling Microscopy Imaging of Alkanethiol Self-Assembled Monolayers. *J. Phys. Chem. B* **2006**, *110* (47), 23926-23937.
21. Mamun, A. H. A.; Son, S.-B.; Hahn, J.-R., Effects of Tunneling Current on STM Imaging Mechanism for Alkanethiol Self-assembled Monolayers on Au(111). *Bull. Korean Chem. Soc.* **2011**, *32* (1), 281-285.
22. Nuzzo, R. G.; Dubois, L. H.; Allara, D. L., Fundamental Studies of Microscopic Wetting on Organic Surfaces. 1. Formation and Structural Characterization of a Self-Consistent Series of Polyfunctional Organic Monolayers. *J. Am. Chem. Soc.* **1990**, *112* (2), 558-569.
23. Nuzzo, R. G.; Korenic, E. M.; Dubois, L. H., Studies of the Temperature-Dependent Phase Behavior of Long Chain *n*-Alkyl Thiol Monolayers on Gold. *J. Chem. Phys.* **1990**, *93* (1), 767-773.
24. Nuzzo, R. G.; Fusco, F. A.; Allara, D. L., Spontaneously Organized Molecular Assemblies. 3. Preparation and Properties of Solution Adsorbed Monolayers of Organic Disulfides on Gold Surfaces. *J. Am. Chem. Soc.* **1987**, *109* (8), 2358-2368.
25. The molecular symmetry relates the twist at positive tilt angle with the twist at negative tilt angle:  $\theta = -\theta$  and  $\varphi = 180^\circ + \varphi$ .
26. The discussion in Ref. 2 sometimes uses odd and even to refer to the number of methylenes  $\text{HS}(\text{CH}_2)_n\text{CH}_3$  and sometimes odd-even with respect to the total number of carbon atoms  $\text{HSC}_n\text{H}_{(2n+1)}$ .
27. Nuzzo, R. G.; Korenic, E. M.; Dubois, L. H., Studies of the Temperature-Dependent Phase Behavior of Long Chain *n*-Alkyl Thiol Monolayers on Gold. *J. Chem. Phys.* **1990**, *93* (1), 767-773.
28. Snyder, R. G., Vibrational Correlation Splitting and Chain Packing for the Crystalline *n*-Alkanes. *J. Chem. Phys.* **1979**, *71* (8), 3229-3235.
29. Porter, M. D.; Bright, T. B.; Allara, D. L.; Chidsey, C. E. D., Spontaneously Organized Molecular Assemblies. 4. Structural Characterization of *n*-Alkyl Thiol Monolayers on Gold by Optical Ellipsometry, Infrared Spectroscopy, and Electrochemistry. *J. Am. Chem. Soc.* **1987**, *109* (12), 3559-3568.
30. Strong, L.; Whitesides, G. M., Structures of Self-Assembled Monolayer Films of Organosulfur Compounds Adsorbed on Gold Single Crystals: Electron Diffraction Studies. *Langmuir* **1988**, *4* (3), 546-558.
31. Bensebaa, F.; Ellis, T. H.; Badia, A.; Lennox, R. B., Thermal Treatment of *n*-Alkanethiolate Monolayers on Gold, As Observed by Infrared Spectroscopy. *Langmuir* **1998**, *14* (9), 2361-2367.
32. Mar, W.; Klein, M. L., Molecular Dynamics Study of the Self-Assembled Monolayer Composed of  $\text{S}(\text{CH}_2)_{14}\text{CH}_3$  Molecules Using an All-Atoms Model. *Langmuir* **1994**, *10* (1), 188-196.
33. IUPAC. Compendium of Chemical Terminology, 2nd ed. (the "Gold Book"). Compiled by A. D. McNaught and A. Wilkinson. Blackwell Scientific Publications, Oxford (1997). XML on-

line corrected version: <http://goldbook.iupac.org> (2006-) created by M. Nic, J. Jirat, B. Kosata; updates compiled by A. Jenkins. ISBN 0-9678550-9-8. <https://doi.org/10.1351/goldbook.T06406>.

34. The definition of +gauche and -gauche is more obvious when the conformation is described in terms of the torsion angle. These describe the same angle, but the dihedral angle is defined between  $0^\circ$  and  $360^\circ$  with the zero at the cis conformation. The torsion angle is defined between  $-180^\circ$  and  $+180^\circ$  with the zero at the trans conformation.
35. Nuzzo, R. G.; Zegarski, B. R.; Dubois, L. H., Fundamental Studies of the Chemisorption of Organosulfur Compounds on Gold(111). Implications for Molecular Self-Assembly on Gold Surfaces. *J. Am. Chem. Soc.* **1987**, *109* (3), 733-740.
36. Gottschalck, J.; Hammer, B., A Density Functional Theory Study of the Adsorption of Sulfur, Mercapto, and Methylthiolate on Au(111). *J. Chem. Phys.* **2002**, *116* (2), 784-790.
37. Hayashi, T.; Morikawa, Y.; Nozoye, H., Adsorption State of Dimethyl Disulfide on Au(111): Evidence for Adsorption as Thiolate at the Bridge Site. *J. Chem. Phys.* **2001**, *114* (17), 7615-7621.
38. Vargas, M. C.; Giannozzi, P.; Selloni, A.; Scoles, G., Coverage-Dependent Adsorption of  $\text{CH}_3\text{S}$  and  $(\text{CH}_3\text{S})_2$  on Au(111): A Density Functional Theory Study. *J. Phys. Chem. B* **2001**, *105* (39), 9509-9513.
39. Morikawa, Y.; Liew, C. C.; Nozoye, H., Methylthiolate Induced Vacancy Formation on Au(111): A Density Functional Theoretical Study. *Surf. Sci.* **2002**, *514* (1-3), 389-393.
40. Morikawa, Y.; Hayashi, T.; Liew, C. C.; Nozoye, H., First-Principles Theoretical Study of Alkylthiolate Adsorption on Au(111). *Surf. Sci.* **2002**, *507-510* (Supplement C), 46-50.
41. Molina, L. M.; Hammer, B., Theoretical Study of Thiol-Induced Reconstructions on the Au(111) Surface. *Chem. Phys. Lett.* **2002**, *360* (3-4), 264-271.
42. Poirier, G. E.; Pylant, E. D., The Self-Assembly Mechanism of Alkanethiols on Au(111). *Science* **1996**, *272* (5265), 1145-1148.
43. Poirier, G. E., Mechanism of Formation of Au Vacancy Islands in Alkanethiol Monolayers on Au(111). *Langmuir* **1997**, *13* (7), 2019-2026.
44. Fenter, P.; Eberhardt, A.; Eisenberger, P., Self-Assembly of *n*-Alkyl Thiols as Disulfides on Au(111). *Science* **1994**, *266* (5188), 1216-1218.
45. Fenter, P.; Schreiber, F.; Berman, L.; Scoles, G.; Eisenberger, P.; Bedzyk, M. J., On the Structure and Evolution of the Buried S/Au Interface in Self-Assembled Monolayers: X-Ray Standing Wave Results. *Surf. Sci.* **1998**, *412-13*, 213-235.
46. Yeganeh, M. S.; Dougal, S. M.; Polizzotti, R. S.; Rabinowitz, P., Interfacial Atomic Structure of a Self-Assembled Alkyl Thiol Monolayer/Au(111): A Sum-Frequency Generation Study. *Phys. Rev. Lett.* **1995**, *74* (10), 1811-1814.
47. Reimers, J. R.; Ford, M. J.; Marcuccio, S. M.; Ulstrup, J.; Hush, N. S., Competition of van der Waals and Chemical Forces on Gold-Sulfur Surfaces and Nanoparticles. *Nat. Rev. Chem.* **2017**, *1*, 0017-12.

48. Maksymovych, P.; Sorescu, D. C.; Yates, J. T., Gold-Adatom-Mediated Bonding in Self-Assembled Short-Chain Alkanethiolate Species on the Au(111) Surface. *Phys. Rev. Lett.* **2006**, *97* (14), 146103-4.
49. Torrelles, X.; Pensa, E.; Cortés, E.; Salvarezza, R.; Carro, P.; Hernández Guerrero, C.; Ocal, C.; Barrena, E.; Ferrer, S., Solving the Long-Standing Controversy of Long-Chain Alkanethiols Surface Structure on Au(111). *J. Phys. Chem. C* **2018**, *122* (7), 3893-3902.
50. Cossaro, A.; Mazzarello, R.; Rousseau, R.; Casalis, L.; Verdini, A.; Kohlmeyer, A.; Floreano, L.; Scandolo, S.; Morgante, A.; Klein, M. L.; Scoles, G., X-ray Diffraction and Computation Yield the Structure of Alkanethiols on Gold(111). *Science* **2008**, *321* (5891), 943-946.
51. Torrelles, X.; Barrena, E.; Munuera, C.; Rius, J.; Ferrer, S.; Ocal, C., New Insights in the  $c(4\times 2)$  Reconstruction of Hexadecanethiol on Au(111) Revealed by Grazing Incidence X-ray Diffraction. *Langmuir* **2004**, *20* (21), 9396-9402.
52. Chaudhuri, A.; Lerotholi, T. J.; Jackson, D. C.; Woodruff, D. P.; Jones, R. G.,  $(2\sqrt{3}\times 3)$ Rect. Phase of Alkylthiolate Self-Assembled Monolayers on Au(111): A Symmetry-Constrained Structural Solution. *Phys. Rev. B* **2009**, *79* (19), 195439-7.
53. Yu, M.; Bovet, N.; Satterley, C. J.; Bengió, S.; Lovelock, K. R. J.; Milligan, P. K.; Jones, R. G.; Woodruff, D. P.; Dhanak, V., True Nature of an Archetypal Self-Assembly System: Mobile Au-Thiolate Species on Au(111). *Phys. Rev. Lett.* **2006**, *97* (16), 166102-4.
54. Longo, G. S.; Bhattacharya, S. K.; Scandolo, S., A Molecular Dynamics Study of the Role of Adatoms in SAMs of Methylthiolate on Au(111): A New Force Field Parameterized from Ab Initio Calculations. *J. Phys. Chem. C* **2012**, *116* (28), 14883-14891.
55. Woodruff, D. P., The Role of Reconstruction in Self-Assembly of Alkylthiolate Monolayers on Coinage Metal Surfaces. *Appl. Surf. Sci.* **2007**, *254* (1), 76-81.
56. Grönbeck, H.; Häkkinen, H.; Whetten, R. L., Gold-Thiolate Complexes form a Unique  $c(4\times 2)$  Structure on Au(111). *J. Phys. Chem. C* **2008**, *112* (41), 15940-15942.
57. Cometto, F. P.; Paredes-Olivera, P.; Macagno, V. A.; Patrino, E. M., Density Functional Theory Study of the Adsorption of Alkanethiols on Cu(111), Ag(111), and Au(111) in the Low and High Coverage Regimes. *J. Phys. Chem. B* **2005**, *109* (46), 21737-21748.
58. Wang, Y.; Chi, Q.; Hush, N. S.; Reimers, J. R.; Zhang, J.; Ulstrup, J., Gold Mining by Alkanethiol Radicals: Vacancies and Pits in the Self-Assembled Monolayers of 1-Propanethiol and 1-Butanethiol on Au(111). *J. Phys. Chem. C* **2011**, *115* (21), 10630-10639.
59. Wang, Y.; Chi, Q.; Zhang, J.; Hush, N. S.; Reimers, J. R.; Ulstrup, J., Chain-Branching Control of the Atomic Structure of Alkanethiol-Based Gold-Sulfur Interfaces. *J. Am. Chem. Soc.* **2011**, *133* (38), 14856-14859.
60. Voznyy, O.; Dubowski, J. J.,  $c(4\times 2)$  Structures of Alkanethiol Monolayers on Au(111) Compatible with the Constraint of Dense Packing. *Langmuir* **2009**, *25* (13), 7353-7358.
61. Nagoya, A.; Morikawa, Y., Adsorption States of Methylthiolate on the Au(111) Surface. *J. Phys.: Condens. Matter* **2007**, *19* (36), 365245-7.

62. Grönbeck, H.; Häkkinen, H., Polymerization at the Alkylthiolate–Au(111) Interface. *J. Phys. Chem. B* **2007**, *111* (13), 3325-3327.
63. Tang, L.; Li, F.; Zhou, W.; Guo, Q., The Structure of Methylthiolate and Ethylthiolate Monolayers on Au(111): Absence of the  $(\sqrt{3} \times \sqrt{3})R30^\circ$  Phase. *Surf. Sci.* **2012**, *606* (5), L31-L35.
64. Maksymovych, P.; Voznyy, O.; Dougherty, D. B.; Sorescu, D. C.; Yates Jr, J. T., Gold Adatom as a Key Structural Component in Self-assembled Monolayers of Organosulfur Molecules on Au(111). *Prog. Surf. Sci.* **2010**, *85* (5-8), 206-240.
65. Comparing to the adatom coverage to unreconstructed Au(111) is complicated because clean bare Au(111) undergoes a  $23 \times \sqrt{3}$  herringbone reconstruction which contains  $\theta = 0.043 = 1/23$  excess of Au atoms. See refs. 67 (Barth, et al.) and 68 (Wöll, et al.).
66. Pensa, E.; Cortés, E.; Corthey, G.; Carro, P.; Vericat, C.; Fonticelli, M. H.; Benítez, G.; Rubert, A. A.; Salvarezza, R. C., The Chemistry of the Sulfur–Gold Interface: In Search of a Unified Model. *Acc. Chem. Res.* **2012**, *45* (8), 1183-1192.
67. Barth, J. V.; Brune, H.; Ertl, G.; Behm, R. J., Scanning Tunneling Microscopy Observations on the Reconstructed Au(111) Surface: Atomic Structure, Long-Range Superstructure, Rotational Domains, and Surface Defects. *Phys. Rev. B* **1990**, *42* (15), 9307-9318.
68. Wöll, C.; Chiang, S.; Wilson, R. J.; Lippel, P. H., Determination of Atom Positions at Stacking-Fault Dislocations on Au(111) by Scanning Tunneling Microscopy. *Phys. Rev. B* **1989**, *39* (11), 7988-7991.
69. Kautz, N. A.; Kandel, S. A., Alkanethiol/Au(111) Self-Assembled Monolayers Contain Gold Adatoms: Scanning Tunneling Microscopy before and after Reaction with Atomic Hydrogen. *J. Am. Chem. Soc.* **2008**, *130* (22), 6908-6909.



## Chapter 2: Background for Molecular Dynamics Simulation

### 2.1 Introduction

Molecular dynamics (MD) is a classical simulation technique that has been used to study the structure of the *n*-alkanethiol self-assembled monolayer (SAM) on the Au(111) substrate for more than 30 years.<sup>1-2</sup> This is the most popular classical simulation method to study the packing of the medium and long alkane chains over a large simulation box containing ~100 molecules. This can be useful to study the SAM structure from different domains and at the domain boundaries. The biggest advantage of the MD method over an *ab initio* method is that it can also be used to simulate larger SAM structures over longer simulation time ( $>\mu\text{s}$ ). First, the SAM is relaxed from the initial structure to achieve the equilibrium structure by minimizing the energy of the system. This part of the MD simulation is called relaxation where the SAM structure finds the global energy minima. After relaxation, the equilibrium structure of the SAM is used to analyze the structural parameters. Sometimes, this is called the dynamics part of the MD simulation where the system fluctuates around the global energy minima. We can also constrain the system from achieving global energy minima in special cases discussed in Chapter 5. In this chapter, we begin with the general principles of MD and initialization of the MD simulation (initial configuration and velocity), then we present a comprehensive discussion on the total energy calculation and its individual components (bonded and non-bonded energy). We compare the predicted chain packing using the all-atom and united-atom models. Finally, we conclude our discussion with simulation techniques and algorithm implementation: the periodic boundary condition (PBC), integration method, and ensemble techniques (NVT).

## 2.2 Fundamental Principles of Molecular Dynamics

Molecular dynamics is used to simulate the classical Newtonian equation of motion (EoM) in discrete time steps for  $N$  interacting particles to predict the time evolution of the system in  $6N$  dimensional phase space ( $3N$  position,  $3N$  momentum). Here, we describe the general Hamiltonian formalism of  $N$  interacting particles. The Hamiltonian ( $H$ ) of  $N$  particles interacting via a potential  $V(\{r_i\})$  is shown here

$$H = \sum_{i=1}^N \frac{p_i^2}{2m_i} + V(\{r_i\}) , \quad (2.1)$$

where  $r_i$  and  $p_i$  are the position and the momentum of the  $i^{\text{th}}$  particle. The  $\alpha^{\text{th}}$  component of the position and the momentum is calculated by the Hamiltonian EoM as follows

$$r_i^\alpha = \frac{\partial H}{\partial p_i^\alpha} \quad \text{and} \quad p_i^\alpha = -\frac{\partial H}{\partial r_i^\alpha} . \quad (2.2)$$

If the force acting on the  $i^{\text{th}}$  particle ( $F_i$ ) is conservative, the  $\alpha^{\text{th}}$  component of the force can be written in terms of the negative gradient of the interaction potential

$$F_i^\alpha = -\nabla_\alpha V(\{r_i\}) , \quad (2.3)$$

where  $i = 1, 2, \dots, N$  and  $\nabla_{\alpha=1} = \nabla_x = \frac{\partial}{\partial x}$ . The Newton's 2<sup>nd</sup> law of motion is written as

$$m_i \ddot{r}_i^\alpha = -\nabla_\alpha V(\{r_i\}) = F_i^\alpha . \quad (2.4)$$

The solution of the Equation 2.4 provides the time evolution of the  $i^{\text{th}}$  particle. This is an inhomogeneous equation that is 2<sup>nd</sup> order in time and 1<sup>st</sup> order in space. So, the equation requires two initial conditions to have an exact solution, namely the initial position and the initial velocity.

Numerical solution of this equation is performed using discrete time steps ( $\Delta t$ ), discussed in the Integration Section (Section 2.8). A suitable choice of  $\Delta t$  is crucial for the stability of the

integration. The time steps cannot be arbitrarily large since we are approximating a continuous dynamics with discrete time steps. Change in position and forces on a particle should be small between the time steps for the approximation to be valid. Otherwise, the simulation becomes unstable and usually results in missing atoms or broken bonds. Approximating the continuous dynamics with discrete time steps results in a positional error of  $O(\Delta t^4)$ , Equation 2.14. Thus, the larger the time steps ( $\Delta t > \text{ps}$ ), the larger the simulation error. For small value of  $\Delta t (< \text{fs})$ , however, the simulation can take much longer to converge, and hence becomes computationally expensive.

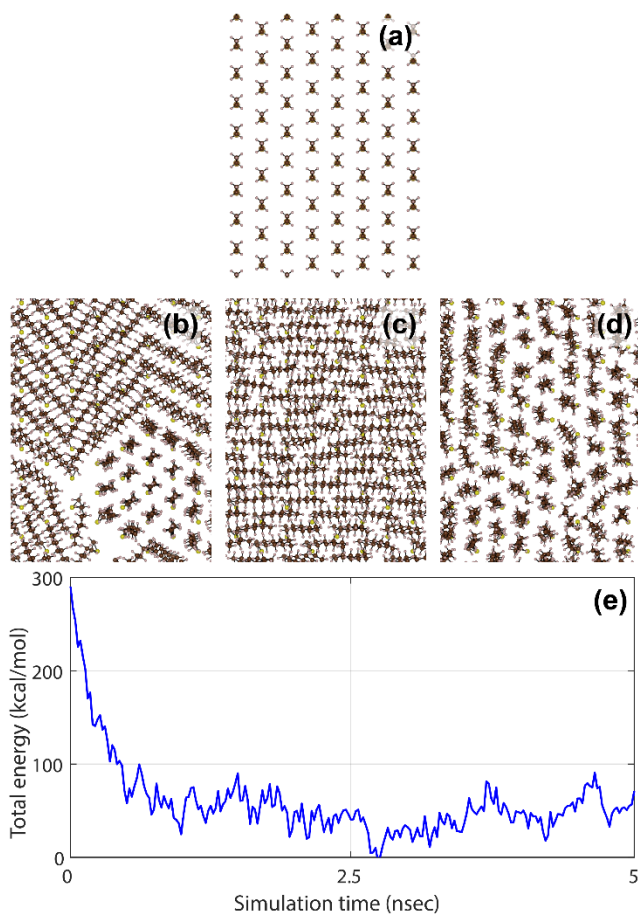


Figure 2.1 Relaxation of *n*-Decanethiol on the Unrelaxed Au(111) at Different Temperatures . The initial structure (a). The top-down view of the relaxed structures (b), (c), (d) at 100 K, 200 K, and 300 K, respectively. Evolution of the total system energy during the relaxation at 200 K is shown in (e).

We have chosen 1 fs time step to simulate the structure of the *n*-alkanethiol self-assembled monolayer on Au(111) substrate.

### 2.3 Initial Configuration

Initial positions ( $\mathbf{r}(0)$ ) are required to solve the Equation 2.4 for the time evolution of the system. Initial positions are defined by the starting position of the atoms.

The initial position of  $N$  particles is provided by a suitable choice of the initial structure of the system. In general, the initial structure is not the equilibrium structure of the system. The energy of the

initial structure is minimized during the relaxation to find the global energy minima (Figure 2.1.e). If the atomic nuclei overlap in the initial structure, the corresponding energy of the system becomes exceedingly high. Relaxation from this high energy initial structure can be computationally expensive, and the simulation becomes unstable. So, a suitable initial structure is important to simulate the structure of the SAM. For alkanethiol SAMs, we start with all the molecules standing perpendicular to the Au(111) substrate (Au atoms are excluded for visual clarity) to avoid structural bias (Figure 2.1.a). Starting from this position requires minimum computational time and results in better structural reproducibility. During the relaxation, the molecules can get trapped in local energy minima and cannot achieve the equilibrium structure. Increasing the simulation temperature provides additional kinetic energy for the molecules to overcome the local energy minima which helps the system to relax in the equilibrium structure. We found that relaxing the SAMs at temperatures  $<200$  K results in molecules trapped into local energy minima manifested by unstable tilt domains (Figure 2.1.b). At temperatures  $>300$  K relaxation introduces significant structural defects in the SAM that compromises the analysis of structural parameters (Figure 2.1.d). Therefore, we have chosen to relax the system at 200 K where the molecules have just enough kinetic energy to overcome the local minima without introducing notable structural defects (Figure 2.1.c). During the relaxation, molecules spontaneously choose the corresponding optimized geometries on which the dynamics was performed. An example of the initial structure (Figure 2.1.a) is given in Appendix A along with the corresponding VMD script to generate the LAMMPS input file for the MD simulation.

## 2.4 Initial Velocity

The initial velocity of each atom is randomly sampled from the Maxwell-Boltzmann distribution for a given initial temperature. The velocity of a particle is adjusted during the simulation to maintain the thermal equilibrium of the system (discussed in Section 2.9). The temperature of the MD simulation is calculated from the equipartition of energy over all degrees of freedom (DoF). The average kinetic energy per DoF is given by

$$\frac{1}{2}k_B T = \left\langle \frac{1}{2} m v_\alpha^2 \right\rangle. \quad (2.5)$$

where  $k_B$  is the Boltzmann constant. The instantaneous temperature for a system with  $N_f$  DoF can be written as

$$T(t) = \sum_{i=1}^N \frac{m_i v_i^2(t)}{K_B N_f}. \quad (2.6)$$

where  $N_f = d(N - 1) - 2$  for  $N$  particles in  $d$  dimensional space with fixed total momentum. The relative fluctuation in the temperature is proportional to  $1/\sqrt{N_f}$ . The structure of the  $n$ -decanethiol SAM contains 3200 atoms ( $N_f \sim 10^4$ ). So, the statistical fluctuation in the temperature is about 1%.

## 2.5 Total Energy Calculation

We turn our attention to calculating the total energy of the system using the MD simulation. The total energy ( $E$ ) of the  $n$ -alkanethiol SAM is calculated using the following equation.

$$E = 4\varepsilon \left\{ \left( \frac{\sigma}{r} \right)^{12} - \left( \frac{\sigma}{r} \right)^6 \right\} + C \frac{q_i q_j}{\varepsilon_0 r} + K_r (r - r_0)^2 + K_\theta (\theta - \theta_0)^2 + K_\varphi^1 (1 + \cos \varphi) + K_\varphi^2 (1 - \cos 2\varphi) + K_\varphi^3 (1 + \cos 3\varphi) \quad (2.7)$$

The first two terms on the right side of the equation represent the non-bonded interaction, van der Waals (vdW) (Lennard-Jones), and Coulombic potential, respectively. The third and the fourth

terms are for the harmonic vibration of the bond stretching and the bond bending, respectively. The last three terms are the first three Fourier components of the dihedral potential. The rest of the section is organized as follows: we begin our discussion with the bonded interaction energy. Then we discuss both the non-bonded energies (the vdW and the Coulombic interactions). Finally, we present the force field (FF) parameters used to simulate the SAM structure.

### ***2.5.1 Bonded Interaction Energy***

The bonded interaction of the MD FF is computationally simpler compared to the non-bonded interaction. Atoms are considered as point masses connected via springs in the bonded interaction. We considered three bonded interactions for the alkanethiol SAMs, bond stretching, bond bending, and dihedral angles.

Atoms in the alkane chain are connected by covalent bonds which are represented by springs in the MD simulation. The strength of a bond is proportional to the spring constant. The spring constant is zero if there is no bond between two atoms, and it is infinity if the bond is rigid. Extension and contraction of the bond from its equilibrium bond length costs the system additional energy. Here we assume that the bond length does not deviate far away from its equilibrium value. The harmonic potential for the bond stretching is the most common model which we use for the alkane chains.

$$E_r = K_r (r - r_0)^2 \quad (2.8)$$

where  $K_r$  is the spring constant for a bond with equilibrium bond length of  $r_0$ . The values of  $K_r$  and  $r_0$  for S-C, C-C, and C-H are listed in Table 2.1. The energy of the bond stretching ( $E_r$ ) is proportional to the square of the deviation from the equilibrium bond length ( $r-r_0$ ). Figure 2.2

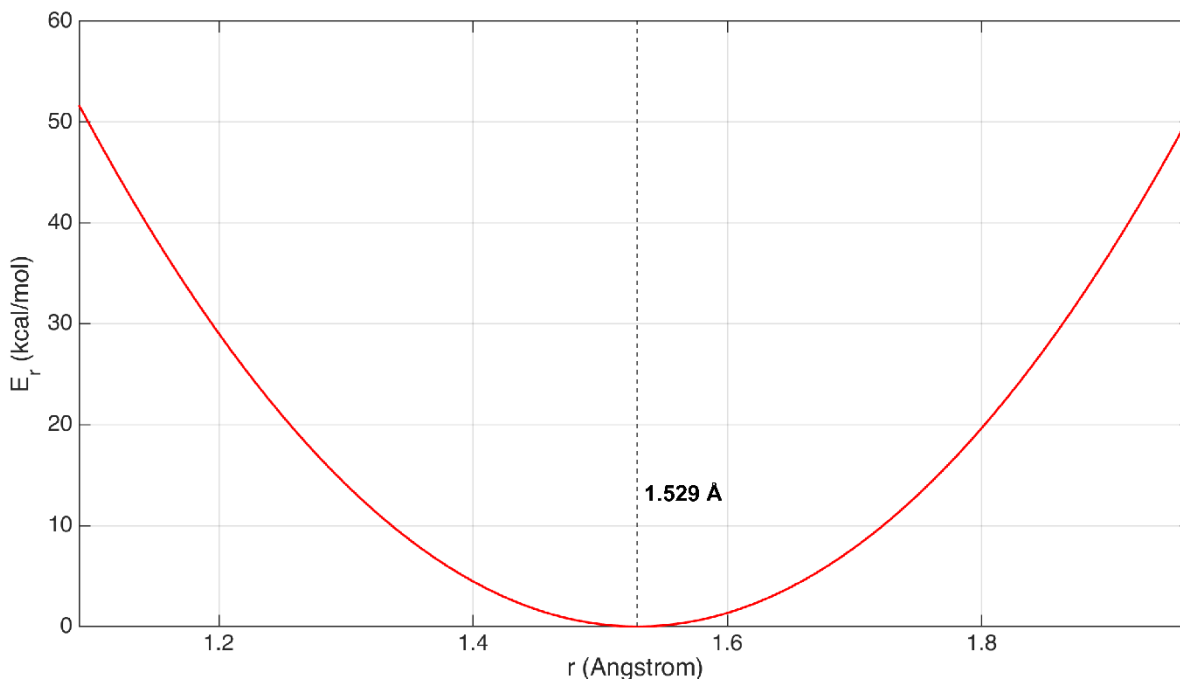


Figure 2.2 The Bond Stretching Potential Energy for the C-C Bond. The equilibrium bond distance is 1.529 Å.

shows the harmonic potential for the C-C bond stretching with equilibrium bond distance of 1.529 Å. Our model for the alkanethiol SAM does not include bond breaking/making. Anharmonic potential models are generally used in such cases.<sup>3</sup>

Similar to bond stretching, bond bending for alkane chains is modeled using the harmonic potential, shown in Figure 2.3 for the C-C-C bond. In this case, deviation from the equilibrium bond angle results in additional energy to the system. The model for the bond bending used for the alkane chain is given below with FF parameters listed in Table 2.2.

$$E_{\theta} = K_{\theta} (\theta - \theta_0)^2 \quad (2.9)$$

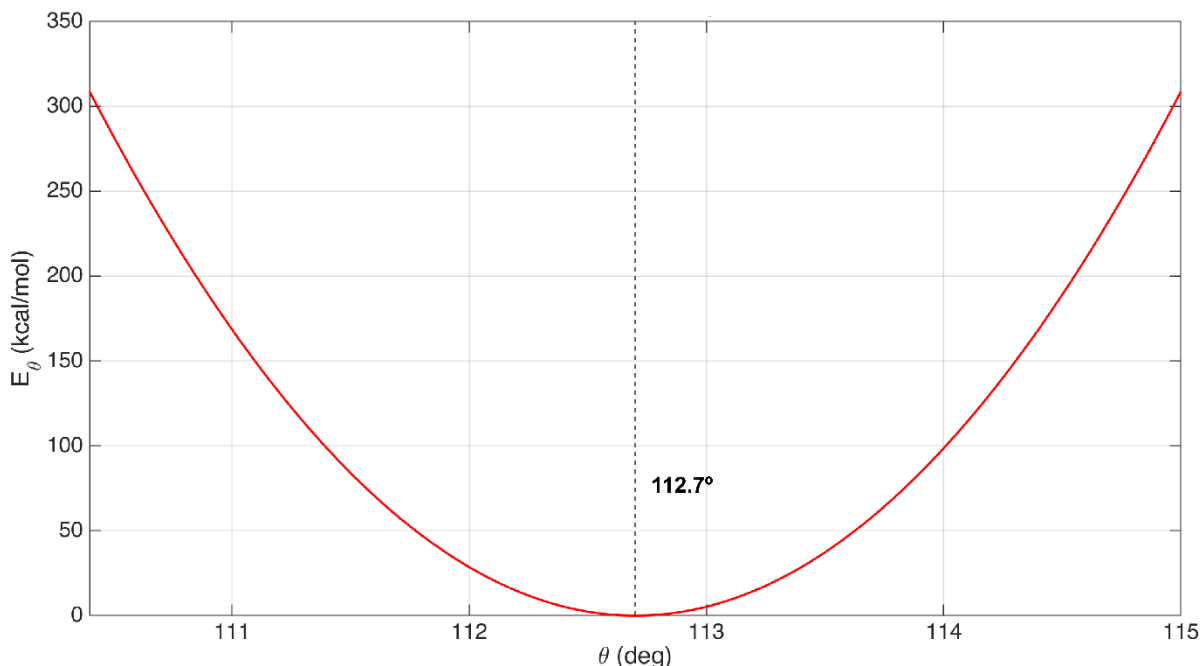


Figure 2.3 The Bond Bending Potential Energy for the C-C-C Bond. The equilibrium bond angle is 112.7°.

There are several models for the dihedral potential. We adopted the OPLS AA FF to model the dihedral potential where four Fourier components of the dihedral angles are used.<sup>4</sup> The Fourier coefficients are listed in Table 2.3 for C-C-C-C, C-C-C-H, and H-C-C-H dihedral angles. The fourth coefficient for all the angles is zero.

$$E_{\varphi} = K_{\varphi}^1 (1 + \cos \varphi) + K_{\varphi}^2 (1 - \cos 2\varphi) + K_{\varphi}^3 (1 + \cos 3\varphi) + K_{\varphi}^4 (1 - \cos 4\varphi) \quad (2.10)$$

The dihedral potential is used to maintain the planarity of the alkane chain, referred as the *trans* configuration where all the C atoms are in one plane. The stronger the dihedral potential, more rigid the alkane chain backbone becomes. Deviation from the *trans* configuration (*gauche* configuration) costs the system additional energy. At 200 K alkane chains are predominantly *trans*, but the chains deviate from the *trans* configuration as the simulation temperature is increased. Figure 1.6 shows the *trans* and *gauche* percentage (right y axis) for the C-C-C-C dihedral potential



(left y axis) for model-A (defined in Chapter 5) at 200 K. The figure shows that the chains are >99% *trans* at 200 K.

### 2.5.2 Non-bonded Interaction Energy

The non-bonded interaction between the atoms is the computationally most expensive part of the MD simulation. Here, we consider two non-bonded interactions, the vdW interaction and the Coulombic interaction to simulate the structure of the SAM.

#### van der Waals interaction energy

We use the Lennard-Jones potential to model the vdW interaction between the atoms of the alkane chains, as shown in the Equation 2.11. The Lennard-Jones potential is a function of the interatomic distance ( $r$ ) with energy and length scales given by  $\varepsilon$  and  $\sigma$  respectively (Table 2.4).<sup>5</sup>

$$E_{vdW} = 4\varepsilon \left\{ \left( \frac{\sigma}{r} \right)^{12} - \left( \frac{\sigma}{r} \right)^6 \right\} \quad (2.11)$$

The attractive part of the potential ( $\sim r^{-6}$ ) is due to the dipole fluctuation, but there is no such physical interpretation for the repulsive part of the potential ( $\sim r^{-12}$ ). The vdW potential is repulsive at short distance, hence the exponent of the corresponding term should be greater than six ( $n > 6$ ). Squaring the attractive term to satisfy this condition is not only computationally efficient, but also successfully models the repulsive part of the potential to reproduce experimental observations, such as the density of gases.<sup>6</sup> Repulsion at a short distance prevents overlapping of the atomic nuclei, whereas the long-distance attraction between atoms helps the alkane chains to spontaneously organize in a 2D SAM crystal. Although, the Lennard-Jones potential is the most

popular model for the vdW interaction, there are other models for the vdW interaction like the Buckingham potential where an exponential term ( $e^{-ar}$ ) is used for the repulsive behavior.<sup>7</sup>

### Coulombic interaction energy

The electrostatic Coulombic energy for  $N$  charged particles located at  $\mathbf{r}_1, \mathbf{r}_2, \dots, \mathbf{r}_N$  can be written as

$$E_C = \sum_{(i,j)} \frac{q_i q_j}{|\mathbf{r}_i - \mathbf{r}_j|}, \quad (2.12)$$

where the sum is over all particles ignoring the self-interaction.  $q_i$  and  $q_j$  are the charges of the  $i^{\text{th}}$  and  $j^{\text{th}}$  particle located at  $\mathbf{r}_i$  and  $\mathbf{r}_j$  respectively (Table 2.4). For the simplicity of our representation, we have chosen  $4\pi\epsilon_0 = 1$ . Although, individual atoms have charge, the SAM as a whole is charge neutral.

### **2.5.3 Force Field Parameters**

The force field parameters used to simulate the structure of the C10 SAM is presented below.

Bond stretching:  $K_r (r - r_0)^2$

Table 2.1. Force Field Parameters for Bond Stretching.

Bond	$r_0$ (Å)	$K_r$ (kcal/ mol Å <sup>2</sup> )
S-C <sup>8</sup>	1.81	222
C-H <sup>9</sup>	1.09	340
C-C <sup>9</sup>	1.529	268

Bond bending:  $K_\theta (\theta - \theta_0)^2$

Table 2.2. Force Field Parameters for Bond Bending.

Bond Angle	$\theta_0$ (°)	$K_\theta$ (kcal/ mol rad <sup>2</sup> )
$\angle\text{S-C-C}^8$	114.7	50.0
$\angle\text{C-C-C}^9$	112.7	58.35
$\angle\text{C-C-H}^9$	110.7	37.5
$\angle\text{H-C-H}^9$	107.8	33.0

Dihedral angle vibration:  $\frac{1}{2}K_\phi^1(1 + \cos\phi) + \frac{1}{2}K_\phi^2(1 - \cos 2\phi) + \frac{1}{2}K_\phi^3(1 + \cos 3\phi)$

Table 2.3. Fourier Components of the Dihedral Angles. The fourth coefficient ( $K^4$ ) is zero for all dihedral angles.

Dihedral Angle	$K_\phi^1$ (kcal/mol)	$K_\phi^2$ (kcal/mol)	$K_\phi^3$ (kcal/mol)
C-C-C-C <sup>10</sup>	0.528	-0.186	0.900
C-C-C-H <sup>4</sup>	0	0	0.366
H-C-C-H <sup>10</sup>	0	0	0.150

Non-bonded interaction:  $4\varepsilon \left\{ \left( \frac{\sigma}{r} \right)^{12} - \left( \frac{\sigma}{r} \right)^6 \right\} + C \frac{q_i q_j}{\varepsilon_0 r}$ , where  $r < r_c = 12 \text{ \AA}$ .

Table 2.4. Force Field Parameters for Non-Bonded Interactions.

Interaction Site	$\sigma$ (Å)	$\varepsilon$ (kcal/mol)	$q_i$ (e)
Au <sub>adatom</sub> <sup>11</sup>	2.934	0.039	0
S <sup>4</sup>	3.550	0.250	0
C (in CH <sub>2</sub> ) <sup>10</sup>	3.5	0.066	-0.12
C (in CH <sub>3</sub> ) <sup>10</sup>	3.5	0.066	-0.18
H (in CH <sub>2</sub> ) <sup>10</sup>	2.5	0.030	0.06
H (in CH <sub>3</sub> ) <sup>10</sup>	2.5	0.030	0.06

The cutoff distance for both the vdW interaction and the Coulombic potential is the same, 12 Å.

The mixing rule used is  $\varepsilon_{ij} = \sqrt{\varepsilon_i \varepsilon_j}$  and  $\sigma_{ij} = \sqrt{\sigma_i \sigma_j}$ . The Coulombic interaction is treated via

PPPM method.<sup>12</sup>

## 2.6 Comparison between United-Atom and All-Atom Model

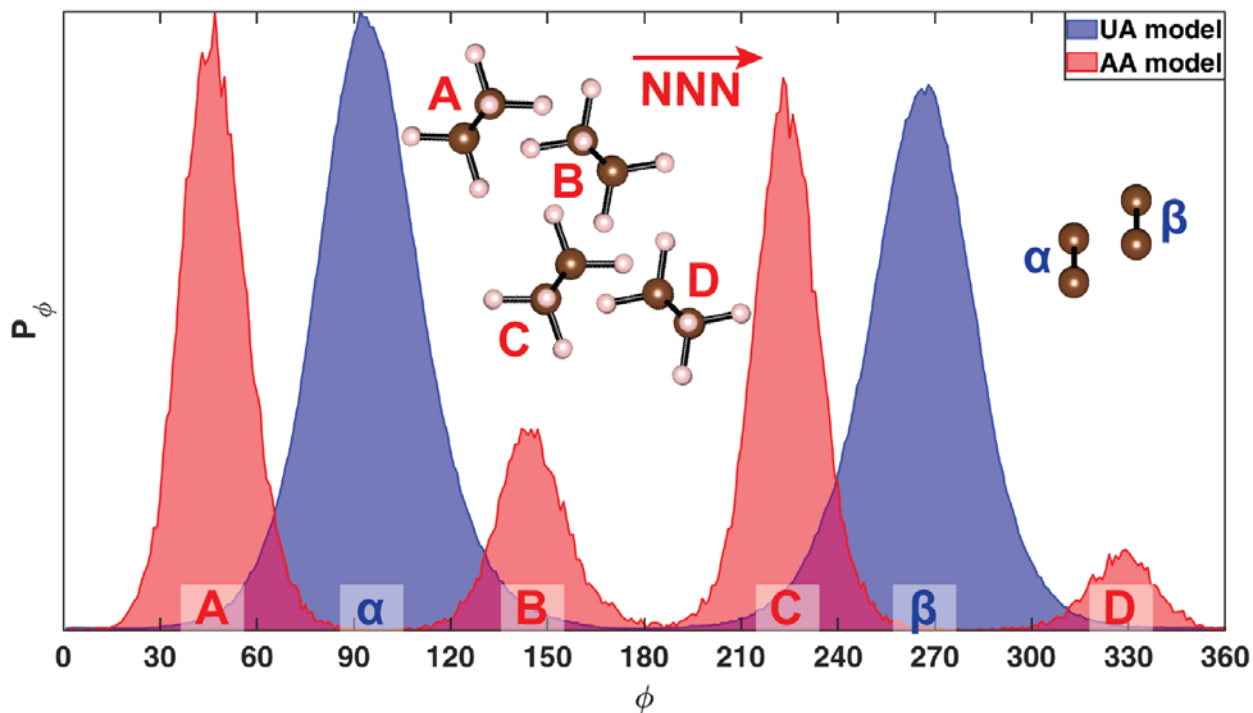


Figure 2.4. Population of the Molecular Twist Predicted by the AA and the UA Models are Compared for the C10 SAM. A ( $50^\circ$ ), B ( $132^\circ$ ), C ( $228^\circ$ ), and D ( $310^\circ$ ) are the twists predicted by the AA model, twist angles  $\alpha$  ( $90^\circ$ ) and  $\beta$  ( $270^\circ$ ) are predicted by the UA model. Interlocking of the chains (looking down the chain axis) are illustrated for both models. Twist A, B, and  $\alpha$  are related to D, C, and  $\beta$  respectively by the mirror symmetry about the tilt plane. IRRAS reported twist A and B per unit cell as predicted by the AA model.

The united-atom and all-atom models are the two most commonly used MD models for alkanethiol SAMs. As the name suggests, all the atoms are explicitly considered in the all-atom (AA) model, whereas the lighter H atoms are united with the bonded C atom in the united-atom (UA) model. The Lennard-Jones parameters are modified accordingly in the UA FF to include the effect of the H atoms. Since the UA does not consider the H atoms explicitly, the number of atoms in the simulation is less than the AA model. As a result, the UA is computationally less expensive. Although the UA is computationally less expensive, it cannot correctly predict the interlocking of the chains, hence the structure of the monolayer.

The structure of the SAM is determined by three geometrical parameters for each chain: tilt angle ( $\theta$ ), tilt direction ( $\chi$ ), and the twist of the molecular backbone ( $\phi$ ).  $\theta$  and  $\chi$  depends on the headgroup spacing and the effective volume of the alkane chain. Both the UA and the AA models predict a molecular tilt of  $\sim 30^\circ$  towards the next-nearest-neighbor (NNN) direction for a saturated SAM, similar to the experimental observations. This is because the FF parameters of the UA are adjusted to replicate the correct chain density. The twist of the molecular backbone, on the other hand, is more sensitive to the interlocking of the chains rather than the average chain density. Experimental IRRAS reported two nearly orthogonal twists ( $50^\circ$  and  $132^\circ$ ) per unit cell for the dense phase alkanethiol SAM, shown in the Figure 2.4. Since the IRRAS cannot distinguish between twists related by the mirror symmetry about the tilt plane, alkane chains can exhibit up to four twist angles ( $50^\circ$ ,  $132^\circ$ ,  $228^\circ$ , and  $310^\circ$ ) per unit cell and still satisfy the experimental observation. The UA predicts two twists related by the mirror symmetry ( $90^\circ$  and  $270^\circ$ ), inconsistent with the experimental observation. The spherical assumption of the  $\text{CH}_2$  and the  $\text{CH}_3$  units in the UA model is responsible for the incorrect chain packing and unable to reproduce the observed molecular twists. The interlocking of the  $\text{CH}_2$  groups is an important feature of the alkane chain interaction that must be included in the model. The AA model of the alkanethiol is necessary to correctly predict the structure of the monolayer despite being computationally more expensive.

## 2.7 Periodic Boundary Condition

We now turn our focus on some techniques and algorithms utilized by the MD simulation. Periodic boundary conditions (PBC) are used to represent an infinite 2D SAM crystal structure with a finite simulation box containing one or more unit cells. The basic idea of PBC is when an atom leaves from one side of the simulation box, it simultaneously reappears from the other side

of the box without encountering any potential barrier at the boundary. For a cubic simulation box containing  $N$  number of atoms, the number of atoms at the boundary is  $N^{2/3}$ . We use 3200 atoms in our simulation box to represent the structure of the SAM. That means around 7% of the atoms (~220 atoms) are at the boundary. So, it is crucial to properly implement the PBC to realistically represent the structure of the infinite SAM.

The most important part of the PBC is to maintain the non-bonded interaction across the boundary. Both short range and long range non-bonded interactions need to be preserved by the

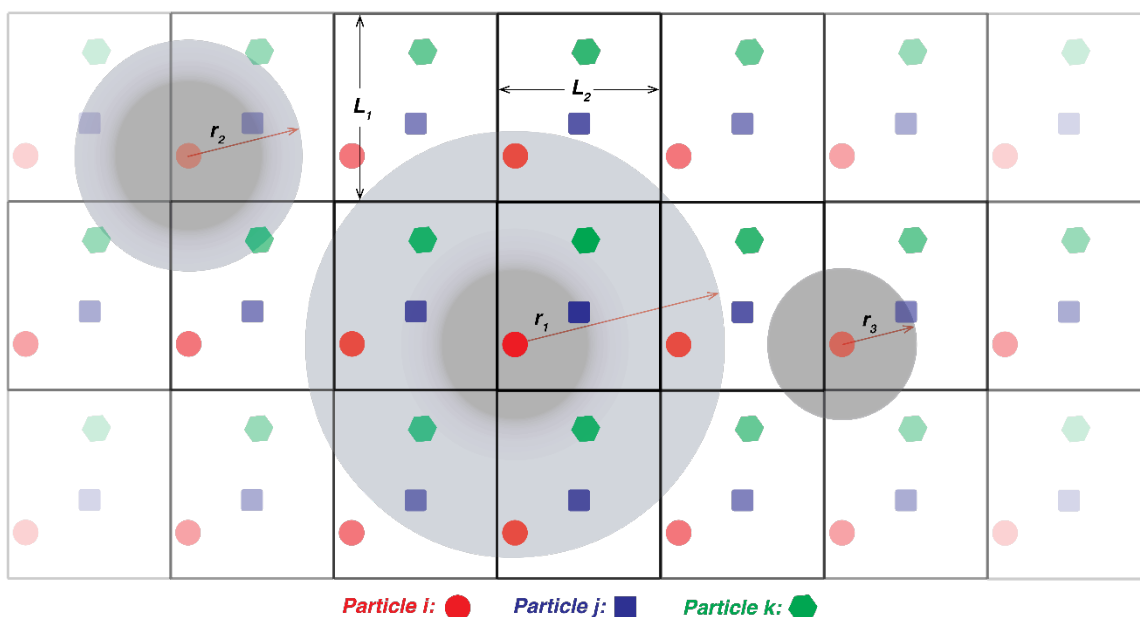


Figure 2.5. The Effect of the PBC on the Central Simulation Box Containing Three Particles. Three non-bonded cutoff radii ( $r_1$ ,  $r_2$ , and  $r_3$ ) of the  $i^{\text{th}}$  particle is demonstrated by the shaded regions.

PBC while integrating the EoM. After each integration step the atomic coordinates are rescaled by the PBC to bring the atoms inside the original simulation box. Figure 2.5 shows that an atom interacts with other atoms within the simulation box as well as the atoms in the periodic image of the simulation box. The interaction depends on the position of the atoms within the simulation box and the cutoff radius of the non-bonded interaction. Three scenarios are demonstrated in Figure

2.5 with non-bonded cutoff radii  $r_1$ ,  $r_2$ , and  $r_3$  where  $r_1 > r_2 > r_3$ . The width and the height of the simulation box containing three particles ( $i$ ,  $j$ , and  $k$ ) are  $L_2$  and  $L_1 (>L_2)$ , respectively. For the smallest cutoff radius ( $r_3$ ), the  $i^{\text{th}}$  particle only interacts with the  $j^{\text{th}}$  particle in the simulation box. However, as the cutoff radius is increased to  $r_2$  the non-bonded interaction of the  $i^{\text{th}}$  particle includes both the  $j^{\text{th}}$  particle and its periodic image along with the  $k^{\text{th}}$  particle. As a result, increasing in the cutoff radius overestimates the non-bonded interaction of the  $i^{\text{th}}$  particle. As we further increase the cutoff radius to  $r_1$ , the non-bonded interaction not only involves the periodic images of  $j^{\text{th}}$  and  $k^{\text{th}}$  particles, but also includes periodic images of the  $i^{\text{th}}$  particle (self-interaction). The overestimation of the non-bonded interaction can be a major source of error when calculating the total energy of the system. Numerical techniques are used to avoid such overestimations.

We conclude our discussion of the PBC by highlighting its two major limitations. The largest wavelength allowed by the PBC is determined by the dimension of the simulation box. As a result, system properties that are dominated by larger wavelengths cannot be represented accurately by the MD simulation. The shape of the simulation box also needs to be space-filling to represent an infinite lattice by the PBC. Hence, PBC cannot be applied to any arbitrary shaped unit cell or simulation box.

## 2.8 Integration Method

The MD simulations of the alkanethiol SAMs are preformed using the LAMMPS<sup>13</sup> MD package with the velocity-Verlet algorithm.<sup>14</sup> The Verlet algorithm is used to simulate the position of the particles by solving the Newton's EoM. We can rewrite Equation 2.4 as follows

$$\ddot{r}_i = \frac{F_i(r(t))}{m_i} = a(r(t)), \quad (2.13)$$

where  $a(r(t))$  is the acceleration, not a function of the velocity. The position of an atom after a time step can be represented by the Taylor expansion as

$$r(t + \Delta t) = 2r(t) - r(t - \Delta t) + a(t)\Delta t^2 + O(\Delta t^4). \quad (2.14)$$

Note that, the first and the third order terms cancel out while adding two Taylor expansions. This makes the Verlet integration an order more accurate than by the simple Taylor expansion. In this case, the error in calculating  $r(t + \Delta t)$  is fourth order in  $\Delta t$ . Equation 2.14 uses the position of the particle from two time steps in the past. So, this equation cannot be used to simulate the position for the initial time step. The equation used for the first time step is given by (Taylor expansion of  $r(\Delta t)$ )

$$r(\Delta t) = r(0) + v(0)\Delta t + \frac{1}{2}a(r(0))\Delta t^2 + O(\Delta t^3). \quad (2.15)$$

The error to calculate the position for the first time step is third order in  $\Delta t$  which is an order less accurate than calculating  $r(t + \Delta t)$ . However, this error in the first time step becomes negligible for a the large number of time steps used in a typical simulation.

The velocity-Verlet algorithm calculates both velocity and position simultaneously. The simulation error is the same as the Verlet algorithm. The velocity for each time step is calculated from the following equation

$$v(t + \Delta t) = v(t) + \frac{a(t) + a(t + \Delta t)}{2} \Delta t. \quad (2.16)$$

The numerical stability of the velocity-Verlet integration combined with the time reversibility and the ability to preserve the simulation area makes it the most popular method of integration for MD.



## 2.9 Ensemble (Nosé–Hoover Thermostat)

We turn our attention to ensembles in MD and techniques for temperature scaling. Here we focus on the canonical ensemble and the Nosé–Hoover thermostat to control the simulation temperature. The number of atoms  $N$ , the volume  $V$ , and the simulation temperature  $T$  stay constant in the canonical ensemble (NVT). We use the NVT ensemble during the relaxation and the dynamics part of the MD simulation where the alkanethiol monolayer explores the minimum energy configuration at a specific temperature. The Nosé–Hoover thermostat is the most popular algorithm for the canonical ensemble, and we chose it for our simulations.

The Nosé–Hoover thermostat treats the external heat reservoir as an external DoF by introducing real  $\{p_i, r_i\}$  and virtual  $\{\pi_i, \rho_i\}$  sets of variables. The new Hamiltonian of the system in terms of the virtual coordinates can be given as

$$H^* = \sum_{i=1}^N \frac{\pi_i^2}{2m_i S} + V(\{\rho_i\}) + \frac{\pi_S^2}{2M_S} + (3N+1)K_B T \ln(S). \quad (2.17)$$

The first two terms are similar to the original Hamiltonian (Equation 2.1), the third term is due to the additional DoF, and the last term is proportional to the kinetic energy. The in the third term,  $\pi_S$  is an additional momentum with an effective mass of  $M_S$ , which is also referred as the thermal inertia parameter that determines the rate of heat flow. The real and the virtual variables are transformed as  $p_i = \rho_i$  and  $r_i = \pi_i$ . The scaling factor  $S$  is a dynamic variable that relates real time  $t$  with the virtual time  $\tau$  as follows

$$S = \frac{d\tau}{dt}. \quad (2.18)$$

The simulation temperature  $T$  can be calculated from the kinetic energy as (equivalent to Equation 2.6)

$$T = \frac{1}{3NK_B} \sum_{i=1}^N \frac{p_i^2}{m_i}. \quad (2.19)$$

After obtaining the EoM from the new Hamiltonian in terms of the virtual variables, we can transform it back in terms of the real variables by introducing a new variable  $\zeta$  such that

$$\zeta = S^2 \frac{\pi_S}{M_S}. \quad (2.20)$$

The set of equations obtained from this recipe describes the Nosé–Hoover thermostat (given below, Equations 21–25) for the canonical ensemble.

$$\frac{dq_i^\alpha}{dt} = \frac{p_i^\alpha}{m_i} \quad (2.21)$$

$$\frac{dp_i^\alpha}{d\tau} = -\frac{\partial V}{\partial q_i^\alpha} - \zeta p_i^\alpha \quad (2.22)$$

$$\frac{\partial \ln(S)}{\partial t} = \zeta \quad (2.23)$$

$$\frac{d\zeta}{dt} = \frac{1}{M_S} \left( \sum_{i=1}^N \frac{p_i^2}{2m_i} - (3N+1)K_B T \right) \quad (2.24)$$

$$p_i = |\mathbf{p}_i| \quad (2.25)$$

## 2.10 Limitations of Molecular Dynamics

MD is an extremely powerful classical simulation technique to simulate large structures over longer simulation time which is not possible using current *ab initio* methods. However, there are some limitations of the MD simulation that needs to be taken into consideration before using MD simulation.

- The quantum mechanical and relativistic phenomena are not explicitly included in the MD simulation. MD is used to predict the classical trajectory of a particle. It assumes infinite accuracy in predicting canonically conjugated variables ( $\mathbf{r}$  and  $\mathbf{p}$ ) simultaneously.
- MD is a classical simulation method applicable to a wide range of materials. However, this classical approximation is not a reliable model when we consider the motion (translational and rotational) of light atoms or molecule (H, He, and H<sub>2</sub>).
- In MD we assume that the system is ergodic, i.e. the time average of a function ( $f(\vec{r}, \vec{p})$ ), which depends on the position ( $\vec{r}$ ) and the momentum ( $\vec{p}$ ) of particles, is same as its ensemble average.<sup>15</sup> Generally, the thermodynamic properties of a system in MD are calculated by averaging over the natural time evolution of the equilibrium state. It is assumed to be related to the ensemble average as follows

$$\bar{f}(\vec{r}, \vec{p}) = \langle f(\vec{r}, \vec{p}) \rangle ,$$

where  $\bar{f}$  and  $\langle f \rangle$  are the time average and the ensemble average, respectively. This hypothesis is not valid in general, and one must be careful while applying MD to non-ergodic cases, such as glassy and metastable phases.

## 2.11 References

1. Hautman, J.; Klein, M. L., Simulation of a Monolayer of Alkyl Thiol Chains. *J. Chem. Phys.* **1989**, *91* (8), 4994-5001.
2. Mar, W.; Klein, M. L., Molecular Dynamics Study of the Self-Assembled Monolayer Composed of S(CH<sub>2</sub>)<sub>14</sub>CH<sub>3</sub> Molecules Using an All-Atoms Model. *Langmuir* **1994**, *10* (1), 188-196.
3. Morse, P. M., Diatomic Molecules According to the Wave Mechanics. II. Vibrational Levels. *Physical Review* **1929**, *34* (1), 57-64.

4. Jorgensen, W. L.; Maxwell, D. S.; Tirado-Rives, J., Development and Testing of the OPLS All-Atom Force Field on Conformational Energetics and Properties of Organic Liquids. *J. Am. Chem. Soc.* **1996**, *118* (45), 11225-11236.
5. Jones, J. E.; Chapman, S., On the Determination of Molecular Fields. -II. From the Equation of State of a Gas. *Proc. Math. Phys.* **1924**, *106* (738), 463-477.
6. Belov, G. V., Real-gas Equations of State Based on the Lennard-Jones Potential. *Math. Models Comput. Simul.* **2009**, *1* (6), 677.
7. Buckingham, R. A.; Lennard-Jones, J. E., The Classical Equation of State of Gaseous Helium, Neon and Argon. *Proc. R. Soc. Lond., A Math. phys. sci.* **1938**, *168* (933), 264-283.
8. Weiner, S. J.; Kollman, P. A.; Nguyen, D. T.; Case, D. A., An All Atom Force Field for Simulations of Proteins and Nucleic Acids. *J. Comput. Chem.* **1986**, *7* (2), 230-252.
9. Kaminski, G.; Jorgensen, W. L., Performance of the AMBER94, MMFF94, and OPLS-AA Force Fields for Modeling Organic Liquids. *J. Phys. Chem.* **1996**, *100* (46), 18010-18013.
10. Murzyn, K.; Bratek, M.; Pasenkiewicz-Gierula, M., Refined OPLS All-Atom Force Field Parameters for *n*-Pentadecane, Methyl Acetate, and Dimethyl Phosphate. *J. Phys. Chem. B* **2013**, *117* (51), 16388-16396.
11. Meena Devi, J., A Simulation Study on the Thermal and Wetting Behavior of Alkane Thiol SAM on Gold (111) Surface. *Prog. Nat. Sci.: Mater. Int.* **2014**, *24* (4), 405-411.
12. Toukmaji, A. Y.; Board, J. A., Ewald Summation Techniques in Perspective: A Survey. *Comput. Phys. Commun.* **1996**, *95* (2), 73-92.
13. Plimpton, S., Fast Parallel Algorithms for Short-Range Molecular Dynamics. *J. Comput. Phys.* **1995**, *117* (1), 1-19.
14. Swope, W. C.; Andersen, H. C.; Berens, P. H.; Wilson, K. R., A Computer Simulation Method for the Calculation of Equilibrium Constants for the Formation of Physical Clusters of Molecules: Application to Small Water Clusters. *J. Chem. Phys.* **1982**, *76* (1), 637-649.
15. According to the apriori theory, all the quantum states (microstates) of a many-body system under equilibrium is equally likely to be occupied by the system. The average of a physical property of the system over such microstates is called the ensemble average.

## Chapter 3: Background for Density Functional Theory Simulation

### 3.1 Scope of this Chapter

Density functional theory (DFT) is used to study the electronic properties at the Au-S interface, such as preferred adsorption sites, sulfur hybridization, and substrate relaxation. In this chapter, we explain the basic concepts of DFT which we later utilized in Chapters 6 and 7.

For a system with  $N$  interacting electrons, the degrees of freedom for the corresponding many-body wavefunction is  $3N$  (three spatial components per electron). Here, we study the adsorption of an isolated methanethiol on the Au substrate using 96 Au atoms (79 electrons per Au atom), one S atom (16 electrons per S atom), one C atom (6 electrons per C atom), and three H atoms (1 electron per H atom). As a result, the number of electrons in the system is 7,609 with the degrees of freedom for the wavefunction being 22,827. Computing the many-body wavefunction for such a large system can be impractical even for the most powerful computer currently available. Instead of computing the complex many-body wavefunction, DFT uses the ground state charge density of an equivalent non-interacting single electron system to evaluate the ground state properties of the original system that requires significantly less computational resources.

### 3.2 Born-Oppenheimer Approximation

The state of a quantum mechanical system can be completely described by its wavefunction  $\psi$ . If  $H$  and  $E$  are the Hamiltonian and the energy of the system respectively, the time independent Schrödinger equation can be written as

$$\hat{H}\psi = E\psi . \quad (3.1)$$

Here, we consider that the Hamiltonian does not explicitly depend on time. Thus, the time independent wavefunctions are the stationary states of the system which are commonly referred as atomic and molecular orbitals in chemistry.

In general, the nuclear and the electronic motion are coupled in the Hamiltonian which makes the eigenvalue problem (Equation 3.1) extremely difficult to solve. Because the mass of an electron is much smaller than that of a proton or a neutron ( $m_p/m_e \sim 10^3$ ), we can approximate the nucleus effectively stationary with respect to the motion of an electron. This is known as the Born-Oppenheimer approximation.<sup>1</sup> As a result, we can separate the electronic motion from the nuclear motion and rewrite the Hamiltonian and the wavefunction:

$$\hat{H} = \hat{H}_e + \hat{H}_{nuc} \quad (3.2)$$

$$\Psi = \Psi_e \Psi_{nuc} \quad (3.3)$$

where  $H_{nuc}$  and  $H_e$  are the nuclear and the electronic part of the Hamiltonian respectively and  $\Psi_{nuc}$   $\Psi_e$  are the nuclear and electronic wavefunctions respectively. The nuclear Hamiltonian results in a constant shift in the total energy of the system ( $E_{nuc}$ ). Instead of tracking this constant throughout our discussion of the DFT, we will ignore it for now and add it at the end to the total energy. The Born-Oppenheimer approximation holds for most of the systems, except when the electron/nucleus interaction is very strong, such as in the case of superconductors and quantum crystals.

### 3.3 Hohenberg-Kohn Theorem

Now, let us consider a system consisting of  $N$  interacting electrons with the many-body Schrödinger equation as follows:

$$\hat{H}_e \psi = E_e \psi$$

$$\begin{aligned} & \left[ \hat{T} + \hat{U} + \hat{V} \right] \psi = E_e \psi \\ & \left[ -\frac{\hbar^2}{2m} \sum_{i=1}^N \nabla^2 + \sum_{i<j}^N \hat{U}(\mathbf{r}_i, \mathbf{r}_j) + \sum_{i=1}^N \hat{V}(\mathbf{r}_i) \right] \psi = E_e \psi , \end{aligned} \quad (3.4)$$

where  $T$  and  $U$  are the universal operators (do not depend on the system), but  $V$  depends on the specifics of a system. This many-body equation cannot be separated into single-particle equations because of the interaction term  $U$ . There are two ways to solve for the many-body wavefunction: using the Hartree-Fock (exchange only) and the post-Hartree-Fock methods by expanding the many-body wavefunction as a Slater determinant,<sup>2-5</sup> or using the DFT method to map the many-body problem (with  $U$ ) onto a non-interacting single-particle problem (without  $U$ ). The former method is computationally extremely demanding and therefore cannot be used for a large and complex system like a molecule. On the other hand, the key variable for the DFT method is the charge density, instead of the high-dimensional many-body wavefunction. Because the computational cost for the DFT is comparatively less expensive, it is generally used to predict the electronic structure of a complex system.

The electron/charge density  $n$  corresponding to the many-body wavefunction is given as

$$n(\mathbf{r}) = N \int d\mathbf{r}_2 \dots \int d\mathbf{r}_N \psi^*(\mathbf{r}, \mathbf{r}_2, \dots, \mathbf{r}_N) \psi(\mathbf{r}, \mathbf{r}_2, \dots, \mathbf{r}_N) . \quad (3.5)$$

Note that the electron density is a function of the 3D spatial coordinate  $\mathbf{r}$ . Using the reverse transformation, we can write the wavefunction as a functional (function of a function) of the charge density:

$$\psi = \psi [n(\mathbf{r})] .$$

Similarly, the corresponding wavefunction ( $\Psi_0$ ) for the ground-state charge density ( $n_0$ ) will be

$$\psi_0 = \psi [n_0(\mathbf{r})] . \quad (3.6)$$

Here the ground-state wave function is uniquely defined by the electron density using to the Hohenberg-Kohn theorem.<sup>6</sup> According to the theorem, the external potential ( $V_{ext}$ )<sup>7</sup> and the total energy of the system is a unique functional of the ground-state electron density ( $n_0$ ). In other words, all the ground-state properties can be determined by the electron density alone. Furthermore, the electron density that minimizes the ground-state energy is the exact ground-state density of the system where the minimization is obtained by the variational method. So, once we obtain the ground-state density, we can (in principle) calculate any properties of a ground-state observable ( $O$ ) as a functional of  $n_0$ :

$$O[n_0] = \langle \psi[n_0] | \hat{O} | \psi[n_0] \rangle . \quad (3.7)$$

For example, the ground-state energy ( $E_0$ ) can be calculated as:

$$\begin{aligned} E_0 = E[n_0] &= \langle \psi[n_0] | \hat{H} | \psi[n_0] \rangle \\ E[n_0] &= \langle \psi[n_0] | \hat{T} + \hat{U} + \hat{V}_{ext} | \psi[n_0] \rangle . \end{aligned} \quad (3.8)$$

For an arbitrary electron density, not necessarily the ground-state density, the energy of the system can be written as:

$$\begin{aligned} E[n] &= \langle \psi[n] | \hat{T} + \hat{U} + \hat{V}_{ext} | \psi[n] \rangle \\ E[n] &= \langle \psi[n] | \hat{T} | \psi[n] \rangle + \langle \psi[n] | \hat{U} | \psi[n] \rangle + \langle \psi[n] | \hat{V}_{ext} | \psi[n] \rangle \\ E[n] &= T[n] + U[n] + \int d\mathbf{r} V_{ext}(\mathbf{r}) n(\mathbf{r}) . \end{aligned} \quad (3.9)$$

Assuming there exists a reliable representation for  $T[n]$  and  $U[n]$ , the ground-state energy can be obtained by minimizing the energy  $E[n]$  with respect to the density  $n$  to represent  $E_0$  as a functional of  $n_0$ .



### 3.4 Kohn-Sham Formalism

So far, we avoid using the computationally complicated and expensive many-body wavefunction, and instead represent all the properties of the system in terms of the charge density using the Hohenberg-Kohn theorem. However, minimizing the  $E[n]$  with respect to the charge density is also computationally difficult and subject to a reliable representation of  $T[n]$  and  $U[n]$  which are, in general, unknown. In practice, the ground-state density is obtained by constructing a fictional non-interacting single particle system whose ground-state density ( $n_{s0}$ ) is exactly equal to that of the original many-body interacting case ( $n_0 = n_{s0}$ ). The set of Schrödinger like equations describing the non-interacting single-particle system is given as:

$$\hat{H}_{KS}\varphi_i(\mathbf{r}) = \varepsilon_i\varphi_i(\mathbf{r})$$

$$\left[ -\frac{\hbar^2}{2m}\nabla^2 + V_{KS}[n(\mathbf{r})] \right] \varphi_i(\mathbf{r}) = \varepsilon_i\varphi_i(\mathbf{r}) , \quad (3.10)$$

where  $H_{KS}$ ,  $\varphi_i$ ,  $\varepsilon_i$ , and  $V_{KS}$  are the effective Kohn-Sham Hamiltonian, Kohn-Sham (single-particle) orbitals, Kohn-Sham orbital energies, and the effective Kohn-Sham potential respectively. The Equation 3.10 is referred as the Kohn-Sham equation.<sup>8</sup> The Kohn-Sham orbitals are orthonormal and the corresponding charge density of the non-interacting particle can be written in terms of the orbitals as:

$$\int d\mathbf{r}\varphi_j^*(\mathbf{r})\varphi_i(\mathbf{r}) = \delta_{i,j}$$

$$n(\mathbf{r}) = \sum_i |\varphi_i(\mathbf{r})|^2 . \quad (3.11)$$

Here, the sum is over all the occupied orbitals. The Kohn-Sham potential, which is a functional of the density, can be separated in the following three components: the external potential, the Hartree potential ( $V_H$ ), and the exchange-correlation potential ( $V_{XC}$ ) that includes the many-body effects.<sup>9</sup>

$$V_{KS} [n(\mathbf{r})] = V_{ext}(\mathbf{r}) + V_H [n(\mathbf{r})] + V_{XC} [n(\mathbf{r})] , \quad (3.12)$$

where the  $V_H$  and  $V_{XC}$  (functionals of  $n$ ) are given as follows:

$$V_H [n(\mathbf{r})] = \int d\mathbf{r}' \frac{n(\mathbf{r}')}{|\mathbf{r} - \mathbf{r}'|} \quad (3.13)$$

$$V_{XC} [n(\mathbf{r})] = \frac{\delta E_{XC} [n(\mathbf{r})]}{\delta n(\mathbf{r})} . \quad (3.14)$$

Now, we obtain the Kohn-Sham potential, we can solve the Kohn-Sham equation for  $\varphi_i$  that corresponds to the ground-state density. Both orbitals and the corresponding charge density are used to construct the Kohn-Sham potential, which is then used to solve for the ground-state. As a consequence, the Kohn-Sham equations have to be solved self-consistently. When the Kohn-Sham orbitals are represented by plane-waves, the Kohn-Sham equations are solved by diagonalizing the Hamiltonian matrix (Equation 3.35). Once we have the solution for the Kohn-Sham orbitals, we can calculate any ground-state observable.

The obvious observable is the Kohn-Sham energy of the system, which can be given as

$$E_{KS} [n(\mathbf{r})] = T_s [n(\mathbf{r})] + \int d\mathbf{r} V_{ext}(\mathbf{r})n(\mathbf{r}) + E_H [n(\mathbf{r})] + E_{XC} [n(\mathbf{r})] , \quad (3.15)$$

where the density ( $n_s$ ) is calculated from the solution of the Kohn-Sham orbitals using the Equation 3.11. The first term of the right-hand side of Equation 3.15 corresponds to the kinetic energy of the non-interacting particle, followed by the external potential energy, the Hartree energy, and the exchange-correlation energy. The Hartree energy can be given as

$$E_H [n(\mathbf{r})] = \frac{1}{2} \int d\mathbf{r} \int d\mathbf{r}' \frac{n(\mathbf{r})n(\mathbf{r}')}{|\mathbf{r} - \mathbf{r}'|} . \quad (3.16)$$

Here, the 1/2 pre-factor is added to prevent double counting.

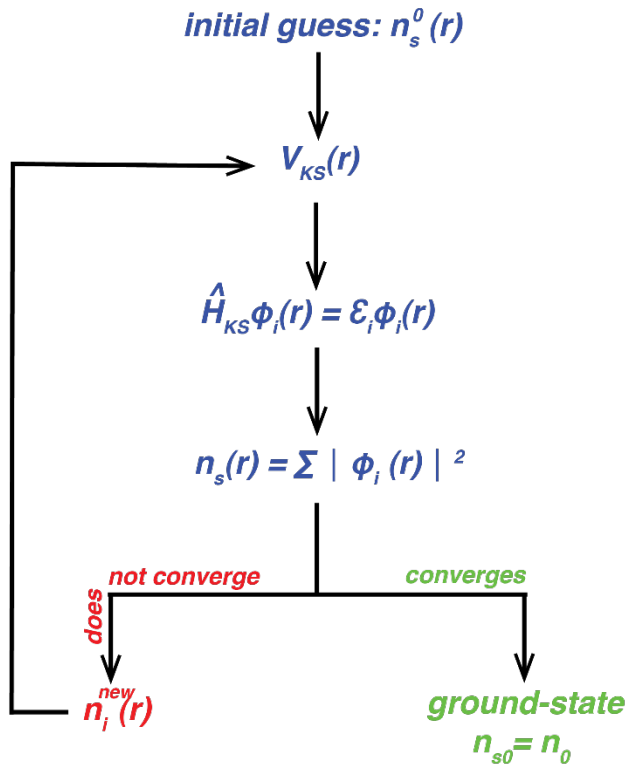


Figure 3.1. Schematic of the DFT Algorithm. It starts with an initial guess for the density. Its used to construct the Kohn-Sham potential to solve the Kohn-Sham equations. The solution for the Kohn-Sham orbitals are used to construct the new density. If the new density is within the tolerance of the previous density, the ground-state density is found. Otherwise, the new density is used to construct the potential and the whole process repeats.

The self-consistent method is schematically shown in the Figure 3.1. It starts with the initial guess for the electron density  $n_s^0$ . An educated guess for the initial density can speed-up the convergence drastically. The corresponding Kohn-Sham potential is evaluated based on the density. One of the trickiest parts of constructing the Kohn-Sham potential is determining a suitable exchange-correlation energy (hence potential) for the system under study. The exchange-correlation energy includes the many-body effects, such as the Pauli exclusion and the many-body Coulombic interaction. Despite the obvious importance of the exchange-correlation, there is no

general representation of this term. There are several approximations for the exchange-correlation term, a few of which we discuss later in this chapter. The success of the DFT calculation depends on the accurate description of the exchange-correlation term, which depends on the properties of the system under investigation. Once, the Kohn-Sham potential is constructed, it is used to solve the Kohn-Sham equation for the orbitals by diagonalizing the Hamiltonian. This is the computationally most intensive part of the DFT process. The new orbitals are used to construct the charge density. This process is repeated until some convergence criterion is satisfied. For example,

if the difference between the new and the previous densities is within the tolerance, the iteration stops, and the ground-state is reached. Otherwise, the new density is mixed with the previous density (for computational stability) to construct the new potential, and the whole process repeats.

### 3.5 Plane Wave Basis

The representation of the Kohn-Sham orbitals depends on the nature of the system. For example, orbitals are represented in the real space to describe a molecule (SIESTA),<sup>10</sup> whereas the reciprocal space representation is generally preferred for a periodic system (VASP).<sup>11-12</sup> It is tricky for a mixed system such as in our case (*n*-alkanethiol self-assembled monolayers on the Au(111) substrate). Here, we confine ourselves to a periodic system by representing the Kohn-Sham orbitals in the reciprocal space using plane wave basis. An orbital  $\varphi_{\mathbf{k}}$  with wavevector  $\mathbf{k}$  can be represented by a real space plane wave  $u(\mathbf{r})$  as:

$$\varphi_{\mathbf{k}}(\mathbf{r}) = e^{i\mathbf{k}\cdot\mathbf{r}} u_{\mathbf{k}}(\mathbf{r}) , \quad (3.17)$$

where the real space plane wave is further expanded in terms of reciprocal lattice plane waves ( $u(\mathbf{G})$ , basis set) as

$$u_{\mathbf{k}}(\mathbf{r}) = \sum_{\mathbf{G}} e^{i\mathbf{G}\cdot\mathbf{r}} u_{\mathbf{k}}(\mathbf{G}) . \quad (3.18)$$

Since the system is periodic, the orbital only picks up a phase after being translated by the real space lattice vector  $\mathbf{R}$  as follows:

$$\varphi_{\mathbf{k}}(\mathbf{r} + \mathbf{R}) = e^{i\mathbf{k}\cdot\mathbf{R}} \varphi_{\mathbf{k}}(\mathbf{r}) . \quad (3.19)$$

The reciprocal space lattice vector  $\mathbf{G}$  is related to  $\mathbf{R}$  by the following equation:

$$e^{i\mathbf{G}\cdot\mathbf{R}} = 1 .$$

Using Equations 3.16 and 3.17 we can construct the orbital in terms of the basis set as follows:

$$\varphi_{\mathbf{k}}(\mathbf{r}) = \sum_{\mathbf{G}} e^{i(\mathbf{k}+\mathbf{G})\cdot\mathbf{r}} u_{\mathbf{k}}(\mathbf{G}) . \quad (3.20)$$

The above equation shows that the orbital is represented by a sphere in the reciprocal space with radius  $\mathbf{k}+\mathbf{G}$ . In principle, we need an infinite number of reciprocal lattice plane waves to represent an arbitrary real space orbital. In practice, however, the number of plane waves used to construct the Kohn-Sham orbitals are limited by the cutoff energy  $E_{cut}$  (proportional to the kinetic energy).

The corresponding real space density can be given using Equations 3.14 and 3.19 as

$$n(\mathbf{r}) = \sum_{\mathbf{k}} |\varphi_{\mathbf{k}}(\mathbf{r})|^2 = \left[ \sum_{\mathbf{G}'} u_{\mathbf{k}}(\mathbf{G}') e^{i\mathbf{G}'\cdot\mathbf{r}} \right] \left[ \sum_{\mathbf{G}} u_{\mathbf{k}}^*(\mathbf{G}) e^{-i\mathbf{G}\cdot\mathbf{r}} \right]$$

$$n(\mathbf{r}) = \sum_{\mathbf{G},\mathbf{G}'} f(\varepsilon_{\mathbf{k}}) (u_{\mathbf{k}}(\mathbf{G}') u_{\mathbf{k}}^*(\mathbf{G})) e^{i(\mathbf{G}'-\mathbf{G})\cdot\mathbf{r}} , \quad (3.21)$$

where  $f(\varepsilon)$  is the fractional occupation. Drawing analogy with the orbitals, the corresponding density is represented in the reciprocal space by a spherical shell with thickness  $\mathbf{G}-\mathbf{G}'$ . Notice that, both the Kohn-Sham orbitals and the density are represented by the plane wave basis set,  $u(\mathbf{G})$ , in the momentum space.

From now on, we will represent all the quantities using the compact bra-ket notation for convenience. The Kohn-Sham orbitals and the corresponding density are represented as follows:

$$|\mathbf{k}\rangle = \sum_{\mathbf{G}} c_{\mathbf{G}} |\mathbf{k} + \mathbf{G}\rangle \quad (3.22)$$

$$|n\rangle = \sum_{\mathbf{G},\mathbf{G}'} f(\varepsilon_{\mathbf{k}}) c(\mathbf{G}') c^*(\mathbf{G}) |\mathbf{G}' - \mathbf{G}\rangle , \quad (3.23)$$

where  $c_{\mathbf{G}}$  are the basis coefficients. Let us also define a generalized planewave as the sum of all the Kohn-Sham orbitals

$$|\varphi\rangle = \sum_{\mathbf{k}} a_{\mathbf{k}} |\mathbf{k}\rangle . \quad (3.24)$$

### 3.6 Pseudo-wavefunction and Pseudopotential

Planewave representation of an entire system is computationally very expensive. Generally, the Kohn-Sham orbitals are used to construct pseudo-wavefunctions to eliminate the core electrons from the calculation, because the core electrons do not participate in the chemical bonds and band structure which is of interest to us. As a consequence, an atom can be described solely by the valance electrons, which feels an effective potential (pseudopotential) that is the nuclear potential screened by the core electrons. The external potential in the Kohn-Sham equation (Equation 3.10) becomes just the sum of the pseudopotentials. Here, we will use the orthogonalized plane wave (OPW) basis for the pseudo-wavefunctions to derive the corresponding pseudopotential.

We use the Kohn-Sham orbitals to construct the OPW basis which are orthogonal to the core state.<sup>1</sup>

$$|\psi_{OPW}^{\mathbf{k}}\rangle = |\mathbf{k}\rangle - \sum_{t,j} |t,j\rangle \langle t,j|\mathbf{k}\rangle \quad (3.25)$$

---

<sup>1</sup> The core states are orthonormal to each other

$$\langle t', j' | t, j \rangle = \delta(t-t')\delta(j-j') .$$

The orthogonality between the core states and the OPW is

$$\langle t', j' | \psi_{OPW}^{\mathbf{k}} \rangle = \langle t', j' | \mathbf{k} \rangle - \sum_{t,j} \langle t', j' | t, j \rangle \langle t, j | \mathbf{k} \rangle = \langle t', j' | \mathbf{k} \rangle - \sum_{t,j} \delta(t-t')\delta(j-j') \langle t, j | \mathbf{k} \rangle$$

$$\langle t', j' | \psi_{OPW}^{\mathbf{k}} \rangle = \langle t', j' | \mathbf{k} \rangle - \langle t', j' | \mathbf{k} \rangle = 0 .$$

The above equation shows that the OPW is constructed by projecting the Kohn-Sham orbitals on the core states

$$|\psi_{OPW}^{\mathbf{k}}\rangle = \left(1 - \sum_{t,j} |t, j\rangle \langle t, j|\right) |\mathbf{k}\rangle = (1 - \hat{P}) |\mathbf{k}\rangle, \quad (3.26)$$

where the projection operator  $P$  is composed of the core states and defined as follows:

$$\hat{P} = \sum_{t,j} |t, j\rangle \langle t, j|. \quad (3.27)$$

Similar to Equation 3.24, the total OPW is related to the generalized plane wave (Equation 3.23) as follows:

$$\begin{aligned} |\psi_{OPW}\rangle &= \sum_{\mathbf{k}} a_{\mathbf{k}} |\psi_{OPW}^{\mathbf{k}}\rangle = \sum_{\mathbf{k}} (1 - \hat{P}) a_{\mathbf{k}} |\mathbf{k}\rangle = (1 - \hat{P}) \sum_{\mathbf{k}} a_{\mathbf{k}} |\mathbf{k}\rangle \\ &= (1 - \hat{P}) |\phi\rangle. \end{aligned} \quad (3.28)$$

Since the core states vanish outside the core radius ( $r_0$ ), the OPW reduces to the generalized wavefunction for the valence electrons:

$$|\psi_{OPW}\rangle = |\phi\rangle, r > r_0. \quad (3.29)$$

Using the OPW basis the Schrödinger equation with the original potential ( $V$ ) and the total energy ( $E$ ) is given

$$\left(-\frac{1}{2}\nabla^2 + \hat{V}\right) |\psi_{OPW}\rangle = E |\psi_{OPW}\rangle. \quad (3.30)$$

Equation 3.27 can be used to derive the pseudopotential  $V_{ps}$  for the system as follows:

$$\begin{aligned} \left(-\frac{1}{2}\nabla^2 + \hat{V}\right) (1 - \hat{P}) |\phi\rangle &= E (1 - \hat{P}) |\phi\rangle \\ \left(-\frac{1}{2}\nabla^2 + \left[\hat{V} + \frac{1}{2}\nabla^2 \hat{P} + E\hat{P} - \hat{V}\hat{P}\right]\right) |\phi\rangle &= E |\phi\rangle \end{aligned}$$

$$\left(-\frac{1}{2}\nabla^2 + \hat{V}_{ps}\right)|\varphi\rangle = E|\varphi\rangle, \quad (3.31)$$

where the pseudopotential is given as:

$$\begin{aligned} \hat{V}_{ps}(\mathbf{r}) &= \hat{V}(\mathbf{r}) - \left(-\frac{1}{2}\nabla^2 + \hat{V}\right)\hat{P} + E\hat{P} \\ &= \hat{V}(\mathbf{r}) - \sum_{t,j} \left(-\frac{1}{2}\nabla^2 + \hat{V}\right)|t,j\rangle\langle t,j| + E\sum_{t,j} |t,j\rangle\langle t,j| \\ &= \hat{V}(\mathbf{r}) - \sum_{t,j} E_c |t,j\rangle\langle t,j| + E\sum_{t,j} |t,j\rangle\langle t,j| \\ \hat{V}_{ps}(\mathbf{r}) &= \hat{V}(\mathbf{r}) - \sum_{t,j} (E_c - E) |t,j\rangle\langle t,j|. \end{aligned} \quad (3.32)$$

As a result, the modified external potential ( $W$ ) becomes

$$W = \sum_i \hat{V}_{ps}^i(r). \quad (3.33)$$

Outside the core radius, the pseudopotential becomes the original potential as the core states vanish. The presence of the second term in Equation 3.31 represents the screening of the nuclear charge by the core electrons effectively reducing the potential seen by the valence electrons. Moreover, the pseudopotential reduces the oscillation of the valence states near the nucleus which would otherwise require a large number of plane waves. There are several ways to construct the pseudopotential. One of the most popular methods is the empirical pseudopotential method (EPM) where the pseudopotential is adjusted to fit the experimental data at many critical points within the Brillouin zone.<sup>13-18</sup>

### 3.7 Hamiltonian Matrix Diagonalization

Finally, the Schrödinger equation is solved by diagonalizing the Hamiltonian matrix. While using the plane wave basis, it is convenient to represent everything in the momentum space. The Kohn-Sham orbitals (within the first Brillouin zone) and the corresponding densities are already



defined in the momentum space by Equations 3.21 and 3.22. We need to represent the potentials in the momentum space as well before constructing the Hamiltonian matrix. The Schrödinger equation can be written as:

$$\hat{H}'|\mathbf{k}\rangle = \varepsilon_{\mathbf{k}}|\mathbf{k}\rangle$$

$$\hat{H}'\sum_{\mathbf{G}}c_{\mathbf{G}}|\mathbf{k}+\mathbf{G}\rangle = \varepsilon_{\mathbf{k}}\sum_{\mathbf{G}}c_{\mathbf{G}}|\mathbf{k}+\mathbf{G}\rangle .$$

Pre-multiplying by  $\langle\mathbf{k}+\mathbf{G}'|$ , we have

$$\sum_{\mathbf{G}}c_{\mathbf{G}}\left[\langle\mathbf{k}+\mathbf{G}'|\hat{H}'|\mathbf{k}+\mathbf{G}\rangle - \varepsilon_{\mathbf{k}}\langle\mathbf{k}+\mathbf{G}'|\mathbf{k}+\mathbf{G}\rangle\right] = 0$$

$$\sum_{\mathbf{G}}\left[\hat{H}_{G,G'}(\mathbf{k})c_{\mathbf{G}}(\mathbf{k}) - \varepsilon_{\mathbf{k}}c_{\mathbf{G}}(\mathbf{k})\right] = 0 . \quad (3.34)$$

For each  $\mathbf{G}$ , the above equation represents one row or one column of the Hamiltonian matrix (without the second term that contains  $\varepsilon_{\mathbf{k}}$ ). The Hamiltonian, and hence the potentials, needs to be represented in the momentum space before diagonalizing the matrix. The Hamiltonian and the potentials are given in the momentum space as follows:

$$\hat{H}'(\mathbf{k}) = \frac{\hbar^2}{2m}|\mathbf{k}+\mathbf{G}|^2\delta_{\mathbf{G},\mathbf{G}'} + W(\mathbf{k}+\mathbf{G},\mathbf{k}+\mathbf{G}') + V_H(\mathbf{G}-\mathbf{G}') + V_{XC}(\mathbf{G}-\mathbf{G}') . \quad (3.35)$$

### 3.8 Exchange-Correlation Functionals

The total Kohn-Sham energy (Equation 3.15) can be separated into different contributions

$$E_{KS} = K.E. + E_{ext} + E_H + E_{XC} , \quad (3.36)$$

where the first term is the kinetic energy of a non-interacting electron, followed by the interaction of the electron with an external field (in this case, nuclear charges). The last two terms arise from the electron-electron interaction: the Hartree energy represents the classical part of the interaction,

whereas the many-body quantum effects are included in the exchange-correlation term. The exchange-correlation term can be further separated into the exchange energy ( $E_X$ ) and the coupling constant averaged correlation energy ( $E_C$ ):

$$E_{XC} = E_X + \bar{E}_C . \quad (3.37)$$

Therefore, the total energy of the electronic system can be expressed with increasing accuracy as

$$E_{XC} [n(\mathbf{r})] = K.E. [\varphi [n(\mathbf{r})]] + E_{ext} [n(\mathbf{r})] + E_H [n(\mathbf{r})] + E_X [\varphi [n(\mathbf{r})]] + \bar{E}_C . \quad (3.38)$$

The external energy and the Hartree energy are explicit functionals of the density. Whereas the kinetic energy and the exchange energy are explicit functionals of the Kohn-Sham orbitals, which are, in turn, (a generally unknown) functional of the density. The correlation between the electrons is the most challenging term. Although the correlation for the homogeneous electron gas has been well-studied,<sup>19</sup> the general representation for the inhomogeneous system is still relatively unknown. The electron density of a molecular system is far from being uniform, therefore using the correlation of the homogeneous electron gas can significantly deteriorate the simulation prediction. Moreover, the really meaningful quantity is the exchange-correlation term, where it is important to treat the exchange and the correlation terms with similar accuracy level. Here we discuss two approximations for the exchange-correlation term: the local density approximation (LDA) and the generalized gradient approximation (GGA).

### ***3.8.1 Local Density Approximation***

The homogeneous electron gas (HEG), such as in metallic systems, with correlated electrons is a natural starting point for our discussion. The exchange energy density of the HEG is known analytically as a function of the charge density (Dirac's expression)<sup>20</sup> as

$$\begin{aligned}
\varepsilon_X^D [n(\mathbf{r})] &= -\frac{3}{4} \left( \frac{3}{\pi} \right)^{1/3} n(\mathbf{r})^{1/3} \\
&= -\frac{3}{4} \left( \frac{9}{4\pi^2} \right)^{1/3} \frac{1}{r_s} ,
\end{aligned} \tag{3.39}$$

where  $r_s$  is the mean interelectronic distance in atomic units, expressed in terms of the density

$$r_s = \left( \frac{3}{4\pi n(\mathbf{r})} \right)^{1/3} .$$

The correlation energy density for the spin polarized and the spin unpolarized HEG is based on the quantum Monte Carlo calculation exact within the numerical precision.<sup>21</sup> It has been parameterized by Perdew and Zunger<sup>22</sup> and can be expressed in the following form:

$$\begin{aligned}
\varepsilon_C^{PW} [n(\mathbf{r})] &= A \ln r_s + B + Cr_s \ln r_s + Dr_s, & r_s \leq 1 \\
&= \gamma / (1 + \beta_1 \sqrt{r_s} + \beta_2 r_s), & r_s > 1 .
\end{aligned} \tag{3.40}$$

In the LDA method, an inhomogeneous electron gas is approximated as locally homogeneous, then the corresponding exchange-correlation hole for the HEG is used for the energy density  $\varepsilon_{XC}$ . Finally, the total energy is calculated by integrating (averaging) the energy density with the position dependent charge density over the volume of the system

$$E_{XC}^{LDA} [n(\mathbf{r})] = \int d\mathbf{r} n(\mathbf{r}) \varepsilon_{XC}^{LDA} [n(\mathbf{r})] . \tag{3.41}$$

In practice, the LDA exchange-correlation energy density is evaluated by adding the exchange and the correlation part of the HEG shown in Equations 3.38 and 3.39, respectively.

$$\varepsilon_{XC}^{LDA} [n(\mathbf{r})] = \varepsilon_X^D [n(\mathbf{r})] + \varepsilon_C^{PW} [n(\mathbf{r})] \tag{3.42}$$

Although, LDA approximation is quite successful for systems with slowly varying electron density (almost uniform), such as bulk metals, it fails to reproduce the electron density of atoms

in the core region. The LDA prediction deviates from the experimental ionization and dissociation energies of a finite system, such as molecules and clusters. It also fails to predict the location and the shape of the image potential on surfaces which is important for accurate prediction of the adsorption energies.<sup>23</sup>

### 3.8.2 Generalized Gradient Approximation

One of the ways to improve the LDA method for inhomogeneous electron density is by expanding the density in terms of its gradient and the higher order terms. Equation 3.40 becomes

$$E_{XC} [n(\mathbf{r})] = \int d\mathbf{r} n(\mathbf{r}) \varepsilon_{XC} [n(\mathbf{r})] F_{XC} [n(\mathbf{r}), \nabla n(\mathbf{r}), \nabla^2 n(\mathbf{r}), \dots] , \quad (3.43)$$

where  $F_{XC}$  represents the modification factor of the LDA expression depending on the change in density around the point of observation (semi-local method). The general form of the second order expansion for the GGA method<sup>23</sup> is given as:

$$E_{XC}^{GGA} [n(\mathbf{r})] = \int d\mathbf{r} A_{XC} [n(\mathbf{r})] n(\mathbf{r})^{4/3} + \int d\mathbf{r} C_{XC} [n(\mathbf{r})] \frac{|\nabla n(\mathbf{r})|^2}{n(\mathbf{r})^{4/3}} . \quad (3.44)$$

The leading term in the equation above corresponds to the LDA approximation. Finite truncation of the density expansion (up to 2<sup>nd</sup> order, in this case) can cause serious issues. For example, the series may not converge or exhibit a singularity, which can only be canceled by the full expansion. In fact, the first-order correction worsens the LDA result, and the second-order correction results in divergence.<sup>24</sup> The expansion of the density needs to be carried out very carefully to include all necessary contributions to the desired order. Moreover, preserving the exact conditions for the exchange-correlation holes, i.e. cancelling the self-interaction term and normalization conditions, is a major factor to improve the exchange energy.<sup>25</sup>

The main idea of the GGA method is to mimic the summation up to infinite order while expanding the density up to second order. There are two approaches for this. Theoretically, the coefficients are formulated to fulfill the exact conditions. In addition, there are several theoretical expressions to mimic the infinite sum. The other method is to fit the coefficient to an empirical dataset that reproduces a number of experimental observations. However, there is no guarantee that coefficients fitted to reproduce a certain set of observations can also accurately describe other properties of a different system. In other words, the later approach lacks transferability. Comparison between different GGA methods is reported by Sousa *et. al.*<sup>26</sup>

One of the most popular GGA functionals is called GGA-PBE after the authors Perdew, Burke, and Ernzerhof.<sup>27</sup> The GGA-PBE satisfies almost all the energetically significant properties and limits for the exchange and correlation functionals. The enhancement factor for the exchange  $F_X$  (modification of Equation 3.42) depends on the local density  $n(\mathbf{r})$ , the magnetization density  $\zeta$  (for spin-dependent systems), and the density gradient  $s$ .

$$F_X = 1 + \kappa - \frac{\kappa}{1 + \mu s^2 / \kappa} \quad (3.45)$$

The density gradient is given as

$$s = \frac{|\nabla n(\mathbf{r})|}{2\kappa_F n(\mathbf{r})}, \quad (3.46)$$

where  $\mu$  and  $\beta$  are constants. The correlation energy in this method<sup>28</sup> is expressed as

$$E_C^{GGA} = \int d\mathbf{r} n(\mathbf{r}) \left[ \varepsilon_C^{LDA}(n(\mathbf{r}), \zeta) + H[n(\mathbf{r}), \zeta, t] \right], \quad (3.47)$$

where

$$H[n(\mathbf{r}), \zeta, t] = \left( \frac{e^2}{a_0} \right) \gamma \varphi^3 \ln \left\{ 1 + \frac{\beta}{\gamma} t^2 \left( \frac{1 + At^2}{1 + At^2 + A^2 t^4} \right) \right\} \quad (3.48)$$

In the above equation,  $t$  is the dimensionless gradient as shown below

$$t = \frac{|\nabla n(\mathbf{r})|}{2\varphi\kappa_S n(\mathbf{r})}$$

$$\varphi(\zeta) = \frac{1}{2} \left\{ (1 + \zeta)^{2/3} + (1 - \zeta)^{2/3} \right\}$$

$$A = \frac{\beta}{\gamma} \left\{ e^{-\epsilon_C^{LDA}[n(\mathbf{r})]/(\gamma\varphi^3 e^2/a_0)} - 1 \right\},$$

where  $\kappa_S$  is the Thomas-Fermi screening wavenumber and  $\gamma$  is a constant. The exchange part of the GGA-PBE satisfies the uniform scaling conditions, obeys the spin-scaling relationship, the uniform electron gas limit, and the local Lieb-Oxford bound.<sup>29</sup> Meanwhile, the correlation part follows the correlation-hole sum rule, maintains the uniform scaling of the density, and correctly predicts the high-density limit.<sup>23</sup>

### 3.9 Dispersion Correction to DFT

Dispersion forces (vdW and Columbic forces) play a significant role for polarizable atoms,<sup>30</sup> molecules, and in the self-assembly process. In such cases, it is important to include the dispersion effects for an accurate prediction. The absence of the dispersion energy  $E_{disp}$  in the DFT calculation can result in inaccurate prediction of the system's properties.<sup>31</sup> DFT simulation does not explicitly

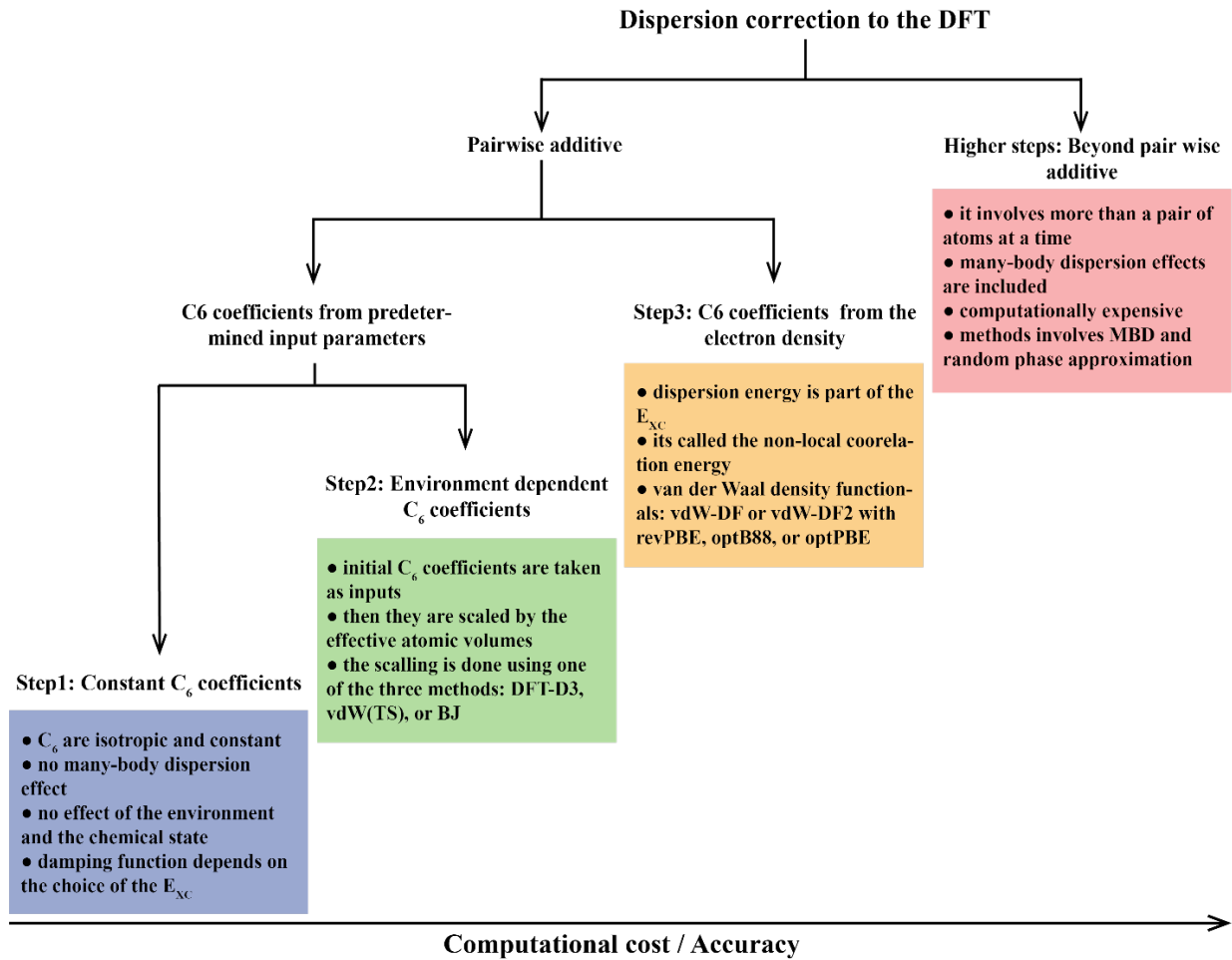


Figure 3.2 The Levels of Approximation for the Long-range Dispersion Energy in the DFT Calculation.

include the dispersion correction, but the dispersion energy can be included in the calculation when necessary. In general, the dispersion energy can be expressed as a function of the interatomic distance ( $r$ ) as follows:

$$E_{disp} = \sum_n \frac{C_n}{r^n} . \quad (3.49)$$

The exact power expansion of the  $E_{disp}$  depends on the nature of the system. For example,  $n = 6$  term dominates for a simple cubic system where each atom has six nearest neighbors, but this approximation is not applicable for a semiconductor.

There are several ways to include the dispersion correction in the DFT calculation. Over the past years, there has been significant development in this field resulting in a number of dispersion correction techniques. These dispersion correction methods can be organized by groups with same level of approximation, similar to the  $E_{XC}$ , from approximate methods to more accurate ones.<sup>32</sup> Here we organize the dispersion correction techniques in Figure 3.2 to emphasize not only their level of approximation, but also using their applicability.

The simplest way to include the dispersion correction in the DFT calculation is by adding a dispersion energy to the total energy of the system,  $E_{tot} = E_{DFT} + E_{disp}$ . In the simplest case, the dispersion energy depends on the  $C_n$  coefficients between the pairs of atoms (A and B),  $C^{AB}$ . It also includes a damping factor  $f$  to avoid the divergence of the  $r^{-n}$  term for small  $r$ . The following equation demonstrate this for  $n = 6$  as

$$E_{disp} = - \sum_{A,B}^{pairwise} f(r_{AB}, A, B) \frac{C^{AB}}{r_{AB}^6} . \quad (3.50)$$

The summation here is pairwise additive which is generally a valid assumption for gas phase and small molecules, and such approximation is applied in step 1, 2, and 3 in Figure 3.2. The coefficients  $C^{AB}$  can be external input parameters to calculate  $E_{disp}$  (step 1 and 2), or  $C^{AB}$  can be calculated directly from the electron density (step 3). The external coefficients are generally taken from the experiments and used in one of the two ways depending on the level of approximation. The coefficients can stay fixed throughout the simulation (step 1), or their values are scaled on the fly based on the effective atomic volumes (step 2). In step 3, the calculation of the coefficients does not require external parameters, the long-range dispersion correction is already included in the exchange-correlation energy

$$E_{XC} = E_X^{GGA} + E_C^{LDA} + E_C^{nl} . \quad (3.51)$$



The non-local correlation energy can be obtained from the electron density ( $n(\mathbf{r})$ ) as

$$E_C^{nl} = \iint d\mathbf{r}_1 d\mathbf{r}_2 n(\mathbf{r}_1) \varphi(\mathbf{r}_1, \mathbf{r}_2) n(\mathbf{r}_2) , \quad (3.52)$$

where  $\varphi(\mathbf{r}_1, \mathbf{r}_2)$  is an integration kernel. All the methods up to step 3 rely on the pairwise additive assumption. One of the drawbacks of this assumption is that the energy between a pair of atoms/molecules remains constant, independent of the separating medium. Although this assumption is acceptable for gas phase, this is not a reliable assumption for the condensed phase. Therefore, dispersion interaction in the condensed phase should extend beyond pairwise interactions (higher steps). Here, we briefly discuss the basic concept behind each level of approximation.

Step 1: This is the simplest method to include the dispersive effects where the external coefficients are isotropic (direction independent) and remains constant (independent of the chemical state and environment) throughout the simulation. These DFT-D methods are the most popular because of their simplicity and being computationally (relatively) inexpensive. One such method was developed by Grimme in 2006 where the coefficients are calculated from the ionization potential and the static polarizability of isolated atoms.<sup>33</sup> This method is known as the DFT-D2. Other functionals at this level of approximation are B97-D<sup>33</sup> and  $\omega$ B97X-D.<sup>34</sup> Apart from the computational advantages of the DFT-D2 method, it does not account for different chemical states and environments during the simulation because the coefficients are constant.

Step 2: At this level of approximation, the dispersion coefficient(s) of an atom in a molecule is scaled during the simulation based on its effective atomic volume. There are three common methods to scale the coefficients on the fly: the Grimme approach (DFT-D3),<sup>35</sup> the Tkatchenko and Scheffler approach (vdW(TS)),<sup>36</sup> and the Becke-Johnson approach (BJ).<sup>37-41</sup>

Step 3: Unlike the last two steps, the effect of the long-ranged dispersion interaction is directly calculated from the electron charge density of the system. The first term on the right-hand side of Equation 3.51  $E^{GGA}$  corresponds to the exchange energy which can be approximated by revPBE, optB88, and optPBE.<sup>42-46</sup> The second term corresponds to the local density approximation (LDA) of the correlation energy, and the last term is the non-local long-ranged correlation correction  $E^{nl}$  which depends on the electron density according to Equation 3.52. The methods at this level of approximation are referred as the van der Waal density functionals (vdW-DF and vdW-DF2).<sup>47-48</sup>

Higher steps: At this stage and beyond the long-ranged dispersion interaction is considered beyond the pairwise assumption. This is important for the condensed phase where the interaction between two atoms is screened by the separating medium. One example of a functional at this level is mPW2PLYP-D.<sup>49-50</sup>

We use DFT to study the effect of the sulfur hybridization on the adsorption geometry of an isolated methanethiol in Chapter 6 and the effect of the substrate relaxation on the most favored adsorption sites (bridge-fcc and bridge-hcp) in Chapter 7. In both cases, we use the projected augmented wave method density functional (PAW)<sup>51</sup> for the electron-ion interaction and PBE for the exchange functional. For the interaction between the substrate and the adsorbate, the dispersion correction of Grimme (DFT-D2) is included. We use 300 eV as our planewave cutoff in both cases. More details are given in the corresponding simulation method sections (Section 6.3 and 7.3).

### 3.10 References

1. Born, M.; Oppenheimer, R., Zur Quantentheorie der Molekeln. *Ann. Phys.* **1927**, *389* (20), 457-484.
2. Slater, J. C., The Self Consistent Field and the Structure of Atoms. *Phys. Rev.* **1928**, *32* (3), 339-348.

3. Hartree, D. R.; Hartree, W., Self-consistent Field, with Exchange, for Beryllium. *Proc. R. Soc. Lond. A*. **1935**, *150* (869), 9-33.
4. Fock, V., Selfconsistent Field mit Austausch für Natrium. *Z. Phys.* **1930**, *62* (11), 795-805.
5. Kaplan, T. A.; Kleiner, W. H., Hartree-Fock Theory: Slater Determinants of Minimum Energy. *Phys. Rev.* **1967**, *156* (1), 1-11.
6. Hohenberg, P.; Kohn, W., Inhomogeneous Electron Gas. *Phys. Rev.* **1964**, *136* (3B), B864-B871.
7. The external potential is the externally exerted potential/field on electrons excluding the kinetic energy of electrons and the interaction between electrons. The simplest case is the potential of the nucleus, which is represented by  $V$  in Equation 3.4. So, from now on we refer the interaction between the nucleus and the electrons as  $V_{ext}$ , instead of  $V$ .
8. Kohn, W.; Sham, L. J., Self-Consistent Equations Including Exchange and Correlation Effects. *Phys. Rev.* **1965**, *140* (4A), A1133-A1138.
9. Burke, K.; Wagner, L. O., DFT in a Nutshell. *Int. J. Quantum Chem.* **2013**, *113* (2), 96-101.
10. Soler, J. M.; Artacho, E.; Gale, J. D.; García, A.; Junquera, J.; Ordejón, P.; Sánchez-Portal, D., The SIESTA Method For ab Initio order-N materials Simulation. *J. Phys. Condens. Matter* **2002**, *14* (11), 2745-2779.
11. Kresse, G.; Hafner, J., Ab initio Molecular Dynamics for Liquid Metals. *Phys. Rev. B* **1993**, *47* (1), 558-561.
12. Kresse, G.; Furthmüller, J., Efficiency of ab-initio Total Energy Calculations for Metals and Semiconductors Using a Plane-wave Basis Set. *Comput. Mater. Sci.* **1996**, *6* (1), 15-50.
13. Brust, D.; Phillips, J. C.; Bassani, F., Critical Points and Ultraviolet Reflectivity of Semiconductors. *Phys. Rev. Lett.* **1962**, *9* (3), 94-97.
14. Brust, D.; Cohen, M. L.; Phillips, J. C., Reflectance and Photoemission From Si. *Phys. Rev. Lett.* **1962**, *9* (9), 389-392.
15. Bassani, F.; Brust, D., Effect of Alloying and Pressure on the Band Structure of Germanium and Silicon. *Phys. Rev.* **1963**, *131* (4), 1524-1529.
16. Brust, D., Electronic Spectra of Crystalline Germanium and Silicon. *Phys. Rev.* **1964**, *134* (5A), A1337-A1353.
17. Cohen, M. L.; Phillips, J. C., Spectral Analysis of Photoemissive Yields in Si, Ge, GaAs, GaSb, InAs, and InSb. *Phys. Rev.* **1965**, *139* (3A), A912-A920.

18. Cohen, M. L.; Bergstresser, T. K., Band Structures and Pseudopotential Form Factors for Fourteen Semiconductors of the Diamond and Zinc-blende Structures. *Phys. Rev.* **1966**, *141* (2), 789-796.
19. Ortiz, G.; Ballone, P., Correlation Energy, Structure Factor, Radial Distribution Function, and Momentum Distribution of the Spin-polarized Uniform Electron Gas. *Phys. Rev. B* **1994**, *50* (3), 1391-1405.
20. Dirac, P. A. M., Note on Exchange Phenomena in the Thomas Atom. *Math. Proc. Camb. Philos. Soc.* **2008**, *26* (3), 376-385.
21. Ceperley, D. M.; Alder, B. J., Ground State of the Electron Gas by a Stochastic Method. *Phys. Rev. Lett.* **1980**, *45* (7), 566-569.
22. Perdew, J. P.; Zunger, A., Self-interaction Correction to Density-functional Approximations for Many-electron Systems. *Phys. Rev. B* **1981**, *23* (10), 5048-5079.
23. Exchange and Correlation in DFT: Approximations and their Performances. In *Electronic Structure Calculations for Solids and Molecules: Theory and Computational Methods*, Kohanoff, J., Ed. Cambridge University Press: Cambridge, 2006; pp 75-120.
24. Ma, S.-k.; Brueckner, K. A., Correlation Energy of an Electron Gas with a Slowly Varying High Density. *Phys. Rev.* **1968**, *165* (1), 18-31.
25. Perdew, J. P., Accurate Density Functional for the Energy: Real-Space Cutoff of the Gradient Expansion for the Exchange Hole. *Phys. Rev. Lett.* **1985**, *55* (16), 1665-1668.
26. Sousa, S. F.; Fernandes, P. A.; Ramos, M. J., General Performance of Density Functionals. *J. Phys. Chem. A* **2007**, *111* (42), 10439-10452.
27. Perdew, J. P.; Burke, K.; Ernzerhof, M., Generalized Gradient Approximation Made Simple. *Phys. Rev. Lett.* **1996**, *77* (18), 3865-3868.
28. Perdew, J. P.; Wang, Y., Accurate and Simple Analytic Representation of the Electron-gas Correlation Energy. *Phys. Rev. B* **1992**, *45* (23), 13244-13249.
29. Lieb, E. H.; Oxford, S., Improved Lower Bound on the Indirect Coulomb Energy. *Int. J. Quantum Chem.* **1981**, *19* (3), 427-439.
30. Reimers, J. R.; Ford, M. J.; Marcuccio, S. M.; Ulstrup, J.; Hush, N. S., Competition of van der Waals and Chemical Forces on Gold-Sulfur Surfaces and Nanoparticles. *Nat. Rev. Chem.* **2017**, *1*, 0017-12.
31. Seema, P.; Behler, J.; Marx, D., Force-Induced Mechanical Response of Molecule-Metal Interfaces: Molecular Nanomechanics of Propanethiolate Self-Assembled Monolayers on Au(111). *Phys. Chem. Chem. Phys.* **2013**, *15* (38), 16001-16011.

32. Klimeš, J.; Michaelides, A., Perspective: Advances and Challenges in Treating van der Waals Dispersion Forces in Density Functional Theory. *J. Chem. Phys.* **2012**, *137* (12), 120901.
33. Grimme, S., Semiempirical GGA-type Density Functional Constructed with a Long-range Dispersion Correction. *J. Comput. Chem.* **2006**, *27* (15), 1787-1799.
34. Chai, J.-D.; Head-Gordon, M., Long-range Corrected Hybrid Density Functionals with Damped Atom–Atom Dispersion Corrections. *Phys. Chem. Chem. Phys.* **2008**, *10* (44), 6615-6620.
35. Grimme, S.; Antony, J.; Ehrlich, S.; Krieg, H., A Consistent and Accurate ab initio Parametrization of Density Functional Dispersion Correction (DFT-D) for the 94 Elements H-Pu. *J. Chem. Phys.* **2010**, *132* (15), 154104-19.
36. Tkatchenko, A.; Scheffler, M., Accurate Molecular van der Waals Interactions from Ground-State Electron Density and Free-Atom Reference Data. *Phys. Rev. Lett.* **2009**, *102* (7), 073005.
37. Becke, A. D., Real-space post-Hartree–Fock Correlation Models. *J. Chem. Phys.* **2005**, *122* (6), 064101.
38. Becke, A. D.; Johnson, E. R., Exchange-hole Dipole Moment and the Dispersion Interaction. *J. Chem. Phys.* **2005**, *122* (15), 154104.
39. Johnson, E. R.; Becke, A. D., A post-Hartree–Fock Model of Intermolecular Interactions. *J. Chem. Phys.* **2005**, *123* (2), 024101.
40. Becke, A. D.; Johnson, E. R., A Density-Functional Model of the Dispersion Interaction. *J. Chem. Phys.* **2005**, *123* (15), 154101.
41. Becke, A. D.; Johnson, E. R., Exchange-Hole Dipole Moment and the Dispersion Interaction Revisited. *J. Chem. Phys.* **2007**, *127* (15), 154108.
42. Zhang, Y.; Yang, W., Comment on "Generalized Gradient Approximation Made Simple". *Phys. Rev. Lett.* **1998**, *80* (4), 890-890.
43. Klimeš, J.; Bowler, D. R.; Michaelides, A., Chemical Accuracy for the van der Waals Density Functional. *J. Phys. Condens. Matter* **2009**, *22* (2), 022201.
44. Klimeš, J.; Bowler, D. R.; Michaelides, A., Van der Waals Density Functionals Applied to Solids. *Phys. Rev. B* **2011**, *83* (19), 195131.
45. Carrasco, J.; Santra, B.; Klimeš, J.; Michaelides, A., To Wet or Not to Wet? Dispersion Forces Tip the Balance for Water Ice on Metals. *Phys. Rev. Lett.* **2011**, *106* (2), 026101.

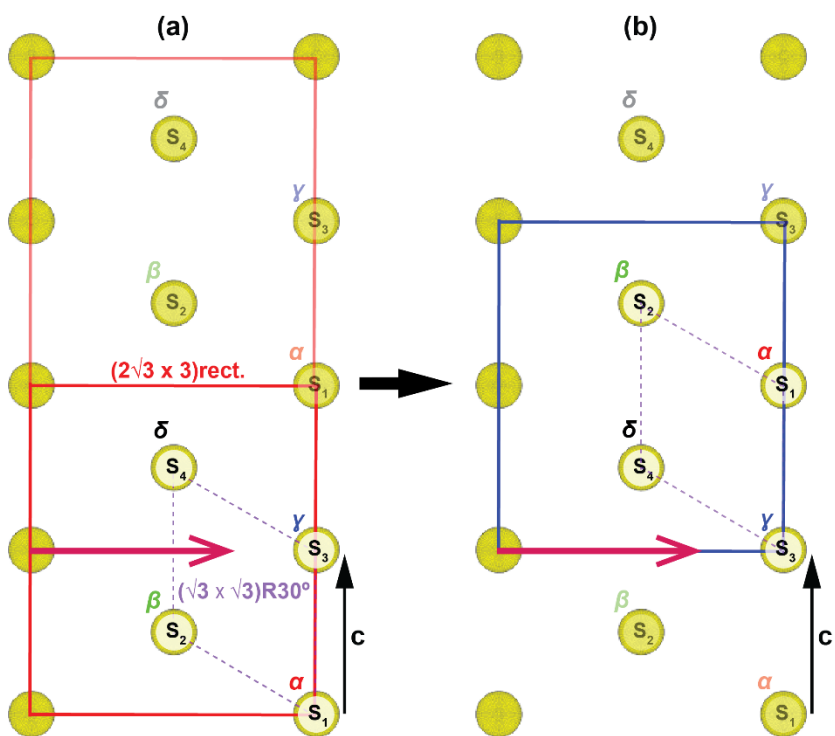
46. Mittendorfer, F.; Garhofer, A.; Redinger, J.; Klimeš, J.; Harl, J.; Kresse, G., Graphene on Ni(111): Strong Interaction and Weak Adsorption. *Phys. Rev. B* **2011**, *84* (20), 201401.
47. Murray, É. D.; Lee, K.; Langreth, D. C., Investigation of Exchange Energy Density Functional Accuracy for Interacting Molecules. *J. Chem. Theory Comput.* **2009**, *5* (10), 2754-2762.
48. Lee, K.; Murray, É. D.; Kong, L.; Lundqvist, B. I.; Langreth, D. C., Higher-Accuracy van der Waals Density Functional. *Phys. Rev. B* **2010**, *82* (8), 081101-4.
49. Krieg, H.; Grimme, S., Thermochemical Benchmarking of Hydrocarbon Bond Separation Reaction Energies: Jacob's Ladder is Not Reversed! *Mol. Phys.* **2010**, *108* (19-20), 2655-2666.
50. Schwabe, T.; Grimme, S., Double-Hybrid Density Functionals with Long-Range Dispersion Corrections: Higher Accuracy and Extended Applicability. *Phys. Chem. Chem. Phys.* **2007**, *9* (26), 3397-3406.
51. Blöchl, P. E., Projector Augmented-wave Method. *Phys. Rev. B* **1994**, *50* (24), 17953-17979.

# Chapter 4: Exploring the Best Packing of Alkane Chains and its Effect on the Head Groups

## 4.1 Scope of this Chapter

The structure of the SAM is determined by the interplay of the Au-S interfacial structure with the alkane chain packing. We use molecular dynamics simulation to study the packing of decanethiol molecules in a dense phase (one molecule per three surface Au atoms) saturation coverage SAM. Here, we find the combination of chain twists and tilt directions that optimize the chain packing.

We are taking a reductionist view to examine the tilt direction and twist combinations that



maximize the alkane chain packing. There are 109 possible combinations that differ in energy by only  $\sim 2.5$  kcal/mol. We study the energy with a fixed packing density with two different constraints on the head groups, 1) fixed to the close-packed site in a plane, 2) constrained to a plane with the headgroups

Figure 4.1 Translation Symmetry of the Head Group Lattice. The example shows that the translation symmetry by the lattice vector  $\mathbf{c}$  yields these two structures, (a) and (b), symmetry equivalent.

allowed to move in the plane.

Previous studies suggested a 4-molecule basis  $(2\sqrt{3} \times 3)$ rect. structure at the Au-S interface.<sup>1</sup> We choose the  $(2\sqrt{3} \times 3)$ rect. unit cell which includes the 1-molecule and 2-molecule basis structures as special cases. We constrain the head groups at the  $(\sqrt{3} \times \sqrt{3})R30^\circ$  lattice sites to compare 109 unique combinations of twist angles and tilt direction. Then we allow the head groups to move in the x-y plane driven by the chain packing. We study the chain packing at 4 K to control and compare the twist structures. Our result shows that the close packing of the alkane chains prefer the 1-molecule basis twist structure when the head groups are constrained at the  $(\sqrt{3} \times \sqrt{3})R30^\circ$  sites. However, head group offset from the  $(\sqrt{3} \times \sqrt{3})R30^\circ$  sites can accommodate multiple twists per unit cell which lead to a 2-molecule basis twist structure. Further investigation is necessary to understand the effect on the twist structure due to the surface interaction, preference for the adsorption sites, and annealing at a higher temperature.



## 4.2 Determination of the Unique Tilt Direction and Twist Combinations

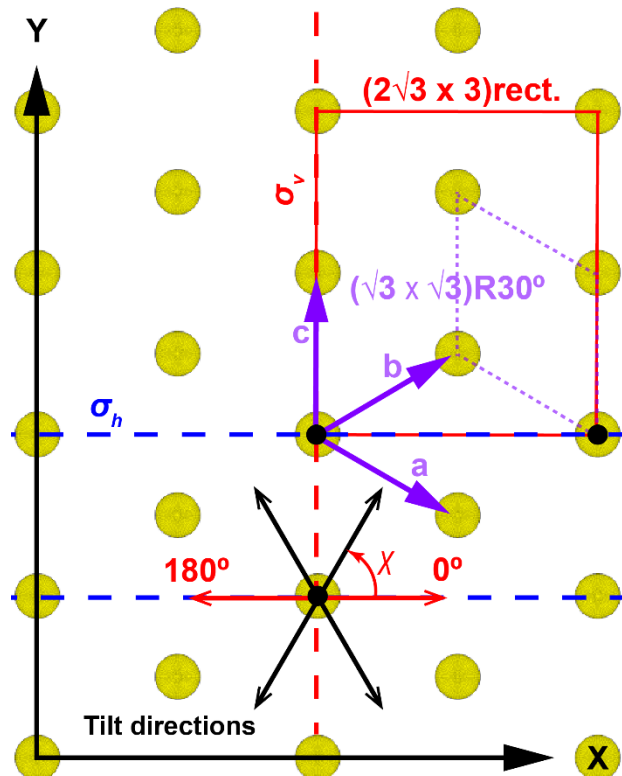


Figure 4.2. Symmetries Provided by the Trigonal Lattice of the Head Groups. Two orthogonal mirror planes ( $\sigma_v$  and  $\sigma_h$ ) are shown by red and blue dotted lines. Three lattice vectors (**a**, **b**, and **c**) are represented by purple arrows. Six tilt directions are shown where  $0^\circ$  tilt direction is along the  $+x$  axis and it increases counterclockwise direction.

We begin our discussion by identifying the structures with unique combinations of twist angles and tilt directions for the given trigonal lattice of the S head groups. In general, there are 1536 ( $4^4 \times 6$ ) structures emerging from four basis molecules in the  $(2\sqrt{3} \times 3)\text{rect.}$  unit cell. Each molecule can have one of four twist angles ( $50^\circ$ ,  $132^\circ$ ,  $228^\circ$ , and  $310^\circ$ ) emerging from the AA-MD chain packing (Section 2.6). The set of molecules can adopt one of six NNN tilt directions. Most of the 1536 combinations are not unique, but related by symmetries of the underlying trigonal lattice. For example, one of the three transitional symmetries of the trigonal lattice is shown in Figure 4.1.a (black arrow) with the 1-molecule basis  $(\sqrt{3} \times \sqrt{3})R30^\circ$  unit

cell (dotted blue rhombus) and the 4-molecule basis  $(2\sqrt{3} \times 3)\text{rect.}$  superlattice (red rectangle). The four basis molecules are shown as  $S_1$ ,  $S_2$ ,  $S_3$ , and  $S_4$  with the tilt direction ( $0^\circ$ ) represented by the pink arrow. If  $S_1$ ,  $S_2$ ,  $S_3$ , and  $S_4$  have twists  $\alpha$ ,  $\beta$ ,  $\gamma$ , and  $\delta$ , respectively, the resulting SAM structure is denoted as  $\{\alpha, \beta, \gamma, \delta; 0^\circ\}$ . Translation of the unit cell along the lattice vector **c** yields a symmetry equivalent structure  $\{\gamma, \delta, \alpha, \beta; 0^\circ\}$ , shown in Figure 4.1.b. In this example, translational symmetry reduces the size of the problem by half. Now, there are in total 16 symmetry operations provided

by the trigonal lattice (Table 4.1 and Figure 4.2) which reduces the size of the problem from 1536 structures to only 109 unique structures. There are three translational symmetries along the three lattice vectors (**a**, **b**, and **c**), two mirror symmetries along the vertical ( $\sigma_v$ ) and the horizontal ( $\sigma_h$ ) mirror planes, and the  $180^\circ$  rotational symmetry ( $C_2$ ). The remaining nine symmetry operations are a combination of those.

Table 4.1. The Symmetry Group of the Trigonal Lattice Consists of 16 Symmetry Operations. The identity operation is given by the symbol e.

e	$C_2$	$\sigma_v$	$\sigma_h$
a	$C_2 \cdot a$	$\sigma_v \cdot a$	$\sigma_h \cdot a$
b	$C_2 \cdot b$	$\sigma_v \cdot b$	$\sigma_h \cdot b$
c	$C_2 \cdot c$	$\sigma_v \cdot c$	$\sigma_h \cdot c$

We use Burnside's lemma<sup>2</sup> from group theory to derive the number of unique structures using the 16 symmetries of the underlying trigonal lattice. Intuitively, we can group the symmetry equivalent structures and count the number of groups (called orbits) to obtain the number of unique structures. However, this is mathematically complex and not scalable. Alternatively, we can apply each symmetry operation to all the 1536 structures and count the number of structures that remain unchanged. These structures are said to be fixed by the symmetry operation (fixed points of the symmetry operation). To apply Burnside's lemma, we add the number of fixed points for all the symmetry operations and divide it by the number of symmetry operations to obtain the number of unique structures. It is useful to state this more formally for our problem. We define a symmetry group ( $G$ ) that contains the 16 symmetry operations and a structure group ( $X$ ) that contains all the 1536 structures. A group element in  $X$  and  $G$  are represented by  $x$  and  $g$ , respectively. If a symmetry operation  $g$  fixes a structure  $x$ , the fixed point can be represented as follows

$$Fix(g) = \{x \in X : g \bullet x = x\} . \quad (4.1)$$

The number of fixed points for the symmetry operation is given by  $|Fix(g)|$ . The presence of  $\sigma_v$  separates the six tilt directions ( $\chi$ ) into two groups (Figure 4.2):  $\{0^\circ, 180^\circ\}$  and  $\{60^\circ, 120^\circ, 240^\circ, 300^\circ\}$ . The number of fixed points for these two sets of tilt directions are listed in Table 4.2. According to Burnside's lemma, the number of unique structures can be calculated from the fixed points as

$$\left| \frac{X}{G} \right| = \frac{1}{|G|} \sum_{g \in G} |Fix(g)| , \quad (4.2)$$

where  $|G|$  is the number of symmetry operations (sixteen in this case). We can separate the above equation for the two sets of tilt directions as

$$\left| \frac{X}{G} \right| = \frac{1}{|G|} \left\{ \text{for } \chi = \{0^\circ, 180^\circ\} \sum_{g \in G} |Fix(g)| + \text{for } \chi = \{60^\circ, 120^\circ, 240^\circ, 300^\circ\} \sum_{g \in G} |Fix(g)| \right\} . \quad (4.3)$$

The total number of fixed points for tilt directions  $\{0^\circ, 180^\circ\}$  is 624, so the number of corresponding unique structures will be 39 (624/16). Similarly, the number of unique structures with tilt directions  $\{60^\circ, 120^\circ, 240^\circ, 300^\circ\}$  will be 70 (1120/16). Using Burnside's lemma, we have reduced the size of the problem from 1536 structures to 109 unique packing structures using the symmetries of the trigonal lattice. Although, the Burnside lemma provides a convenient method to calculate the number of unique structures for a given set of symmetries, it does not provide the structures. We developed an algorithm to generate the 109 unique combinations of tilt direction and twist angles (Appendix D).

Table 4.2. Symmetry Operations and the Number of Corresponding Fixed Points for Two Sets of Tilt Directions Used to Calculate the Number of Unique Structures.

$\chi = \{0^\circ, 180^\circ\}$							
$g$	$ Fix(g) $	$g$	$ Fix(g) $	$g$	$ Fix(g) $	$g$	$ Fix(g) $
e	512	$C_2$	0	$b \cdot C_2$	0	$c \cdot \sigma_v$	0
a	8	$\sigma_v$	0	$c \cdot C_2$	0	$a \cdot \sigma_h$	8
b	8	$\sigma_h$	16	$a \cdot \sigma_v$	0	$b \cdot \sigma_h$	8
c	32	$a \cdot C_2$	0	$b \cdot \sigma_v$	0	$c \cdot \sigma_h$	32
$\chi = \{60^\circ, 120^\circ, 240^\circ, 300^\circ\}$							
e	1024	$C_2$	0	$b \cdot C_2$	0	$c \cdot \sigma_v$	0
a	16	$\sigma_v$	0	$c \cdot C_2$	0	$a \cdot \sigma_h$	0
b	16	$\sigma_h$	0	$a \cdot \sigma_v$	0	$b \cdot \sigma_h$	0
c	64	$a \cdot C_2$	0	$b \cdot \sigma_v$	0	$c \cdot \sigma_h$	0

### 4.3 Simulation Method

The all-atom molecular dynamics simulations were performed on the 109 unique structures using the large-scale atomic/molecular massively parallel simulator (LAMMPS)<sup>3</sup> package with the velocity-Verlet algorithm (Section 2.8). The structure of the all-atom force field and the corresponding force field parameters are given in Section 2.5 and Table 2.1 to 2.4. The simulation

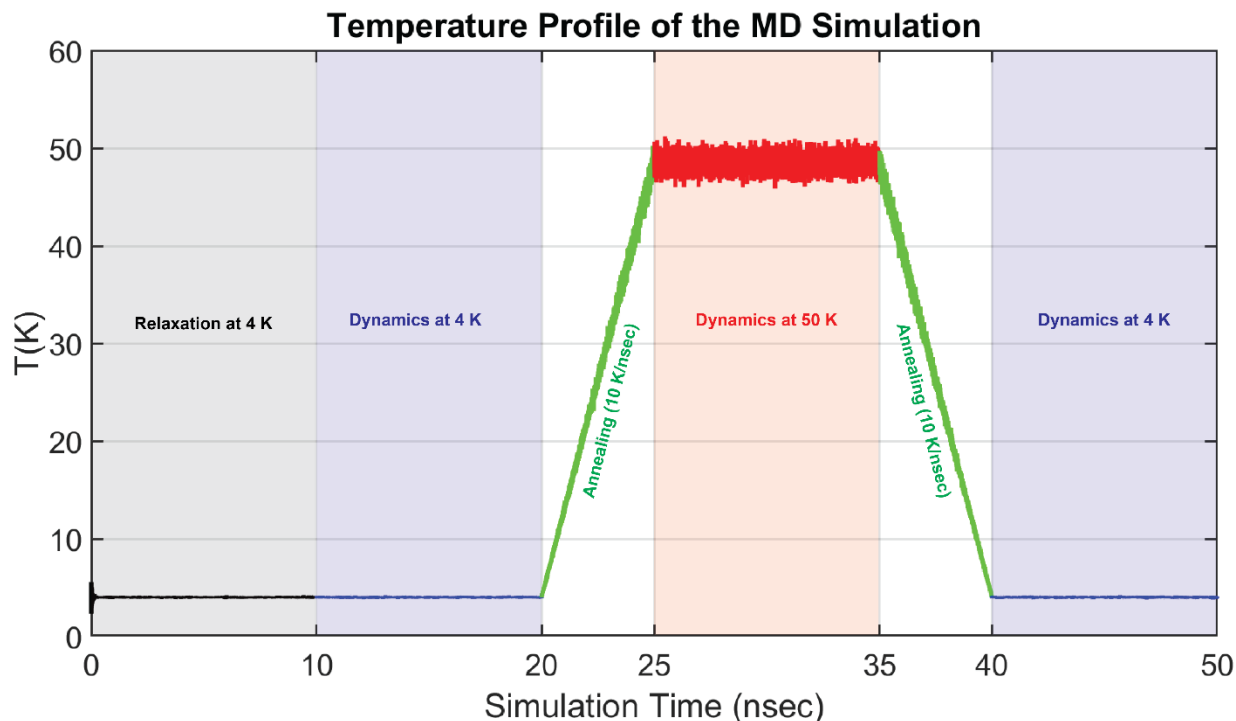


Figure 4.3. The Temperature Profile During the Entire Simulation. The initial structure relaxes over the first 10 ns at 4 K, followed by the dynamics at 4 K for another 10 ns. The structure is then annealed at 50 K with 10 K/ns temperature ramp. After the dynamics run at 50 K for 10 ns, we cool it back to 4 K with the same temperature ramp and perform a final dynamics run at 4 K for 10 ns.

box contains  $5 \times 5 (2\sqrt{3} \times 3)$  rect. unit cell with 100 decanethiol molecules to simulate the structure of the SAM. Periodic boundary conditions are applied on the simulation box of dimension  $(43.2563 \text{ \AA} \times 49.9481 \text{ \AA})$  along the x and y axis to represent a two dimensional infinite SAM crystal.

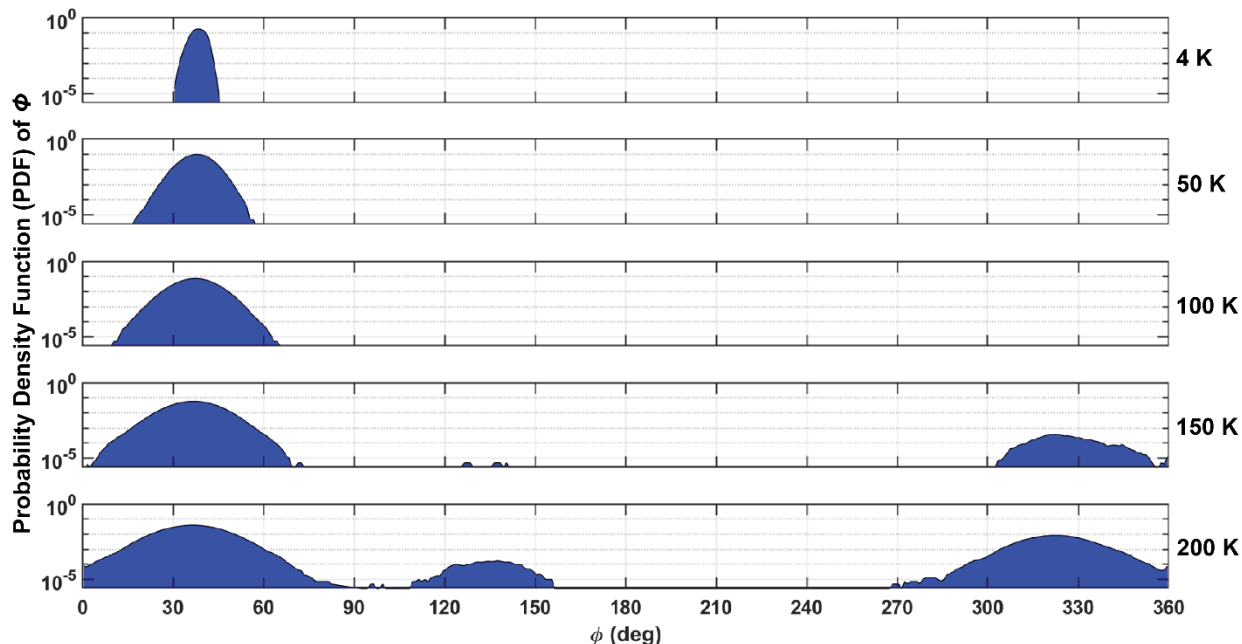


Figure 4.4. Twist Distribution for the Initial Structure  $\{50^\circ, 50^\circ, 50^\circ, 50^\circ; 0^\circ\}$  at Different Temperatures. The distribution becomes broader with the temperature and eventually hops over to a different twist between 100 K and 150 K. Annealing the structure at 50 K allows to explore the neighborhood of the local minima without randomizing the twist.

We initialize the structure using one of the unique combinations of tilt direction and twist angles with the chains in the all-trans conformation. Each of the 109 combinations is hypothesized to represent a local minimum of the system. We need to initialize the SAM structure in the well of the particular local minimum without adding so much potential energy that the system jumps to a different well before it has fully relaxed. To achieve this, we initialize the structures with a smaller tilt angle of  $20^\circ$  (lower volume density) to reduce the potentially large initial repulsive forces between the neighboring chains. We call this initialization strategy *soft landing*. During the relaxation, the molecules come closer together via the non-bonded attractive interactions (vdW and Coulombic interactions) to achieve the typical  $\sim 30^\circ$  tilt angle. We relax the initial structure at 4 K over 10 ns to minimize the kinetic energy (Figure 4.3). The Nose-Hoover thermostat (NVT ensemble, Section 2.9) is used to maintain the temperature by scaling the velocities with 1 fs time

step. We annealed the structure at 50 K with a temperature rate of 10 K/ns so that the molecular twist can explore the neighborhood of the local minima for a better packing without hopping over to a different twist. Figure 4.4 shows the twist distribution at different temperatures for the initial structure  $\{50^\circ, 50^\circ, 50^\circ, 50^\circ; 0^\circ\}$ . As the temperature increases, the twist distribution becomes broader around its initial value. Between 100 K and 150 K the chains gain enough thermal energy to hop over the barrier to a different twist local minimum. Annealing at 50 K enables us to achieve a better chain packing while controlling the SAM structure about the initial twist structure.

We use two constraints to compare the packing of the alkane chains in a dense-phase monolayer of a decanethiol SAM. In Constraint 1 all the S head groups are fixed at the close-packed  $(\sqrt{3} \times \sqrt{3})R30^\circ$  sites throughout the simulation. Note that the orientation of the S-C bond is constrained by the tilt and twist angles. In Constraint 2, the head groups are initially at the close-packed sites, but are allowed to move in the x-y plane. For the latter constraint, we prevent concerted drifting (translation) of the model during the simulation by fixing one of the basis molecules to anchor the system. The relaxed constraints are applied to the S head groups of the other three basis molecules. This allows the chains to reorganize within the unit cells while enforcing the  $(2\sqrt{3} \times 3)$ rect. symmetry. The alkyl chains are allowed to relax in all directions to achieve the best packing.

## 4.4 Results and Discussion

The packing of the alkane chains is highly sensitive to the symmetry and the separation of the S head groups.<sup>4-5</sup> We begin our study by constraining the S head groups at the  $(\sqrt{3} \times \sqrt{3})R30^\circ$  sites (Constraint 1) to find the most preferred combination of twist angles and tilt direction. We use this set of calculations as our baseline to compare the structures where the head groups are allowed to offset from the  $(\sqrt{3} \times \sqrt{3})R30^\circ$  sites due to the close packing of the alkane chains. The effect of the substrate interaction is not included in this study because the force field parameters at the Au-S

interface are not available.

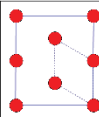
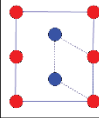
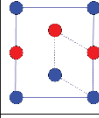
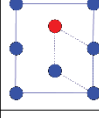
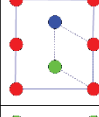
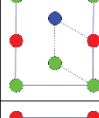

<b>1-molecule basis</b>	<b>1 unique <math>\varphi</math></b>			<b>(6)</b>
<b>2-molecule basis</b>		<b>2 straight rows</b>		<b>(10)</b>
	<b>2 unique <math>\varphi_s</math></b>	<b>2 zigzag rows</b>		<b>(10)</b>
		<b>1 straight row + 1 zigzag row</b>		<b>(18)</b>
		<b>4-molecule basis</b>	<b>1 straight row</b>	
		<b>3 unique <math>\varphi_s</math></b>	<b>1 zigzag row</b>	
	<b>4 unique <math>\varphi_s</math></b>			<b>(11)</b>

Figure 4.5 Grouping Scheme of the 109 Unique Structures Based on the Symmetries. An example for each group is shown with the same basis convention as in Figure 4.1 (tilt direction  $0^\circ$  for all examples). Twist angle  $50^\circ$ ,  $132^\circ$ ,  $228^\circ$ , and  $310^\circ$  are represented by red, green, blue, and black circles, respectively. The number of structures for each group is given in the last column.

We begin by grouping the 109 structures (shown in Figure 4.5) based on their symmetries to facilitate our discussion on chain packing. We group the structures based on the size of the unit cell: 1-molecule basis (6 structures), 2-molecule basis (10 structures), and 4-molecule basis (93 structures). The 1-

molecule basis structure has only one unique twist per  $(2\sqrt{3} \times 3)\text{rect. unit cell}$ , but they can



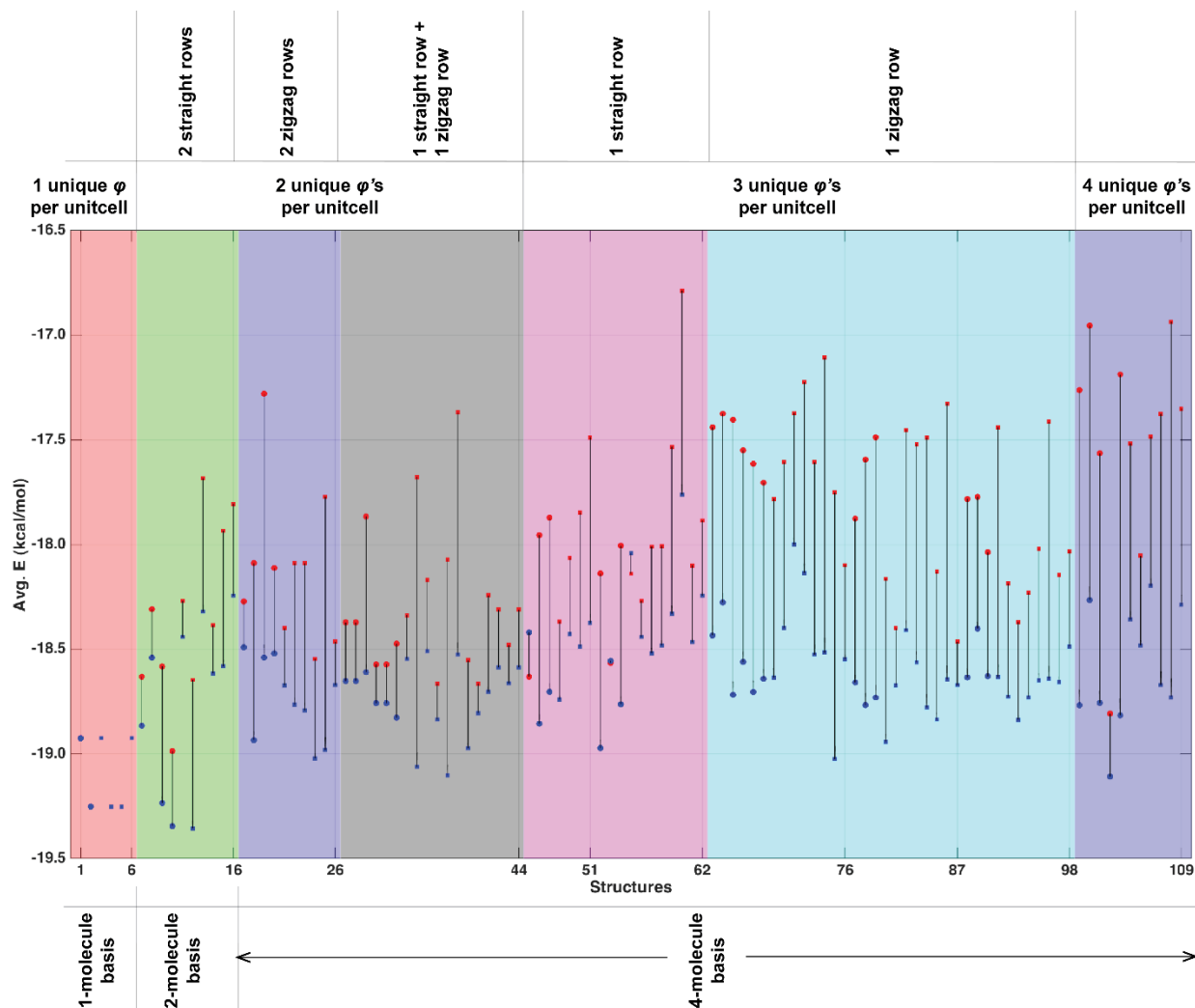


Figure 4.6 The Average System Energy for the 109 Unique Structures at 4 K for Head-Group Constraints 1 and 2. The energies for Constraint 1 is shown in red and Constraint 2 in blue. We use solid circles and squares to indicate  $0^\circ$  and  $60^\circ$  tilt directions for each symmetry groups, respectively. For each structure, the vertical black line indicates the energy difference between Constraint 1 and Constraint 2.

have two distinct tilt directions ( $0^\circ$  and  $60^\circ$ ). We can also have two, three, and four unique twists per unit cell with two tilt directions. The two unique twists per unit cell can be further divided into three subgroups: two straight rows, two zigzag rows, and a combination of one straight row and one zigzag row. An example of each group is shown in Figure 4.5 along with the number of structures for each group (given in parentheses in the last column). Structures with three unique

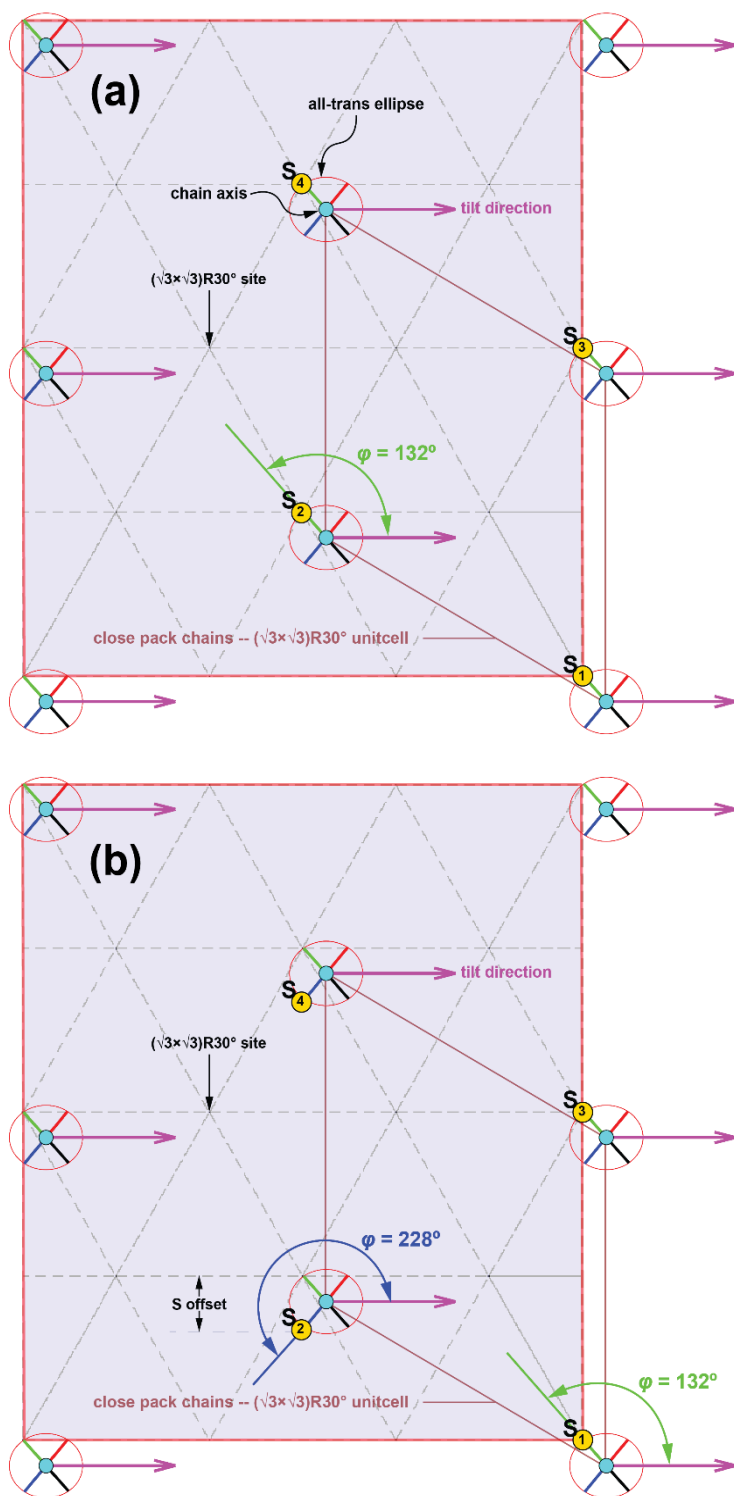


Figure 4.7 The Structures with the Best Alkyl Chain Packing for Constraints 1 and 2. (a) Constraint 1 yields a 1-molecule basis structure. (b) Constraint 2 yields a 2-molecule basis structure. Both the constraints on the head group and the close packing of the chains determines the preferred combination of twist angles and tilt direction.

twists per unit cell are subdivided into one straight row and one zigzag row. Finally, we have 11 4-molecule basis structures with four unique twists per unit cell.

The close-packed structure of the alkane chains reduces the energy of the system because of the efficient chain packing for a given head group constraint. We use the average system energy (averaged over all 100 molecules and 10 nsec dynamics at a given temperature) to compare the chain packing resulting from Constraint 1 and Constraint 2 to study the effect of the headgroup offset. In Figure 4.6, we group the average energies (before annealing) based on the symmetries described in the previous paragraph. The energy for Constraint 1 and Constraint 2 are shown in red and blue, respectively.

For each symmetry group, the tilt direction can either be  $0^\circ$  (solid circle) or  $60^\circ$  (solid square). As we constrain the head groups at the  $(\sqrt{3} \times \sqrt{3})R30^\circ$  sites, only one twist per unit cell (1-molecule basis) allows the close packing of the chains. As a result, 1-molecule basis twist structure is preferred for Constraint 1. Figure 4.7.a shows an example of a 1-molecule basis structure where only  $\phi = 132^\circ$  is allowed ( $\chi = 0^\circ$ ) for all the basis molecules by the close-packing of the alkane chains while constraining the head groups at the  $(\sqrt{3} \times \sqrt{3})R30^\circ$  sites. The packing of the chains does not depend on the tilt direction since the twist angle is defined with respect to the direction of the tilt. A 2-molecule basis twist structure is preferred by the chain packing when the head groups are allowed to move in the x-y plane. One of the minimum energy structures for Constraint 2 is shown in Figure 4.7.b,  $\{132^\circ, 228^\circ, 132^\circ, 228^\circ; 0^\circ\}$ . For the close packing of the alkane chains (efficient interlocking of  $\text{CH}_2$  groups), the sulfur head groups must deviate from the  $(\sqrt{3} \times \sqrt{3})R30^\circ$  sites to accommodate multiple twists. The deviation of the head group from the  $(\sqrt{3} \times \sqrt{3})R30^\circ$  is denoted by the S atom offset which is driven by the packing of the chains. As a result, two unique twists ( $132^\circ$  and  $228^\circ$ ) per unit cell emerges as two straight rows (2-molecule basis twist structure). Allowing additional motion of the head groups in the x-y plane (Constraint 2) also reduces the energy of the system, shown by the vertical black lines in Figure 4.6. Average energies for the 1-molecule basis structure are indistinguishable for Constraint 1 and Constraint 2 (energy difference  $\sim 10^{-4}$  kcal/mol,  $k_B \approx 8 \times 10^{-3}$  kcal/mol at 4 K). As a result, the red and the blue points overlap for the 1-molecule basis structures (Figure 4.6). The maximum energy difference (the energy difference between the least and the most favored structure) is 35% lower for Constraint 2 because the spacing between the alkyl chains adjust. There are three structures with one straight row symmetry ( $\{50^\circ, 132^\circ, 50^\circ, 228^\circ; 0^\circ\}$ ,  $\{50^\circ, 132^\circ, 310^\circ, 132^\circ; 0^\circ\}$ , and  $\{50^\circ, 132^\circ, 228^\circ, 132^\circ; 60^\circ\}$ ) where the average system energy increases (1.13%, 0.05%, and 0.53%, respectively) for

Constraint 2. This could be due to artificially constraining the head groups, but further investigation is needed to understand the origin of this anomaly.

## 4.5 Conclusions

We use AA MD simulation to study the packing of the decanethiol SAM with two sets of constraints on the head groups. For a given head group constraint, the efficient interlocking of the CH<sub>2</sub> groups leads to a close-packed structure of the alkane chains that reduces the energy of the system. Our study shows that the 1-molecule basis twist structure is preferred when the head groups are constrained at the  $(\sqrt{3} \times \sqrt{3})R30^\circ$  lattice sites and is independent of the tilt direction. The 2-molecule basis twist structure is preferred by the chain packing when the head groups are allowed to offset from the  $(\sqrt{3} \times \sqrt{3})R30^\circ$  lattice sites to accommodate multiple twists per unit cell.

Further investigation is needed to understand the effect of chain packing when the head groups are allowed to relax in all directions ( $x, y, z$ ). This will help us understand the effect of the vertical offset (observed for reconstructed Au/S interfaces, Chapter 5) of the head groups on the chain packing. The effect of annealing at a higher temperature ( $>200$  K) is also yet to be studied. Annealing at a higher temperature will allow the chains to explore all twist possibilities that can lead to a better chain packing. It is important to note that annealing at 300 K or higher can introduce significant gauche defects which renders the the twist angle less valuable as a structure parameter (see Section 5.5 for more details).

## 4.6 References

1. Bhattacharya, S.; Yothers, M. P.; Huang, L.; Bumm, L. A., Interaction of the  $(2\sqrt{3} \times 3)$ rect. Adsorption-Site Basis and Alkyl-Chain Close Packing in Alkanethiol Self-Assembled Monolayers

on Au(111): A Molecular Dynamics Study of Alkyl-Chain Conformation. *ACS Omega* **2020**, 5 (23), 13802-13812.

2. Burnside, W., *Theory of Groups of Finite Order*. Cambridge University Press: Cambridge, 2012.

3. Plimpton, S., Fast Parallel Algorithms for Short-Range Molecular Dynamics. *J. Comput. Phys.* **1995**, 117 (1), 1-19.

4. Ulman, A., Formation and Structure of Self-Assembled Monolayers. *Chem. Rev.* **1996**, 96 (4), 1533-1554.

5. Ulman, A.; Eilers, J. E.; Tillman, N., Packing and molecular orientation of alkanethiol monolayers on gold surfaces. *Langmuir* **1989**, 5 (5), 1147-1152.

## Chapter 5: Chain Packing on Reconstructed Substrate

### 5.1 Scope of this Chapter

We study the packing of dense phase decanethiol SAMs on reconstructed Au(111) substrates using MD simulation. The adsorption sites are offset from the  $(\sqrt{3} \times \sqrt{3})R30^\circ$  lattice in these models. We fixed the head groups at the adsorption sites given by 10 proposed surface structures from the literature to study the structure of the SAM determined by the packing of the alkyl chains.

We show the adsorption site basis of the  $(2\sqrt{3} \times 3)\text{rect.}$  phase of *n*-alkanethiol self-assembled monolayers (SAMs) plays a key role in determining the molecular conformation of the close-packed alkyl chains. Ten proposed reconstructed Au-S interfaces are used to explore the minimized-energy alkyl-chain packing of *n*-decanethiol molecules using molecular dynamics with the all-atom description. In this comparative study, all models have the same alkyl-chain surface density of four molecules per unit cell, thus differences are due to the headgroup spacing within the four-molecule basis as opposed to the average surface density. We demonstrate for the first time the 4-molecule-basis twist structure driven by the packing of alkanethiol molecules in a large simulation box (100 molecules, 25 unit cells) using molecular dynamics. Our results validate the prediction put forward by Mar and Klein that to achieve the 4-molecule-basis twist symmetry observed by experiment the headgroups must deviate from the high-symmetry  $(\sqrt{3} \times \sqrt{3})R30^\circ$  sites. The key structural parameters: tilt, twist, and end-group height, as well as their spatial order are compared with experimental results, which we show is a highly sensitive approach that can be used to vet proposed Au-S interfacial models.

## 5.2 Introduction

In this study we chose ten Au-S models and study the alkyl-chain driven SAM structures resulting from the adsorption site constraints. We use all-atom molecular dynamics models with *n*-decanethiol. The simulations begin with the Au-S interface in the post-adsorption structures proposed in each of the ten models. The Au and S atoms are static (not allowed to move) in this MD study. Only the alkyl chains are allowed to relax during the simulation. The Au-S-CH<sub>2</sub> bonding potential is set to zero which allows the S-CH<sub>2</sub> bond to adopt any orientation with respect to the surface. Its orientation is controlled only by the relaxation of the rest of the system. This approximation for C10 molecules is reasonable as demonstrated by previous studies.<sup>1-3</sup> The SAM structures we present, represent those that provide the best alkyl chain packing given the constraints of adsorption sites. Prior MD studies reported a 1-molecule basis structure for headgroups constrained in  $(\sqrt{3} \times \sqrt{3})R30^\circ$  adsorption sites, where all the chains adopt the same twist (Chapter 4).<sup>4-6</sup> In contrast, experiments observe at least two nearly orthogonal chain twists per unit cell arranged in a 4-molecule basis zig-zag structure.<sup>7-9</sup> In order for multiple chain twists to emerge for close packed molecules, the headgroups must deviate from the high symmetry  $(\sqrt{3} \times \sqrt{3})R30^\circ$  sites within the  $(2\sqrt{3} \times 3)$ rect. unit cell. This requirement was first proposed by Mar and Klein.<sup>3</sup> Although the molecular packing is known to be sensitive to the symmetry and the separation of the headgroups,<sup>10-11</sup> multi-unit cell MD simulations using the  $(2\sqrt{3} \times 3)$ rect. reconstruction have not been studied for medium and long chains. We choose ten Au-S interface

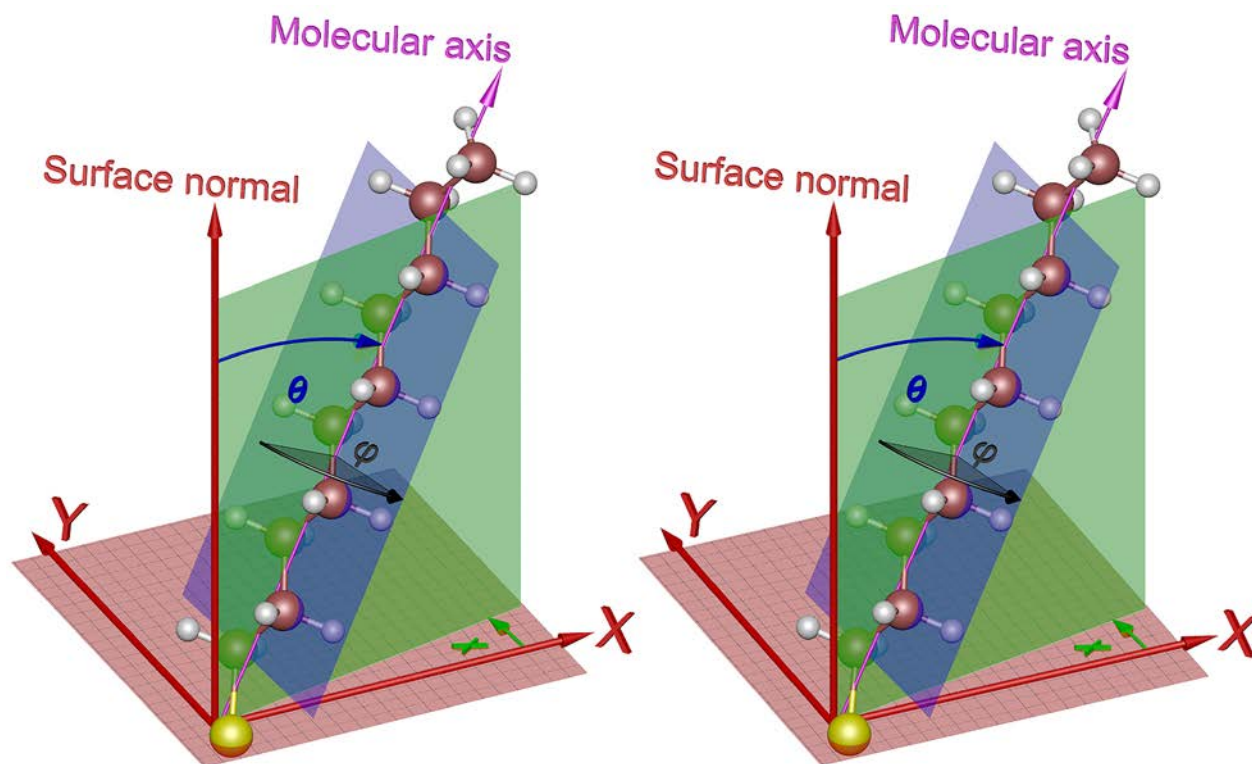


Figure 5.1 An Eye-cross Stereo Image Pair of the SAM Molecular Geometry. In this alkyl-chain centric model, the molecular axis passes through the origin where it intersects the surface. The tilt angle ( $\theta$ ) is defined by the angle between the surface normal and the axis of the molecule (molecular axis). The twist of the molecular backbone ( $\phi$ ) is defined by the angle between the tilt plane (green plane) containing the surface normal and the molecular axis and the plane of the alkyl carbon atoms (blue plane). Zero twist angle is defined where these two planes coincide and the bond between the head group and the alpha methylene makes the largest angle with respect to the surface normal ( $\alpha$ -CH<sub>2</sub> is closer to the substrate). A positive increasing twist angle is defined in the counterclockwise direction while looking down the molecular axis toward the surface as is standard for a right-handed coordinate system. The direction of the tilt ( $\chi$ ) is the angle between the positive x-axis and the projection of the molecular axis on the plane of the substrate (xy-plane).

models to study Mar and Klein's conjecture, and compare other structural parameters with experimental observations. Our results show that the vdW-driven close packing of the chains leads to significantly different SAM structures depending on the Au-S interfaces.

This well-known sensitivity of the alkyl chain structures to the headgroup spacing also can be exploited as a method for examining proposed Au-S interface models. We compare the SAM alkyl chain geometries obtained from the energy minimized MD simulation with experiment. Ab initio methods have been used to study the Au-S interface and have proposed a variety of structures for



short alkyl chains. However, the technically interesting SAMs are made using alkyl chains with 8 carbon atoms and longer where the chain packing is a major component of the adsorption energy.<sup>12</sup> Most of the experimental work has been performed on these longer chain SAMs. The complexity of the Au-S interface combined with the critical importance of the vdW energy, and the number of atoms that would need to be included for longer chains, makes the full problem beyond the reach of ab initio methods. In this work we demonstrate an approach for comparison of proposed Au-S interfaces to experiment via MD simulations of the alkyl-chain packing structures which bridges this computational gap. We are not aware of any comparable studies of the long chain (C10) alkanethiol molecules in large scale simulation ( $\geq 100$  molecules) over 100 ns on the reconstructed  $(2\sqrt{3} \times 3)$ rect. unit cell of the Au-S interface.

### 5.3 Interface Models

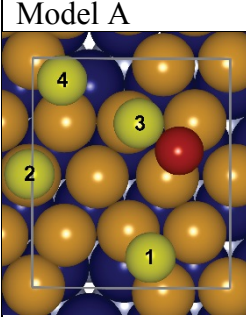
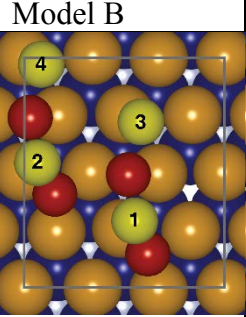
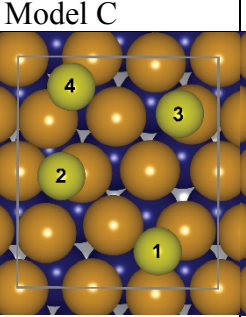
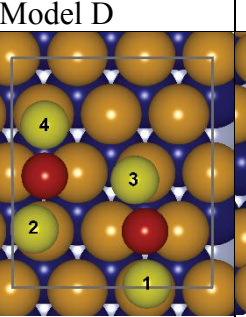
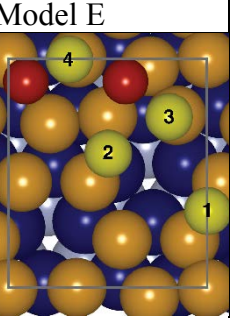
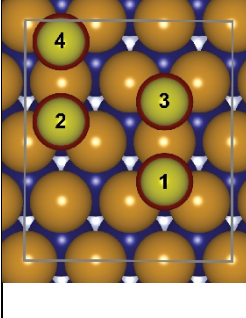
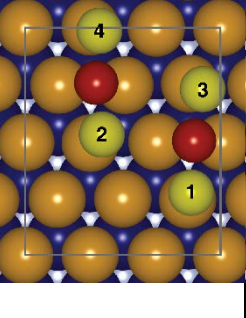
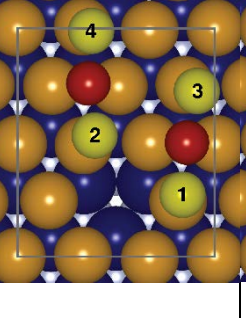
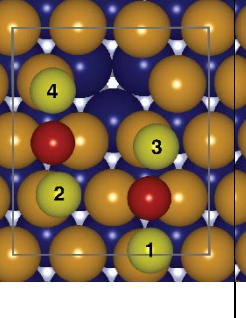
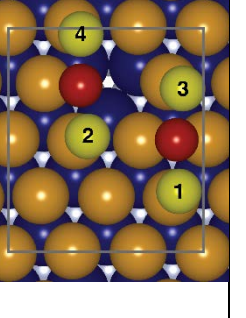
Several models of the atomic structure of the Au-S interface have been proposed based on the experimental results, which was sometimes accompanied by the atomistic modeling. In other models, ab initio methods are used to find minimized-energy structures of the Au-S interface. Most of these models contain adatoms and/or vacancies and their surface coverage is quantified with respect to the substrate Au atoms in Section 1.2.3.2. For example, model F (Table 5.1) is proposed based on a symmetry argument to explain the LEED pattern observed from butanethiol SAMs.<sup>13</sup> In this model, the headgroup is attached on top of an adatom ( $\theta_{ad} = 0.333$ ) which is connected to the substrate at the fcc or hcp hollow site with no surface vacancy per unit cell ( $\theta_{vac} = 0$ ). In contrast, models B, C, and D were proposed based on the ab initio calculations alone while comparing with the other Au-S interface models.<sup>14-16</sup> In these models  $\theta_{ad} = 0, 0.167,$  and  $0.333$  for C, D, and B respectively. Ab initio methods also have been employed to develop models used to fit GIXRD or

STM experimental results. For example, Cossaro et al. proposed model E as the best fit structure to the GIXRD measurements of hexanethiol SAMs.<sup>17</sup> The complex reconstructions in models D, G, H, I and J are strikingly similar, each with a two staple motifs oriented in the long axis of the unit cell. The latter three have one Au substrate vacancy per unit cell. The complex reconstruction in model E shows the coexistence of the extended staple motif and the adsorption of the headgroups at the bridge sites with fractional occupancies per unit cell ( $\theta_{\text{ad}} = 0.1$  and  $\theta_{\text{vac}} = 0.23$ ). For our study we used the fixed occupancies shown in the model E diagram ( $\theta_{\text{ad}} = 0.167$  and  $\theta_{\text{vac}} = 0.167$ ). The motivation for the other five models (A, G–J) were to reproduce the 4-molecule basis surface structure observed in STM.<sup>18-20</sup> Apart from models A, C, and F, all the models have 2 adatoms per unit cell ( $\theta_{\text{ad}} = 0.167$ ), and models A, H, I, and J have 1 surface vacancy per unit cell ( $\theta_{\text{vac}} = 0.083$ ).

The sulfur adsorption sites in these ten models are all offset from the high symmetry ( $\sqrt{3} \times \sqrt{3}$ )R30° sites of a simple close packed overlayer. In other words, the adsorption sites are not uniformly spaced within the unit cell. Although this is an obvious consequence of the lower ( $2\sqrt{3} \times 3$ )rect. translational symmetry with a four molecule basis, it is significant because the alkyl chains prefer a close packed lattice. Our work is the first classical MD study of the effect of sulfur headgroup offsets on the alkyl chain structure. Our approach is quite different from the ( $\sqrt{3} \times \sqrt{3}$ )R30° Au-S adsorption sites of the unreconstructed surface generally used in the molecular dynamics studies.<sup>3-6, 21</sup> The deviation of the headgroup from ( $\sqrt{3} \times \sqrt{3}$ )R30° sites in these ten models is critical for stabilizing the nontrivial twist structures observed in experiment. This is the first demonstration where a 4-molecule basis twist structure has emerged spontaneously in molecular dynamics simulation. The selected ten Au-S interfacial models are shown in Table 5.1. The coordinates for the sulfur headgroups and adatoms are given in Table 5.2. The rest of the chapter is organized as follows: we first present the details of the MD modeling, then compare the

structure of the SAMs for different interfacial models with the experimental results and examine the effect of the headgroup basis on the alkane chain conformations.

Table 5.1. Atomic Structure of the  $(2\sqrt{3} \times 3)$ rect. Unit Cell for Ten Au-S Interfacial Models.

				
$\theta_{\text{ad}} = 0.083$ $\theta_{\text{vac}} = 0.083$ Ref. 18	$\theta_{\text{ad}} = 0.333$ $\theta_{\text{vac}} = 0$ Ref. 14	$\theta_{\text{ad}} = 0$ $\theta_{\text{vac}} = 0$ Ref. 15	$\theta_{\text{ad}} = 0.167$ $\theta_{\text{vac}} = 0$ Ref. 16	$\theta_{\text{ad}} = 0.1$ $\theta_{\text{vac}} = 0.23$ Ref. 17
				
$\theta_{\text{ad}} = 0.333$ $\theta_{\text{vac}} = 0$ Ref. 22	$\theta_{\text{ad}} = 0.167$ $\theta_{\text{vac}} = 0$ Ref. 19	$\theta_{\text{ad}} = 0.167$ $\theta_{\text{vac}} = 0.083$ Ref. 19	$\theta_{\text{ad}} = 0.167$ $\theta_{\text{vac}} = 0.083$ Ref. 20	$\theta_{\text{ad}} = 0.167$ $\theta_{\text{vac}} = 0.083$ Ref. 20

Three layers of Au atoms are shown for each model, top layer (gold), 2<sup>nd</sup> layer (dark blue), and bottom layer (light blue). The basis site of each S atom (yellow) is identified by number. The Au adatoms (red) and the vacancies per unit cell are given as a fraction of the surface Au atoms in an unreconstructed Au(111) substrate, containing 12 Au atoms in  $(2\sqrt{3} \times 3)$ rect. unit cell. The subsurface Au layers were modeled as unreconstructed Au(111) for models A and D, because their coordinates were not published. The unit cell for model C and I were rotated 180° to be consistent with the underlying crystal structure of the rest of the models. The subsurface layers of Au(111) are shown to visualize the fcc and hcp hollow sites.

Initially, the coordinates for the sulfur and Au adatoms are taken from the references mentioned in (Table 5.1). However, due to the inconsistent  $(2\sqrt{3} \times 3)$ rect. unit cell dimensions, we have

rescaled all the coordinates using the Au-Au distance of 2.88376 Å.<sup>23</sup> The corresponding size of the unit cell is (8.65127 Å × 9.98963 Å). All the Au/S interface models are simulated with and without the top layer of Au atoms (nominal Au(111) surface atoms). Inclusion of these Au atoms did not affect the simulation results for the SAMs, but does increase the computational expense. Thus, we conclude the top-layer gold atoms are not a critical component for our MD modeling of the SAM structure, and therefore not reported in Table 5.2. The coordinates of the sulfur atoms and the gold adatoms for each model are reported in Table 5.2. We have used 6 significant figures to reduce round-off errors.

Table 5.2. Sulfur and Gold Adatom Coordinates for Ten Au/S Interface Models.

Model	Adatoms	Vacancies	S Atom Coordinates [x, y, z] (Å)	Au Adatom Coordinates [x, y, z] (Å)
A	1	1	[-8.32380, 3.31830, 13.32000]; [-4.69710, 5.39830, 13.32000]; [-9.65710, 8.81170, 13.92000]; [-5.17710, 10.89170, 13.92000].	[-3.52380, 9.77170, 13.32000].
B	4	0	[6.47838, 3.77866, 1.36841]; [2.17786, 6.35487, 1.44976]; [6.74862, 8.15539, -0.05977]; [2.34536, 10.70081, -0.07553].	[7.05530, 2.32384, -0.42612]; [2.94827, 4.95950, -0.33068]; [6.19585, 5.82202, 0.14563]; [1.85646, 8.34482, 0.12379].
C	0	0	[-6.09580, -0.95400, 14.43490]; [-2.38030, 1.95350, 14.09960]; [-6.51550, 5.19760, 14.89380]; [-1.43590, 7.87580, 14.94380].	N/A
D	2	0	[-2.79830, 0.22660, 5.0300]; [-7.60550, 2.58650, 5.0300]; [-3.32270, 4.68420, 5.0300]; [-7.16840, 7.04400, 5.0300].	[-2.88570, 2.49908, 5.47000]; [-7.16840, 4.85900, 5.47000].
E	1.2	2.8	[6.97806, 1.12880, 16.00281]; [2.65246, 3.62619, 16.00281]; [5.29453, 5.22251, 16.70918]; [0.96893, 7.71989, 16.70918].	[3.40381, 6.76089, 16.38680]; [-0.92179, 6.76089, 16.38680].
F	4	0	[-10.09329, 5.82739, 4.80000]; [-5.76760, 8.32483, 4.80000]; [-10.09329, 9.15733, 4.80000]; [-5.76760, 11.65478, 4.80000].	[-10.09329, 5.82739, 2.40000]; [-5.76760, 8.32483, 2.40000]; [-10.09329, 9.15733, 2.40000]; [-5.76760, 11.65478, 2.40000].
G	2	0	[7.52002, 2.91155, 9.87941]; [3.49748, 5.52212, 9.93266]; [8.03580, 7.56142, 9.83508]; [3.38609, 10.17833, 9.73591].	[7.65434, 5.24762, 9.72556]; [3.24224, 7.84172, 9.69442].
H	2	1	[7.40589, 2.86455, 9.78721]; [3.48157, 5.51290, 9.83151]; [8.04538, 7.50390, 9.84549]; [3.32828, 10.18725, 9.67556].	[7.60367, 5.20053, 9.69969]; [3.20234, 7.84312, 9.64630].
I	2	1	[7.59130, 2.70457, 9.74405]; [3.48331, 5.20823, 9.80910]; [7.86329, 7.37781, 9.80354]; [3.22494, 9.88605, 9.80267].	[7.55506, 5.05234, 9.64422]; [3.22828, 7.53903, 9.67939].
J	2	1	[7.62810, 2.73302, 9.80484]; [3.47979, 5.22554, 9.76598]; [7.79187, 7.39795, 9.73822]; [3.17904, 9.86675, 9.79834].	[7.52526, 5.07040, 9.64368]; [3.17018, 7.53873, 9.59298].

## 5.4 Simulation Details

The MD simulations of C10 SAMs were performed utilizing the LAMMPS<sup>24</sup> MD package using the velocity-Verlet algorithm and AA FF (OPLS-AA<sup>25</sup>). The structure of the FF is given below, with the values of the parameters tabulated in the Section 2.5.3 (Table 2.1 to 2.4).

$$E = 4\varepsilon \left\{ \left( \frac{\sigma}{r} \right)^{12} - \left( \frac{\sigma}{r} \right)^6 \right\} + C \frac{q_i q_j}{\varepsilon_0 r} + K_r (r - r_0)^2 + K_\theta (\theta - \theta_0)^2 + K_\varphi^1 (1 + \cos \varphi) + K_\varphi^2 (1 - \cos 2\varphi) + K_\varphi^3 (1 + \cos 3\varphi) \quad (5.1)$$

The first two terms on the right side of the equation represent the non-bonded interaction, vdW (Lennard-Jones), and Coulombic potential, respectively. The third and the fourth terms are for the harmonic vibration of the bond stretching and the bond bending, respectively. The last three terms are the first three Fourier components of the dihedral angles. The higher-order Fourier components of the dihedral were not used in the OPLS-AA dihedral potential for alkanes.<sup>25</sup> Note that, the AA description of the molecules is required to correctly model the alkyl chain twist in the SAMs; the simpler united atom (UA) description does not model the twist correctly (Section 2.6).<sup>3-4, 26</sup>

A simulation box with  $5 \times 5 (2\sqrt{3} \times 3)$  rect. unit cells (100 molecules) was used. The Au and S atoms were fixed with only the alkyl chains were allowed to relax. The Au-S-CH<sub>2</sub> bond bending potential is set to zero so that the orientation of the S-CH<sub>2</sub> bond will be determined by the alkyl chain packing. To find the equilibrium structure of the SAMs, we started with all 100 C10 molecules (all-trans) standing perpendicular to the substrate with zero tilt and zero twist angle (for the molecular geometry, see Figure 5.1), with periodic boundary conditions applied to the simulation box of dimension  $43.2563 \text{ \AA} \times 49.9481 \text{ \AA}$ . The structure is relaxed under the NVT ensemble over 10 ns using the Nose-Hoover thermostat at 200 K with a 1 fs time step. We found that relaxing the SAMs at temperatures  $< 200 \text{ K}$ , results in the molecules becoming trapped into local minima manifested by unstable tilt domains. At temperatures  $> 300 \text{ K}$  relaxation introduces

significant gauche defects into the SAM. Therefore, we have chosen to relax the system at 200 K where the molecules have enough kinetic energy to overcome the local minima without introducing notable structural defects. During the relaxation, the molecules spontaneously choose the corresponding optimized geometries on which the dynamics was performed. The dynamical data was collected on the relaxed SAM structures at different temperatures (200, 250, and 300 K) for 10 ns, as well as during the annealing process with 10 K/ns temperature rate. The structural parameters of the monolayer are calculated using the constant temperature regions of the simulation. For example, the average twist at 200 K (Figure 5.8) and 250 K (Figure 5.9) are calculated from the dynamical data between 0-10 nsec and 15-25 nsec respectively, as shown in the time-temperature profile on the bottom part of Figure 5.2.

## **5.5 Results and Discussion**

In order to examine the influence of the adsorption site basis, we need to examine each of the alkyl chain structural parameters. It is also instructive to compare the resulting alkyl chain geometry from the chain packing alone with experimental observations to speculate which proposed Au-S interfacial structure is the best match. In our MD study the gold and sulfur atoms are fixed in the positions defined by each model. Thus, our study does not include surface diffusion and/or desorption of the molecules which would occur at temperatures above those of interest for the well-ordered SAMs in this study. In particular, we use these models to reproduce the structure of the monolayer at room temperature and below, where the monolayer is crystalline, and the alkyl chains are predominantly in the all-trans conformation. Four symmetry inequivalent adsorption sites per unit cell is a general feature of the proposed models which may also include Au adatoms and/or Au vacancies. These models allow us to study the structural effects not only of different

adsorption sites, but also due to the presence of adatoms and vacancies. The resultant monolayer was evaluated for each model using the structural parameters (height, twist angle, tilt angle, tilt direction, and gauche fraction), their spatial patterns, and the thermal stability of the SAM. We also comment how well each of the models reproduces the experimentally measured structural parameters. The rest of the section is organized as follows: first, we study the dependence of the average gauche fraction on simulation temperature and its impact on the tilt angle, then we analyze the height of the molecules, the molecular twist, the tilt direction, and the thermal stability of the resultant structures. With these we can examine the effect of the adsorption site offset on the geometry of the close packed alkyl chains.



### 5.5.1 Gauche Fraction and Tilt Angle

The alkyl chains are known to be predominantly in the all-trans conformation at room temperature from IRRAS.<sup>8, 27-28</sup> Both infrared measurements and MD simulations show that the

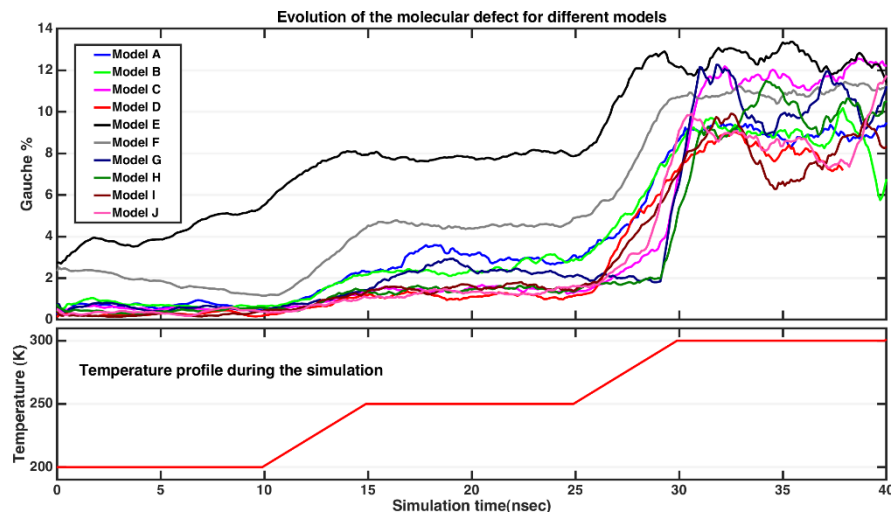


Figure 5.2. The Average Gauche Fraction (%) Compared at 200 K, 250 K, and 300 K. Note that at 300 K it rises above 5% for all models.

conformational order decreases with decreasing chain length and decreases with increasing temperature. Most of the gauche defects are concentrated near the methyl termini at 300 K

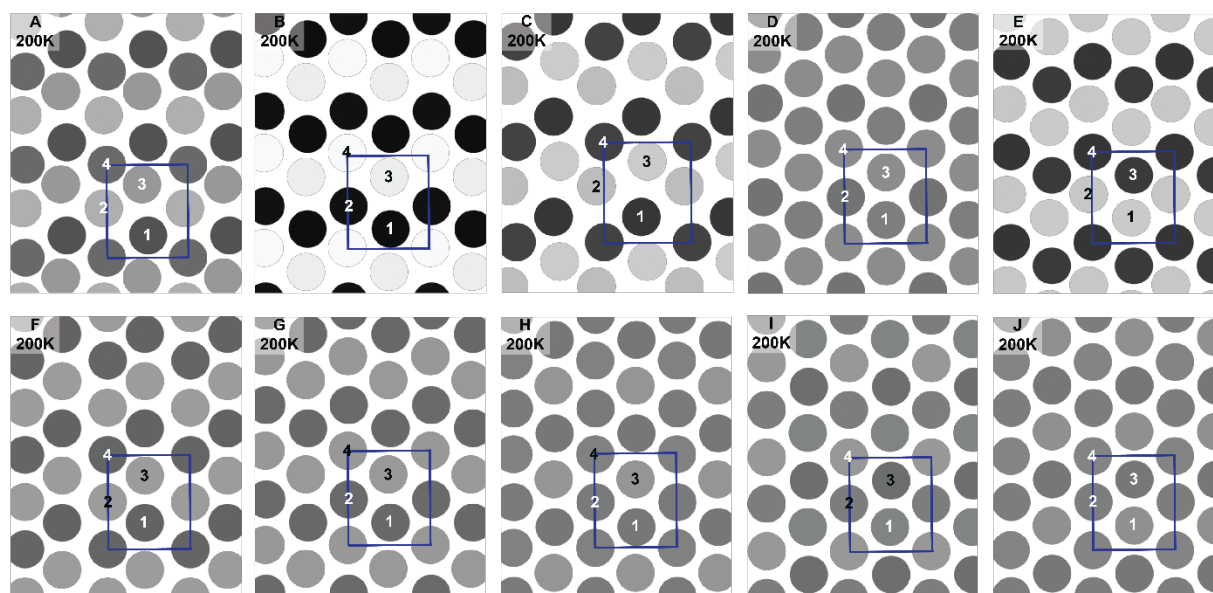


Figure 5.3. The Spatial Distribution of the Height Difference of the Methyl Interface for the Models at 200 K. The numbering scheme for the basis types is the same as in Table 5.1. For better visualization, the  $(2\sqrt{3} \times 3)$ rect. unit cell (blue box) is tiled  $3 \times 3$  for easy visualization of the patterns. The position of the circles is the average position of the methyl groups and the color of the circle represent the average height of the molecule. The higher molecules are represented by the lighter shades.

but penetrate deeper into the monolayer as the temperature is increased.<sup>3</sup> The deviation from all-trans can be quantified by the gauche fraction (defined in Section 1.2.2). Conformational defects in the alkyl chains can significantly influence the structure of the monolayer. Disorder in the alkyl chain reduces the volume density because increasing gauche fraction effectively increases the diameter of the chain (becoming shorter and fatter) evolving toward a random coil in the limiting case.<sup>28</sup> Hence, for a fixed surface density of molecules, the fatter the chain becomes, the smaller the tilt angle. For the modest temperatures of interest in our study, the effect of gauche defects is to slightly decrease the tilt angle of the chains.

Our simulations show gauche defects in the alkyl chains increase with rising temperature as expected. Figure 5.2 shows the average gauche fraction for the temperatures used in this study (200, 250, and 300 K) exceeds 5% for  $T \geq 300$  K for all models. In particular, the gauche fraction for model E is significantly larger than the other models. This indicates that the monolayer structure predicted by model E might be unstable (discussed in detail later in this section). The increase in gauche fraction occurs at lower temperatures than found in an earlier study,<sup>3</sup> which we attribute to the chosen force field (FF). (The problem of transferability of the FF parameters.) The experimentally observed disorder at room temperature correlates with a gauche fraction  $< 2\%$ ,<sup>29</sup> which matches most closely with our 200 K and 250 K simulations. In addition, because the gauche fraction and the tilt angle are related, the higher gauche fraction at 300 K in these models drives the tilt angles to be too small for meaningful comparison with experiments (less than  $25^\circ$  for all models at 300 K). Therefore, we will focus our discussion on 200 and 250 K simulation results as most representative of the experimental system at room temperature.

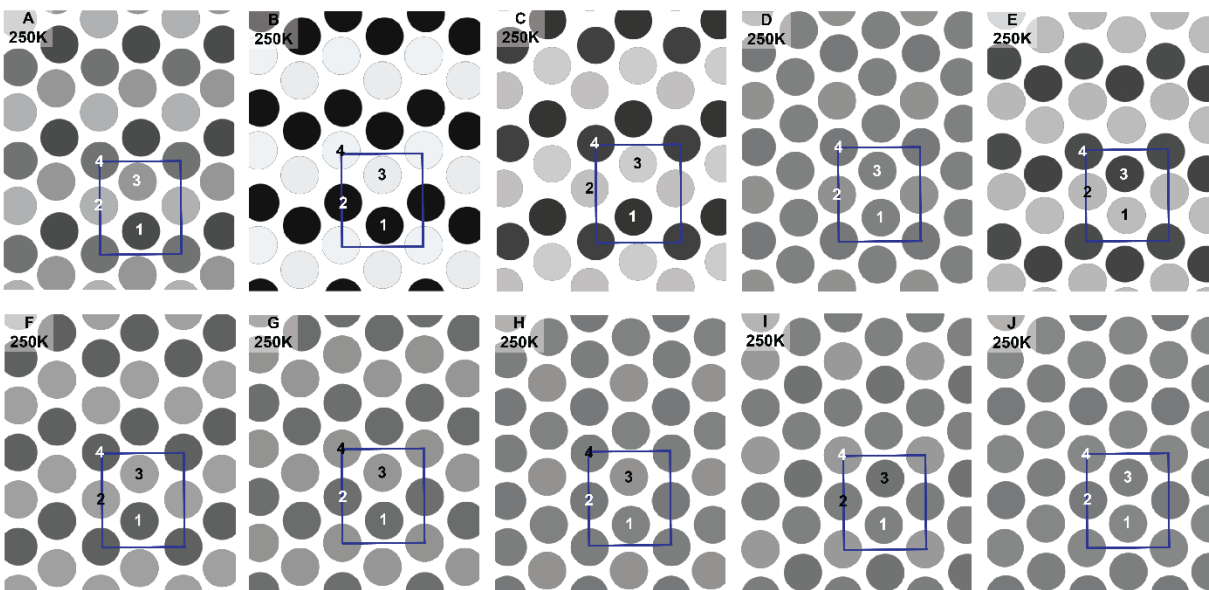


Figure 5.4. The Spatial Distribution of the Height Difference of the Methyl Interface for the Models at 250 K. The numbering scheme for the basis types is same as that shown in Table 5.1. For better visualization, the  $(2\sqrt{3} \times 3)$  rect. unit cell (blue box) is tiled  $3 \times 3$  for easy visualization of the patterns. The position of the circles is the average position of the methyl groups and the color of the circle represent the average height of the molecule. The gray scale is kept the same for all the models for better comparison, the higher molecules are represented by the lighter shades.

### 5.5.2 Molecular Height

The height of the terminal methyl groups and the symmetry of their arrangement at the outer surface depends on the details of the atomic structure at the Au-S interface. We define the height of the molecule as the distance of the methyl carbon above the plane of the nominal Au(111) surface atoms. Constant current STM images of alkanethiol SAMs show different phases of the 4-molecule basis surface symmetry with a height difference between the lowest and the highest basis type ranging from 50 to 90 pm.<sup>30-31</sup> We compare our simulation results with the experimental observations keeping in mind that our model shows the physical height difference between the basis types, whereas the STM height difference is a convolution of the physical height with molecular conductivity. Figure 5.3 shows the spatial distribution of the average height at 200 K

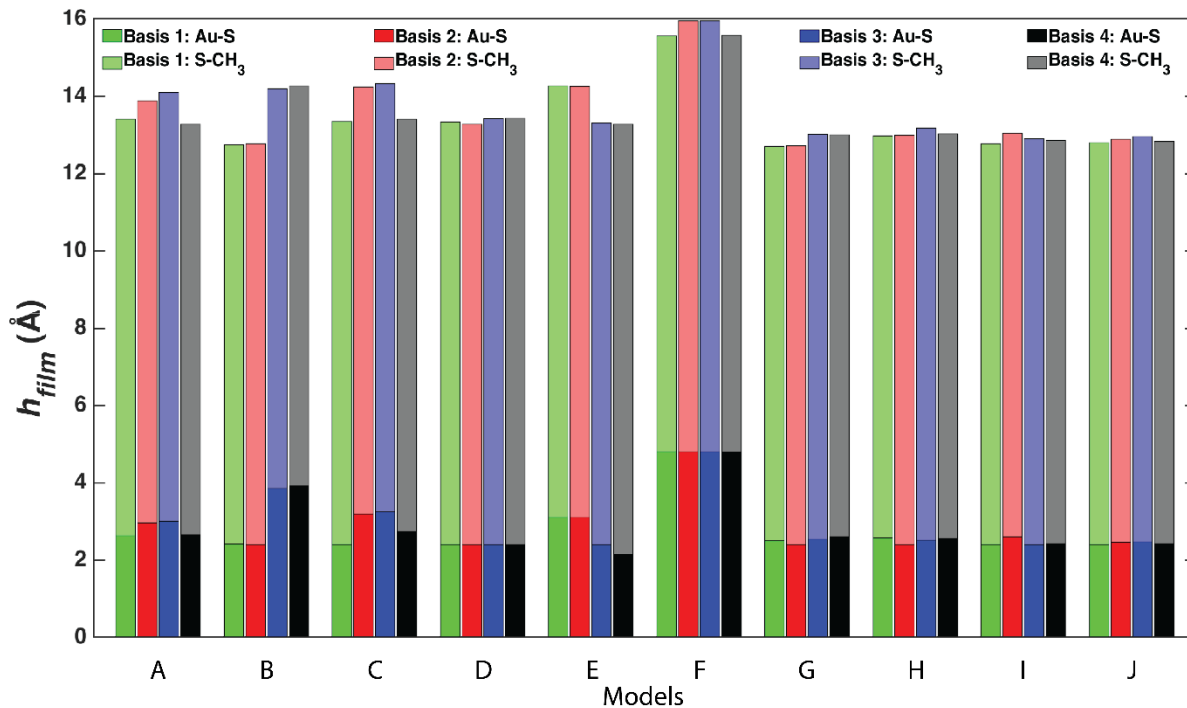


Figure 5.5. The Average Height of the Four Basis-Type Methyl-Group C Atoms from the Au(111) Substrate for Each Model at 200 K Separated by Contribution. The darker segments (Au-S) represent the z-height of the S head groups from the Au(111) substrate, the contribution to the z-height from the S atom adsorption site. The lighter segments (S-CH<sub>3</sub>) represent the z-height of the methyl group C atoms from the corresponding S atoms, the contribution to the z-height from the molecular conformation.

for the ten models where the height of a molecule is averaged over both the simulation time for a given temperature and over the basis type. (see Figure 5.4 for 250 K simulation results.) All the models exhibit a four-molecule basis in height difference similar to the STM result. Model D and J exhibit height differences significantly smaller than the other models which are too small to reproduce the STM observations on physical height alone. Although small, these height differences are statistically significant and exhibit a four-molecule basis (Figure 5.7). In summary, models D and J are unlikely candidates to represent the real SAM structure.

The relative height of a basis type depends both on the molecular geometry and the height of the corresponding headgroup from the substrate. To understand the influence of these separately on the height of a molecule, we divide the physical height of a molecule into the height of the

sulfur headgroup from the substrate and the height of the methyl carbon from the corresponding sulfur atom. Figure 5.5 shows the average height of each basis type for all the models at 200 K (Figure 5.6 for 250 K). The large height differences due to the sulfur adsorption site can be seen directly in the heights of the corresponding terminal methyl groups (models B, C, and E). Model B exhibits a particularly strong height difference  $152 \pm 7$  pm enforced by the underlying adsorption sites. On the other hand, the sulfur atoms for model F are all at the same height from the substrate, yet the methyl height difference is distinct. Therefore, the height difference between the basis molecules in model F is only due to the differences in the molecular conformation—the molecular twist and the averaged gauche defects. We also studied the temperature dependence of the molecular height and found that the height of the molecules at 250 K is higher than at 200 K, Figure 5.6, which is a manifestation of the decrease in tilt angle. The tilt angle is closely associated with order and the density of the monolayer, with all-trans chains packing most efficiently forming the largest tilt angles ( $25\text{--}35^\circ$ ) and highest volume density.<sup>8, 32-33</sup> We conclude that the height of a molecule is determined by a combination of the corresponding sulfur adsorption site and the molecular conformation.

### ***5.5.3 Molecular Twist***

The alkyl chain twist is the most sensitive of the structural parameters, thus provides an important comparison with experiment. Experimental IRRAS measurements show two equal populations of near mutually orthogonal chain twists per unit cell,  $50^\circ$  and  $132^\circ$ .<sup>34</sup> Because IRRAS measures the surface normal component of the transition dipole moment, these measurements cannot distinguish between angles with mirror symmetry about the plane of the molecular tilt (Figure 5.1). Therefore, for comparison to the IRRAS results, we have used this mirror symmetry

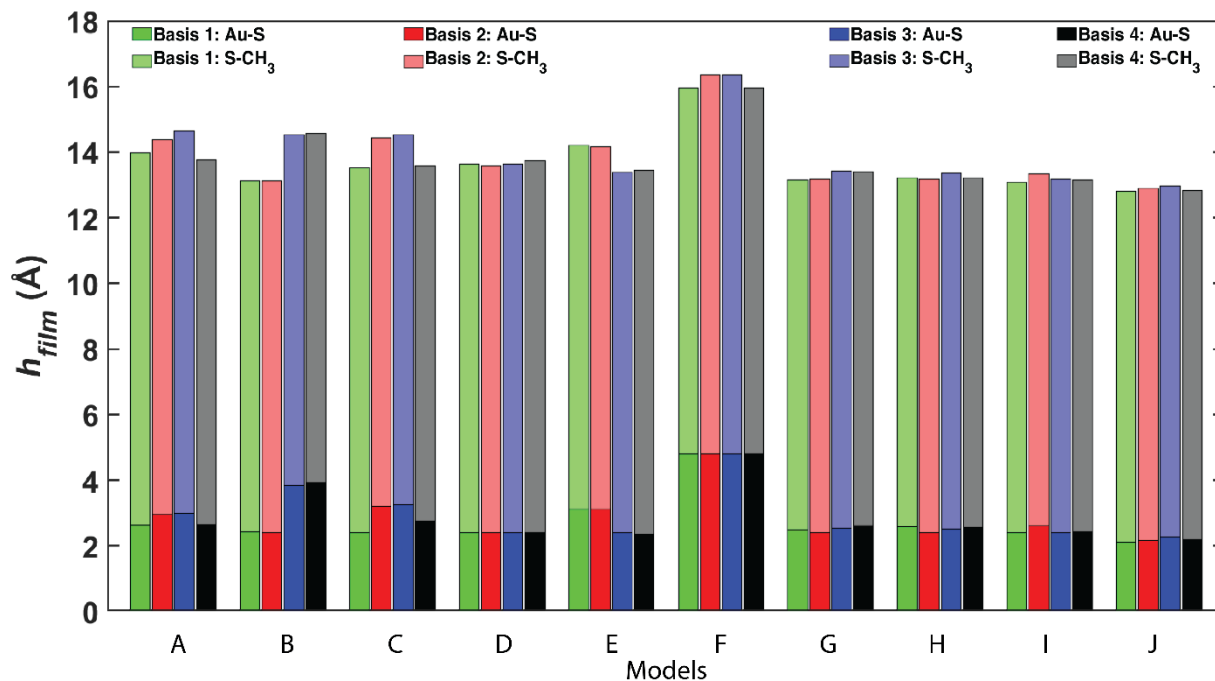


Figure 5.6. The Average Height of the Four Basis-Type Methyl-Group C Atoms from the Au(111) Substrate for Each Model at 250 K Separated by Contribution. The darker segments (Au-S) represent the z-height of the S head groups from the Au(111) substrate, the contribution to the z-height from the S atom adsorption site. The lighter segments (S-CH<sub>3</sub>) represent the z-height of the methyl group C atoms from the corresponding S atoms, the contribution to the z-height from the molecular conformation.

to fold the 0° to 360° twists angles into the interval 0° to 180° which we designate as folded twist. Each unit cell could contain two, three, or four different twist angles and satisfy the experimental observations. In MD simulations of SAMs, four distinct twist angles can be observed at temperatures where there is some twist disorder indicating that these are local energy minima for alkyl chain packing.<sup>3, 35</sup> One twist angle occurs in each of the four quadrants in the range 0° to 360°. These collapse to two quadrants in the folded twist shown color coded in Figure 5.8 and 5.9, first quadrant 0–90° (blue), and second quadrant 90–180° (red). The average twist of a basis molecule is evaluated by the spatial average over the basis type as well as time average for a given temperature. Figure 5.8 shows the spatial distribution of the average twist for all the models at 200 K, similar plots are given at 250 K (Figure 5.9). At 200 K, models A, B, C, E and F exhibit two

twists  $>90^\circ$  and two  $<90^\circ$  per unit cell. Models G, H, I, and J exhibit a single twist angle. Model D exhibits two twist angles with a population of three to one. The twist angles for model B are  $72 \pm 6^\circ$  and  $110 \pm 6^\circ$ , which are not orthogonal to each other. Therefore, models B, D, G, H, I, and J do not exhibit the correct twist characteristics. This leaves models A, C, E, and F consistent with the experimental IRRAS measurements.

### 5.5.4 Tilt Direction and Thermal Stability

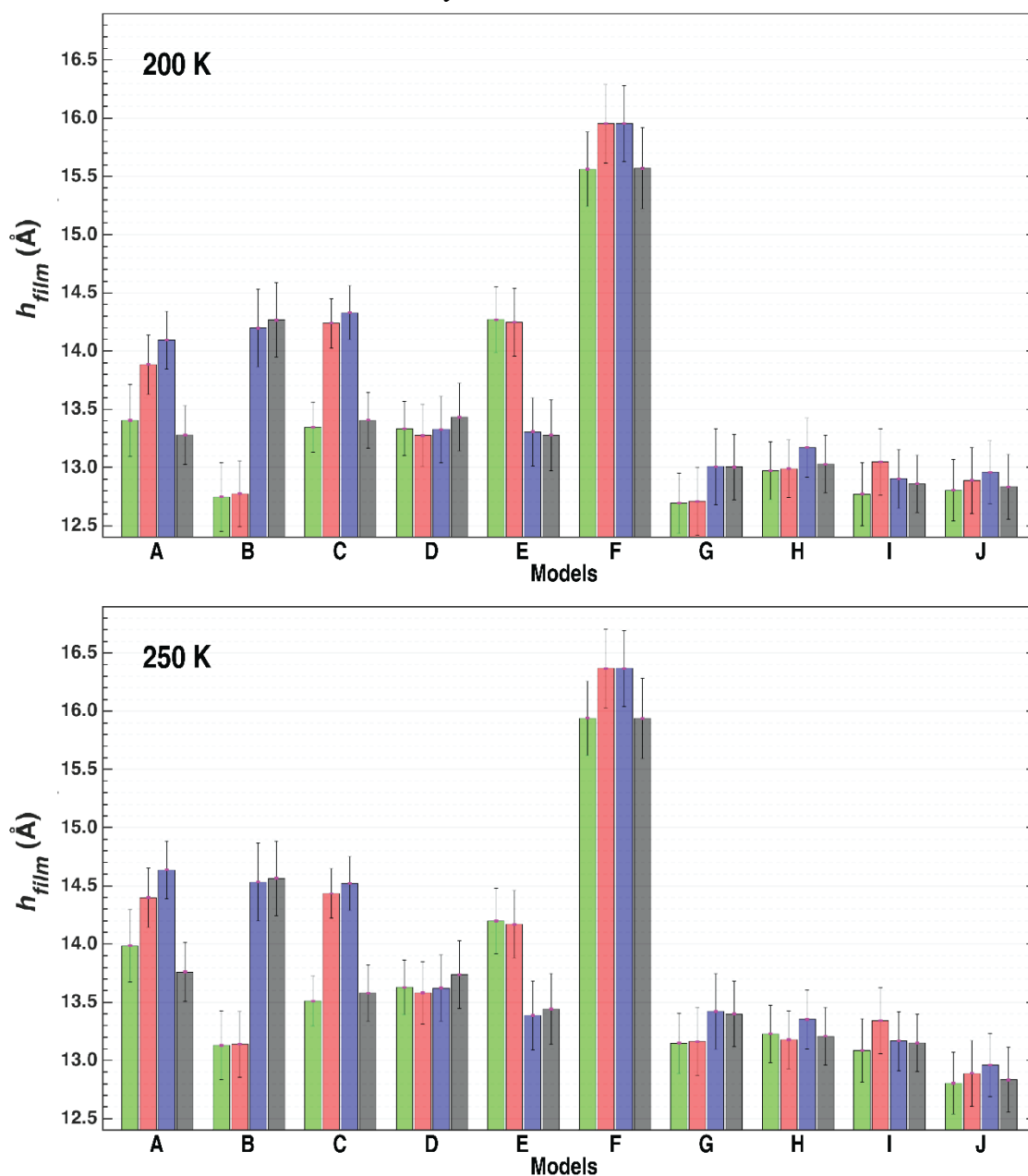


Figure 5.7. The Standard Deviation (SD) and the Standard Deviation of the Mean (SDoM) of Molecular Heights for Each Basis Type for the Models. The black vertical error bars represent the SD of height, whereas the small ( $\sim 50$  time smaller than the SD) magenta bars shows the corresponding SDoM. Notice the height difference between 200 K and 250 K and the larger SD error bars for 250 K.

We also compare the models using the tilt direction and their thermal stability. The tilt direction of the molecules in an ordered SAM should be along the NNN direction to optimize the interchain



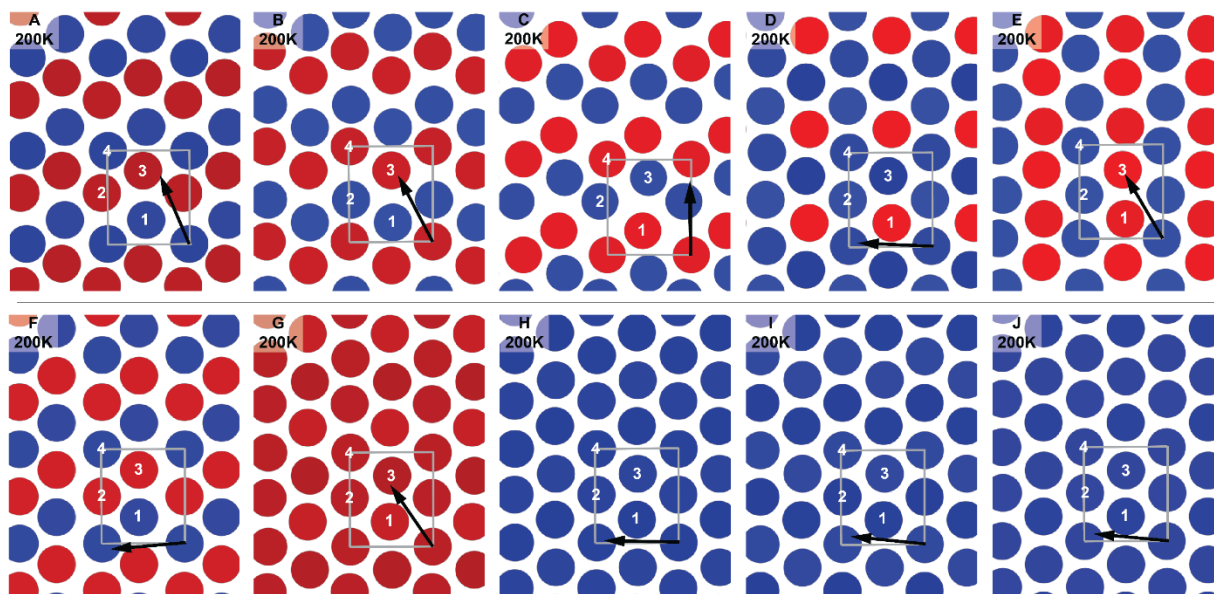


Figure 5.8. The Spatial Distribution of the Molecular Twist for the Models at 200 K. The position of the circles is the average position of the methyl groups, and the color of the circle represents the average value of the folded twist; Blue:  $0^\circ \leq \phi < 90^\circ$  and Red:  $90^\circ \leq \phi < 180^\circ$ . The corresponding tilt direction (black arrow) and the  $(2\sqrt{3} \times 3)\text{rect.}$  unit cell (gray rectangle) are shown for comparison. The numbering scheme for the basis molecules is the same as in Table 5.1. The  $(2\sqrt{3} \times 3)\text{rect.}$  unit cell is tiled  $3 \times 3$  for easy visualization of the patterns.

vdW interaction.<sup>36</sup> We have observed that crowding of the headgroups, such as in models C and E, has a significant effect on the tilt direction and the thermal stability of the SAMs. For instance, the average tilt direction for model C is towards the nearest neighbor (NN) direction for both 200 K (Figure 5.8) and 250 K (Figure 5.9). Although, molecules are tilted towards their NNN direction in model E at 200 K, the direction changes to a symmetry inequivalent direction with increasing temperature (see Figures 5.8.E and 5.9.E). Moreover, the spatial distribution of the twist has a 2-molecule basis surface structure at 200 K which is changed into a 4-molecule basis at 250 K. Combined with the anomalously high gauche fraction already discussed, the change in the tilt direction and the symmetry of the twist with respect to the temperature indicates that model E is unlikely to represent the observed structure of the monolayer. As a result, models C and E are not good candidate to represent the *n*-decanethiol SAM.

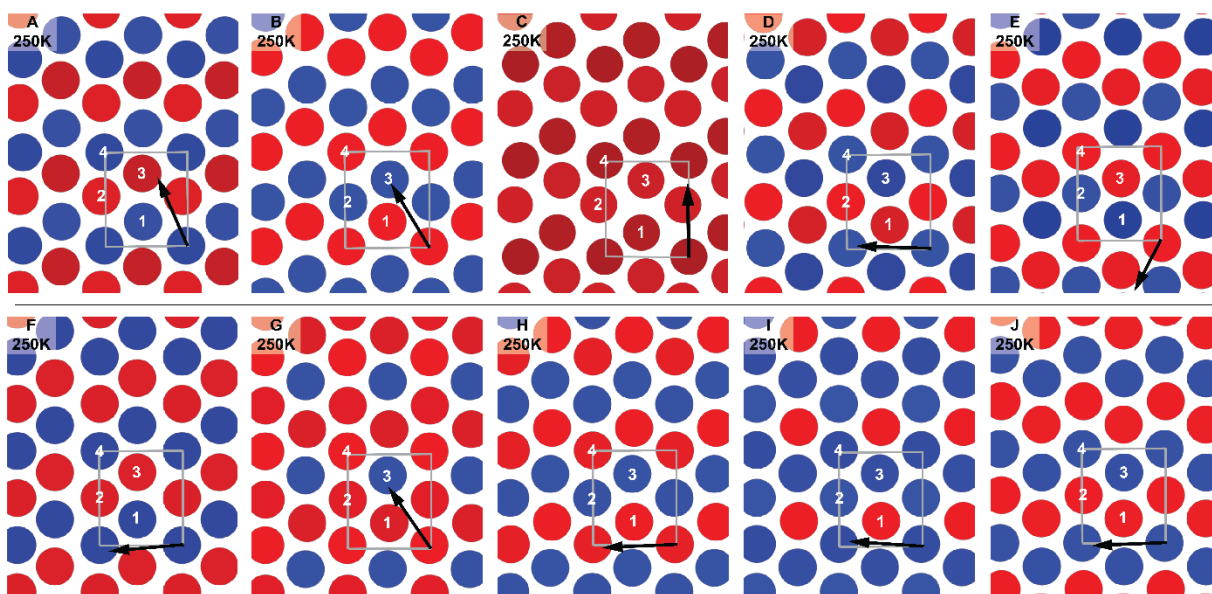


Figure 5.9. The Spatial Distribution of the Molecular Twist for the Models at 250 K. The position of the circles is the average position of the methyl groups, and the color of the circle represents the average value of the folded twist; Blue:  $0^\circ \leq \phi < 90^\circ$  and Red:  $90^\circ \leq \phi < 180^\circ$ . The corresponding tilt direction (black arrow) and the  $(2\sqrt{3} \times 3)\text{rect.}$  unit cell (gray rectangle) are shown for comparison. The numbering scheme for the basis molecules is the same as in Table 5.1. The  $(2\sqrt{3} \times 3)\text{rect.}$  unit cell is tiled  $3 \times 3$  for easy visualization of the patterns.

### 5.5.5 Basis Offset and Molecular Geometry

Finally, we study the relationship between the basis site offset from the high symmetry  $(\sqrt{3} \times \sqrt{3})R30^\circ$  basis sites and the resultant geometry of the alkyl chains driven by their close packing, particularly chain tilt direction and chain twist. First, we must remove a complication that arises because the sulfur adsorption sites in these models are not only offset from their ideal basis sites, but also have different basis heights above the nominal substrate plane (Figure 5.5). Height differences of the sulfur sites translate to a difference in lateral spacing of the alkyl chains in the tilt direction. In order to accurately compare the offsets, the adsorption sites and alkyl chain axes must be referenced to a common plane. For our analysis, the position of the headgroups are projected along the alkyl chain axis to a common plane parallel to the unreconstructed Au(111)

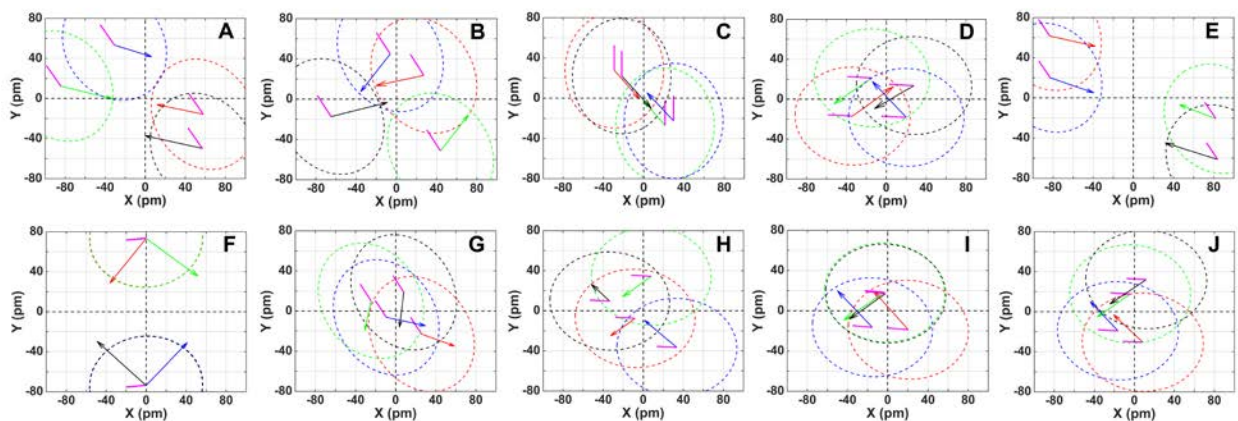


Figure 5.10. Comparison of the SAM Sulfur Adsorption Sites and Alkyl Chain Molecular Geometry for the Models. The locations are shown in the reference frame of the reduced close-packed coordinate system (see text). The head group positions are at the vertex of the arrow and the magenta lines. The chain axis is located at the end of the arrow. The magenta lines for each arrow indicated the chain tilt direction. The twist is the angle between the magenta line and the arrow. The dotted ellipses show the possible positions of the idealized all-trans alkyl chain axis as the twist is swept in a full circle. The basis types are indicated by the color of the arrows (red = 1, green = 2, blue = 3, and black = 4).

substrate plane. The position of the alkyl chain axis is taken as the point where it intersects this plane. Now we can define a reduced coordinate system with respect to the associated close-packed lattice, the high-symmetry  $(\sqrt{3} \times \sqrt{3})R30^\circ$  sub-lattice of the  $(2\sqrt{3} \times 3)$ rect. unit cell. For simplicity we choose an origin of the close packed lattice such that the four offset vectors sum to zero. To achieve this, we first align the unit cell origin with one of the adsorption sites. The offset vectors of the four sites to the corresponding  $(\sqrt{3} \times \sqrt{3})R30^\circ$  sub-lattice sites are determined. The sum of the offset vectors is the position of the best-fit unit cell origin. The unit cell origin is then translated to the new coordinate frame. Rotation is not allowed because that would violate long-range translational symmetry. The resulting offset vectors are in a reduced close-packed (RCP) coordinate system (Figure 1.5).

Figure 5.10 shows the resulting SAM structures for each model in the RCP coordinate frame. The headgroup offset for each basis site is represented by origin of the arrows and are colored to

identify each basis type. The root mean square (rms) average offset for the four basis sites ( $a_S$ ), a measure of the deviation from the close-packed lattice, is given in the Table 5.3. The possible locations of the chain axis, in the case of ideal all-trans alkyl chains, trace out an ellipse around each sulfur that is elongated in the tilt direction (see Figure 5.11). The average position of the molecular axes in the simulations is at the tip of the arrows. The molecular twist is the angle between the tilt direction (magenta line) and the arrow. For further analysis, we shift the origin of the coordinates for the alkyl chain axes such that the sum of their offset vectors is zero, as we did for the sulfur headgroups, and report the rms average offset ( $a_C$ ) and standard deviation ( $\sigma_C$ ) of the four basis-site chain axes in the Table 5.3. The standard deviation is a measure of the stability and fluctuation of the chain axis fit during the simulation time. Larger standard deviation indicates higher gauche fraction. The simulation results for a reference structure with the sulfur headgroups in  $(\sqrt{3} \times \sqrt{3})R30^\circ$  sites on unreconstructed Au(111) substrate at 200 K is included for comparison.

Table 5.3 clearly shows that in all ten models the headgroups are offset from a close-packed lattice and the alkyl chains adjust to reduce that offset. The propensity for the chains to close pack is also evident in Figure 5.10 from the tendency of the chain axes to be more tightly clustered than the headgroups. However, none of the models allow perfect packing of all-trans alkyl chains. If this were possible, the four chain-axis ellipses would intersect with each of the alkyl chain twists close to one of the four optimum twist angles. The chains can adapt to adverse headgroup packing by adding gauche defects near the surface thereby facilitating the remaining portion of the chain to adopt a more optimal close-packed geometry. For example, model E has the largest headgroup rms average offset ( $a_S$ ) and the alkyl chains achieve the poorest close packing, as shown by the highest  $a_C$  and  $\sigma_C$ . This is consistent with the significantly higher gauche fraction observed in the

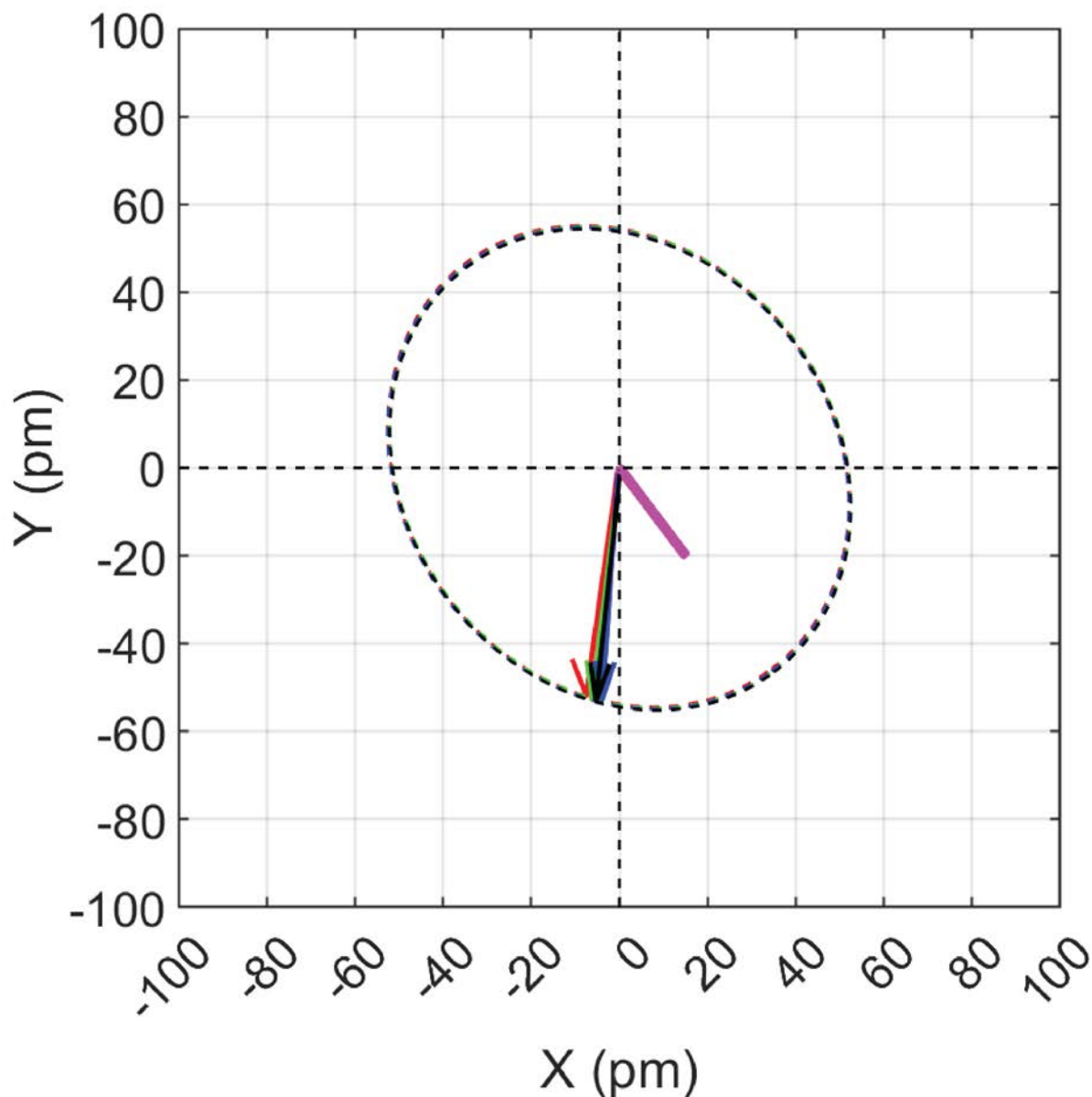


Figure 5.11. The RCP View of the SAM Sulfur Adsorption Sites and Alkyl Chain Molecular Geometry for the Head Groups on the Ideal  $(\sqrt{3} \times \sqrt{3})R30^\circ$  Sites.

simulations compared to the other models. In contrast, the reference structure where the sulfur headgroups were exactly in close-packed sites (Table 5.3) allows better close packing of the chains than any of the ten models studied, as evidenced by the smallest  $a_c$  and  $\sigma_c$ . Visualizing this structure in the RCP coordinate frame in Figure 5.11 shows the alkyl chains adopt a single twist. All four headgroups are at the origin with identical overlapping ellipses (Figure 5.11). The chain

axes all fall close to the same point on the ellipse, the small deviation due the thermal gauche defects. Models F and A have the next highest  $a_s$ , but their  $a_C$  values are strikingly different. Model A allows the alkyl chains to achieve better close packing, with model F exhibiting an  $a_C$  and  $\sigma_C$  over 3 times larger. Graphically, models A, C, E, and F show a clear propensity for the molecular axes being more tightly clustered than their headgroups (Figure 5.10). Although that trend is less apparent for the rest of the models, it is very evident from the  $\sigma_C$  values. It is interesting that the chain packing as quantified by  $a_C$  are all similar except for models E and F. The models where the chain axes fall nearer to the ellipses exhibit a smaller  $\sigma_C$ , as expected. The value of  $a_C$  for all the models except model E and F is comparable to the reference structure indicating they achieve an ordered close-packed SAM structure.

The extreme sensitivity of the alkyl chain conformation to the headgroup spacing is well illustrated by the models D, G, H, I, and J which are visually very similar, but have distinct headgroup offsets in the RCP coordinate frame. These lead to very different chain twist combinations, and in the case of model G, a different tilt direction than the other four. The  $a_C$  and  $\sigma_C$  values of the five models are very close, indicating that the efficiency of the chain packing is similar.

Figure 5.10 illustrates how multiple twist combinations arise as a natural consequence of the basis site offset of the sulfur headgroups from ideal close packed sites. For example, in model A the alkyl chains adjust to optimize their close packing by adjusting the chain twist (and tilt) to bring the chain axes closer together. Without the headgroup offset, neighboring chains cannot adopt different twists without conflict. This requirement was first proposed by Mar & Klein.<sup>3</sup>

Table 5.3. Comparison of the rms Deviation of the Sulfur Head Groups ( $a_S$ ) and the Alkyl Chain Axes ( $a_C$ ) from the Close-Packed Lattice for Ten Models. The standard deviation of the alkyl chain axes are also tabulated ( $\sigma_C$ ).

Model	A	B	C	D	E	F	G	H	I	J	$(\sqrt{3}\times\sqrt{3})R30^\circ$
$a_S$ (pm)	142.8	111.8	71.8	61.3	189.8	147.0	49.4	76.2	43.8	67.2	0
$a_C$ (pm)	10.6	10.9	8.7	9.4	36.1	34.6	8.7	8.5	10.6	8.7	8.4
$\sigma_C$ (pm)	2.4	2.3	3.2	2.9	6.9	6.9	3.3	3.3	3.2	3.2	2.1

Models A and F reproduce all the experimentally observed structural parameters of height difference symmetry, tilt direction, and chain twist. Model A exhibits two chain twists and model F exhibits all four. The alkyl-chain packing is not as optimal in model F and as such displays more disorder. Model A is the best candidate based on the chain packing. We have eliminated models D and J, since the resulting molecular height symmetry is not a 4-molecule basis. Models B, D, G, H, I, and J do not produce an equal population of orthogonal molecular twist angles. We eliminate model C because the molecules tilt towards the NN instead of NNN. These results (Table 5.4) demonstrate that the SAM structure is quite sensitive to the Au-S interface.

Table 5.4. Comparison Between Simulation and Experimental Results for Different Models.

	Model	$T$ (K)	Tilt angle ( $^{\circ}$ )	Tilt direction <sup>a</sup> ( $^{\circ}$ )	Twist angle <sup>b</sup> ( $^{\circ}$ )	$\Delta h^c$ (pm)
Simulation	A	200	$32 \pm 1$	$5.26 \pm 2.37^{\circ}$	$(46 \pm 5), (139 \pm 5)$	81.5
		250	$26 \pm 1$	$6.62 \pm 3.17^{\circ}$	$(49 \pm 10), (138 \pm 10)$	87.8
	B	200	$36 \pm 1$	$3.27 \pm 0.492^{\circ}$	$(72 \pm 6), (110 \pm 6)$	151.9
		250	$32 \pm 2$	$0.876 \pm 0.478^{\circ}$	$(75 \pm 7), (108 \pm 9)$	143.4
	C	200	$31 \pm 1$	$29.5 \pm 1.40^{\circ}$	$(39 \pm 5), (140 \pm 5)$	98.7
		250	$29 \pm 1$	$29.3 \pm 1.38^{\circ}$	$(137 \pm 7)$	101.1
	D	200	$32 \pm 1$	$3.26 \pm 1.79^{\circ}$	$(40 \pm 5), (135 \pm 5)$	19.3
		250	$28 \pm 3$	$1.83 \pm 1.39^{\circ}$	$(43 \pm 6), (136 \pm 7)$	19.1
	E	200	$30 \pm 2$	$4.46 \pm 5.53^{\circ}$	$(43 \pm 6), (143 \pm 8)$	99.3
		250	$21 \pm 3$	$3.95 \pm 4.39^{\circ}$	$(47 \pm 12), (137 \pm 12)$	81.1
	F	200	$30 \pm 1$	$5.12 \pm 2.12^{\circ}$	$(47 \pm 5), (139 \pm 5)$	42.9
		250	$25 \pm 1$	$6.94 \pm 2.41^{\circ}$	$(51 \pm 9), (137 \pm 9)$	39.2
	G	200	$36 \pm 1$	$3.19 \pm 0.770^{\circ}$	$(141 \pm 5)$	31.4
		250	$32 \pm 1$	$4.38 \pm 0.854^{\circ}$	$(46 \pm 7), (140 \pm 7)$	27.1
	H	200	$35 \pm 1$	$2.65 \pm 1.15^{\circ}$	$(42 \pm 5)$	19.9
		250	$33 \pm 1$	$2.61 \pm 1.15^{\circ}$	$(45 \pm 7), (139 \pm 7)$	17.4
	I	200	$35 \pm 1$	$5.26 \pm 1.51^{\circ}$	$(41 \pm 5)$	27.6
		250	$33 \pm 2$	$6.22 \pm 1.16^{\circ}$	$(42 \pm 6)$	25.7
J	200	$36 \pm 1$	$3.26 \pm 1.22^{\circ}$	$(41 \pm 5)$	15.7	
	250	$33 \pm 1$	$2.53 \pm 1.08^{\circ}$	$(42 \pm 7), (140 \pm 7)$	9.9	
<b>Experimental</b>			$25 - 35^8$	NNN <sup>7, 9</sup>	$50, 132^{34}$	$\sim 90^{31}$

<sup>a</sup> The direction of the tilt angle is shown in Figure 5.8 and 5.9. The angle is measure from the NNN direction.

<sup>b</sup> The twist angles are calculated for the folded twist, see the text for more details.

<sup>c</sup> The maximum height difference between the molecular heads measured in STM depends on the tunneling conditions, the nature of the bonding of the headgroups to the substrate, and the length of the molecules, because the STM image is a convolution of the physical height and the electronic properties of the molecules. Here we are reporting only the maximum physical height difference ( $\Delta h$ ) between the basis methyl carbon atoms. Therefore, the discrepancy between the experimental and the simulated values can be attributed to the excluded electronic effects of the molecule.

## 5.6 Conclusions

Most of the recent effort to understand the structure of SAMs has focused on the Au-S interface and models for the complex reconstruction of the Au(111) surface. That body of work has resulted in a wide variety of  $(2\sqrt{3} \times 3)$ rect. unit cell models for the reconstructed Au-S interface. However,



a simplified ( $\sqrt{3} \times \sqrt{3}$ )R30° adsorption geometry of the interface is commonly considered for the MD simulation. We have shown how the headgroup deviation from the idealized ( $\sqrt{3} \times \sqrt{3}$ )R30° sites strongly effects the geometry of the chains. We chose ten complex reconstructions of the Au-S interface for our study. From these we have constructed models of C10 SAMs and compared the resulting monolayer with experimental measurements of the alkyl chain structure. The pattern of molecule heights at the outer surface were compared to STM images. The tilt, twist, and tilt direction of the molecular backbone were compared to IRRAS measurements. Deviation of the headgroup from the ideal sites in these reconstructed models drives the molecules to obtain different twists for efficient packing. This results in equal population of at least two nearly orthogonal twists for models A, B, C, E, and F that is consistent with the IRRAS observation. This is the first report of the 4-molecule basis twist structure using the molecular dynamics that is consistent with the experiment. Two of the ten Au-S structures considered (models A and F) reproduced all the experimentally observed alkyl chain structure parameters despite all models having the same alkanethiol coverage.

Our model can be improved with realistic potentials for Au-S-CH<sub>2</sub> bond bending and dihedral for the low symmetry adsorption sites prevalent in the Au-S models. An all-atom force field trained for SAMs would be advantageous, although sensible results are obtained with simple temperature scaling. It is important to note that SAMs have application at higher temperatures where the crystalline order diminishes.<sup>37-39</sup> It was not the intent of this work to promote any particular structure as correct or incorrect because these results may also be sensitive to the Au-S-CH<sub>2</sub> bond potential. Our study underscores the value to develop the crucial MD FF parameters at the Au-S interface for more realistic simulation of the SAM structure.

## 5.7 References

1. Wang, Y.; Solano Canchaya, J. G.; Dong, W.; Alcamí, M.; Busnengo, H. F.; Martín, F., Chain-Length and Temperature Dependence of Self-Assembled Monolayers of Alkylthiolates on Au(111) and Ag(111) Surfaces. *J. Phys. Chem. A* **2014**, *118* (23), 4138-4146.
2. Wang, Y.; Solano-Canchaya, J. G.; Alcamí, M.; Busnengo, H. F.; Martín, F., Commensurate Solid–Solid Phase Transitions in Self-Assembled Monolayers of Alkylthiolates Lying on Metal Surfaces. *J. Am. Chem. Soc.* **2012**, *134* (32), 13224-13227.
3. Mar, W.; Klein, M. L., Molecular Dynamics Study of the Self-Assembled Monolayer Composed of S(CH<sub>2</sub>)<sub>14</sub>CH<sub>3</sub> Molecules Using an All-Atoms Model. *Langmuir* **1994**, *10* (1), 188-196.
4. Hautman, J.; Klein, M. L., Simulation of a Monolayer of Alkyl Thiol Chains. *J. Chem. Phys.* **1989**, *91* (8), 4994-5001.
5. Hautman, J.; Klein, M. L., Molecular Dynamics Simulation of the Effects of Temperature on a Dense Monolayer of Long-chain Molecules. *J. Chem. Phys.* **1990**, *93* (10), 7483.
6. Ta-Wei Li, I. C., and Yu-Tai Tao, Relationship between Packing Structure and Headgroups of Self-Assembled Monolayers on Au(111): Bridging Experimental Observations through Computer Simulations. *J. Phys. Chem. B* **1998**, *102* (16), 2935-2946.
7. Camillone, N.; Chidsey, C. E. D.; Liu, G.-Y.; Scoles, G., Superlattice Structure at the Surface of a Monolayer of Octadecanethiol Self-Assembled on Au(111). *J. Chem. Phys.* **1993**, *98* (4), 3503-3511.
8. Nuzzo, R. G.; Dubois, L. H.; Allara, D. L., Fundamental Studies of Microscopic Wetting on Organic Surfaces. 1. Formation and Structural Characterization of a Self-Consistent Series of Polyfunctional Organic Monolayers. *J. Am. Chem. Soc.* **1990**, *112* (2), 558-569.
9. Nuzzo, R. G.; Korenic, E. M.; Dubois, L. H., Studies of the Temperature-Dependent Phase Behavior of Long Chain *n*-Alkyl Thiol Monolayers on Gold. *J. Chem. Phys.* **1990**, *93* (1), 767-773.
10. Ulman, A., Formation and Structure of Self-Assembled Monolayers. *Chem. Rev.* **1996**, *96* (4), 1533-1554.
11. Ulman, A.; Eilers, J. E.; Tillman, N., Packing and Molecular Orientation of Alkanethiol Monolayers on Gold Surfaces. *Langmuir* **1989**, *5* (5), 1147-1152.
12. Mete, E.; Yortanl, M.; Dansman, M. F., A van der Waals DFT Study of Chain Length Dependence of Alkanethiol Adsorption on Au(111): Physisorption vs. Chemisorption. *Phys. Chem. Chem. Phys.* **2017**, *19* (21), 13756-13766.
13. Chaudhuri, A.; Lerotholi, T. J.; Jackson, D. C.; Woodruff, D. P.; Jones, R. G., (2√3×3)Rect. Phase of Alkylthiolate Self-Assembled Monolayers on Au(111): A Symmetry-Constrained Structural Solution. *Phys. Rev. B* **2009**, *79* (19), 195439-195447.
14. Voznyy, O.; Dubowski, J. J., c(4×2) Structures of Alkanethiol Monolayers on Au(111) Compatible with the Constraint of Dense Packing. *Langmuir* **2009**, *25* (13), 7353-7358.

15. Longo, G. S.; Bhattacharya, S. K.; Scandolo, S., A Molecular Dynamics Study of the Role of Adatoms in SAMs of Methylthiolate on Au(111): A New Force Field Parameterized from Ab Initio Calculations. *J. Phys. Chem. C* **2012**, *116* (28), 14883-14891.
16. Grönbeck, H.; Häkkinen, H.; Whetten, R. L., Gold–Thiolate Complexes form a Unique  $c(4\times 2)$  Structure on Au(111). *J. Phys. Chem. C* **2008**, *112* (41), 15940-15942.
17. Cossaro, A.; Mazzarello, R.; Rousseau, R.; Casalis, L.; Verdini, A.; Kohlmeyer, A.; Floreano, L.; Scandolo, S.; Morgante, A.; Klein, M. L.; Scoles, G., X-ray Diffraction and Computation Yield the Structure of Alkanethiols on Gold(111). *Science* **2008**, *321* (5891), 943-946.
18. Wang, J.-G.; Selloni, A., The  $c(4\times 2)$  Structure of Short- and Intermediate-Chain Length Alkanethiolate Monolayers on Au(111): A DFT Study. *J. Phys. Chem. C* **2007**, *111* (33), 12149-12151.
19. Wang, Y.; Chi, Q.; Zhang, J.; Hush, N. S.; Reimers, J. R.; Ulstrup, J., Chain-Branching Control of the Atomic Structure of Alkanethiol-Based Gold–Sulfur Interfaces. *J. Am. Chem. Soc.* **2011**, *133* (38), 14856-14859.
20. Wang, Y.; Chi, Q.; Hush, N. S.; Reimers, J. R.; Zhang, J.; Ulstrup, J., Gold Mining by Alkanethiol Radicals: Vacancies and Pits in the Self-Assembled Monolayers of 1-Propanethiol and 1-Butanethiol on Au(111). *J. Phys. Chem. C* **2011**, *115* (21), 10630-10639.
21. Meena Devi, J., A Simulation Study on the Thermal and Wetting Behavior of Alkane Thiol SAM on Gold (111) Surface. *Prog. Nat. Sci.: Mater. Int.* **2014**, *24* (4), 405-411.
22. Chaudhuri, A.; Lerotholi, T. J.; Jackson, D. C.; Woodruff, D. P.; Jones, R. G.,  $(2\sqrt{3}\times 3)$ rect Phase of Alkylthiolate Self-assembled Monolayers on Au(111): A Symmetry-constrained Structural Solution. *Phys. Rev. B* **2009**, *79* (19), 195439.
23. Wyckoff, R. W. G., *Crystal Structures*. 2nd ed.; Wiley: New York, 1963; Vol. 1.
24. Plimpton, S., Fast Parallel Algorithms for Short-Range Molecular Dynamics. *J. Comput. Phys.* **1995**, *117* (1), 1-19.
25. Murzyn, K.; Bratek, M.; Pasenkiewicz-Gierula, M., Refined OPLS All-Atom Force Field Parameters for *n*-Pentadecane, Methyl Acetate, and Dimethyl Phosphate. *J. Phys. Chem. B* **2013**, *117* (51), 16388-16396.
26. Ryckaert, J.-P.; Klein, M. L.; McDonald, I. R., Computer Simulations and the Interpretation of Incoherent Neutron Scattering Experiments on the Solid Rotator Phases of Long-Chain Alkanes. *Mol. Phys.* **1994**, *83* (3), 439-458.
27. Nuzzo, R. G.; Korenic, E. M.; Dubois, L. H., Studies of the Temperature-Dependent Phase Behavior of Long Chain *n*-Alkyl Thiol Monolayers on Gold. *J. Chem. Phys.* **1990**, *93* (1), 767-773.
28. Bensebaa, F.; Ellis, T. H.; Badia, A.; Lennox, R. B., Thermal Treatment of *n*-Alkanethiolate Monolayers on Gold, As Observed by Infrared Spectroscopy. *Langmuir* **1998**, *14* (9), 2361-2367.
29. Dubois, L. H.; Nuzzo, R. G., Synthesis, Structure, and Properties of Model Organic Surfaces. *Annu. Rev. Phys. Chem.* **1992**, *43* (1), 437-463.

30. Poirier, G. E.; Tarlov, M. J., The  $c(4 \times 2)$  Superlattice of *n*-Alkanethiol Monolayers Self-Assembled on Au(111). *Langmuir* **1994**, *10* (9), 2853-2856.
31. Lüsse, B.; Müller-Meskamp, L.; Karthäuser, S.; Waser, R., A New Phase of the  $c(4 \times 2)$  Superstructure of Alkanethiols Grown by Vapor Phase Deposition on Gold. *Langmuir* **2005**, *21* (12), 5256-5258.
32. Porter, M. D.; Bright, T. B.; Allara, D. L.; Chidsey, C. E. D., Spontaneously Organized Molecular Assemblies. 4. Structural Characterization of *n*-Alkyl Thiol Monolayers on Gold by Optical Ellipsometry, Infrared Spectroscopy, and Electrochemistry. *J. Am. Chem. Soc.* **1987**, *109* (12), 3559-3568.
33. Strong, L.; Whitesides, G. M., Structures of Self-Assembled Monolayer Films of Organosulfur Compounds Adsorbed on Gold Single Crystals: Electron Diffraction Studies. *Langmuir* **1988**, *4* (3), 546-558.
34. Laibinis, P. E.; Whitesides, G. M.; Allara, D. L.; Tao, Y. T.; Parikh, A. N.; Nuzzo, R. G., Comparison of the Structures and Wetting Properties of Self-Assembled Monolayers of *n*-Alkanethiols on the Coinage Metal Surfaces, Copper, Silver, and Gold. *J. Am. Chem. Soc.* **1991**, *113* (19), 7152-7167.
35. Bareman, J. P.; Klein, M. L., Collective Tilt Behavior in Dense, Substrate-Supported Monolayers of Long-Chain Molecules: A Molecular Dynamics Study. *J. Phys. Chem.* **1990**, *94* (13), 5202-5205.
36. Fenter, P.; Eisenberger, P.; Liang, K. S., Chain-Length Dependence of the Structures and Phases of  $\text{CH}_3(\text{CH}_2)_{n-1}\text{SH}$  Self-Assembled on Au(111). *Phys. Rev. Lett.* **1993**, *70* (16), 2447-2450.
37. Ulman, A., *An Introduction to Ultrathin Organic Films*. Academic: Boston, 1991.
38. Ulman, A., Formation and Structure of Self-Assembled Monolayers. *Chem. Rev.* **1996**, *96* (4), 1533-1554.
39. Love, J. C.; Estroff, L. A.; Kriebel, J. K.; Nuzzo, R. G.; Whitesides, G. M., Self-Assembled Monolayers of Thiolates on Metals as a Form of Nanotechnology. *Chem. Rev.* **2005**, *105* (4), 1103-1170.

## Chapter 6: Effect of Sulfur Hybridization on Methanethiol

### Adsorption Geometry on Unrelaxed Au(111)

#### 6.1 Scope of this Chapter

In this chapter, we study the effect of the interaction at the Au-S interface on the preferred adsorption sites using an unrelaxed Au(111) substrate. We present a new study of the bonding geometry of methanethiol on Au(111). It is well known that alkanethiols adsorbed on Au(111) prefer the bridge-fcc and bridge-hcp sites with a strong preference for the S-C azimuthal angle dependent on the site, however the reason for this preference has not been studied. We use the electron localization function (ELF), bond order analysis (DDEC6), and charge density difference to show that the preferred geometries and system energies can be rationalized from the strong preference for the  $sp^3$  hybridization of the adsorbed thiol sulfur atom. We also show that the asymmetry between the preferred sites is due to participation of the second and lower Au layers.

#### 6.2 Introduction

Alkanethiol self-assembled monolayers on Au(111) substrates have attracted considerable scientific interest<sup>1-2</sup> for their diverse applications in biomedical,<sup>4</sup> nanotechnology,<sup>5</sup> surface modification,<sup>6</sup> electronics,<sup>7</sup> and chemical sensing.<sup>8</sup> The robustness of the structure and the ease of preparation contributes to the popularity of alkanethiol SAMs for fundamental and applied studies. Alkanethiol SAMs are also regarded as a model system to study the binding of organic molecules to metal surfaces via the thiol functional group. Understanding the SAM structure is important to have better control of its applications. The packing of the alkane chains and hence the structure of the SAM is significantly influenced by the coordination geometry of the adsorbed sulfur head

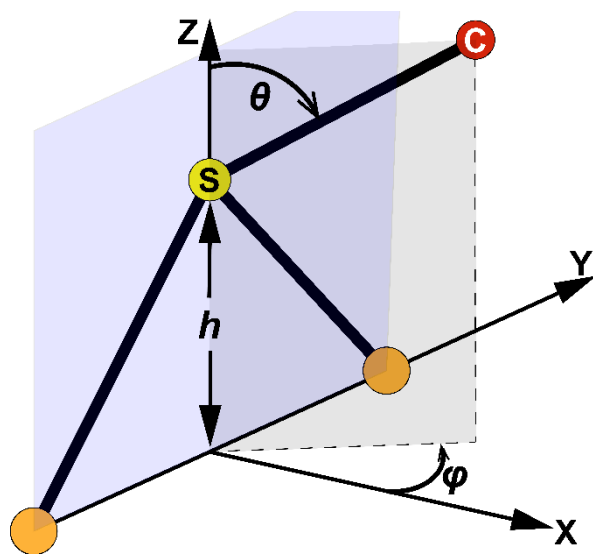


Figure 6.1. Geometrical Parameters of an Adsorbed Methanethiol Molecule. The height of the S atom from the substrate, polar angle, and azimuthal angle are denoted by  $h$ ,  $\theta$ , and  $\phi$ , respectively.

group and the orientation of the S-C bond.<sup>9-10</sup> A description of the manner in which the thiol sulfur atom bonds to the substrate has been quite controversial, with several different sites being discussed.<sup>11</sup> Density functional theory studies have shown that the most stable adsorption sites for the thiol S atom on unreconstructed Au(111) are the two bridge-related sites, the bridge-fcc and the bridge-hcp. In a previous study the strong S-C bond orientation preference of these sites and the asymmetry between the sites was

studied.<sup>3</sup> It was found that the bridge-fcc is more stable by 8.1 meV and increased on relaxation of the Au substrate to 26.1 meV. In this study this previous work is expanded, using dispersion corrected DFT, to explore the underlying cause for the offset from the bridge site, the strong S-C bond orientation preference, and the asymmetry the bridge-fcc and bridge-hcp sites.

Previous studies reported strong dependence of the polar angle and the azimuthal angle (defined in Figure 6.1) on the adsorption sites.<sup>12-13</sup> The S-C bond often considered to align with the surface normal at the 3-fold hollow sites ( $\theta \sim 0^\circ$  for fcc and hcp)<sup>12-15</sup>, but is significantly tilted from the surface normal for the atop ( $\sim 70^\circ$ )<sup>16-18</sup> and the bridge sites ( $\sim 55^\circ$  for bridge-fcc and bridge-hcp).<sup>12-13, 16-22</sup> For the fcc 3-fold hollow site, additional polar angles have been reported ( $\sim 50^\circ$ ) due the existence of additional local minima.<sup>16-17</sup> The azimuthal angle ( $\phi$ ) of the S-C bond changes with the adsorption site.<sup>12-13</sup> The effect is the strongest at the bridge site, but the atop site is azimuthally symmetric. The preferred  $\phi$  (in region 1) for the bridge-fcc site is  $0^\circ$ , whereas for the bridge-hcp

site it is  $180^\circ$  such that the S-C bond is oriented across the bridge site in both cases.<sup>3, 14</sup> Although, the steric effect between the adsorbate and the substrate were previously proposed, the origin of the S-C bond directionality and the adsorption site dependence of the preferred molecular geometry is yet to be understood.<sup>15</sup>

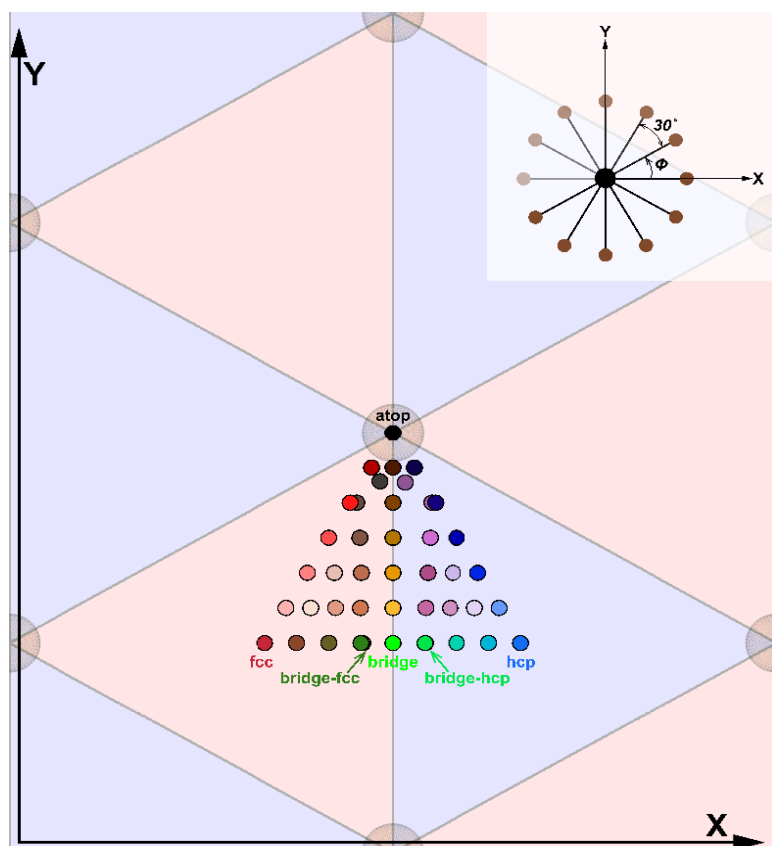


Figure 6.2. The 43 Adsorption Sites Are Shown within the Principle Triangle on the Unreconstructed Au(111) Substrate. Symmetry equivalent sites across the surface are generated using the inherent mirror symmetries and the rotational symmetries of the substrate (see text). Previously studied six adsorption sites, atop, bridge, bridge-fcc, bridge-hcp, fcc and hcp 3-fold hollow sites, are indicated. The inset shows 12 azimuthal angles of the S-C bond we used for each site.

surface Au atoms measures the strength of the electronic interaction and are calculated using DDEC6. Charge density difference analysis is used to probe the participation of the second-layer Au atoms. A low density of adsorbed methanethiol molecules is used in order to minimize the

In this study, understanding of the bridge-fcc and bridge-hcp sites are gained from the landscape in which they reside. To achieve that 43 adsorption sites were studied, each with 12 S-C bond orientations shown in Figure 6.2 (516 adsorption geometries of methanethiol). The coordination geometry of the sulfur is measured using the Au-S-C bond angles. The hybridization of the sulfur atom is inferred from the electron lone pairs, visualized using the electron localization function. The Au-S bond orders for the individual

methyl-methyl interaction and to allow focus on the thiol-sulfur interaction with the gold substrate. These analyses are applied to a subset of the data, namely sites on the path from bridge to atop, fcc-bridge-hcp, the S-C azimuth dependence at the high symmetry sites, and to the bridge-fcc and bridge-hcp sites. Throughout the discussion, the convention of referring to the adsorbate by the precursor, methanethiol, is adopted. This sidesteps assignment of the chemical nature of the adsorbate, which can have characteristics spanning a thiyl (radical) to a thiolate (anion). A preference of methanethiol for the bridge-fcc and the bridge-hcp sites and the strong S-C bond orientation can be explained as best accommodating  $sp^3$  hybridization on the S atom. The lower energy of the bridge-fcc site is linked to bonding along Au<110> columns in the sub-surface, which is only possible on the fcc side of the bridge site.

### 6.3 Simulation Details

DFT calculations are performed using the VASP 5.4.4 computational package,<sup>23-24</sup> on the Agave system at Arizona State's Research Computing Center and on the Oklahoma University Supercomputing Center for Education and Research (OSCER). The projector augmented wave method density functional (PAW) is used for the electron-ion interaction along with the Perdew-Burke-Ernzerhof (PBE) exchange functional.<sup>25-26</sup> The functional is denoted as PAW-PBE and it is most commonly used to model the adsorption of organic molecules on metal surfaces.<sup>19, 27-28</sup> The van der Waals (vdW) forces play an important role in such weakly interacting systems. Therefore the dispersion correction of Grimme<sup>29</sup> (DFT-D2) is included for more realistic simulation of the interaction between the adsorbate and the Au(111) substrate. A planewave cutoff of 300 eV is used for structural optimization. Justification for the planewave cutoff is given in a previous paper.<sup>3</sup> The Brillouin zone integration is performed using the Monkhorst-Pack sampling with  $9 \times 9 \times 1$



$\Gamma$ -centered  $\mathbf{k}$ -grid for a surface unit cell. The electron localization function (ELF)<sup>30</sup> in VASP was performed on the optimized structures using a planewave cutoff of 400 eV. ELF is used to study the change in surface bonding and infer sulfur hybridization using lone pair electrons for different adsorption sites and bonding geometries.<sup>31-32</sup> The bond orders were computed by the chgemo program using Manz's bond-order equation with DDEC6 partitioning<sup>33-34</sup> also using a planewave cutoff of 400 eV. The charge-density difference (CDD) is used to study the reorganization of spatial charge due to methanethiol adsorption. If the charge density of an isolated methanethiol, an isolated Au substrate, and methanethiol adsorbed on the substrate are  $\rho_{\text{CH}_3}$ ,  $\rho_{\text{Au}}$ , and  $\rho_{\text{CH}_3+\text{Au}}$ , respectively, the difference in charge density upon methanethiol adsorption is obtained by the following equation.

$$\text{CDD} = \rho_{\text{CH}_3+\text{Au}} - (\rho_{\text{CH}_3} + \rho_{\text{Au}}) \quad (6.1)$$

CDD then is used to study the effect of the specific adsorption site on the change of electronic charge density at the Au/S interface using VESTA.<sup>35</sup>

Geometries are considered optimized when the Hellmann-Feynman forces on ions are less than  $10^{-2}$  eV  $\text{\AA}^{-1}$ . During the geometry optimization, all six layers of Au atoms are kept fixed in their bulk positions (unreconstructed substrate) with equilibrium lattice constant of 4.10  $\text{\AA}$ . A  $(4 \times 2\sqrt{3})$  rectangular unit cell with 16 Au atoms per layer is used to reduce the lateral interaction between the adsorbate images (one adsorbate per 16 surface Au atoms).

For this study, the S atom is placed at selected positions on the surface (Figure 6.2) and the system is solved for different S-C bond orientations. The system is allowed to relax to optimize the height of the S atom above the surface, while the S-C bond is allowed to optimize in both length and polar angle. The methyl hydrogens are completely free to move. To achieve this, the S atom is constrained in  $x,y$  so that only motion along the  $z$  direction is allowed. The C atom is

constrained to relax in a vertical plane containing the S atom, either  $x$ - $z$  or  $y$ - $z$  depending on the azimuthal angle desired. This approach limits the choice of S-C bond orientation to those that reside in one of the two cartesian planes, thus four different orientations. The symmetry of the Au(111) surface allows us to study twelve different S-C bond orientations at each surface site by using three symmetry related surface sites (Figure 6.3).

In VASP DFT, the S-C bond orientation is easily constrained in the Cartesian planes  $x$ - $z$  and  $y$ - $z$  to control the azimuthal angle. The principal region (region 1, Figure 6.3a) with the unique

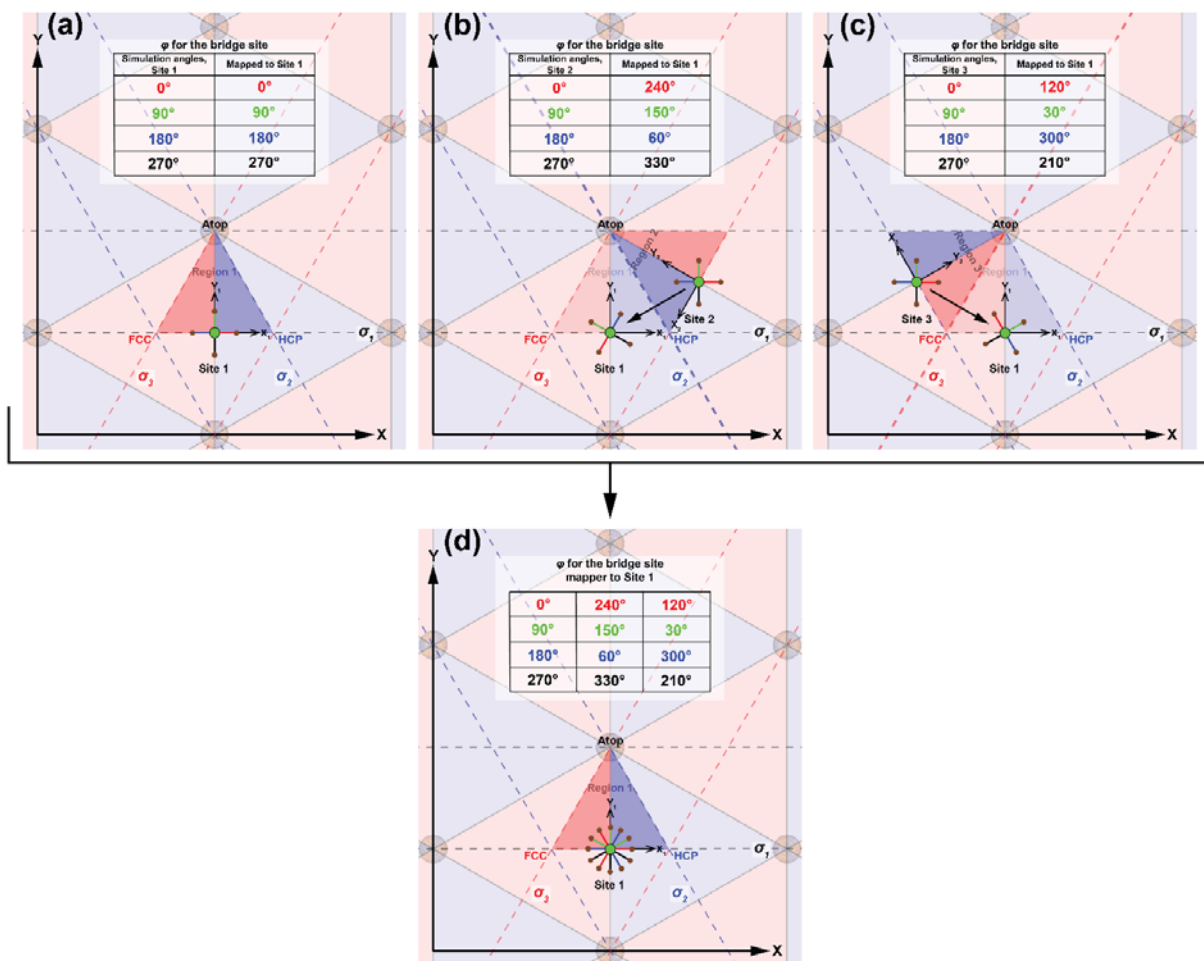


Figure 6.3. Scheme for Relaxing the SCH<sub>3</sub> in Twelve Azimuthal Orientations. The VASP Cartesian coordinate is denoted as  $x$  and  $y$ ,  $z$  is perpendicular to the plane. Regions 2 and 3 are related to the central principal triangle (region 1) by the mirror planes  $\sigma_2$  and  $\sigma_3$  respectively. The bridge sites 1, 2, and 3 are in regions 1, 2, and 3, respectively. Azimuthal angles derived from each site are listed in the table.

triangle with corners at atop, fcc, and hcp. Regions 2 and 3 (Figures 6.3b and c, respectively) are related to region 1 by the mirror planes  $\sigma_2$  and  $\sigma_3$ , respectively. Because regions 2 and 3 are aligned differently to the  $x$ - $z$  and  $y$ - $z$  planes, each region provides four different azimuthal angles. Relating all these results back to region 1, twelve azimuthal angles in  $30^\circ$  intervals are obtained. For example, consider three bridge sites 1, 2, and 3 in their respective regions. For this discussion, it is convenient to define a local coordinate frame consistent with atomic surface directions within each triangular region, with the bridge site as the origin. The  $+x$  direction is directed toward the hcp corner and the  $+y$  direction is directed toward the atop corner. The simulation coordinate frame is defined by the simulation box. These will be termed the local frame and simulation frame, respectively. The local frame in region 1 is aligned with the simulation frame. Therefore, constraining the S-C bond to the  $x$ - $z$  or  $y$ - $z$  planes directly provides the four azimuthal angles in the local frame ( $\phi_{site1}$ ):  $0^\circ$ ,  $90^\circ$ ,  $180^\circ$ , and  $270^\circ$ . The local frames in regions 2 and 3 are flipped with respect to region 1 by the mirror planes in addition to the rotation. Mapping the simulation frame angles from region 2 to the simulation frame angles (and therefore the local frame angles) in region 1 involves reflection through  $\sigma_2$ .

$$\phi_{site1} = (180^\circ - \phi_{site2}) - 60^\circ \quad (6.2)$$

In the same way, mapping from region 3 to region 1 involves reflection through  $\sigma_3$ .

$$\phi_{site1} = (180^\circ - \phi_{site3}) + 60^\circ \quad (6.3)$$

The four simulation frame angles  $0^\circ$ ,  $90^\circ$ ,  $180^\circ$ , and  $270^\circ$  in regions 2 and 3 provide the local frame angles  $240^\circ$ ,  $150^\circ$ ,  $60^\circ$ , and  $330^\circ$  and  $120^\circ$ ,  $30^\circ$ ,  $300^\circ$ , and  $210^\circ$ , respectively. The corners of the triangle are special points, as the atop, fcc, and hcp sites have  $C_3$  symmetry not shared by the other points in the region. At these points, no new information is obtained by repeating the calculations

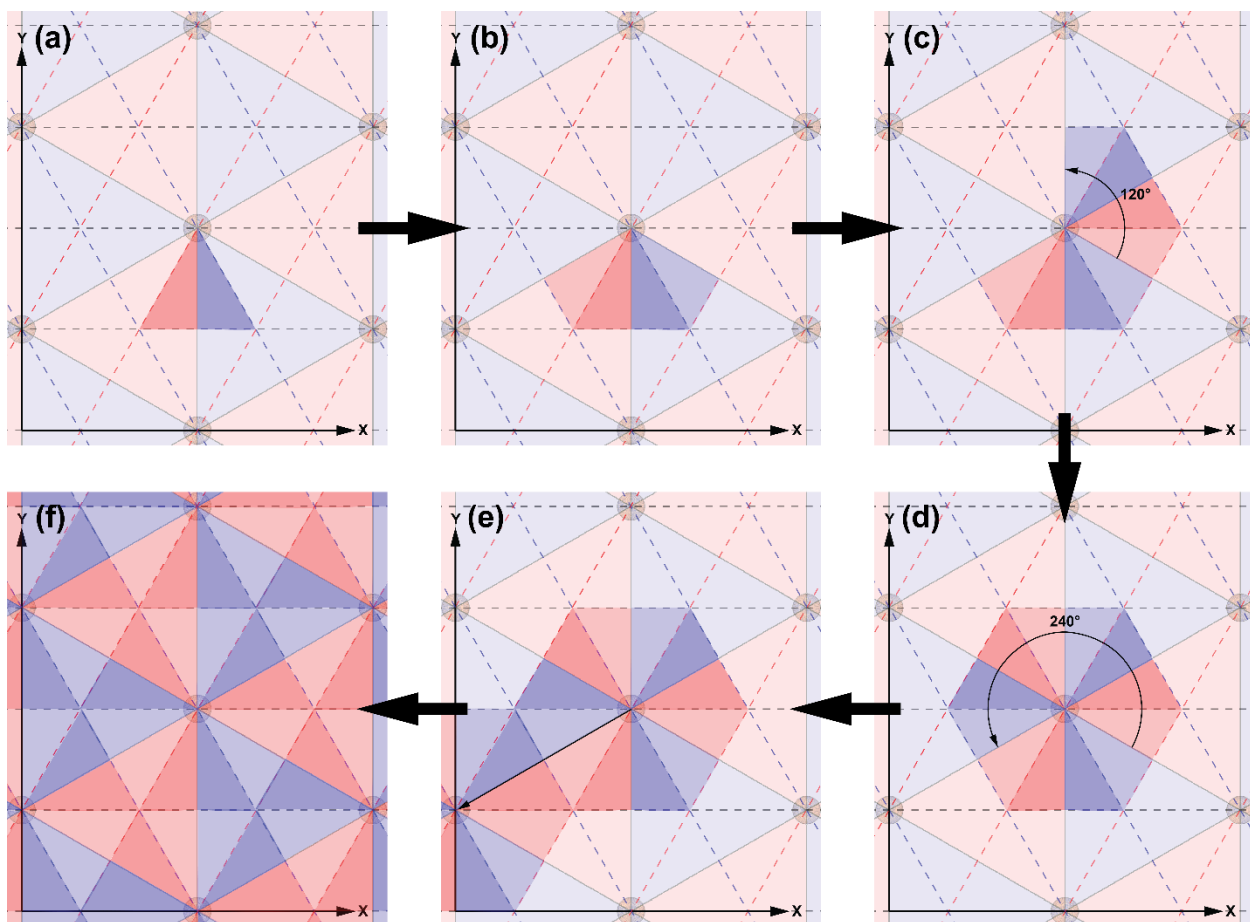


Figure 6.4 Tiling Scheme to Create the Full Surface from Region 1 using the Surface Symmetry.

in regions 2 and 3. The  $C_3$  symmetry is used to generate the additional 8 angles from  $0^\circ$ ,  $90^\circ$ ,  $180^\circ$ , and  $270^\circ$ . The results from all three regions are collected into the local frame of region 1 to provide all 12 azimuthal angles.

The full surface is obtained by tiling the local frame results as shown in the Figure 6.4. The right and left halves of region 1 (Figure 6.4.a) are expanded to fill 1/3 of the central hexagon (Figure 6.4.b) using the  $\sigma_2$  and  $\sigma_3$  mirror planes, respectively. The  $C_3$  rotation axis of the central hexagon is used to replicate that expanded region to complete the hexagon (Figures 6.4.c and 6.4.d). The Au lattice translational symmetry is used to fill the remaining surface (Figures 6.4.e and 6.4.f).

## 6.4 Results and Discussion

The energy for adsorption of methanethiol Au(111) is strongly dependent on the site and the azimuthal orientation of the S-C bond. The goal of this study is to understand the origin of this behavior. Here, the discussion begins with the overview of the energy landscape of an isolated methanethiol, followed by more detailed analysis along four paths connecting the high symmetry sites. Preference for tetrahedral coordination geometry on the S atom is shown to be the driving factor, not the adsorbate-surface bond order. It is also shown that the second and third sub-surface layers also participate and the directional interactions along the  $\langle 110 \rangle$  atomic columns are responsible for the bridge-site asymmetry.

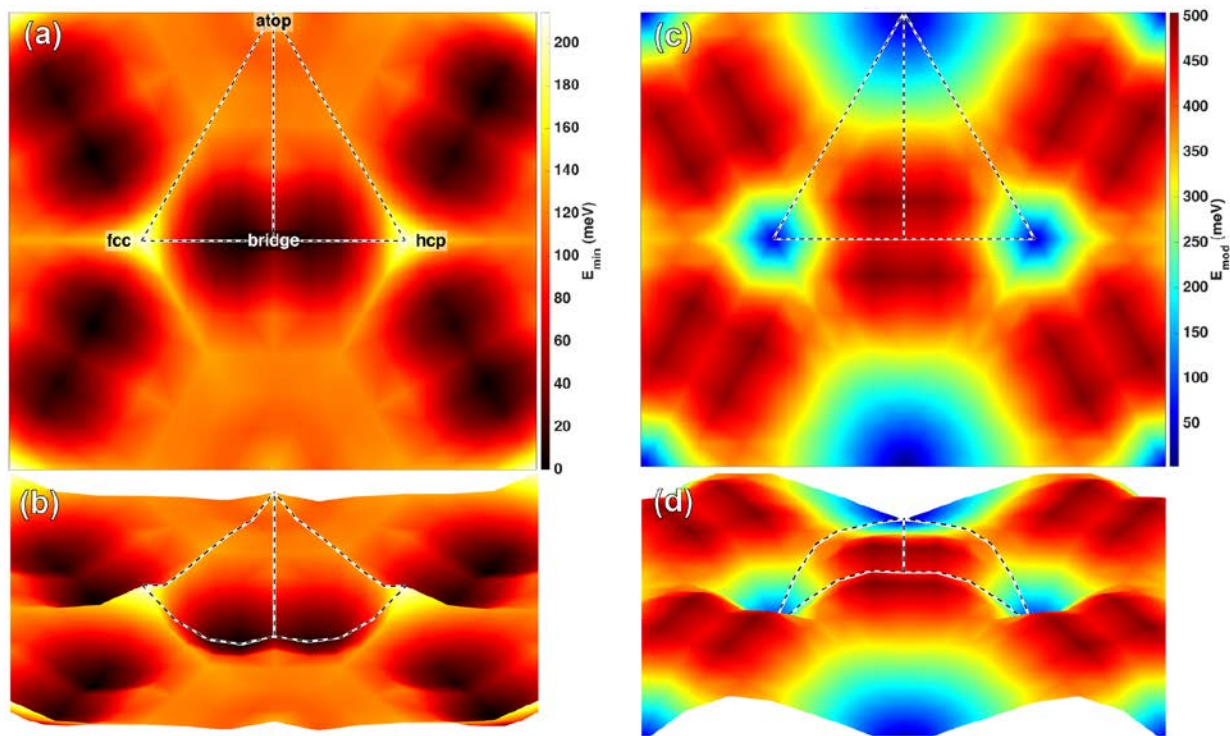


Figure 6.5. The Energy and Modulation Landscape. The top-down (a) and the side (b) view of the energy landscape of an isolated methanethiol on unrelaxed Au(111) is shown for the lowest energy S-C bond orientation. Three energy ridges are indicated by the dotted lines connecting the high symmetry adsorption sites. The top-down (c) and the side (d) view of the energy modulation due to changing the S-C bond orientation. This shows how the sensitivity of the system to the bond orientation depends on position.

The analysis begins with the energy landscape of an isolated methanethiol molecule on the unrelaxed Au(111) substrate. In Figure 6.5a and 6.5b, the map of the minimum energy at each of the 43 adsorption sites is shown. The minimum energy is that of the lowest energy of the 12 explored S-C bond orientations for that site. The most favorable adsorption sites are the bridge-fcc and the bridge-hcp sites with the latter 8.1 meV higher, consistent with our previous study.<sup>3</sup> In this discussion, system energy for the bridge-fcc site is used as our energy reference. The details are summarized in Table 6.1. The fcc and hcp sites are the least favorable at 214.2 and 212.8 meV, respectively. The atop is 136.6 meV. The atop is a local maximum surrounded by a shallow annular

local well 28.7 meV deep ~24 pm from the atop site. We will refer to this feature as the atop moat. There is also an energy ridge between the hollow sites and the atop site.

Table 6.1. Summary of the Characteristics for Selected Surface Sites. The minimum energy, energy modulation from S-C bond orientation, and the orientations of the energy minima.

Site	Energy (meV)	$\Delta E$ mod (meV)	Min E S-C Orientation (deg)
fcc	214.2	35.24	0, 120, 240
hcp	212.8	32.99	60, 180, 300
atop	136.6	2.531	0, 60, 120, 180, 240, 300
atop moat	109.6	102.5	radially toward atop
bridge	28.42	444.1	0, 180
bridge-fcc	0	454.4	0
bridge-hcp	8.1	444.5	180
max $\Delta E$ mod	34.90	552.9	0

The preferred S-C bond orientation is summarized in Figure 6.6 along with the optimized polar angle and the height of the S atom from the substrate. There are three preferred orientations within the triangular region bounded by the hollow site Au atoms. Each of the sub regions within that are bounded by the hollow site and two bounding atoms. Within each sub-region the preferred

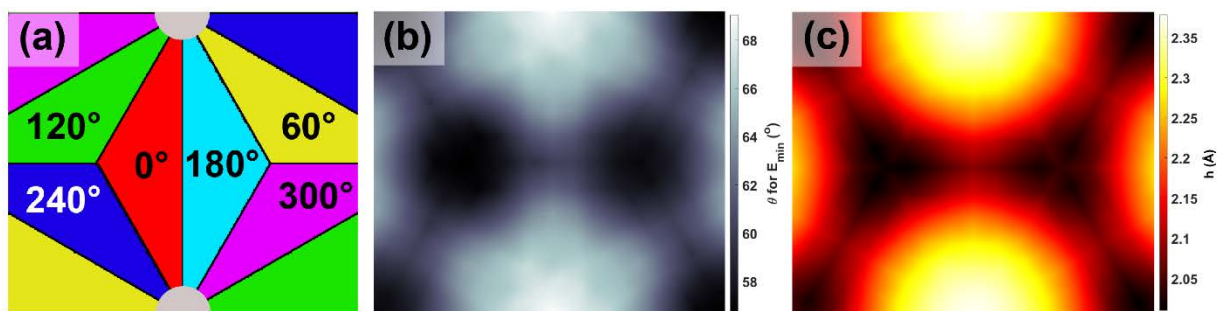


Figure 6.6. The Variation of the Molecular Geometry Corresponding to the Energy Landscape. (a), (b), and (c) shows the variation of  $\phi$ ,  $\theta$ , and  $h$  respectively. Corresponding color bars are given to the right of the figure (b) and (c).

orientation is perpendicular to the line connecting the two edge atoms. The sensitivity of the system energy to the S-C bond orientation (maximum-minimum) is mapped in Figure 6.5c and d, an effect

which is termed the *modulation* for simplicity. The greatest modulation occurs around the bridge site, and is over 500 meV, as will be discussed in more detail later. The weakest modulation occurs at the atop site,  $\sim 2$  meV, which is attributed to the interaction of the methyl group with the surface. The hollow sites have modulation of  $\sim 33$ - $35$  meV. The energy versus S-C bond orientation angle exhibits three energy minima corresponding to the three preferred orientations in the sub-regions surround the hollow site. The path from hollow site to atop traverses a saddle point in modulation. The energy versus S-C bond orientation angle for points along this path exhibit two energy minima corresponding to the two preferred orientations in the sub-regions on either side of the path. These orientation preferences do not hold in the region within the outer rim of the atop moat (gray region in Figure 6.6a). There the modulation is  $\sim 100$  meV with a broad energy minimum for the preferred orientation which is radially toward the atop atom.

We can study the system in more depth by observing the changes along the four paths between the high symmetry sites, bridge-atop, fcc-bridge-hcp, atop-fcc, and atop-hcp. Figure 6.7 shows the system energy along these paths for the minimum energy orientation. Note the approximate symmetry between the bridge-fcc and bridge-hcp paths and also between the atop-fcc and atop-hcp paths. The minima in the fcc region are slightly lower than the analogous minima in the hcp region in contrast to the 3-fold sites which are maxima, with the fcc site slightly higher than the hcp. Although energy is a critical parameter, it does not give the chemical intuition into the bonding of the sulfur to the gold that is sought. A focus on the S atom, the bond-order with the Au atoms, the bonding geometry, and the electron lone pairs will illustrate this better.



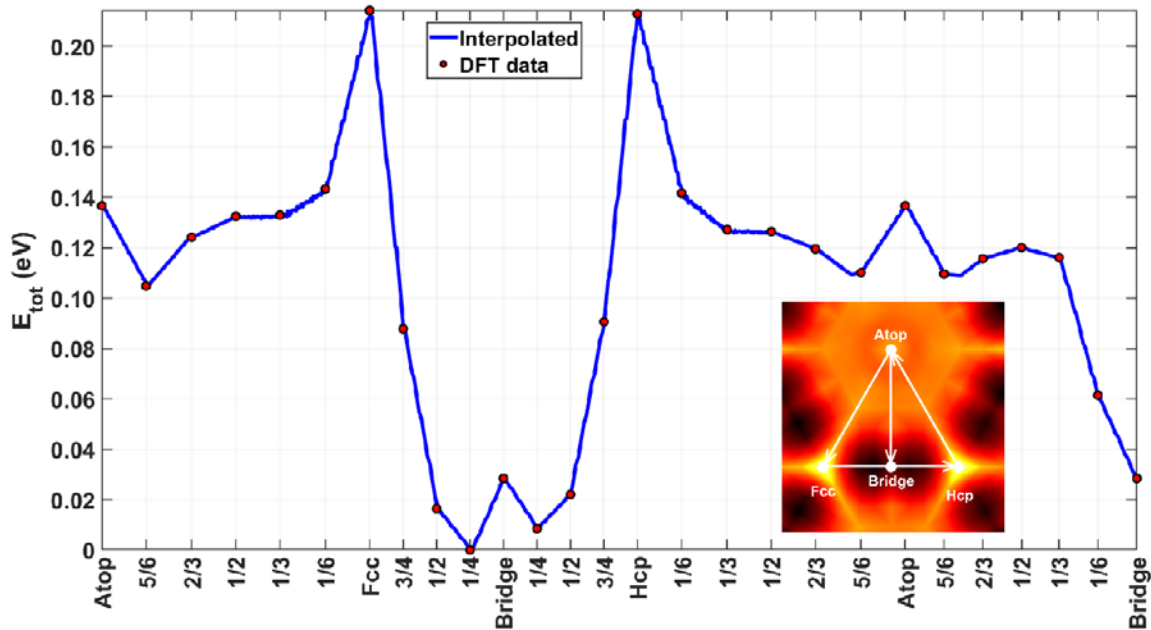


Figure 6.7. Energy Profile Along Four Paths between the High Symmetry Sites Taken from the Energy Landscape. The red dots correspond to the energy values directly taken from the DFT calculation. The blue line is the interpolation between the adsorption sites from the surface in Figure 6.5a.

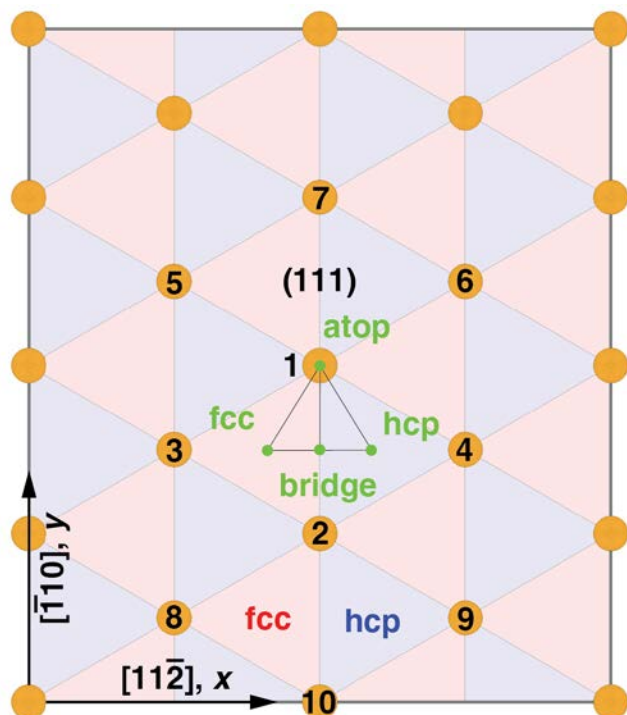


Figure 6.8. Diagram of the Au(111) Surface in the Simulation. The numbering of the Au surface atoms in the discussion shown, as are the specific sites (green) and the paths (black).

The S atom on the bridge-to-atop path transitions from bonding to two Au atoms (bridge, Au<sub>1</sub> and Au<sub>2</sub>) to one (atop, Au<sub>1</sub>). The numbering scheme for the surface Au atoms is shown in Figure 6.8. The bond order (BO) to each bridge site Au atom is shown in Figure 6.9 for three S-C orientations. At the bridge site for the 0° orientation, the BO for each bridge site Au atom is the same (0.61). The DDEC6 calculation also assigns BOs to the other neighboring surface Au atoms, predominately with the two Au atoms on the

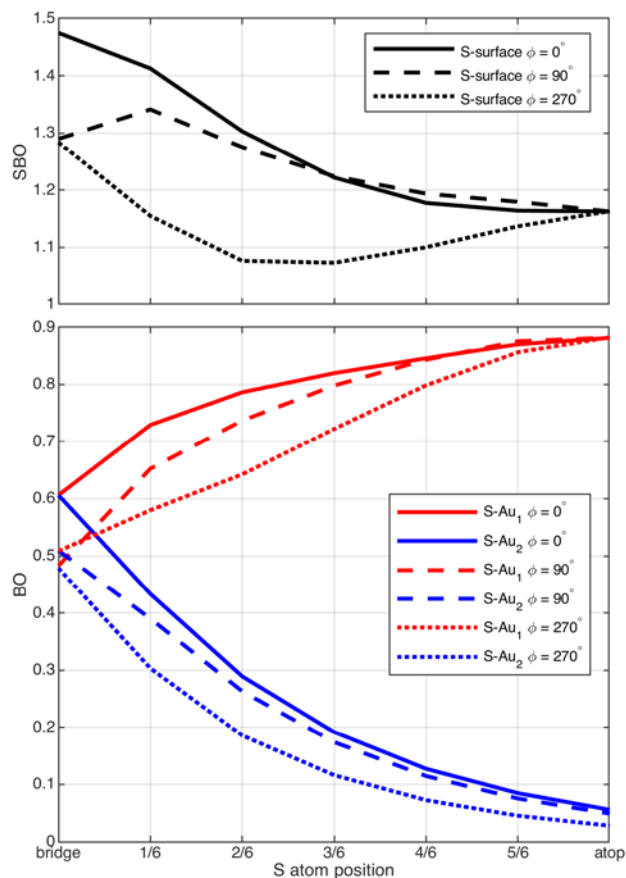


Figure 6.9. The Au-S DDEC6 Bond Orders for Three S-C Azimuthal Angles at Seven Sites from Bridge to Atop. The angles are:  $0^\circ$  (solid),  $90^\circ$  (dashed), and  $270^\circ$  (dotted). Top) The total bond order of sulfur to the Au surface (all Au surface atoms). Bottom) The bond order to each bridge site Au atom.

neighborhood. The changes in the electron lone pairs can be visualized in Figure 6.10. On the bridge site, the lone pairs form a single basin consistent with an ammonia-like pyramidal geometry. On the atop site, the lone pairs form two basins, consistent with a water-like bent geometry. The transition from one to two basins occurs between  $1/6$  (Figure 6.10.b) and  $2/6$  (Figure 6.10.c) leading us to conclude that the bond to the far-bridge atom,  $Au_2$ , effectively breaks at that point.

opposite sides of the fcc and hcp hollow sites,  $Au_3$  and  $Au_4$ , respectively. The total BO of the S atom with the surface Au atoms (SBO) is 1.47, with 0.25 contributed by the Au neighbors. The longer-range contribution is important to appreciate when evaluating how the BO changes as the S atom moves along the path from the bridge to the atop site. Continuing with the  $0^\circ$  orientation on the atop site, the BO with the atop atom,  $Au_1$ , increases to 0.88. The BO with the far-bridge atom,  $Au_2$ , decreases to 0.06 with no obvious discontinuity to suggest bond breaking. However, by  $2/6$  of the way toward the atop site, the BO contribution from  $Au_2$  has fallen to 0.30, only slightly greater than that of the other

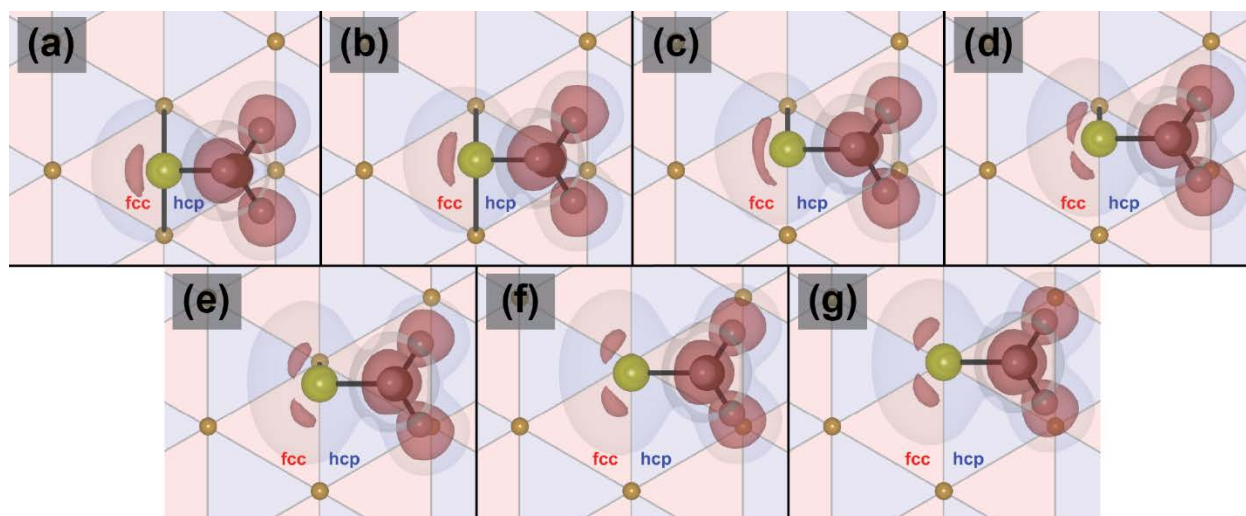


Figure 6.10. The Distribution of the Sulfur Electron Lone Pairs for Seven Different Sulfur Atom Locations from the Bridge to the Atop Site with a  $0^\circ$  S-C Bond Azimuthal Angle. Two ELF isosurfaces are shown. The ball and stick model and the surface are included for orientation. Note the progression from a single lobe on the bridge site to two lobes at the atop site.

The  $90^\circ$  and  $270^\circ$  orientations are at significantly higher energy ( $\sim 450$  meV) compared to the  $0^\circ$  and  $180^\circ$  orientations. Because the S, C, and bridge Au atoms lie in a plane, these orientations do not allow the pyramidal geometry at the bridge site. The BOs with each bridge site Au atoms are 0.48 and 0.51 and the SBO is 1.29, the higher bond order is with the bridge atom that makes the larger Au-S-C bond angle. As the S atom is moved along the path bridge to atop, the BO increases more rapidly for the more favorably oriented  $90^\circ$  orientation, but both reach the same 0.88 BO on the atop site, as expected. Interestingly, on the atop site the BO with Au<sub>2</sub> is dependent on the orientation. It is lowest (0.03) when that bond would make the smallest Au-S-C angle for the  $270^\circ$  orientation and  $\sim 0.06$  for the  $0^\circ$  and  $90^\circ$  orientations. The electron lone pairs (Figure 6.11) show two basins for all positions on this path. In the figure, the mirror symmetry has been used to show the  $270^\circ$  orientation path bridge to the Au<sub>1</sub> atop as the  $90^\circ$  orientation path bridge to the Au<sub>2</sub> atop. This gives a  $90^\circ$  orientation path between the two atop sites through the bridge.

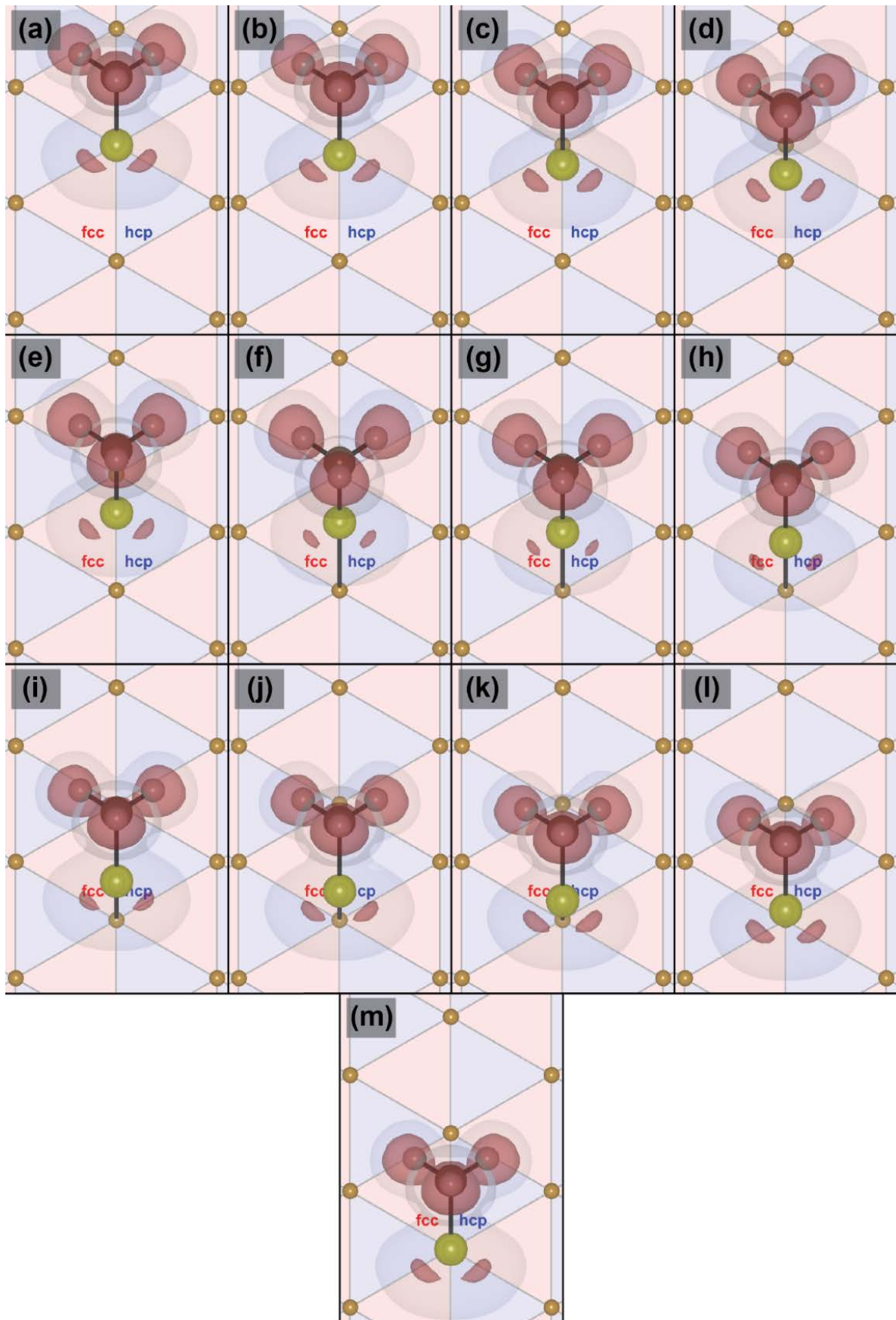


Figure 6.11. The Distribution of the Sulfur Electron Lone Pairs for Fifteen Different Sulfur Atom Locations from One Atop Site to the Other through the Bridge Site with a  $90^\circ$  S-C Bond Azimuthal Angle. These are derived using symmetry from the  $90^\circ$  and  $270^\circ$  S-C bond orientations, the bridge to upper atop site and the bridge to lower atop site, respectively. Two ELF isosurfaces are shown. The ball and stick model and the surface are included for orientation. Note the progression from a single lobe on the bridge site to two lobes at the atop site.

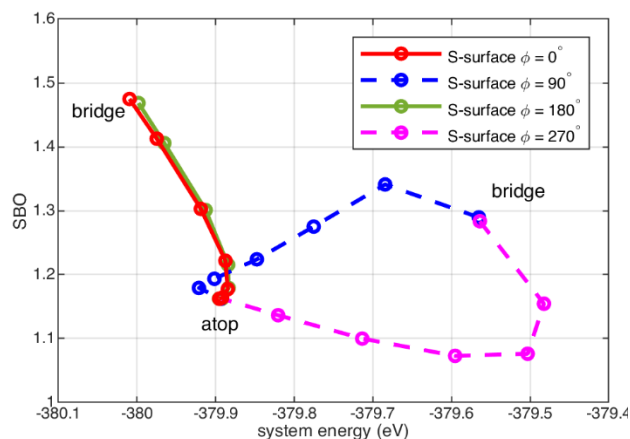


Figure 6.12. The Au-S DDEC6 Bond Orders Versus System Energy for 0°/180° and 90°/270° S-C Azimuthal Angles at Seven Sites from Bridge to Atop.

The relationship between the SBO and the system energy is explored in Figure 6.12 along the bridge-to-atop path for four orientations. The 0° and 180° orientations are used to illustrate the close similarity and the slight asymmetry. The highest SBO and lowest energy in this set is achieved at the bridge site for the 0° orientation, with 180° a close second.

The atop moat is more favorable than the atop site for 90°. The highest energy is for 270° 1/6 offset from the bridge site. The lowest SBO (1.07) is also along that path. The 90° path has its highest SBO (1.34) 1/6 offset from the bridge site. Note that the maxima in SBO do not correlate with the energy minima. As atoms are brought closer together, the BO increases monotonically. In contrast, the system energy may display a minimum (balance of attraction and repulsion) before the eventual energy increase (net repulsion) at small distances. In this study, the system was relaxed at each position with a set of constraints that can leave substantial forces between the S atom and the surface Au atoms. It may be postulated that the higher SBO with higher system energy is a consequence of the S and Au atoms being closer than in the fully optimized structure. That is especially evident on the fcc-bridge-hcp path which is discussed next.



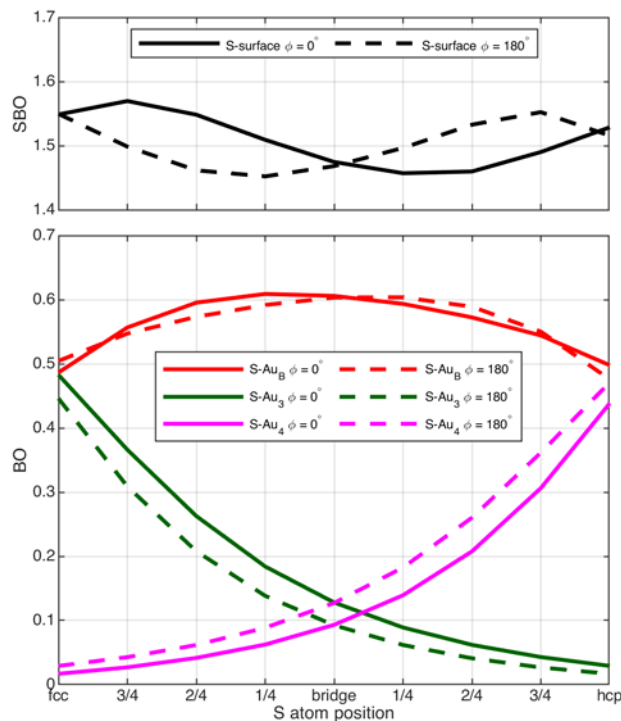


Figure 6.13. The Au-S DDEC6 Bond Orders for  $0^\circ$  and  $180^\circ$  S-C Azimuthal Angles at Nine Sites Along the Path fcc to Bridge to hcp. The two bridge site Au atoms are symmetry identical therefore have identical curves, denoted  $Au_B$ . Top) The total bond order of sulfur to the Au surface (all Au surface atoms). Bottom) The BOs of the bridge site Au atoms and the two atoms in the adjacent hollow sites.

atom. The BO with each bridge atom is maximum (0.61) at  $1/4$  fcc for  $0^\circ$  and (0.60) at  $1/4$  hcp for  $180^\circ$ . At the bridge site the BO with each bridge site atom is 0.606 for  $0^\circ$  and 0.0603 for  $180^\circ$ .

There is a substantial BO contribution from the neighboring hollow site atoms for each orientation, 0.13 and 0.09, with the higher BO corresponding the Au atom opposite the methyl group. For the hcp site the pattern is the same as the fcc, interchanging the orientations and

Now consider the fcc-bridge-hcp path for the  $0^\circ$  and  $180^\circ$  orientations, which includes the energy maxima and minima on the surface. The BOs and SBOs are shown in Figure 6.13, which illustrate the approximate mirror symmetry through the bridge plane. The BOs for the two bridge site atoms ( $Au_1$  and  $Au_2$ ) are identical, as expected by symmetry, therefore the BO of only one is shown and designated as  $Au_B$ . Starting with the fcc site, for  $0^\circ$  the BO with each bridge atom is 0.49 and slightly lower 0.48 for the other hollow site atom ( $Au_3$ ). For the  $180^\circ$  orientation the BO with the hollow site atoms is more asymmetric, 0.55 with each bridge atom and 0.45 for the other hollow site

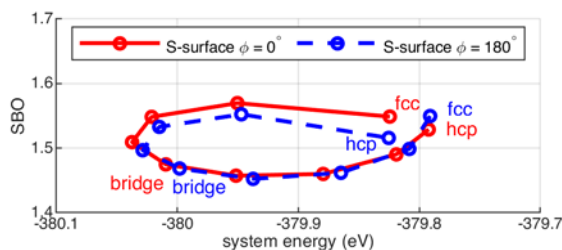


Figure 6.14. The Au-S DDEC6 Bond Orders Versus System Energy for  $0^\circ$  and  $180^\circ$  S-C Azimuthal Angles at Nine Sites Along the Path fcc to Bridge to hcp.

with the BOs slightly decreased. For  $180^\circ$  the BO to each  $Au_B$  is 0.48 and 0.47 to  $Au_4$ , and for  $0^\circ$ , 0.50 and 0.44, respectively. The SBO is maximum at  $\frac{3}{4}$  fcc for  $0^\circ$  and  $\frac{3}{4}$  hcp for  $180^\circ$ . It is interesting to note that the SBO is minimum at  $\frac{1}{4}$  hcp for  $0^\circ$  and  $\frac{1}{4}$  fcc for  $180^\circ$ . The SBO versus system energy graph shows the fcc-hcp paths form open loops with the  $0^\circ$  and  $180^\circ$  in opposite directions, counterclockwise and clockwise, respectively (Figure 6.14). The  $\frac{1}{4}$  fcc  $0^\circ$  and  $\frac{1}{4}$  hcp  $180^\circ$  minimize the system energy but do not maximize the SBO. The basin of the electron lone pairs is deepest near the bridge site (Figure 6.15 for  $\varphi=0^\circ$  and 6.16 for  $\varphi=180^\circ$ ). The coordination geometry of the S atom on the fcc-hcp path, measured via the Au-S-C bond angles (Figure 6.17),

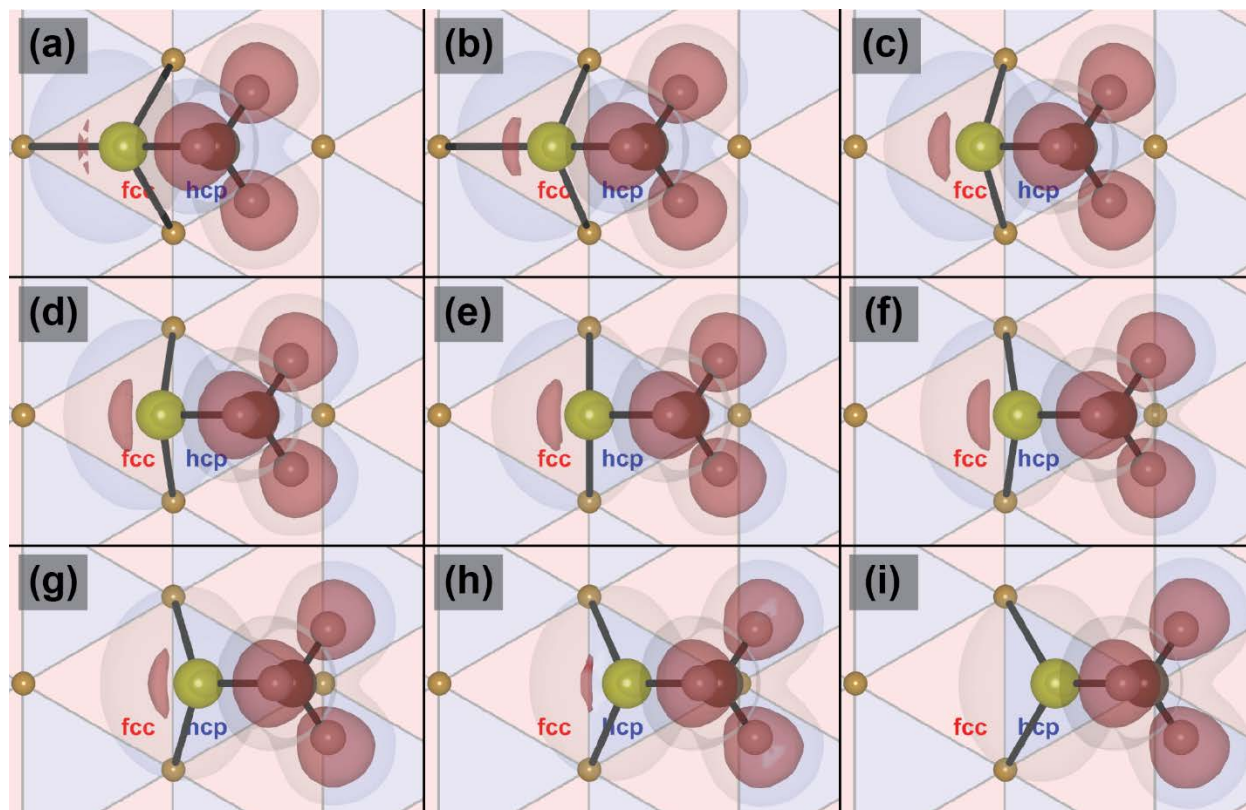


Figure 6.15. The Distribution of the Sulfur Electron Lone Pairs at Nine Sites Along the Path fcc to Bridge to hcp with a  $0^\circ$  S-C Bond Azimuthal Angle. Two ELF isosurfaces are shown. The ball and stick model and the surface are included for orientation. Note the basin for the electron lone pairs is shallow on the hollow sites and deepest in the vicinity of the bridge site.



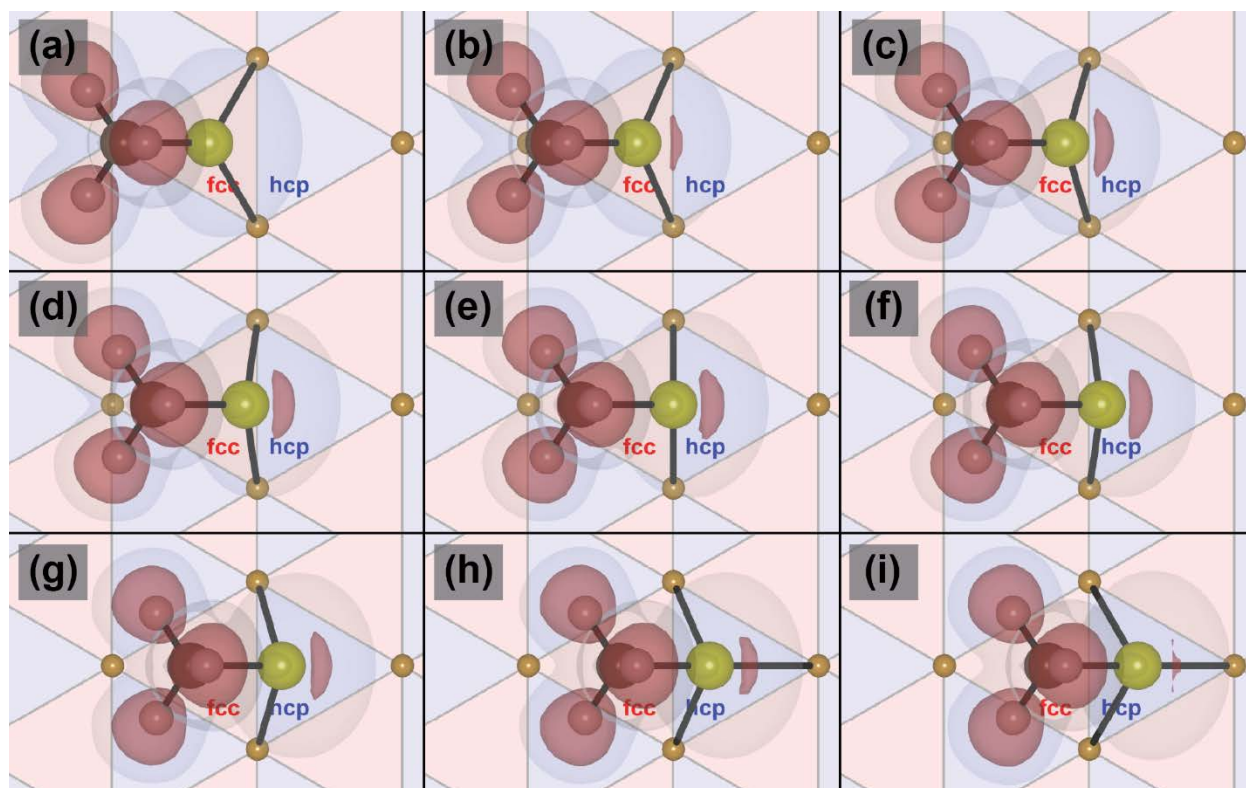


Figure 6.16. The Distribution of the Sulfur Electron Lone Pairs at Nine Sites Along the Path fcc to Bridge to hcp with a  $180^\circ$  S-C Bond Azimuthal Angle. Two ELF isosurfaces are shown. The ball and stick model and the surface are included for orientation. Note the basin for the electron lone pairs is shallow on the hollow sites and deepest in the vicinity of the bridge site.

is closest to the tetrahedral angle for the minimum energy structures at  $\frac{1}{4}$  fcc and  $\frac{1}{4}$  hcp. The Au-S-Au is also the largest at these positions at  $\sim 70^\circ$ , but is constrained by not relaxing the Au(111) surface. The respective angles are also shown (open symbols) for the energy minimum structures relaxed with no constraints on the adsorbate and the top three Au layers. That allows the Au-S-Au angle to open up to  $\sim 80^\circ$  with the Au-S-C angle remaining very close to the tetrahedral angle.

The underlying cause of the asymmetry between the  $\frac{1}{4}$  fcc  $0^\circ$  and  $\frac{1}{4}$  hcp  $180^\circ$  can be visualized with a charge density difference (CDD) study (Figure 6.18). Although the effect is small, it is unmistakable. Bonding to the Au<sub>1</sub> and Au<sub>2</sub> bridge site atoms leads to participation of the 2<sup>nd</sup> layer Au atoms bonded to those atoms. The interaction is directional, propagating into the 3<sup>rd</sup> layer along  $\langle 110 \rangle$  columns (the nearest neighbor directions, shown in Figure 6.19). In order to visualize this

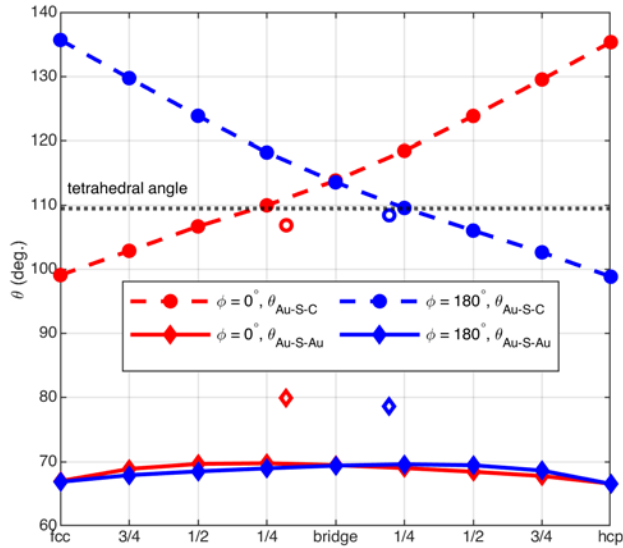


Figure 6.17. The Au-S-C and Au-S-Au Bond Angles for  $0^\circ$  and  $180^\circ$  S-C Azimuthal Angles at Nine Sites Along the Path fcc to Bridge to hcp. The angle is an indication of the coordination geometry of the sulfur atom. The tetrahedral angle is achieved just off the bridge site,  $1/4$  toward the fcc for  $0^\circ$  and  $1/4$  toward hcp for  $180^\circ$ . The bond angle for the fully relaxed structures, bridge fcc and bridge-hcp, using the corresponding open symbols (see ref 3).

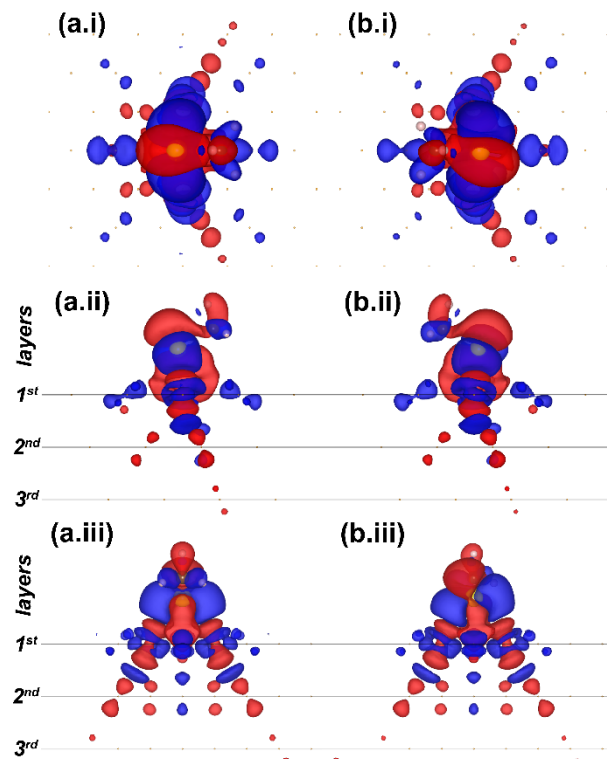


Figure 6.18 CDD for  $1/4$  fcc ( $\phi = 0^\circ$ ) and  $1/4$  hcp ( $\phi = 180^\circ$ ). a) and b) are for  $1/4$  fcc and  $1/4$  hcp, respectively. Note the directional bonding propagation into the sublayer of the Au(111) crystal along the  $\langle 110 \rangle$  direction.

better, consider that each surface Au atom sits in

an fcc hollow of the  $2^{\text{nd}}$  Au layer. Each bridge site Au atom then has three  $\langle 110 \rangle$  column directions into the surface, one through each of its  $2^{\text{nd}}$  layer nearest neighbors. The strongest interaction is along the two  $\langle 110 \rangle$  columns starting from the fcc hollow site through the bridge site atoms (type 1 column). The next strongest is along the  $\langle 110 \rangle$  columns with the  $2^{\text{nd}}$  layer atoms on either side of the surface fcc hollow (type 2 column). The remaining  $\langle 110 \rangle$  columns pass through the  $2^{\text{nd}}$  layer atom below the hcp hollow site (type 3 column). It is particularly interesting that interaction into the  $3^{\text{rd}}$  layer extends along the type 1 columns in contrast to percolation through nearest neighbors which would spread the charge density uniformly. It may be hypothesized that the CDD

is propagating along  $sd^5$  hybrid orbitals in the Au. The directional interaction extends to the sulfur, which at the  $\frac{1}{4}$  fcc site aligns best with the type 1 columns compared to the more offset  $\frac{1}{4}$  hcp site. This is a smaller effect than the methyl-group orientation which directly effects the directional bonding on the S atom. The electron density is decreased by the  $SCH_3$  adsorption in the type 1 and 2 columns, whereas the electron density increases on the 1<sup>st</sup> layer nearest neighbor Au atoms and the 2<sup>nd</sup> layer atom below the hcp hollow site. The type 3 column does not appear to be involved, perhaps because it is the most misaligned with the Au-S bond. Interestingly the type 3 columns emanating from both bridge site Au atoms also intersect on this site. The 2<sup>nd</sup> layer Au atom (under the hcp hollow site) is also close to the S atom. More direct interaction with the S atom might overshadow any propagation of CDD along these columns and be responsible for the different behavior of this 2<sup>nd</sup> layer Au atom. The effect of the azimuthal angle of the S-C bond on the directional bonding at the bridge site is shown in Figure 6.20. The sensitivity of the CDD in the sublayers is striking. The  $90^\circ$  ( $270^\circ$ ) orientation effectively turns off the interaction along the type

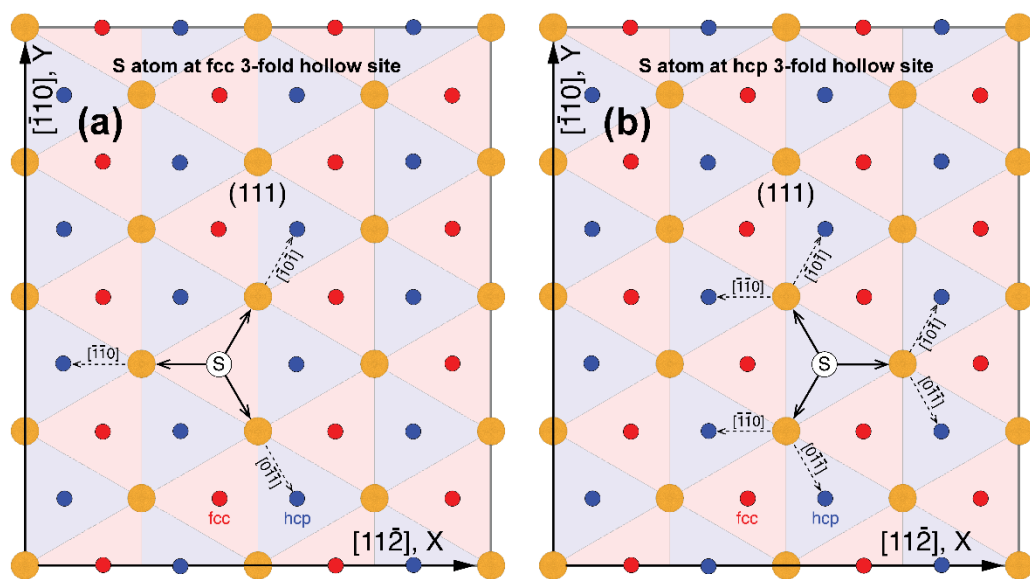


Figure 6.19 Nearest-neighbor Au Bond Directions Along the  $\langle 110 \rangle$  Columns. Bond propagation for an adsorbate at the fcc (a) and the hcp (b) 3-fold hollow sites are shown. The bridge site is denoted by the S atom.

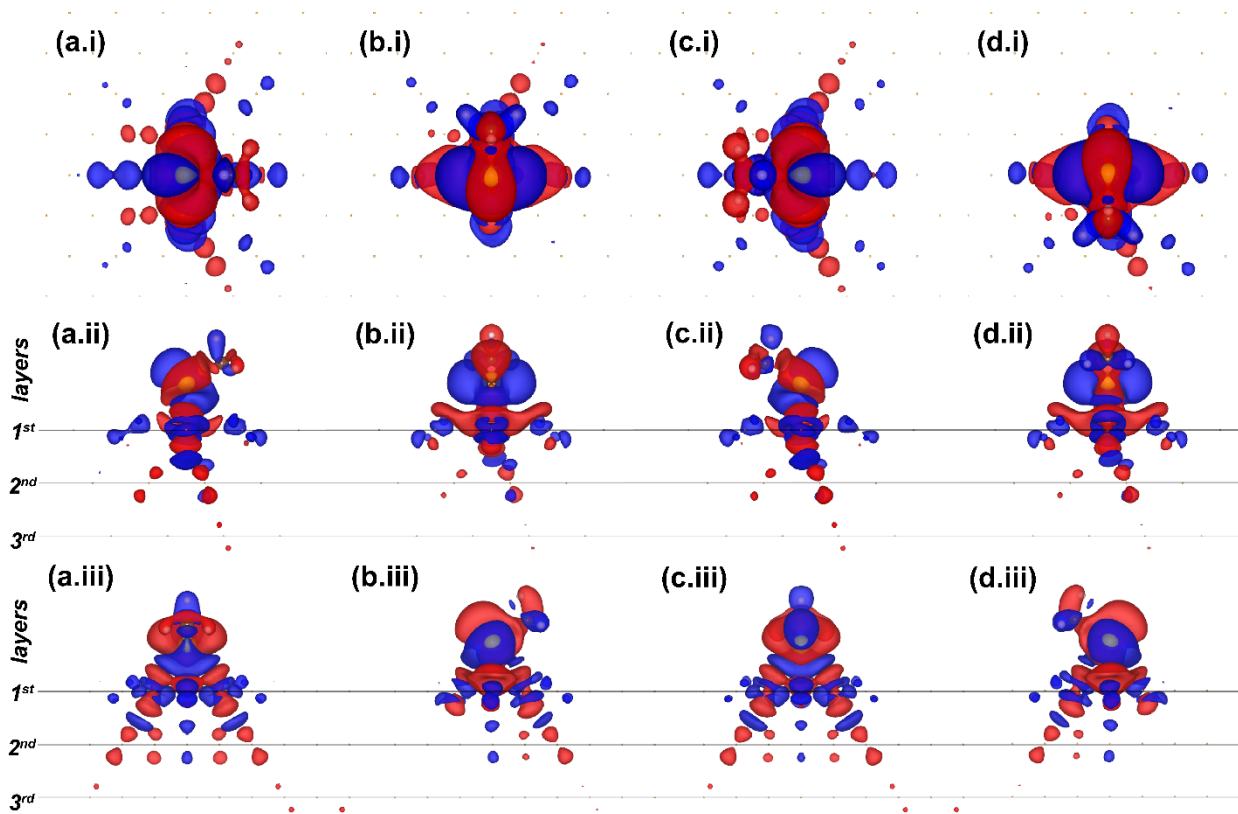


Figure 6.20. CDD at the Bridge Site for Four Orientations of the S-C Bond. ( $a = 0^\circ$ ,  $b = 90^\circ$ ,  $c = 180^\circ$ , and  $d = 270^\circ$ ) The first row (i) is the top-down view along  $[\bar{1}\bar{1}\bar{1}]$ . Side-views along  $[\bar{1}\bar{1}0]$  and  $[\bar{1}\bar{1}2]$  (See Figure 6.8 for the crystal directions) are shown in the second (ii) and the third (iii) rows, respectively. The complete set of CDD for all azimuthal angles at the bridge site is given in Appendix E.

1 and 2 columns for the  $Au_2$  ( $Au_1$ ) atom, which indicates there is a very different interaction between the S atom and these two Au atoms. This was at first surprising because the BOs with the bridge site Au atoms are nearly identical, for the  $90^\circ$  orientation the BOs with  $Au_1$  and  $Au_2$  are 0.48 and 0.51. However, the forces on the two Au atoms are very different. Although the forces these constrained simulations cannot be assigned directly to forces between specific atoms, comparison of the forces between these closely related structures does provide insight. The force on  $Au_2$  is approximately four times the force on  $Au_1$  and is directed away from the S atom (repulsive) and for  $Au_1$  the force is away for the surface (attractive). The force on the S atom is approximately parallel to the surface toward the  $Au_1$  atop site. Due to the constraints (the Au atoms fixed and the

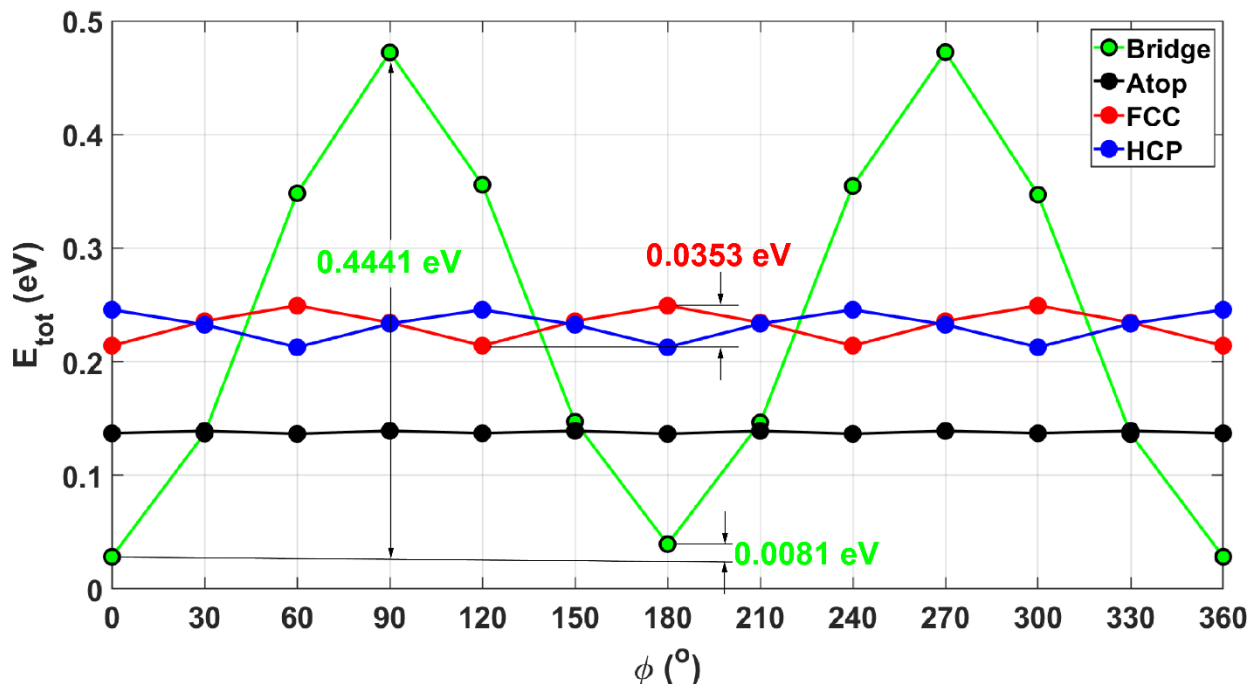


Figure 6.21. Variation of the Total System Energy with respect to the Azimuthal Angle of the S-C Bond for Four High Symmetry Sites. Bridge site has by far the strongest dependence.

S atom only allowed to move in z) these forces represent a balance of the attractive force to  $Au_1$  and the repulsive force with  $Au_2$ . The forces on the S,  $Au_1$ , and  $Au_2$  atoms interchange for  $270^\circ$ . These forces of course reflect the system energy gradients evident in Figure 6.12 for these two orientations on the bridge-atop path. The electronic coupling to the sub-surface Au atoms is weak through the bridge site Au atom with the repulsive Au-S interaction.

Finally, the azimuthal orientation dependence at the bridge, atop, and the fcc and hcp hollow sites will be considered. Figure 6.21 shows the energy modulation for these four sites. The energy modulation is the greatest at the bridge site and the smallest for the atop site. The symmetry of the energy modulation is consistent with that of the surface sites, approximately  $C_2$  for the bridge,  $C_3$  for the hollow sites, and approximately  $C_6$  for the atop site. The tetrahedral coordination geometry of the S atom at the bridge site (Au-S-C bond angle, Figure 6.22) minimizes the energy of the system. The energy minima for the hollow sites occurs when the S-C bond is oriented between

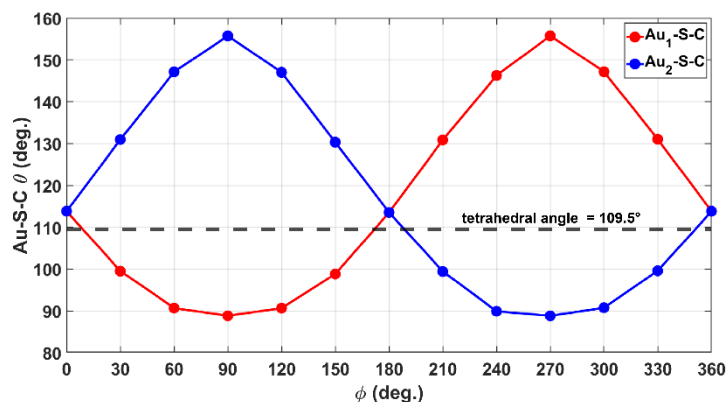


Figure 6.22 The Au-S-C Bond Angles at the Bridge Site for Twelve Different Azimuthal Angles. The  $0^\circ$  and  $180^\circ$  orientations achieve the closest to the tetrahedral angle.

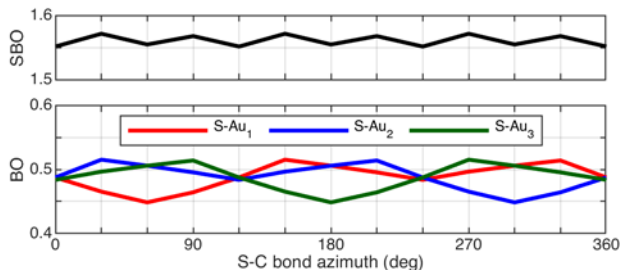


Figure 6.23. The Au-S DDEC6 Bond Orders for the Sulfur Atom on the fcc Site for Twelve Different S-C Bond Azimuthal Angles. Top) The total bond order of sulfur to the Au surface (all Au surface atoms). Bottom) The bond order to each bridge site Au atom and the three atoms in the adjacent hollow sites.

The orientational dependence of the BO contributed by the atop nearest neighbors is qualitatively the same as for the three atoms of the fcc and hcp hollow sites, which leads to the conclusion that the behavior is a property of the directional S atom bonding with the surface. In all three sites, two minima are displayed. The

two of the three hollow site atoms. The SBO modulates  $\sim 0.03$  around 1.56 and 1.53 for the fcc and hcp hollow sites, respectively (Figures 6.23 and 6.24). The BOs for the fcc and hcp hollow site atoms modulate  $\sim 0.06$  for maxima/minima at  $0.52/0.45$  and  $0.51/0.44$ , respectively. The energy

modulation at the atop site is the smallest. The SBO and the BO with the atop Au atom are 1.16 and 0.88, respectively, both modulating  $\sim 0.001$  (Figure 6.25). The six nearest neighbor Au atoms surrounding the atop site contribute a total of 0.28 to the SBO, with maxima/minima of  $0.06/0.03$ , respectively.

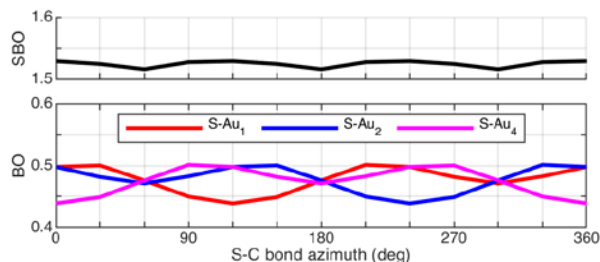


Figure 6.24. The Au-S DDEC6 Bond Orders for the Sulfur Atom on the hcp site for Twelve Different S-C Bond Azimuthal Angles. Top) The total bond order of sulfur to the Au surface (all Au surface atoms). Bottom) The bond order to each bridge site Au atom and the three atoms in the adjacent hollow sites.



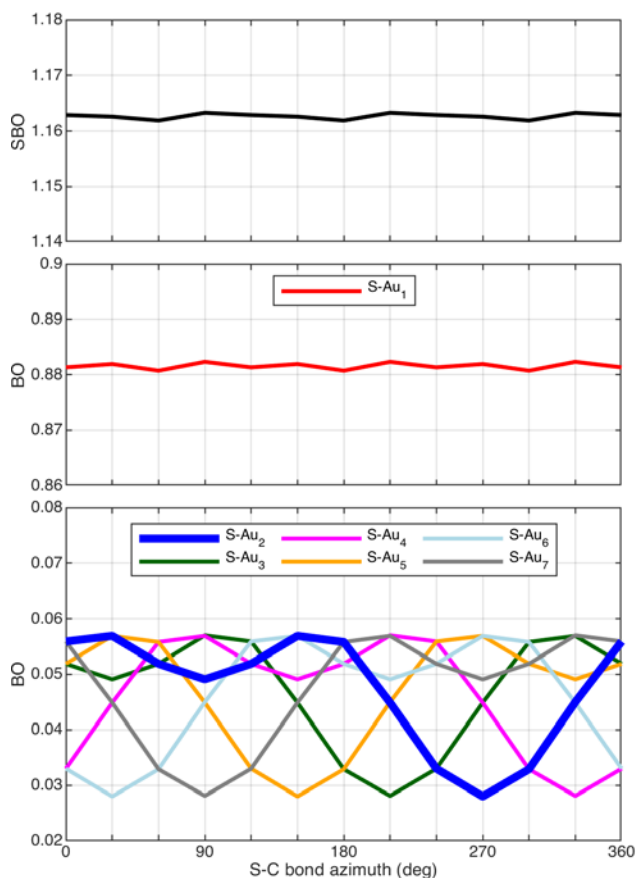


Figure 6.25. The Au-S DDEC6 Bond Orders for the Sulfur Atom on the Atop Site for Twelve Different S-C Bond Azimuthal Angles. Top) The total bond order of sulfur to the Au surface (all Au surface atoms). Middle) The bond order to the atop Au atom, Au<sub>1</sub>. Bottom) The bond order to each of the 6 Au atoms surrounding the atop atom.

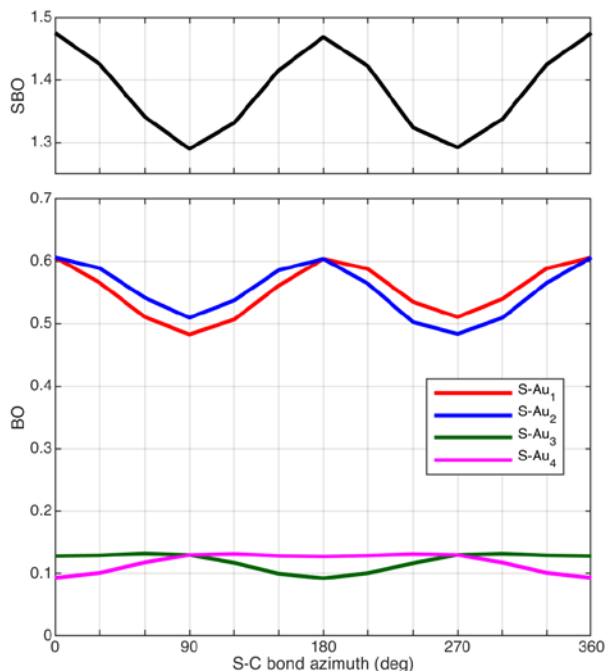


Figure 6.26. The Au-S DDEC6 Bond Orders for the Sulfur Atom on the Bridge Site for Twelve Different S-C Bond Azimuthal Angles. Top) The total bond order of sulfur to the Au surface (all Au surface atoms). Bottom) The bond order to each bridge site Au atom and the two atoms in the adjacent hollow sites.

deepest occurs when the S-C bond is oriented toward the Au atom. The secondary minimum occurs when oriented away from the Au atom.

The maxima occur 60° on either side of the secondary minimum for the atop site and 90° on either side for the hollow sites. The BO maxima for the atop neighboring atoms occur when a lobe of the S atom electron lone pairs is oriented over those atoms. A similar effect is likely for the hollow sites, but the basin of the lone pairs is more elongated in azimuth when the S atom is on those sites.

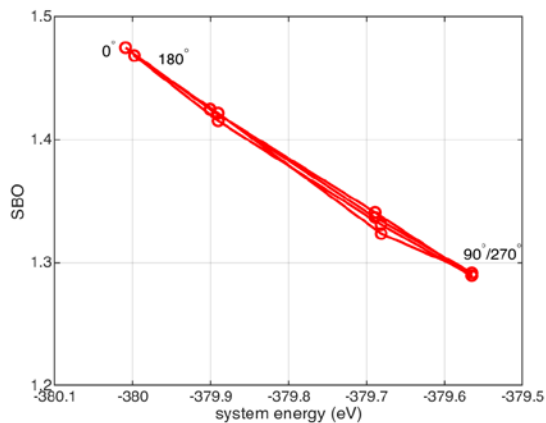


Figure 6.27. The Au-S DDEC6 Bond Orders Versus System Energy for the Sulfur Atom on the Bridge Site for Twelve Different S-C Bond Azimuthal Angles.

The energy modulation on the bridge site is largest at 444 meV, which exhibits both the energy minima and maxima for the four sites. The main features of the orientation dependence of the SBO and BOs each bridge site atom ( $Au_1$  and  $Au_2$ ), the maxima, minima, and their asymmetry, have already been discussed, but can be better appreciated from Figure 6.26. The orientational dependence of the BO with the Au atoms on the far side of the fcc and hcp hollow sites,  $Au_3$  and  $Au_4$ , respectively, follow the same qualitative behavior as the BO with the atop nearest neighbors and the hollow site atoms already discussed. The primary minima occur with the S-C bond oriented toward the Au atom neighbor and a BO of  $\sim 0.09$ . The secondary minima are very shallow and nearly the same BO as the maxima at  $\sim 0.13$ . The maxima occur  $60^\circ$  on either side of the secondary minima. The near absence of the secondary minimum is likely due to the interaction of the ammonia-like lone pair of the bridge-bonded S atom that is oriented toward these atoms at their secondary minima ( $180^\circ$  for  $Au_3$  and  $0^\circ$  for  $Au_4$ ). The SBO-energy relationship is approximately linear for a full rotation of the S-C bond orientation, cycling over the SBO-energy path twice (Figure 6.27). The topology of the lone pairs on the bridge site is dependent on the S-C bond orientation (Figure 6.28). The ELF study shows a single basin for the orientational regions  $330^\circ$ - $0^\circ$ - $30^\circ$  and  $150^\circ$ - $180^\circ$ - $210^\circ$ . Two basins are observed in the regions  $60^\circ$ - $90^\circ$ - $120^\circ$  and  $240^\circ$ - $270^\circ$ - $300^\circ$ . Interestingly, total the BO with the bridge site Au atoms only drops from 1.2 to 1.0 as the orientation changes from  $0^\circ$  to  $90^\circ$ , yet the system energy increases by 444 meV indicating that



the planar geometry at  $90^\circ$  is highly unfavorable. The appearance of two lone pairs is indication that the S atom is attempting to maintain  $sp^3$  hybridization under unfavorable circumstances. Two lone pairs implies that the S is bonding primarily to the Au surface via a single  $sp^3$  bonding orbital. We assign that bond to  $Au_1$  ( $90^\circ$ ) because the electronic interaction appears stronger based on the directional propagation of the charge differences into the sub-surface Au layers (CDD).

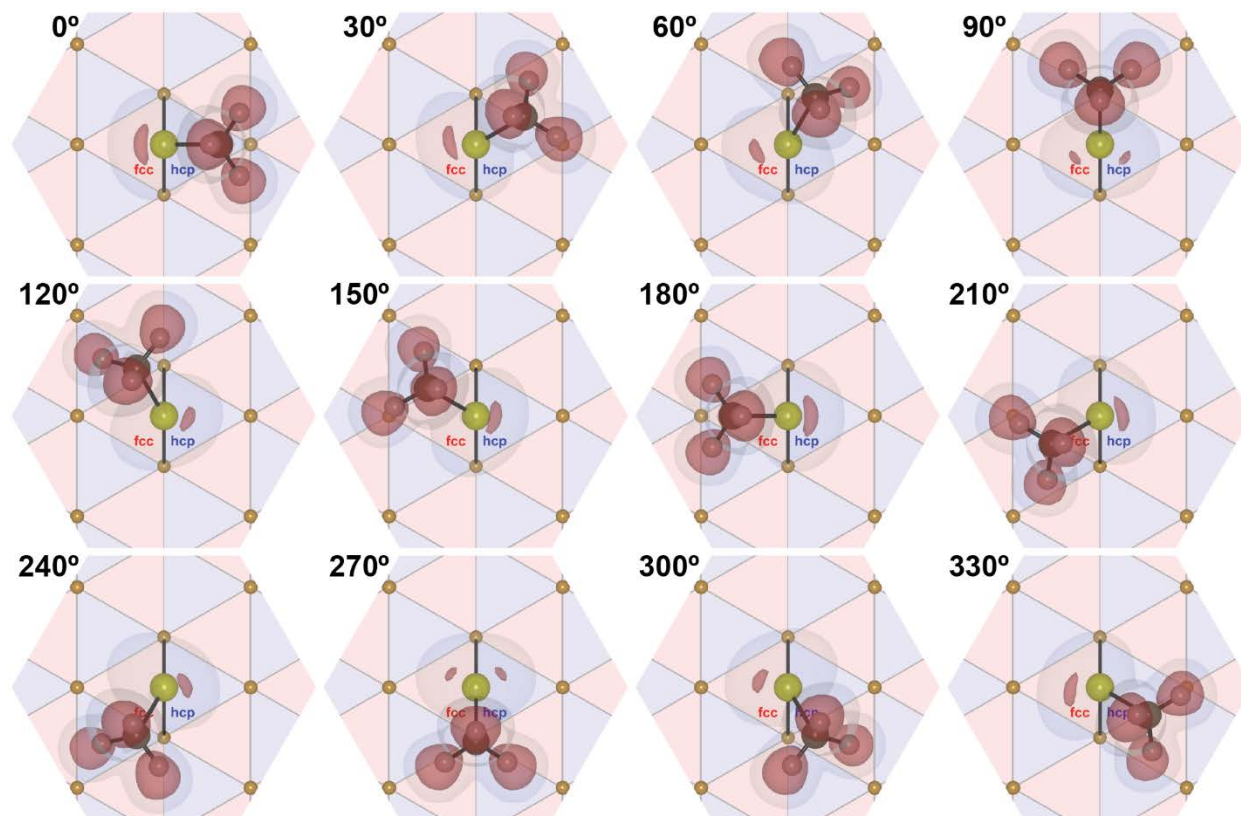


Figure 6.28. The Distribution of the Sulfur Electron Lone Pairs for the Sulfur Atom on the Bridge Site for Twelve Different S-C Bond Azimuthal Angles. Two ELF isosurfaces are shown. The ball and stick model and the surface are included for orientation. Note the progression from a single lobe for angles  $0^\circ$  and  $180^\circ$  to two lobes at  $90^\circ$  and  $270^\circ$ .

## 6.5 Conclusions

The adsorption site geometry of the  $SCH_3$  on Au(111) is driven by the propensity of the S atom to adopt  $sp^3$ -related coordination geometries. In particular the strong azimuthal orientation

dependence of the S-C bond at the bridge-fcc and bridge-hcp are a manifestation of that preference. ELF has been used to demonstrate that the topology of the electron lone pairs on the S atom are consistent with the apparent surface-bonding geometry. DDEC6 bond order analysis shows that the influence of the bonding to the Au surface atoms is strongly dependent on the SCH<sub>3</sub> orientation. The fcc-hcp asymmetry of the bridge site and the bridge-fcc and bridge-hcp path is due to Au bonding with the sub-surface layers through Au sd<sup>5</sup> hybrid orbitals along <110> atomic columns emanating from the surface Au atoms with the principle S-Au adsorbate bonds.

## 6.6 References

1. Nuzzo, R. G.; Allara, D. L., Adsorption of Bifunctional Organic Disulfides on Gold Surfaces. *J. Am. Chem. Soc.* **1983**, *105* (13), 4481-4483.
2. Bain, C. D.; Biebuyck, H. A.; Whitesides, G. M., Comparison of Self-assembled Monolayers on Gold: Coadsorption of Thiols and Disulfides. *Langmuir* **1989**, *5* (3), 723-727.
3. Bhattacharya, S.; Speyer, G.; Ferry, D. K.; Bumm, L. A., A Comprehensive Study of the Bridge Site and Substrate Relaxation Asymmetry for Methanethiol Adsorption on Au(111) at Low Coverage. *ACS Omega* **2020**, *5* (33), 20874-20881.
4. Hasan, A.; Pandey, L. M., 6 - Self-assembled Monolayers in Biomaterials. In *Nanobiomaterials*, Narayan, R., Ed. Woodhead Publishing: 2018; pp 137-178.
5. Love, J. C.; Estroff, L. A.; Kriebel, J. K.; Nuzzo, R. G.; Whitesides, G. M., Self-Assembled Monolayers of Thiolates on Metals as a Form of Nanotechnology. *Chem. Rev.* **2005**, *105* (4), 1103-1170.
6. Magnussen, O. M.; Vogt, M. R.; Scherer, J.; Behm, R. J., Double-Layer Structure, Corrosion and Corrosion Inhibition of Copper in Aqueous Solution. *Appl. Phys. A* **1998**, *66* (1), S447-S451.
7. Casalini, S.; Bortolotti, C. A.; Leonardi, F.; Biscarini, F., Self-Assembled Monolayers in Organic Electronics. *Chem. Soc. Rev.* **2017**, *46* (1), 40-71.
8. Fujihira, M.; Tani, Y.; Furugori, M.; Akiba, U.; Okabe, Y., Chemical Force Microscopy of Self-Assembled Monolayers on Sputtered Gold Films Patterned by Phase Separation. *Ultramicroscopy* **2001**, *86* (1), 63-73.

9. Ta-Wei Li, I. C., and Yu-Tai Tao, Relationship between Packing Structure and Headgroups of Self-Assembled Monolayers on Au(111): Bridging Experimental Observations through Computer Simulations. *J. Phys. Chem. B* **1998**, *102* (16), 12.
10. Hautman, J.; Klein, M. L., Simulation of a Monolayer of Alkyl Thiol Chains. *J. Chem. Phys.* **1989**, *91* (8), 4994-5001.
11. Bhattacharya, S.; Yothers, M. P.; Huang, L.; Bumm, L. A., Interaction of the  $(2\sqrt{3} \times 3)$ rect. Adsorption-Site Basis and Alkyl-Chain Close Packing in Alkanethiol Self-Assembled Monolayers on Au(111): A Molecular Dynamics Study of Alkyl-Chain Conformation. *ACS Omega* **2020**, *5* (23), 13802-13812.
12. Maksymovych, P.; Sorescu, D. C.; Yates, J. T., Methanethiolate Adsorption Site on Au(111): A Combined STM/DFT Study at the Single-Molecule Level. *J. Phys. Chem B* **2006**, *110* (42), 21161-21167.
13. Franke, A.; Pehlke, E., Adsorption and Diffusion of SCH<sub>3</sub> Radicals and Au(SCH<sub>3</sub>)<sub>2</sub> Complexes on the Unreconstructed Au(111) Surface in the Submonolayer Coverage Regime. *Phys. Rev. B* **2009**, *79* (23), 235441.
14. Yourdshahyan, Y.; Rappe, A. M., Structure and Energetics of Alkanethiol Adsorption on the Au(111) Surface. *J. Chem. Phys.* **2002**, *117* (2), 825-833.
15. Cao, Y.; Ge, Q.; Dyer, D. J.; Wang, L., Steric Effects on the Adsorption of Alkylthiolate Self-Assembled Monolayers on Au (111). *J. Phys. Chem. B* **2003**, *1107* (16), 3803-3807.
16. Gottschalck, J.; Hammer, B., A Density Functional Theory Study of the Adsorption of Sulfur, Mercapto, and Methylthiolate on Au(111). *J. Chem. Phys.* **2002**, *116* (2), 784-790.
17. Ciriaco, F.; Mavelli, F.; Cassidei, L., Benchmark Calculations of Density Functionals for Organothiol Adsorption on Gold Surfaces. *Comput Theor Chem.* **2013**, *1009*, 60-69.
18. Akihiro, N.; Yoshitada, M., Adsorption States of Methylthiolate on the Au(111) Surface. *J. Phys.: Condens. Matter* **2007**, *19* (36), 365245.
19. Mete, E.; Yortanl, M.; Dansman, M. F., A van der Waals DFT Study of Chain Length Dependence of Alkanethiol Adsorption on Au(111): Physisorption vs. Chemisorption. *Phys. Chem. Chem. Phys.* **2017**, *19* (21), 13756-13766.
20. Cometto, F. P.; Paredes-Olivera, P.; Macagno, V. A.; Patrino, E. M., Density Functional Theory Study of the Adsorption of Alkanethiols on Cu(111), Ag(111), and Au(111) in the Low and High Coverage Regimes. *J. Phys. Chem. B* **2005**, *109* (46), 21737-21748.
21. Grönbeck, H.; Häkkinen, H., Polymerization at the Alkylthiolate–Au(111) Interface. *J. Phys. Chem. B* **2007**, *111* (13), 3325-3327.

22. Nadler, R.; Sánchez-de-Armas, R.; Sanz, J. F., Coverage and Charge Dependent Adsorption of Butanethiol on the Au(111) Surface: A Density Functional Theory Study. *Comput Theor Chem.* **2011**, *975* (1), 116-121.
23. Kresse, G.; Furthmüller, J., Efficiency of ab-initio Total Energy Calculations for Metals and Semiconductors Using a Plane-wave Basis Set. *Comput. Mater. Sci.* **1996**, *6* (1), 15-50.
24. Kresse, G.; Joubert, D., From Ultrasoft Pseudopotentials to the Projector Augmented-wave Method. *Phys. Rev. B* **1999**, *59* (3), 1758-1775.
25. Blöchl, P. E., Projector Augmented-wave Method. *Phys. Rev. B* **1994**, *50* (24), 17953-17979.
26. Perdew, J. P.; Burke, K.; Ernzerhof, M., Generalized Gradient Approximation Made Simple. *Phys. Rev. Lett.* **1996**, *77* (18), 3865-3868.
27. Gautier, S.; Steinmann, S. N.; Michel, C.; Fleurat-Lessard, P.; Sautet, P., Molecular Adsorption at Pt(111). How Accurate are DFT Functionals? *Phys. Chem. Chem. Phys.* **2015**, *17* (43), 28921-28930.
28. Yuan, D.; Liao, H.; Hu, W., Assessment of van der Waals Inclusive Density Functional Theory Methods for Adsorption and Selective Dehydrogenation of Formic Acid on Pt(111) Surface. *Phys. Chem. Chem. Phys.* **2019**, *21* (37), 21049-21056.
29. Grimme, S.; Antony, J.; Ehrlich, S.; Krieg, H., A Consistent and Accurate ab initio Parametrization of Density Functional Dispersion Correction (DFT-D) for the 94 Elements H-Pu. *J. Chem. Phys.* **2010**, *132* (15), 154104.
30. Savin, A.; Nesper, R.; Wengert, S.; Fässler, T. F., ELF: The Electron Localization Function. *Angew. Chem. Int. Ed.* **1997**, *36* (17), 1808-1832.
31. Becke, A. D.; Edgecombe, K. E., A Simple Measure of Electron Localization in Atomic and Molecular Systems. *J. Chem. Phys.* **1990**, *92* (9), 5397-5403.
32. Savin, A.; Nesper, R.; Wengert, S.; Fässler, T. F., ELF: The Electron Localization Function. *Angew Chem. Int. Ed. Engl.* **1997**, *36* (17), 1808-1832.
33. Manz, T. A.; Limas, N. G., Introducing DDEC6 Atomic Population Analysis: Part 1. Charge Partitioning Theory and Methodology. *RSC Advances* **2016**, *6* (53), 47771-47801.
34. Manz, T. A.; Sholl, D. S., Methods for Computing Accurate Atomic Spin Moments for Collinear and Noncollinear Magnetism in Periodic and Nonperiodic Materials. *J. Chem. Theory Comput.* **2011**, *7* (12), 4146-4164.
35. Momma, K.; Izumi, F., VESTA 3 for Three-dimensional Visualization of Crystal, Volumetric and Morphology Data. *J. Appl. Crystallogr.* **2011**, *44* (6), 1272-1276.

## Chapter 7. Effect of Substrate Relaxation on Thiol Adsorption

### 7.1 Scope of this Chapter

In this chapter, we study the effect of the substrate relaxation on the preferred adsorption sites, specifically the asymmetry between the bridge-fcc and the bridge-hcp sites. We use density functional theory to explore the bridge site asymmetry for methanethiol adsorbed on Au(111) with two different S-C bond orientations. The preference for bridge-fcc versus bridge-hcp SCH<sub>3</sub> adsorption sites is determined by the S-C bond orientation. The system energy difference favors the bridge-fcc site by 8.1 meV on the unrelaxed Au(111) surface. Relaxing the Au substrate increased this energy difference to 26.1 meV. This asymmetry is also reflected in the atomic

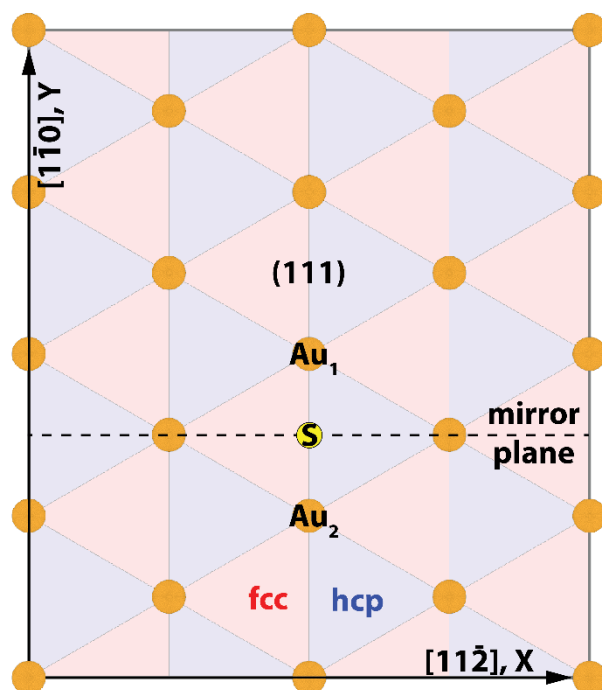


Figure 7.1. The Top-down View of the Simulation Box Showing the Au(111) Bridge Site Studied with the Adsorbed S Atom. The S atom is on the mirror plane (dotted line) provided by the bridge site. The top layer Au atoms are shown here. The fcc and hcp 3-fold hollow sites are identified by the red and blue triangles, respectively. The S atom is bonded to the substrate via the Au<sub>1</sub> and Au<sub>2</sub> bridge-site atoms. The crystallographic directions are shown on the edge of the unit cell (gray rectangle) along with the coordinate system used for the DFT computations. Specifically, the crystallographic  $[11\bar{2}]$  direction is aligned with the DFT +x coordinate direction, the  $[1\bar{1}0]$  with +y, and the  $[111]$  with +z.

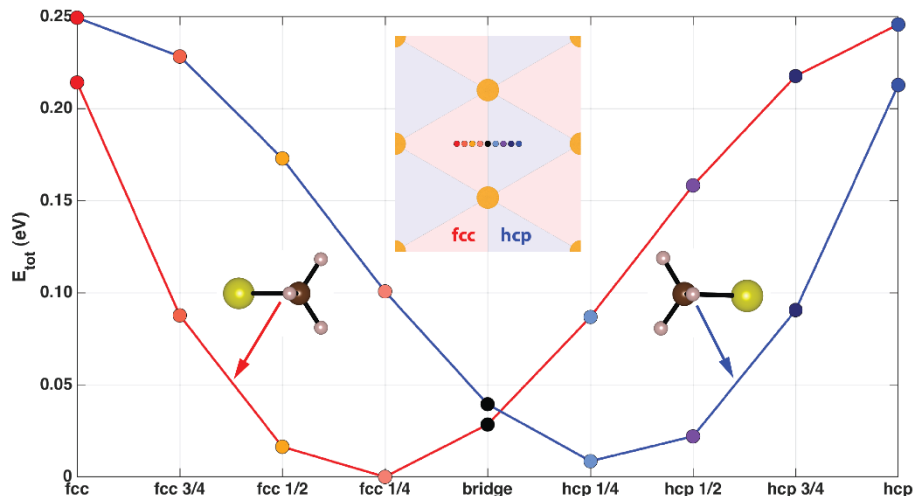


Figure 7.2. The Energy for Adsorption Sites Along the Transition Path from the fcc 3-fold Hollow Site to the hcp 3-fold Hollow Site for Two Orientations of the S-C Bond. Color coded adsorption sites are shown in the inset. The energy shows strong dependence on the S-C bond orientation. The most stable configuration is the fcc-1/4. The hcp-1/4 is 8.5 meV less favorable than the fcc-1/4.

displacement of the relaxed Au surface, where the bridge site Au atoms shift away from the fcc 3-fold hollow site in both cases. We confirm that the adsorption energy is strongly dependent on the S-C bond orientation and the sulfur position, which has important implications for alkanethiol surface diffusion and the structure of their self-assembled monolayers.

## 7.2 Introduction

Density functional theory studies have found the bridge-fcc site and the staple motif to be the two most energetically favorable adsorption structures on the Au(111) substrate.<sup>1-3</sup> The staple motif requires complex reconstruction of the substrate that involves adatoms,<sup>4-5</sup> while the bridge site does not.<sup>1</sup> In this chapter, we focus our discussion on the simpler bridge site and the resultant substrate relaxation in the absence of complex substrate reconstruction. The minimum energy position of the thiol S atom for adsorption at the bridge site is offset from the bridge site towards the fcc 3-fold hollow site (bridge-fcc) with the S-C bond azimuth towards the hcp 3-fold hollow site (hereafter hcp oriented). A second analogous minimum occurs on the opposite side at the

bridge-hcp site with the S-C bond azimuth towards the fcc 3-fold hollow site (hereafter fcc oriented). Previous studies of these two sites found the bridge-hcp site to be 30 meV less favorable than the bridge-fcc site.<sup>2</sup> In our work we find a slightly smaller energy difference 26.1 meV, which we presume is due to inclusion of the dispersion correction. The asymmetry between these sites extends beyond the orientation of the S-C bond. The bonding at the S atom was also found to be asymmetric as indicated by the different polar angles of the S-C bond—the angle between the surface normal and the S-C bond,  $43.2^\circ$  for the bridge-fcc site and  $51.3^\circ$  for the bridge-hcp site.<sup>1</sup> Because the energy difference between these two sites is on the order of  $kT$  at room temperature, both sites could be candidates for the SAM Au/S interface or play a role in SAM grow and surface diffusion. In this chapter, we study the effect of the substrate relaxation on the asymmetry of the bridge-fcc and the bridge-hcp sites.

The bridge site is one of the simple adsorption sites on the Au(111) substrate. The top-down view of a bridge adsorbed sulfur is shown in Figure 7.1. The sulfur atom is bonded to two surface Au atoms ( $Au_1$  and  $Au_2$ ) along the  $[1\bar{1}0]$  direction. In the perpendicular  $[11\bar{2}]$  direction, the fcc 3-fold hollow site is to the left of the bridge site and the hcp 3-fold hollow site is to the right, denoted by the red and the blue triangles, respectively. The bridge site does not have a mirror plane along  $[1\bar{1}0]$  or  $C_2$  axis because the fcc and hcp 3-fold hollow sites are symmetry inequivalent (fcc-hcp asymmetry). However, the bridge site has a mirror plane parallel to the  $[11\bar{2}]$  direction (bridge-site mirror plane) such that  $Au_1$  and  $Au_2$  are symmetry equivalent. We examine the bridge site mirror plane symmetry during the substrate relaxation and find the symmetry is preserved for the bridge-fcc site and approximately preserved for the bridge-hcp site.

The effect of the substrate relaxation on the asymmetry of these two sites has not been previously studied. We have chosen methanethiol as the adsorbate to explore the substrate

relaxation for bridge-fcc and bridge-hcp adsorption sites. In this paper we study the asymmetry of the adsorption energy for two S-C bond orientations on the unrelaxed and relaxed Au(111) surface. We first explore the asymmetry of the adsorption energy on position of the adsorption site along the line through the bridge site between the fcc and hcp 3-fold hollow sites. Then we study the relaxation of the bare Au(111) substrate, followed by the relaxation induced by the methanethiol initially adsorbed at the bridge site as it relaxed into the bridge-fcc and bridge-hcp sites.

### 7.3 Theoretical Methods

Our DFT calculations are performed using the VASP 5.4.4 computational package.<sup>6-7</sup> These calculations are carried out with the Agave system at Arizona State's Research Computing Center. The projected augmented wave method density functional (PAW) is used for the electron-ion interaction along with the Perdew-Burke-Ernzerhof (PBE) exchange functional.<sup>8-9</sup> The functional

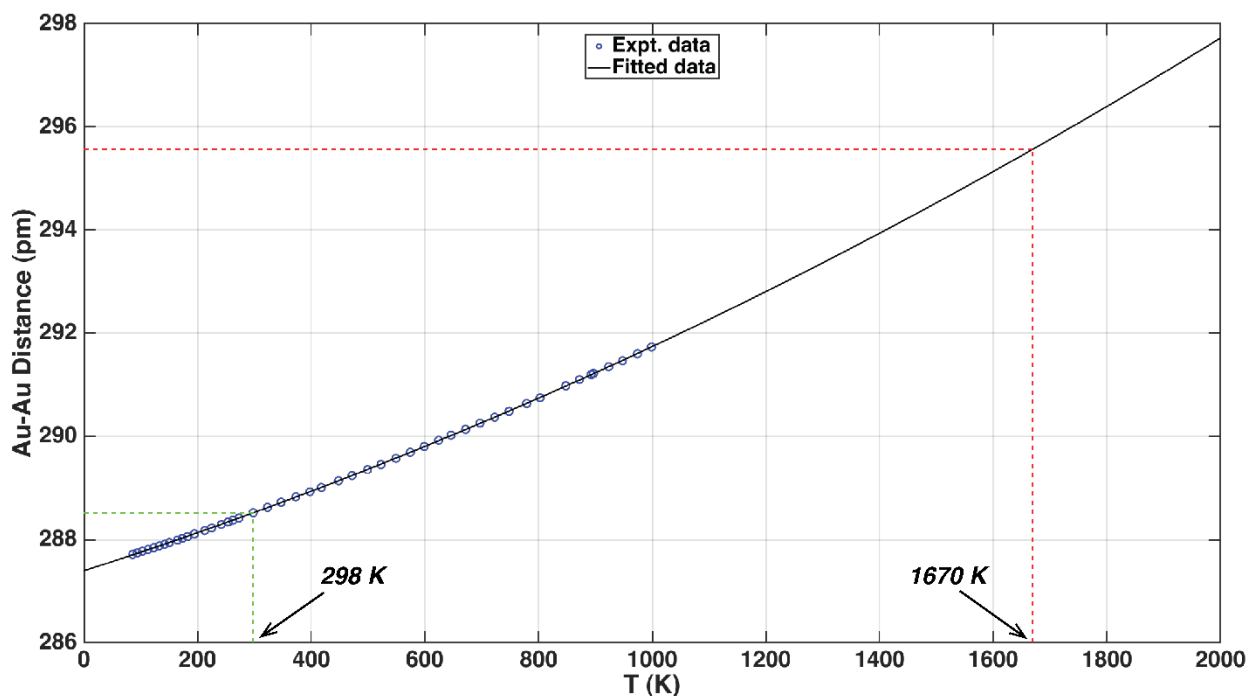


Figure 7.3. The Thermal Expansion of the Au Lattice Constant. The Au-Au distance at room temperature (298 K) is 288.43 pm. The expanded Au-Au distance of 295.57 pm corresponds to an extrapolated temperature of 1670 K.



is denoted as PAW-PBE and it is most commonly used to model the adsorption of organic molecules on metal surfaces.<sup>10-12</sup> The van der Waals forces play an important role in such weakly interacting systems. Therefore the dispersion correction of Grimme (DFT-D2) is included for more realistic simulation of the interaction between the adsorbate and the Au(111) substrate.<sup>13</sup> A planewave cutoff of 300 eV is used. The Brillouin zone integration is performed using the Monkhorst-Pack sampling with  $9 \times 9 \times 1$   $\Gamma$ -centered  $\mathbf{k}$ -grid for a surface unit cell. Geometries are considered optimized when the Hellmann-Feynman forces on ions are less than  $10^{-2}$  eV  $\text{\AA}^{-1}$ . In our fully relaxed structures, the adsorbate atoms are allowed to relax in all directions during the geometry optimization. The top two layers of Au atoms are allowed to relax in our study of substrate relaxation. For the line-scan series, we control the azimuthal direction for the S-C bond as the S atom is moved in steps across the unrelaxed Au substrate using selective constraints on the adsorbate. The S atom is constrained in xy-plane and allowed to relax in z alone to maintain a specified position on the substrate. The C atom is constrained in y and allowed to relax in the xz-plane. The H atoms are unconstrained. In this way the Au-S-CH<sub>3</sub> bond lengths and angles are allowed to relax while the azimuthal orientation of the S-C bond is constrained.

Selecting a set of DFT parameters that closely replicate the Au lattice constant is a natural starting point. An accurate representation of the Au(111) substrate is important to achieve the proper adsorbate interactions. The weighted average of the Au lattice constant of 4.07895(4)  $\text{\AA}$  (25  $^{\circ}\text{C}$ ) is experimentally known to much higher accuracy than current DFT results typically yield.<sup>14-15</sup> The simulated lattice constant depends on the combination of the pseudo-potential, the exchange-correlation functional, and the dispersion correction.<sup>10, 16-17</sup> Without the dispersion correction, DFT has reported lattice constants as high as 4.18  $\text{\AA}$  (~2.5% higher than the experimental value) which results in ~7.6% lower electron density.<sup>18</sup> To put this large lattice

constant into perceptible, to achieve this through thermal expansion requires a temperature of 1670 K, well above the melting point of gold.<sup>19</sup> The thermal expansion coefficient of the Au lattice is taken from Nix and MacNair and it is used to calculate the Au-Au distance for extrapolated temperature as shown in the Figure 7.3.<sup>20</sup> The data are presented in terms of the Au-Au nearest-neighbor distance ( $d$ ) instead of the fcc lattice constant ( $a$ ). The relationship is  $d = a/\sqrt{2}$ . Inclusion of the dispersion correction significantly improved the lattice constant (4.094 Å) along with other properties of the Au lattice.<sup>21</sup>

Table 7.1. Comparison of the Optimized Au Lattice Constant (Å) for Different DFT Functionals.

PAW+LDA+D2	USPP+LDA+D2	PAW+LDA	USPP+LDA	Experiment	PAW+PBE+D2	PAW+GGA+ D2	USPP+GGA+D2	PAW+PBE	PAW+GGA	USPP+GGA
4.01	4.02	4.05	4.07	4.08	4.10	4.12	4.13	4.16	4.18	4.18

To determine suitable DFT functionals for our study, we explored combinations of two pseudo-potentials (PAW and ultra-soft pseudo-potential (USPP)), three exchange functionals (PBE, generalized gradient approximation (GGA), and local density approximation (LDA)), and the D2 correction to determine which produces a lattice constant closest to the experimental value. Following the conventional equation of state approach, single-point energy bulk calculations were performed while varying the unit cell dimensions. The energy vs lattice constant values were fit to a 5<sup>th</sup> order polynomial (Figure 7.4). The vertex of the resulting curve yields a minimum energy lattice constant for that functional (Table 7.1). The combination of PAW, PBE, and the D2 dispersion correction yields a lattice constant of 4.10 Å, which is second closest to the experimental

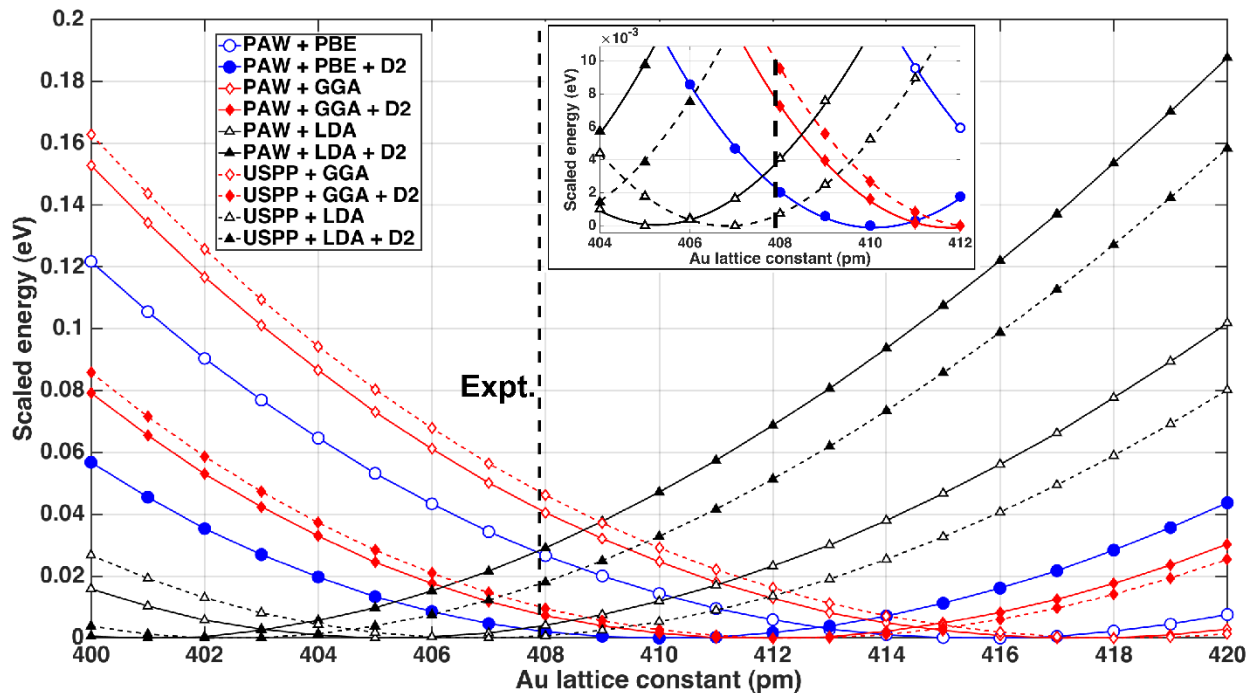


Figure 7.4. The Equation of State Calculation for Bulk Au with Different Combinations of DFT Functionals. The vertical dashed line represents the experimental value of the Au lattice constant at 25 °C. The symbols are the calculated values. The lines are a 5th-order polynomial fit to those values. The inset is a view of the same data expanded to better visualize the minima close to the experimental lattice constant. The most suitable combination to replicate the experimental lattice constant is (PAW + PBE + D2).

value after USPP LDA. Although the latter combination achieves a closer lattice constant, the LDA functional lacks the accurate representation of more localized and fast varying electron densities in atoms and clusters.<sup>22</sup> Therefore we chose the PAW+PBE combination with the D2 dispersion for our study.

The most common recipe for DFT surface studies is to construct a supercell composed of a substrate slab and a vacuum layer. The vacuum layer must be thick enough that the interaction between the periodic images can be neglected (*viz.* the top of the slab and its adsorbates with the periodic image of the bottom of the slab on the other side of the vacuum layer). However, increasing the volume of the supercell is computationally expensive in the plane wave basis, so the vacuum thickness is limited in practice. A vacuum thickness 10–15 Å has been found to be a

good compromise.<sup>5,23</sup> The periodic images of the slab in our simulations are separated by 13 Å of vacuum.

The number of Au layers in the slab need to be large enough to reduce the interaction between the top and the bottom of the slab. Increasing the number of Au layers adds computational expense. There are also symmetry considerations; the fcc structure of the Au lattice has a three-layer ABC stacking along the [111] direction (Figure 7.1).<sup>24</sup> Four layers of Au are adequate to approximate the bulk gold substrate, but for a clean termination of the bulk Au(111) we include six layers to preserve the ABC stacking.<sup>5,23,25</sup>

We have chosen a  $(4 \times 2\sqrt{3})$  rectangular unit cell with 16 Au atoms per layer to provide lateral separation between the adsorbate images and simulate a low adsorption surface density. To minimize the effect of the inter- and intra-chain vdW interaction of the adsorbates on the system energy, we have used the shortest alkane chain length (methanethiol, SCH<sub>3</sub>).

Placing an adsorbate on one side of the slab results in an asymmetric charge density with respect to the top and the bottom surface of the slab. In addition, allowing only the atoms one side of the slab to relax introduces an analogous asymmetry. Both create a difference in the electrostatic potential at the cell boundary, which produces in an artificial electric field in the vacuum region. To compensate, a tunable dipole layer is introduced in the vacuum region of the supercell, which compensates for the electrostatic potential difference and nulls the electric field.<sup>26-27</sup>

## 7.4 Results and Discussion

Before looking at the Au surface relaxation we get a picture of the inherent bridge-site asymmetry by studying the position dependent adsorption energy on unrelaxed Au. Then, using the bare Au relaxation as our baseline, we compare the additional asymmetry induced through the

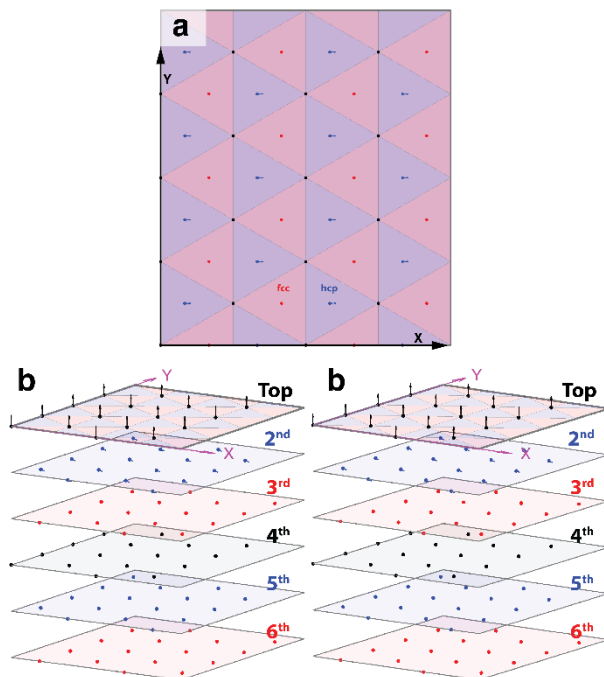


Figure 7.5. The Au(111) Surface After Relaxation Showing the Displacement Vectors. (a) The top-down view showing the top three Au layers. The top layer atoms (black) are at the vertices of the 3-fold-hollow-site triangles. The second layer atoms (blue) are below the hcp 3-fold hollow sites (blue triangles) and the third layer atoms (red) are below the fcc-3-fold hollow sites (red triangles). (b) A parallel-view stereo pair of the side view of the relaxed Au substrate. Arrows represent the deviation of the Au atoms compared to their ideal unrelaxed position. The arrow length is magnified  $10\times$  for visualization. The atoms are shown in their initial unrelaxed position with the displacement vectors originating from their unrelaxed positions.

substrate relaxation for the minimized energy bridge-fcc and the bridge-hcp sites. Finally, we compare the molecular geometry to further analyze the asymmetry between the bridge-fcc and the bridge-hcp sites.

We consider two sets of simulations to probe the inherent fcc-hcp asymmetry of the bridge site on unrelaxed Au(111) and the effect of the S-C bond orientation. We study the system energy of

the adsorption sites at discrete positions along a path from the fcc 3-fold hollow site to the hcp 3-fold hollow site through the bridge site on the unrelaxed substrate (Figure 7.2). We consider two sets of simulations: one with the S-C bond pointing towards the hcp 3-fold hollow site (red line); and the other with the S-C bond pointing towards the fcc 3-fold hollow site (blue line). Each set shows a single minimum on opposite sides of the bridge site. The lowest energy in this series is achieved with the S-C bond is hcp oriented and the S atom  $1/4$  of the fcc-bridge distance off the bridge site towards the fcc 3-fold hollow site (fcc- $1/4$ ). The equivalent lowest energy position with the S-C bond fcc oriented and the S atom  $1/4$  of the hcp-bridge distance off the bridge site toward the hcp 3-fold hollow site (hcp- $1/4$ ). The fcc- $1/4$  is favored over the hcp- $1/4$  by 8.5 meV. In this series, both sites are very close to the energy minimized energy structures obtained when the system is allowed to relax without constraints: the bridge-fcc and the bridge-hcp, respectively. When the S atom is allowed to optimize its position on the surface, the system finds the bottom of these two curves where the energy difference between the bridge-fcc and the bridge-hcp reduces to 8.1 meV, Table 7.2. The energy difference between two sides of the bridge site is inherent to the bridge site bonding because the substrate is unrelaxed. The energy of the system strongly depends on the orientation of the S-C bond, even for high symmetry 3-fold hollow sites. The energy difference between the two S-C bond orientations exactly at the bridge site is 11.1 meV, which is about three times less than the energy differences at the fcc 3-fold hollow site (35.3 meV) and at the hcp 3-fold hollow site (33.0 meV). Table 7.2. Comparison of the energy of the system with respect to bridge-hcp on unreconstructed Au.

Table 7.2. Comparison of the System Energy with respect to Bridge-hcp on Unreconstructed Au.

System	$\Delta E$ (meV)
Bridge-fcc on bulk Au – Bridge-hcp on bulk Au	-8.1
Bridge-hcp on relaxed Au – Bridge-hcp on bulk Au	-316.9
Bridge-fcc on relaxed Au – Bridge-hcp on bulk Au	-343.0

The relaxation of the bare Au(111) surface is examined first as a reference point. The top two layers are allowed to relax. We examine the displacement of each atom from its unrelaxed position as well as the average displacement of each layer. The latter is calculated by averaging the displacement of the 16 Au atoms in each layer. For discussion we separate the motion of the Au atoms into two components, in the plane of the substrate (in-plane: xy-plane) and perpendicular to the plane of the substrate (out-of-plane: along the z axis). As shown in Figure 7.1, the +x direction in the simulation coordinates is along the  $[11\bar{2}]$  crystallographic direction, the +y along the  $[1\bar{1}0]$ , and the +z is along  $[111]$ , the surface normal. The average displacement of the Au layers is given in the Table 7.3. The displacement of the individual atoms is shown in Figure 7.5 and magnified  $10\times$  for visualization.

Relaxation of the bare Au substrate results in significant out-of-plane relaxation as expected (Table 7.3). The slab expands in the  $[111]$  direction pushing the top Au layer into the vacuum  $0.0571 \text{ \AA}$  while the second layer moves closer to the third layer  $0.0058 \text{ \AA}$  (Figure 7.5.b). This expansion is caused by the formation of a surface dipole due to the work function of the Au and the truncation of the lattice. The average in-plane displacement is more than two orders of magnitude smaller than the average out-of-plane motion of the top layer Au layer. In contrast, the second layer shifts in-plane  $0.0202 \text{ \AA}$  along the +x axis, which we believe to be a simulation artifact. Note that although in nature the Au(111) surface undergoes the well-known herringbone

reconstruction, it is not our intent to simulate that because the reconstruction is lifted by alkanethiol adsorption. Furthermore, simulating the herringbone reconstruction requires a larger ( $22 \times \sqrt{3}$ ) unit cell containing extra surface atoms (46 surface Au atoms in 44 bulk positions).<sup>28</sup>

Table 7.3. Displacement for the Top Two Au Layers from their Unrelaxed Positions.

system	layer	$\bar{x}$ (Å)	$\bar{y}$ (Å)	$\bar{z}$ (Å)
Relaxed bare Au – Unrelaxed Au	Top layer	0.0002	0	0.0571
	2 <sup>nd</sup> layer	0.0202	0.0001	-0.0058
Bridge-fcc on relaxed Au – Unrelaxed Au	Top layer	0.0608	0	0.0718
	2 <sup>nd</sup> layer	-0.0045	0	0.0011
Bridge-hcp on relaxed Au – Unrelaxed Au	Top layer	0.0326	0.0072	0.0715
	2 <sup>nd</sup> layer	-0.0064	0.0017	0.0013

The net displacement is considered to be zero if it is less than  $10^{-4}$  Å. While we report these numbers, we do not believe the DFT is as accurate as 4 significant figures. Nevertheless, they have a comparative value.



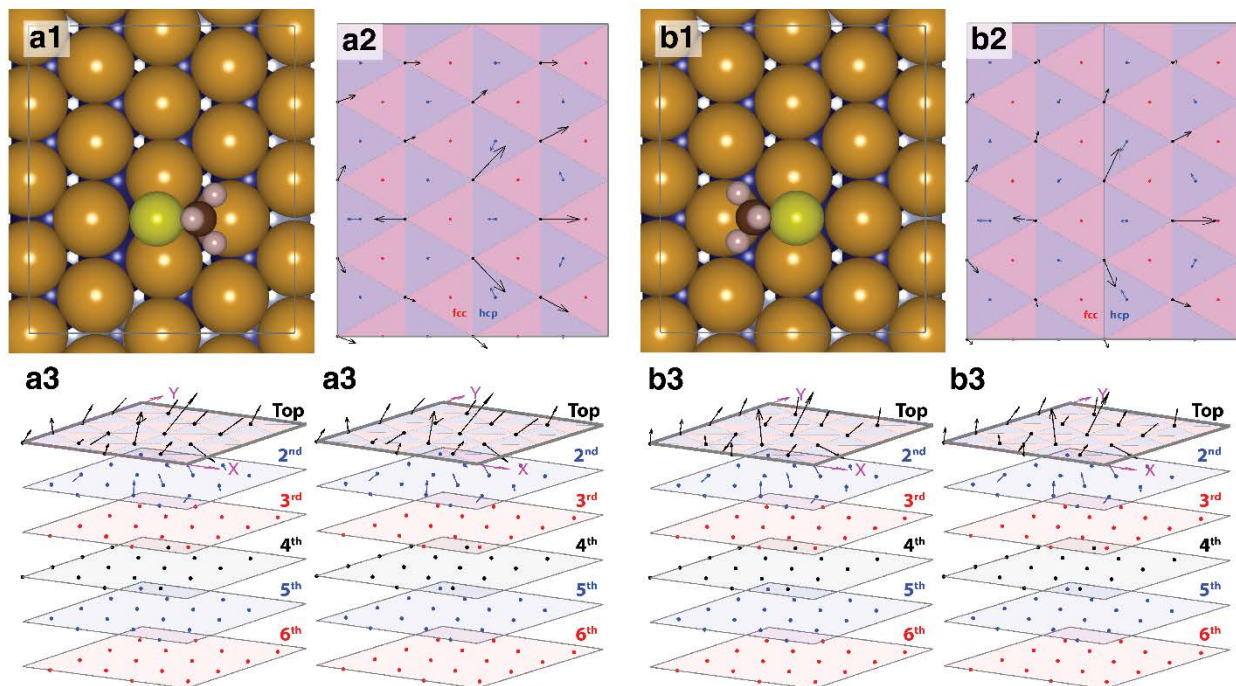


Figure 7.6. The Au Atom Displacement for  $\text{SCH}_3$  Adsorbed at the Bridge-fcc and the Bridge-hcp Sites. (a1, bridge-fcc and b1, bridge-hcp) The top-down view showing the atomic position for the adsorbates on the surface. (a2-a3 and b2-b3) Views showing the displacement of the Au atoms due to relaxation. The arrows are magnified  $10\times$  for visualization (see figure 3 for a detailed description). (a2 and b2) Top-down views showing the top three Au layers and their in-plane displacement vectors. (a3 and b3) Parallel-view stereo pairs showing all the layers with their relaxation vectors in 3D.

Next, we turn our attention to the Au relaxation in the presence of bridge adsorbed  $\text{SCH}_3$ . The methanethiol is initially adsorbed at the bridge site with S-C bond hcp orientated. These initial structures relaxed to the bridge-fcc (Figure 7.6.a) or the bridge-hcp sites (Figure 7.6.b), respectively. All simulations are started with the Au in the unrelaxed positions similar to the bare Au relaxation with the top 2 Au layers allowed to relax. The energy difference between the bridge-fcc and the bridge-hcp sites increases to 26.1 meV, consistent with previous calculations (Table 7.2, difference between the last two lines).<sup>2, 29</sup> The average out-of-plane displacement of the top two Au layers is qualitatively similar to the bare Au. The top layer expands about 25% more while the second layer moved far less in magnitude, but in the opposite direction compared to the bare Au, consistent with changes to the work function on adsorption (Table 7.3).<sup>29</sup> The average in-plane

displacements of the first Au layer occur almost exclusively in the +x direction for both adsorption sites, an indication of the asymmetry induced by the adsorption of SCH<sub>3</sub>. The Au relaxation for the bridge site prefers displacement toward the hcp 3-fold hollow site, although the sulfur moves in the opposite directions for bridge-fcc and bridge-hcp sites. The relaxation for the second layer is an order of magnitude smaller in the opposite direction. We expect the bridge-site mirror plane symmetry should also be manifested in the Au relaxation. That symmetry is well preserved for the bridge-fcc site, where the average displacement in y is zero (within the floating-point accuracy). In contrast, the bridge-hcp site shows a small asymmetry in y. To test if this was a convergence problem, we modified the resultant structure by enforcing the mirror plane symmetry and ran the simulation again from this symmetric initial condition very close to the relaxed structure. This procedure reproduced the original y asymmetry. The non-zero average y component for the bridge-hcp is a property of this configuration but may be an artifact of another aspect of the simulation.

Turning now to the bonding geometry with respect to the S atom. In all cases, Au atoms of the bridge bond relax to increase the angle of the two bonds, which brings the S atom closer to the surface (Table 7.4), and S atom moves in a manner that forces the bridge bonded Au atoms to move apart. Figure 7.6 shows the displacement of the individual Au atoms. The height of the S atom is the furthest away from the top layer for the bridge-hcp and closest for the bridge-fcc. The height difference is 0.0443 Å between bridge-hcp and bridge-fcc showing that the S atom moves closer to the surface for bridge-fcc due to stronger adsorption. The bond distances between the S atom and the bridge-site Au atoms (S-Au<sub>1</sub> and S-Au<sub>2</sub>, Figure 7.1) are symmetric for both the bridge-fcc and the bridge-hcp. The bond angle of the S atom with the bridge-site atoms (Au<sub>2</sub>-S-Au<sub>1</sub>) is within 1° for all cases studied. The Au-S-C bond angles for the methanethiol adsorption are within 106–109°, in agreement with previous results.<sup>1</sup>

Our results demonstrate the inherent asymmetry of the bridge-fcc and the bridge-hcp is amplified by the relaxation of the substrate as demonstrated by the increased difference in adsorption energy and the asymmetric relaxation of the Au surface. We also demonstrate the energy of an adsorption site depends on the direction of the S-C bond orientation of the alkanethiol molecule with respect to the underlying substrate. The strength of the energy dependence varies from site to site.

Table 7.4. Geometric Parameters of the Adsorbate ( $\text{SCH}_3$ ). The values in square brackets are for relaxed methanethiol on the unrelaxed substrate.

	bridge-fcc on relaxed Au	bridge-hcp on relaxed Au
S-top layer (Å)	1.99 [2.06]	2.03 [2.07]
S-Au <sub>1</sub> (Å)	2.44 [2.52]	2.45 [2.52]
S-Au <sub>2</sub> (Å)	2.44 [2.52]	2.45 [2.54]
Au <sub>1</sub> -Au <sub>2</sub> (Å)	3.14 [2.89]	3.10 [2.89]
Au <sub>2</sub> -S-Au <sub>1</sub> (°)	79.83 [69.77]	78.54 [69.57]
S-C and surface normal (°)	59.44 [59.76]	58.71 [60.25]
Au <sub>1</sub> -S-C (°)	106.84 [110.08]	108.05 [108.72]
Au <sub>2</sub> -S-C (°)	106.84 [110.08]	108.76 [109.91]

We feel that the structure and relaxation on the Au surface is due to the S atom binding and not the presence of the methyl. To check this, we removed the methyl and replaced it with a H atom—the S atom position and Au relaxation was largely as described above. The SH was initially absorbed at the bridge site on the unrelaxed substrate with S-C bond either hcp or fcc oriented. In one study, only the adsorbate could relax. In another, the top two layers of the Au substrate are relaxed along with the adsorbate. In both studies, the SH behaved very similar to  $\text{SCH}_3$ , where the

S atom relaxed to the bridge-fcc (hcp oriented) or the bridge-hcp (fcc oriented) site dependent on the S-C bond orientation. The Au surface relaxation is shown in Figure 7.7, analogous to Figure 7.6 for SCH<sub>3</sub>. The results of the SH study are summarized in Tables 7.5-7.8. Table 7.8 compares the geometric parameters for SH and SCH<sub>3</sub>.

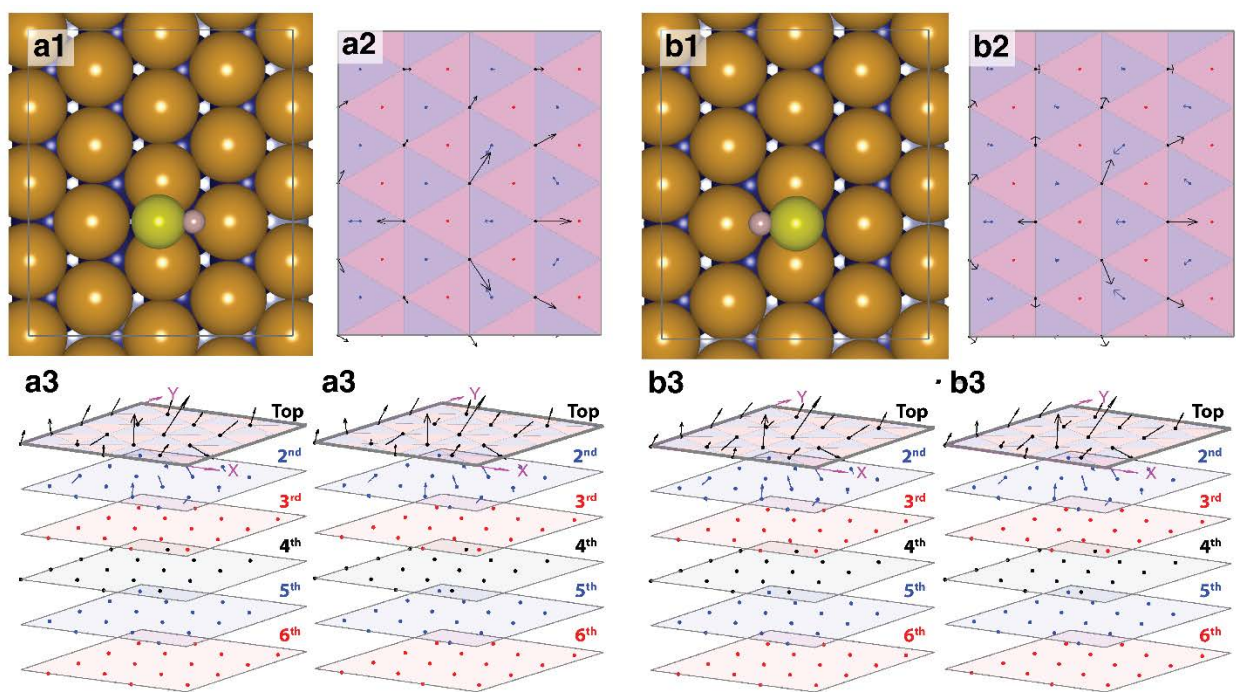


Figure 7.7. The Au Atom Displacement for SH Adsorbed at the Bridge-fcc and the Bridge-hcp Sites. (a1,bridge-fcc and b1, bridge-hcp) The top-down view showing the atomic position for the adsorbates on the surface. (a2-a3 and b2-b3) Arrows represent the deviation of the Au atoms compared to their ideal unrelaxed position. The arrow length is magnified 10× for visualization. The atoms are shown in their unrelaxed position with the displacement vectors originating from their unrelaxed positions. (a2 and b2) Top-down views showing the top three Au layers and their in-plane displacement vectors. The top layer atoms (black) are at the vertices of the 3-fold-hollow-site triangles. The second layer atoms (blue) are below the hcp 3-fold hollow sites (blue triangles) and the third layer atoms (red) are below the fcc-3-fold hollow sites (red triangles). (a3 and b3) Parallel-view stereo pairs showing all the layers with their relaxation vectors in 3D.

Table 7.5. Comparison of the System Energy with respect to SH (S-H, bridge-hcp) on Bulk Au.

System	$\Delta E$ (meV)
SH(S-H, bridge-hcp) + unrelaxed Au – SH(S-H, bridge-hcp) + unrelaxed Au	0
SH(S-H, bridge-fcc) + unrelaxed Au – SH(S-H, bridge-hcp) + unrelaxed Au	-7.4752
SH(S-H, bridge-hcp) + relaxed Au – SH(S-H, bridge-hcp) + unrelaxed Au	-293.2137
SH(S-H, bridge-fcc) + relaxed Au – SH(S-H, bridge-hcp) + unrelaxed Au	-299.4319

Table 7.6. Displacement for the Top Two Au Layers from the Relaxed Bare Au Positions.

system	layer	$\bar{x}$ (Å)	$\bar{y}$ (Å)	$\bar{z}$ (Å)
SH(S-H, bridge-fcc)+Au – Relaxed Au	Top layer	0.0384	0	0.0115
	2 <sup>nd</sup> layer	-0.0272	0	0.0066
SH(S-H, bridge-hcp)+Au – Relaxed Au	Top layer	0.0547	0	0.0126
	2 <sup>nd</sup> layer	-0.0260	0	0.0067
Bridge-fcc on relaxed Au – Relaxed Au	Top layer	0.0605	0	0.0147
	2 <sup>nd</sup> layer	-0.0247	0	0.0070
Bridge-hcp on relaxed Au – Relaxed Au	Top layer	0.0324	0.0072	0.0144
	2 <sup>nd</sup> layer	-0.0266	0.0016	0.0072

Note that, the out-of-plane displacement for the 2<sup>nd</sup> layer with respect to the relaxed bare Au is larger than the unrelaxed Au. This is because the 2<sup>nd</sup> layer of the relaxed bare Au moves closer to the 3<sup>rd</sup> layer, whereas it moves away from the 3<sup>rd</sup> layer with the adsorbate during relaxation.

Table 7.7. Displacement for the Top Two Au Layers from their Unrelaxed Positions.

System	layer	$\bar{x}$ (Å)	$\bar{y}$ (Å)	$\bar{z}$ (Å)
Relaxed bare Au – unrelaxed Au	Top layer	0.0002	0	0.0571
	2 <sup>nd</sup> layer	0.0202	0.0001	-0.0058
SH(S-H, bridge-fcc)+Au – unrelaxed Au	Top layer	0.0386	0	0.0686
	2 <sup>nd</sup> layer	-0.0070	0	0
SH(S-H, bridge-hcp)+Au – unrelaxed Au	Top layer	0.0549	0	0.0697
	2 <sup>nd</sup> layer	-0.0058	0	0
Bridge-fcc on relaxed Au – unrelaxed Au	Top layer	0.0608	0	0.0718
	2 <sup>nd</sup> layer	-0.0045	0	0.0011
Bridge-hcp on relaxed Au – unrelaxed Au	Top layer	0.0326	0.0072	0.0715
	2 <sup>nd</sup> layer	-0.0064	0.0017	0.0013

Table 7.8. Geometric Parameters of the SH and SCH<sub>3</sub> Adsorbates. The values in the square brackets are for the relaxed adsorbate on unrelaxed Au.

	SH (X = H)		SCH <sub>3</sub> (X = C)	
	bridge-fcc+Au	bridge-hcp+Au	Bridge-fcc+Au	Bridge-hcp+Au
S-top layer(Å)	2.03 [2.10]	2.06 [2.11]	1.99 [2.06]	2.03 [2.07]
S-Au <sub>1</sub> (Å)	2.47 [2.55]	2.48 [2.56]	2.44 [2.52]	2.45 [2.52]
S-Au <sub>2</sub> (Å)	2.47 [2.55]	2.48 [2.56]	2.44 [2.52]	2.45 [2.54]
Au <sub>1</sub> -Au <sub>2</sub> (Å)	3.12 [2.89]	3.07 [2.89]	3.14 [2.89]	3.10 [2.89]
Au <sub>2</sub> -S-Au <sub>1</sub> (°)	78.28 [68.91]	76.35 [68.76]	79.83 [69.77]	78.54 [69.57]
S-X, surface normal (°)	75.63 [77.97] (X = H)	79.04 [78.06] (X = H)	59.44 [59.76] (X = C)	58.71 [60.25] (X = C)
Au <sub>1</sub> -S-X(°)	97.71 [98.18] (X = H)	98.18 [97.23] (X = H)	106.84 [110.08] (X = C)	108.05 [108.72] (X = C)
Au <sub>2</sub> -S-X(°)	97.71 [98.18] (X = H)	98.18 [97.23] (X = H)	106.84 [110.08] (X = C)	108.76 [109.91] (X = C)

## 7.5 Conclusion

In our study, we have chosen the simplest methanethiol adsorption scenario on the Au(111) substrate without adatoms and/or vacancies to study the asymmetry of the bridge-fcc and the bridge-hcp sites and the effect of the substrate relaxation on the asymmetry. The energy of an adsorption site depends on the orientation of the S-C bond. The line scan from the fcc 3-fold hollow site through the bridge site to the hcp 3-fold hollow site shows the inherent bridge-site asymmetry and its dependence on the S-C bond orientation. Then the bridge adsorbed SCH<sub>3</sub> is allowed to relax to its energy minimized structure, the S atom moves to the side of the bridge opposite to the methyl group (bridge-fcc and the bridge-hcp sites). When the Au surface is also allowed to relax, the SCH<sub>3</sub> exhibit the same preference for different sides of the bridge while in both cases the bridging Au atoms are displaced away from the fcc 3-fold hollow site. The intrinsic energy difference between the bridge-fcc and the bridge-hcp sites on the unrelaxed bulk Au substrate is 8.1 meV due to the bridge site bonding. The energy difference between these two sites is increased to 26.1 meV after the substrate relaxation. The relaxation of the substrate magnifies the intrinsic asymmetry of the bridge-fcc and the bridge-hcp sites. This asymmetry between these two sites is also evident on the molecular geometry of the adsorbate in terms of the S-C bond orientation and the height of the S atom from the substrate. This result is further evidence that the energy of the adsorption sites across the surface also depends on the S-C bond orientation. We explore this possibility in detail in elsewhere.

## 7.6 References

1. Yourdshahyan, Y.; Rappe, A. M., Structure and Energetics of Alkanethiol Adsorption on the Au(111) Surface. *J. Chem. Phys.* **2002**, *117* (2), 825-833.

2. Cao, Y.; Ge, Q.; Dyer, D. J.; Wang, L., Steric Effects on the Adsorption of Alkylthiolate Self-Assembled Monolayers on Au (111). *J. Phys. Chem. B* **2003**, *1107* (16), 3803-3807.
3. Nagoya, A.; Morikawa, Y., Adsorption States of Methylthiolate on the Au(111) Surface. *J. Phys.: Condens. Matter* **2007**, *19* (36), 365245-7.
4. Maksymovych, P.; Sorescu, D. C.; Yates, J. T., Gold-Adatom-Mediated Bonding in Self-Assembled Short-Chain Alkanethiolate Species on the Au(111) Surface. *Phys. Rev. Lett.* **2006**, *97* (14), 146103-4.
5. Cossaro, A.; Mazzarello, R.; Rousseau, R.; Casalis, L.; Verdini, A.; Kohlmeyer, A.; Floreano, L.; Scandolo, S.; Morgante, A.; Klein, M. L.; Scoles, G., X-ray Diffraction and Computation Yield the Structure of Alkanethiols on Gold(111). *Science* **2008**, *321* (5891), 943-946.
6. Kresse, G.; Furthmüller, J., Efficiency of ab-initio Total Energy Calculations for Metals and Semiconductors Using a Plane-wave Basis Set. *Comput. Mater. Sci.* **1996**, *6* (1), 15-50.
7. Kresse, G.; Joubert, D., From Ultrasoft Pseudopotentials to the Projector Augmented-wave Method. *Phys. Rev. B* **1999**, *59* (3), 1758-1775.
8. Blöchl, P. E., Projector Augmented-wave Method. *Phys. Rev. B* **1994**, *50* (24), 17953-17979.
9. Perdew, J. P.; Burke, K.; Ernzerhof, M., Generalized Gradient Approximation Made Simple. *Phys. Rev. Lett.* **1996**, *77* (18), 3865-3868.
10. Gautier, S.; Steinmann, S. N.; Michel, C.; Fleurat-Lessard, P.; Sautet, P., Molecular Adsorption at Pt(111). How Accurate are DFT Functionals? *Phys. Chem. Chem. Phys.* **2015**, *17* (43), 28921-28930.
11. Mete, E.; Yortanl, M.; Dansman, M. F., A van der Waals DFT Study of Chain Length Dependence of Alkanethiol Adsorption on Au(111): Physisorption vs. Chemisorption. *Phys. Chem. Chem. Phys.* **2017**, *19* (21), 13756-13766.
12. Yuan, D.; Liao, H.; Hu, W., Assessment of van der Waals Inclusive Density Functional Theory Methods for Adsorption and Selective Dehydrogenation of Formic Acid on Pt(111) Surface. *Phys. Chem. Chem. Phys.* **2019**, *21* (37), 21049-21056.
13. Grimme, S.; Antony, J.; Ehrlich, S.; Krieg, H., A Consistent and Accurate ab initio Parametrization of Density Functional Dispersion Correction (DFT-D) for the 94 Elements H-Pu. *J. Chem. Phys.* **2010**, *132* (15), 154104-19.
14. Eisenmann, B.; Schäfer, H., Structure data of elements and intermetallic phases. In *Landolt-Börnstein. Group III, Condensed Matter*, Hellwege, K.-H.; Hellwege, A. M., Eds. Springer: Berlin, 2006; Vol. 14a.



15. Wyckoff, R. W. G., *Crystal structures*. John Wiley & Sons: New York, London, 1963; Vol. 1.
16. Lee, K.; Murray, É. D.; Kong, L.; Lundqvist, B. I.; Langreth, D. C., Higher-Accuracy van der Waals Density Functional. *Phys. Rev. B* **2010**, *82* (8), 081101-4.
17. Steinmann, S. N.; Corminboeuf, C., Comprehensive Benchmarking of a Density-Dependent Dispersion Correction. *J. Chem. Theory Comput.* **2011**, *7* (11), 3567-3577.
18. Bilić, A.; Reimers, J. R.; Hush, N. S.; Hafner, J., Adsorption of Ammonia on the Gold (111) Surface. *J. Chem. Phys.* **2002**, *116* (20), 8981-8987.
19. Haynes, W. M.; Lide, D. R.; Bruno, T. J., *CRC handbook of chemistry and physics*. 97th ed.; CRC Press: Boca Raton, 2016.
20. Nix, F. C.; MacNair, D., The Thermal Expansion of Pure Metals: Copper, Gold, Aluminum, Nickel, and Iron. *Phys. Rev.* **1941**, *60* (8), 597-605.
21. Seema, P.; Behler, J.; Marx, D., Force-Induced Mechanical Response of Molecule–Metal Interfaces: Molecular Nanomechanics of Propanethiolate Self-Assembled Monolayers on Au(111). *Phys. Chem. Chem. Phys.* **2013**, *15* (38), 16001-16011.
22. Rietmann, T.; Sohn, S.; Schröder, M.; Lipinsky, D.; Arlinghaus, H. F., Comparison of Detection Efficiencies of Negatively Charged Gold-Alkanethiolate-, Gold-Sulfur- and Gold-Clusters in ToF-SIMS. *Appl. Surf. Sci.* **2006**, *252* (19), 6640-6643.
23. Wang, J.-G.; Selloni, A., The c(4×2) Structure of Short- and Intermediate-Chain Length Alkanethiolate Monolayers on Au(111): A DFT Study. *J. Phys. Chem. C* **2007**, *111* (33), 12149-12151.
24. Jette, E. R.; Foote, F., Precision Determination of Lattice Constants. *J. Chem. Phys.* **1935**, *3* (10), 605-616.
25. Grönbeck, H.; Häkkinen, H., Polymerization at the Alkylthiolate–Au(111) Interface. *J. Phys. Chem. B* **2007**, *111* (13), 3325-3327.
26. Neugebauer, J.; Scheffler, M., Adsorbate-substrate and Adsorbate-adsorbate Interactions of Na and K Adlayers on Al(111). *Phys. Rev. B* **1992**, *46* (24), 16067-16080.
27. Bengtsson, L., Dipole Correction for Surface Supercell Calculations. *Phys. Rev. B* **1999**, *59* (19), 12301-12304.
28. Hanke, F.; Björk, J., Structure and Local Reactivity of the Au(111) Surface Reconstruction. *Phys. Rev. B* **2013**, *87* (23), 235422.

29. Cometto, F. P.; Paredes-Olivera, P.; Macagno, V. A.; Patrito, E. M., Density Functional Theory Study of the Adsorption of Alkanethiols on Cu(111), Ag(111), and Au(111) in the Low and High Coverage Regimes. *J. Phys. Chem. B* **2005**, *109* (46), 21737-21748.

## Chapter 8: Conclusions and Future Outlook

In this dissertation, we advance our understanding of the alkanethiol SAM on the Au(111) substrate using a reductionist method. We use molecular dynamics and density functional theory simulations to explore alkane chain packing and properties at the Au-S interface, and compare our results with experimental observations. We showed that the offset of the sulfur head groups from the  $(\sqrt{3}\times\sqrt{3})R30^\circ$  sites is necessary to accommodate multiple chain twists per unit cell in a close packed SAM, as observed in IRRAS experiments. The chain twist of the basis molecules and their relative population within the  $(2\sqrt{3}\times 3)\text{rect.}$  unit cell depends on the details of the symmetry and the spacing of the headgroups. The  $sp^3$  hybridization of the headgroup determines the interaction at the Au-S interface. The sulfur atom adopts a tetrahedral geometry at the energetically preferred bridge-fcc and bridge-hcp sites. The azimuthal angle of the S-C bond has significant effect on the surface bonding which propagates deeper into the Au(111) crystal along the  $\langle 110 \rangle$  direction. The asymmetry between the preferred sites is due to the contribution of the second and the third layer of Au atoms. Relaxation of the surface magnifies the asymmetry by more than three times in favor of the bridge-fcc site. In the rest of the chapter, we emphasize the physical insights gained from each chapter with possible future directions.

In Chapter 4, we found that the close packing of the alkane chains prefers a 1-molecule basis twist structure when the head groups are constrained at the  $(\sqrt{3}\times\sqrt{3})R30^\circ$  sites. When we relax the headgroup constrained in the x-y plane, the close-packed alkane chains offset the headgroups from the  $(\sqrt{3}\times\sqrt{3})R30^\circ$  sites. As a result of the headgroup offset, multiple chain twists per unit cell emerges with a preference for the 2-molecule basis twist structure. The energy difference between the least and the most favored twist combinations also reduces by 35% when the headgroups are allowed to relax in the x-y plane.

The effect of the interaction at the Au-S interface on the chain packing can manifest in two ways: preferred adsorption sites driven by the Au-S interaction alone, and site dependent preferred orientation of the S-C bond. The preference to the adsorption sites also changes with the relaxation and the reconstruction of the substrate. In Chapter 5, we study the effect of substrate reconstruction on the chain packing and compare our results with experimental observations. We adopted a simulation method to overcome the computational limitations by using the atomic structure at the Au-S interface predicted by DFT to study the effect on the chain packing using MD simulation. We selected ten proposed Au-S interfacial models from the literature where the S atoms are offset from the  $(\sqrt{3}\times\sqrt{3})R30^\circ$  sites. The headgroups were fixed at these sites to compare the resulting monolayer structure. For the first time, we report the emergence of a 4-molecule basis twist structure of long chain alkanethiol SAM using molecular dynamics, consistent with the experimental observation. We also showed the high sensitivity of the atomic structure at the Au-S interface that results in a great variation of the SAM structure in terms of tilt, twists, end-group height, and their spatial order.

Our study underscores the importance for developing a site-dependent dihedral force field for molecular dynamics that controls the orientation of the S-C bond. The molecular twist of an all-trans alkane chain also influences the orientation of the S-C bond. Thus, including the dihedral potential for the S-C bond will improve our models by combining the effects of the chain packing and the interaction at the Au-S interface. The symmetry of the dihedral potential depends on the adsorption sites which determines the preferred orientation of the S-C bond (demonstrated in Chapter 6). Different adsorption sites within the  $(2\sqrt{3}\times 3)\text{rect.}$  unit cell may prefer different S-C bond orientations based on the site-dependent dihedral potential. The close packing of the alkyl chains and the preferred S-C bond orientations for the four basis molecules will ultimately

determine the molecular twists within the  $(2\sqrt{3}\times 3)$ rect. unit cell. In this way we can improve our model by combining the interaction of the Au-S interface and the chain packing to determine the overall structure of the SAM.

With these improved models we can use the molecular dynamics data to simulate STM images and IRRAS spectra to directly compare with experiments. This will allow us to gain further insight of the internal SAM structure. For instance, the STM image provides the topological information of the molecule-air interface. We can predict the corresponding molecular geometry and the structure at the Au-S interface by comparing experimental STM images with simulated STM images. Another example is the prediction of two mutually orthogonal twists ( $50^\circ$  and  $132^\circ$ ) by fitting the experimental IRRAS spectra. In contrast, the molecular dynamics simulation of the close-packed alkyl chains results in four distinct molecular twists per unit cell ( $50^\circ$ ,  $132^\circ$ ,  $228^\circ$ , and  $310^\circ$ ). The discrepancy between these two results is because IRRAS cannot distinguish between mirror twists about the tilt plane ( $50^\circ$  and  $310^\circ$ ;  $132^\circ$  and  $228^\circ$ ). Comparing simulated spectra from the molecular dynamics data with the IRRAS observation will provide us more detailed structure of the SAM without fitting complex Fermi resonance modes and weak methyl modes. Our preliminary models of STM and IRRAS are described in Appendix F and G, respectively. We compared the simulated results with the experimental observation using Model A at 200 K. We highlighted the possible reasons for the discrepancy between the simulated results and the experiments, and proposed possibilities for improvement.

We now turn our attention to the interaction at the Au-S interface and its effect on the preferred adsorption geometry. In chapter 6, we use an isolated methanethiol on the unreconstructed Au(111) substrate to minimize the chain-chain interaction and focus on the interaction at the Au-S interface. We present a detailed energy landscape of different adsorption geometries in which the preferred

bridge-fcc and bridge-hcp sites reside. The bond order to the bridging Au atoms maximizes for these preferred adsorption sites—indicating stronger surface bonding. The low energy difference between these two preferred sites ( $8.1 \text{ meV} < k_B T$  at room temperature) suggests that they can coexist in the SAM structure at room temperature. However, the bridge-fcc site with  $\phi = 0^\circ$  and bridge-hcp site with  $\phi = 180^\circ$  are separated by high energy ridges that the molecule cannot overcome at room temperature (on a static Au(111) surface). The energy landscape shows that the methanethiol can move between the preferred adsorption sites via the energy plateau at a lower energy cost. Our result shows that the energy of the system for an adsorption site strongly depends on the azimuthal angle of the S-C bond. The symmetry of this dependence (energy modulation) is consistent with that of the surface site. The preference of the adsorption site and the strong S-C bond orientation can be explained as best accommodating  $sp^3$  hybridization of the sulfur headgroup. The hybridization is manifested by the energetically preferred tetrahedral coordination geometry of the headgroup. Electron lone pair analysis shows the transition from an ammonia-like pyramidal geometry at the bridge site to a water-like bent geometry at the atop site. This transition begins with one of the bridging Au-S bond breaking near the bridge site.

The energy of the system depends on the alignment of the Au-S bond with the bonds between the nearest neighbor Au atoms within the Au(111) crystal. In contrast with the  $sp^3$  hybridization of the sulfur headgroup, our result suggests that the NN Au bonds propagate along the  $sd^5$  hybridized orbitals. Further investigation is needed for a qualitative analysis of this hybridization. Bonding within the Au crystal is significantly affected by the deviation from the preferred tetrahedral coordination of the sulfur atom. This results in strikingly different sub-surface Au-Au bonds for different azimuthal angles of the S-C bond. We demonstrate the change in bonding along the  $\langle 110 \rangle$  crystal direction as we move between the high symmetry sites. The asymmetry between

the preferred adsorption sites (bridge-fcc and bridge-hcp) is due to the strong contribution from the second and the third Au layers. The preference for the adsorption site and the methanethiol geometry is slightly affected by the relaxation of the substrate (Chapter 7). The asymmetry between the bridge-fcc and bridge-hcp sites, on the other hand, magnifies from 8.1 meV to 26.1 meV upon substrate relaxation. The bridging Au atoms are displaced away from the fcc 3-fold hollow site for both cases. The S atom nestles closer to the relaxed substrate by opening up the Au-S-Au angle, pushing apart the bridging Au atoms. This indicates a stronger methanethiol bonding due to substrate relaxation.

The key contributions of our work to understanding the structure of SAMs are the insights from the studies of alkyl-chain packing and the studies of the Au-thiol adsorption geometry. We show that alkyl-chain packing is exquisitely sensitive to the Au-S interface. Our results offer the first demonstration of the spontaneous emergence of mutually orthogonal chain twists driven by alkyl-chain packing. That result is also significant because it is consistent with experiments. The Au-thiol adsorption geometry strongly indicates the propensity of the sulfur head group to be  $sp^3$  hybridized. The tetrahedral coordination geometry of the sulfur atom is a manifestation of this hybridization which determines the azimuthal orientation of the S-C bond. Our results also demonstrate the significance of the Au sub-layer contribution to the surface bonding of thiol and its effect during substrate relaxation.





simulate the dynamics. We use a VMD script to convert the .xyz format to a LAMMPS readable format. The steps to prepare the initial structure for LAMMPS are shown in Figure A.1.

Once the initial structure is prepared, we setup the molecular dynamics simulation using a LAMMPS script. The script calls different functions to perform different parts of the simulation. The syntax of the LAMMPS script can be found in the LAMMPS documentation (<https://www.lammps.org/>). Below is an example of a LAMMPS script from which we call seven functions (in.pbc, in.lj, in.bond, in.angle, in.dihedral, in.output\_parameters, and in.ensemble). The in.pbc is used to define the units, implement the periodic boundary condition, reading the initial structure, replicating the unit cell, and setting up the time step. The non-bonded force fields are defined in the in.lj function. The bonded force fields are defined in in.bond, in.angle, and in.dihedral functions. The in.output\_parameter function is used to provide the initial velocity, creating different groups of atoms, setting up the check points, implementing constraints on a group of atoms, and configuring the output of the thermodynamic variables. Finally, we use the in.ensemble function to define our ensemble, number of iterations for each simulation section, and writing the structural data in different formats that are used by the post-analysis scripts.

---

```
##### Author: Soumya Bhattacharya, 2016-08-15 #####
#-----Initialization and Reading Initial Structure-----#
include in.pbc
    units real
    dimension 3
    newton on
    boundary p p p
    atom_style full
    read_data c10.out
    replicate 5 5 1
    timestep 1.0

#-----Non-bonded Interaction-----#
include in.lj
    set atom 1 charge -0.12
    set atom 2 charge 0.06
    set atom 3 charge 0.0
    pair_style lj/cut/coul/cut 12.00
    pair_coeff 1 1 0.0660 3.500 # C
    pair_coeff 2 2 0.0300 2.500 # H
    pair_coeff 3 3 0.2500 3.550 # S
```

```

pair_modify mix geometric

#-----Bond Stretching Potential-----#
include in.bond
bond_style harmonic
bond_coeff 1 268.0 1.529 # C-C
bond_coeff 2 340.0 1.090 # C-H
bond_coeff 3 222.0 1.810 # C-S

#-----Bond Bending Potential-----#
include in.angle
angle_style harmonic
angle_coeff 1 58.35 112.7 # C-C-C
angle_coeff 2 37.50 110.7 # C-C-H
angle_coeff 3 62.14 114.0 # C-C-S
angle_coeff 4 33.00 107.8 # H-C-H
angle_coeff 5 37.50 110.7 # H-C-S

#-----Dihedral Potential-----#
include in.dihedral
dihedral_style opl
dihedral_coeff 1 0.528 -0.186 0.900 0.00 # C-C-C-C
dihedral_coeff 2 0.000 0.0000 0.366 0.00 # C-C-C-H
dihedral_coeff 3 1.876 0.0000 0.000 0.00 # C-C-C-S
dihedral_coeff 4 0.000 0.0000 0.150 0.00 # H-C-C-H
dihedral_coeff 5 0.000 0.0000 0.452 0.00 # H-C-C-S

#-----Simulation Setup-----#
include in.output_parameters
thermo 1000
thermo_style custom step vol temp press pe ke etotal enthalpy evdwl
thermo_modify line one
group molecule type 1 2 3 4
group substrate type 5
group methyl type 3
group mol type 1 2 3 4 5
velocity molecule create 4.0 293288 dist gaussian mom yes rot yes
velocity substrate create 4.0 293288 dist gaussian mom yes rot yes
restart 1000000 restart.*
neighbor 0.3 bin
neigh_modify delay 2 every 1 check yes
fix freeze substrate setforce 0.0 0.0 0.0

#-----Relaxation + Dynamics-----#
include in.ensemble
#-----Relaxation part
fix 1 molecule nvt temp 4.0 4.0 100.0
run 10000000
unfix 1
#-----Dynamics at 4K
fix 2 molecule nvt temp 4.0 4.0 100.0
dump 1 all custom 100000 c14_velocity.*.txt id type xu yu zu vx vy vz
dump_modify 1 sort id
dump 2 mol xyz 100000 structure.*.xyz
dump_modify 2 sort id
dump 3 all cfg 100000 cfg.*.cfg mass type xs ys zs vx vy vz fx fy fz
dump_modify 3 element C H S
dump_modify 3 sort id
run 10000000

#####The End#####

```

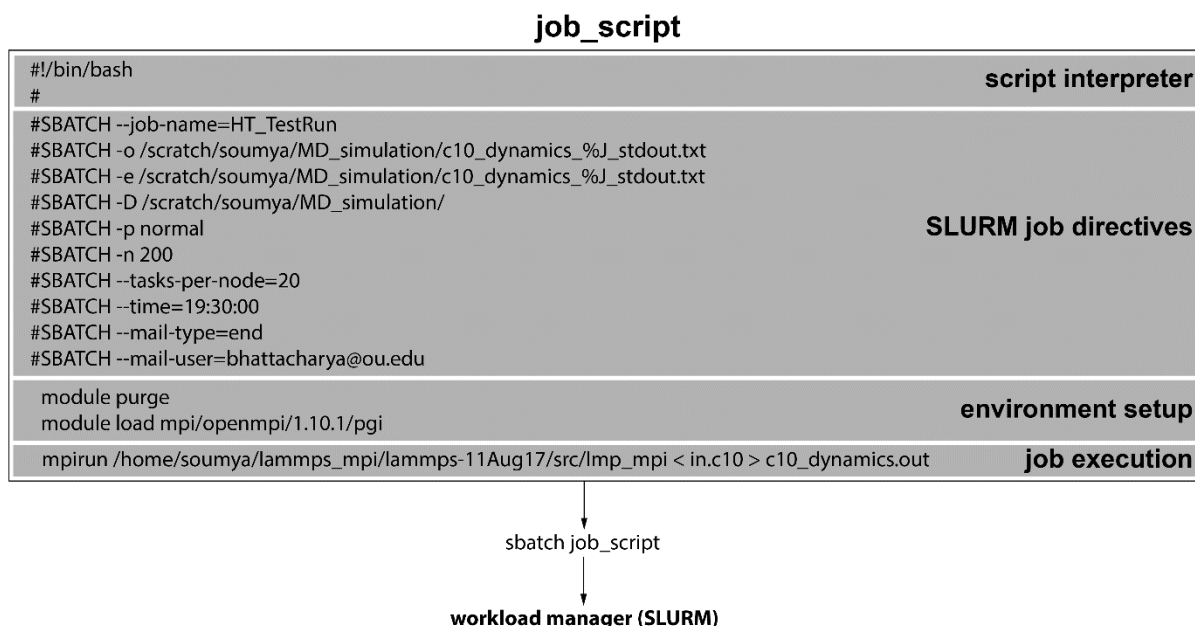


Figure A.2 LAMMPS Batch Script Example for OSCER. The script uses the SLURM workload manager to run our molecular dynamics simulation.

We use a job script to submit the LAMMPS job to a workload manager on the supercomputer. Here, we explain the job submission process for the OSCER supercomputer using an example job script (Figure A.2). We cannot directly access the compute nodes of a supercomputer which runs the LAMMPS job. We submit our LAMMPS job to the SLURM workload manager on OSCER, which assigns the computing resources and schedules the job. The priority is assigned using the fairshare algorithm (more information can be found in SLURM documentation, <https://slurm.schedmd.com/documentation.html>). There are four sections of the job submission script. First, we define the interpreter for the job script. We use a BASH script in our case. We then define the SLURM directives, such as working directory, type of compute node, number of CPU cores, simulation time, and so on. After this, we set up the environment to run the LAMMPS job by first cleaning the environment (for better reproducibility) and then loading the appropriate module. Now we can run the LAMMPS script by calling the corresponding executable.

We developed post-analysis software packages to interpret the simulation data. We transfer the simulated data from the supercomputer to our local workstation to perform the post-analysis using interactive MATLAB scripts. The software takes the .xyz structure files from LAMMPS output to perform various data analysis and data visualizations. The post-analysis scripts are made available in the GitHub repository (<https://github.com/bhat2094/MD-Post-Analysis-Scripts>).

## Appendix B: Benchmark for LAMMPS

We benchmark our molecular dynamics calculations on OSCER (Haswell) and Stampede2 (Knights Landing and Skylake) supercomputers to determine the most efficient use of our computational resources. We use 46,080 atoms in the simulation box for all our benchmarks with 10,000 iterations (10 ps) at 300 K. We compare the speed up of the LAMMPS script from three Intel architectures (Haswell, Knights Landing, and Skylake) in Figure B.1. We define the speed up of our calculation with  $N$  CPU cores as the ratio between the simulation time of a single core and the simulation time for  $N$  CPU cores. In an ideal case, we will get a speed up of our calculation proportional to the number of CPU cores being used (black dotted line in Figure B.1). The speed up for all three architectures is proportional to the number of CPU cores when the number of CPU cores is less ( $<25$ ). As we use more cores, the speed up decreases from the ideal case. For the

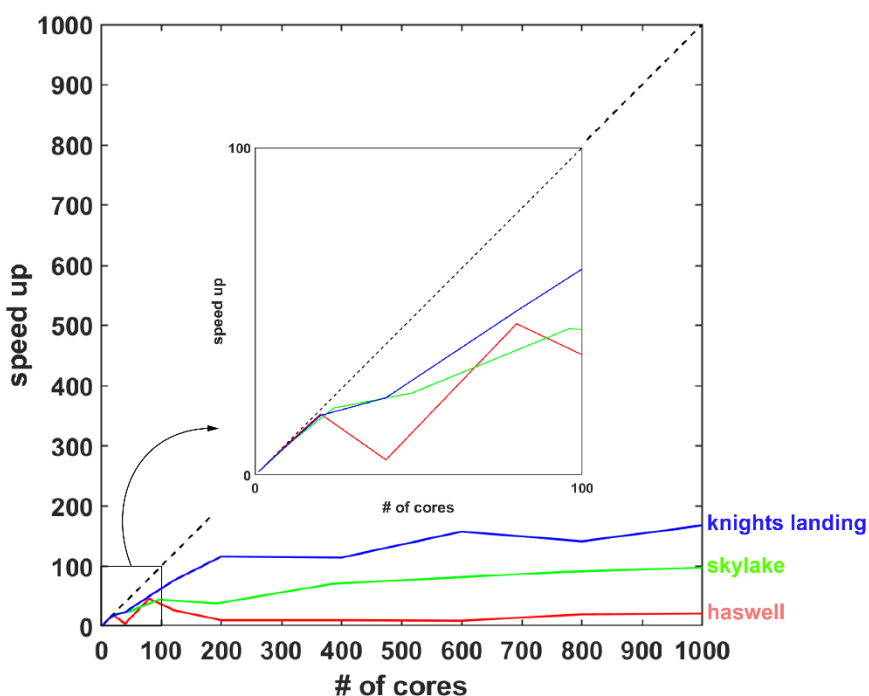


Figure B.1. LAMMPS Benchmarks on Three Different Intel Architectures. The ideal speed up is shown by the dotted line. In our case, it deviates significantly from the ideal case beyond 200 CPU cores and saturates at a constant value.

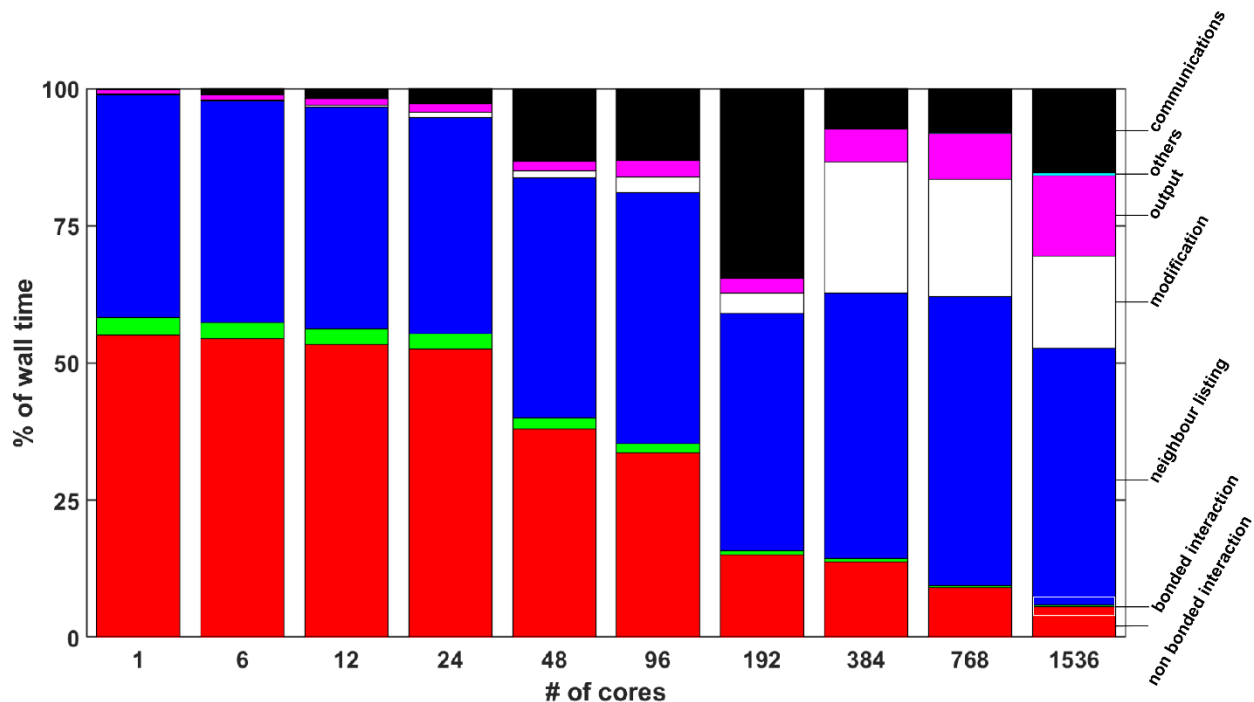


Figure B.2. Distribution of the Total Computational Time (Wall Time) for the Intel Skylake Architecture. As the number of CPU cores increases, most of the wall time is taken by the communication over the network and read/write of the data. The analysis is done based on single data point for each # of (CPU) cores. For better statistics, we need to have at least ten points for each # of cores.

Haswell architecture on OSCER, the speed up saturates after 200 CPU cores. Therefore, asking for more than 200 CPU cores does not improve the speed of our simulation, but we now wait longer on the SLURM's job queue since we are asking for more resources. We concluded from our benchmarks that for our molecular dynamics the most efficient simulation on OSCER needs 200 CPU cores.

We further analyze the saturation of speed up for the Skylake architecture on Stampede2, shown in Figure B.2. We divide the total simulation time (wall time) into individual LAMMPS processes for each number of CPU cores. For a single core, there is no communication cost, and all the wall time is dedicated for the LAMMPS simulation which involves non-bonded and bonded interaction, neighbor listing and so on. As we use more CPU cores, more time is used communicating between

the cores than performing molecular dynamics simulation. As a result, the speed up of our simulation decreases from the ideal case and saturates after some time.

## Appendix C: Running DFT Simulations using VASP

Our DFT simulations are performed using VASP 5.4.4 ab initio simulation package. Ionic relaxations are carried out by Dr. Gil Speyer with the Agave System at the Arizona State's Research Computing center. Dr. Lloyd A. Bumm performed the ELF and the bond order calculations, and I analyzed the charge density difference with OSCER. I also prepared the initial structures and analyzed the simulation data using my post-analysis MATLAB scripts. We use four input files for our DFT simulation: POSCAR for the initial structure, KPOINTS to specify the k-points which is used to sample the Brillouin zone, INCAR to provide information about what kind of calculation to perform and how to perform it, and POTCAR file (proprietary) that is used for the pseudopotential of each atom. The name of the files and their purpose are very specific in VASP. An example of the input files for the bridge site ( $\varphi = 0^\circ$ ) adsorption of methanethiol on the unrelaxed Au(111) substrate is give here along with the job submission script. The energy of the relaxed structure is given in the OUTCAR file. The structural and charge analysis are performed using CONTCAR and CHGCAR files, respectively. The WAVECAR file is the largest output file (~ 25 GB) that contains the details of the wavefunctions which can be used to restart the simulation.

---

### *INCAR file example*

```
# Relaxation
System = bridge fcc with top two Au layers relaxed
# New Calculation
ISTART = 0
ICHARG = 2
#####
# Electronic Optimization
# Cutoff energy of the planewave basis set in eV
ENCUT = 300
# Gaussian smearing
ISMEAR = 2
SIGMA = 0.2
#####
# Ionic Optimization
# Relaxing atoms without changing the cell size
ISIF = 2
```



```

# CG Algorithm for ionic relaxation
IBRION = 2
# Maximum number of ionic steps: copy the CONTCAR (optimized structure) file to POSCAR
(new input file), 0 means only the electronic-SC calculations should be performed
NSW = 0
# Relaxation of the electronic DOF will be stop once this energy cutoff is reached
EDIFF = 1E-6
# Forces smaller than 0.01 A/ev
EDIFFG = -.01
#####
# Dispersion Correction
# Activating D2 correction
IVDW = 10
# Cutoff radius (A) in pair interaction
VDW_RADIUS = 30.0
# Scaling factor
VDW_SCALING = 0.75
# Damping parameter
VDW_D = 20.0
# C6 parameters (Jnm^6mol^-1) for each species in the POSCAR file
VDW_C6 = 0.14 1.75 5.57 40.62
# R0 parameters (A) for each species in the POSCAR file
VDW_R0 = 1.001 1.452 1.683 1.772
#####
# Specifying Calculation Parameters
# Electronic minimization algorithm. Fast -- mixture of the Davidson and RMM-DIIS
algorithms
ALGO = Fast
# Spin polarization. 2 -- spin polarized calculations (collinear) are performed
ISPIN = 2
# Time step or time width scaling
POTIM = 0.8
# Use of reciprocal/real space: Auto -- recommended for system with more than 20 atoms
LREAL = Auto
# Switches on corrections to the potential and forces
LDIPOL = .TRUE.
# Switches on monopole/dipole and quadrupole corrections to the total energy. 3 -- the
dipole moment will be calculated only parallel to the direction of the first, second or
third lattice vector, respectively.
IDIPOL = 3
#####
# Writing Output Files
# Determines whether the total local potential is written to the LOCPOT file
LVTOT = .TRUE.
# Determines whether the wavefunctions are written to the WAVECAR file at the end of a
run
LWAVE = .TRUE.
# Determines whether the charge densities (files CHGCAR and CHG) are written
LCHARG = .TRUE.
# The all-electron charge density will be reconstructed explicitly and written out to
file (file names: AECCAR0, AECCAR1, and AECCAR2)
LAECHG = .TRUE.

```

---

*POSCAR file example*

```

idealized methyl
1.0000000000000000
  9.996299999999997    0.0000000000000000    0.0000000000000000
  0.0000000000000000    11.5427000000000000    0.0000000000000000
  0.0000000000000000    0.0000000000000000    24.725899999999993
  H      C      S      Au
  3      1      1      96
Selective dynamics
Direct
  0.6177773308130128  0.3750006497613256  0.6408248432656691  T  T  T
  0.7014529089924650  0.2968489480685577  0.5869976011792133  T  T  T

```

0.7014529089924650	0.4531523514540936	0.5869976011792133	T	T	T
0.6431582426105749	0.3750006497613256	0.5973003028118598	T	T	T
0.4851351907594221	0.3750006497613256	0.5597627964973881	T	T	T
0.0067315439730820	0.9978108780814736	0.4796914076356558	T	T	T
0.5052443804586204	0.9961371451179133	0.4791030962585197	T	T	T
0.0028687525763686	0.5047322004199941	0.4801072961533848	T	T	T
0.5120438651558175	0.5108565150647379	0.4847441003401372	T	T	T
0.2539349660691599	0.1236546160860499	0.4776088226058519	T	T	T
0.7602991230764573	0.1203705401710025	0.4799896275174902	T	T	T
0.2539349660691599	0.6263475497850166	0.4776088226058519	T	T	T
0.7602991230764573	0.6296316257000640	0.4799896275174902	T	T	T
0.0028687525763686	0.2452708317994947	0.4801072961533848	T	T	T
0.5120438651558175	0.2391465171547580	0.4847441003401372	T	T	T
0.0067315439730820	0.7521904214411634	0.4796914076356558	T	T	T
0.5052443804586204	0.7538641544047238	0.4791030962585197	T	T	T
0.2386374418735073	0.3750006497613256	0.4734732471882737	T	T	T
0.7644951965829136	0.3750006497613256	0.4733911975759284	T	T	T
0.2556026172919204	0.8750032488066068	0.4795575504078187	T	T	T
0.7562786215444603	0.8750032488066068	0.4807889656711524	T	T	T
0.0835479225543168	0.1248104607424025	0.3806984417672368	T	T	T
0.5815240393898407	0.1281062277383711	0.3839309433366509	T	T	T
0.0835479225543168	0.6251917051286640	0.3806984417672368	T	T	T
0.5815240393898407	0.6218959381326954	0.3839309433366509	T	T	T
0.3340703158643521	0.2503675638901441	0.3814130347528035	T	T	T
0.8318891789676996	0.2472246593340941	0.3798550993814089	T	T	T
0.3347447900884646	0.7502326210156838	0.3807338696544775	T	T	T
0.8331345393671015	0.7509412267384761	0.3809557002692543	T	T	T
0.0783671102680543	0.3750006497613256	0.3794590498600172	T	T	T
0.5805398552202661	0.3750006497613256	0.3833972841502984	T	T	T
0.0843166910195734	0.8750032488066068	0.3810226613422856	T	T	T
0.5851385209517801	0.8750032488066068	0.3802906647160711	T	T	T
0.3340703158643521	0.4996354683293518	0.3814130347528035	T	T	T
0.8318891789676996	0.5027783728854018	0.3798550993814089	T	T	T
0.3347447900884646	0.9997686785069533	0.3807338696544775	T	T	T
0.8331345393671015	0.9990600727841610	0.3809557002692543	T	T	T
0.1666666666666643	0.0000000000000000	0.2858718995061835	F	F	F
0.6666656662965309	0.0000000000000000	0.2858718995061835	F	F	F
0.1666666666666643	0.5000017326968518	0.2858718995061835	F	F	F
0.6666656662965309	0.5000017326968518	0.2858718995061835	F	F	F
0.4166661664815976	0.1250010829355332	0.2858718995061835	F	F	F
0.9166651661114642	0.1250010829355332	0.2858718995061835	F	F	F
0.4166661664815976	0.6250010829355332	0.2858718995061835	F	F	F
0.9166651661114642	0.6250010829355332	0.2858718995061835	F	F	F
0.1666666666666643	0.2500012995226442	0.2858718995061835	F	F	F
0.6666656662965309	0.2500012995226442	0.2858718995061835	F	F	F
0.1666666666666643	0.7500012995226371	0.2858718995061835	F	F	F
0.6666656662965309	0.7500012995226371	0.2858718995061835	F	F	F
0.4166661664815976	0.3750006497613256	0.2858718995061835	F	F	F
0.9166651661114642	0.3750006497613256	0.2858718995061835	F	F	F
0.4166661664815976	0.8750032488066068	0.2858718995061835	F	F	F
0.9166651661114642	0.8750032488066068	0.2858718995061835	F	F	F
0.0000000000000000	0.0000000000000000	0.1905811315260522	F	F	F
0.4999989996298666	0.0000000000000000	0.1905811315260522	F	F	F
0.0000000000000000	0.5000017326968518	0.1905811315260522	F	F	F
0.4999989996298666	0.5000017326968518	0.1905811315260522	F	F	F
0.2500005001850667	0.1250010829355332	0.1905811315260522	F	F	F
0.7499994998149333	0.1250010829355332	0.1905811315260522	F	F	F
0.2500005001850667	0.6250010829355332	0.1905811315260522	F	F	F
0.7499994998149333	0.6250010829355332	0.1905811315260522	F	F	F
0.0000000000000000	0.2500012995226442	0.1905811315260522	F	F	F
0.4999989996298666	0.2500012995226442	0.1905811315260522	F	F	F
0.0000000000000000	0.7500012995226371	0.1905811315260522	F	F	F
0.4999989996298666	0.7500012995226371	0.1905811315260522	F	F	F
0.2500005001850667	0.3750006497613256	0.1905811315260522	F	F	F
0.7499994998149333	0.3750006497613256	0.1905811315260522	F	F	F
0.2500005001850667	0.8750032488066068	0.1905811315260522	F	F	F
0.7499994998149333	0.8750032488066068	0.1905811315260522	F	F	F
0.0833339335554157	0.1250010829355332	0.0952907679801385	F	F	F
0.5833328331482619	0.1250010829355332	0.0952907679801385	F	F	F
0.0833339335554157	0.6250010829355332	0.0952907679801385	F	F	F
0.5833328331482619	0.6250010829355332	0.0952907679801385	F	F	F
0.333332329631952	0.2500012995226442	0.0952907679801385	F	F	F

0.8333313325930618	0.2500012995226442	0.0952907679801385	F	F	F
0.3333323329631952	0.7500012995226371	0.0952907679801385	F	F	F
0.8333313325930618	0.7500012995226371	0.0952907679801385	F	F	F
0.0833339335554157	0.3750006497613256	0.0952907679801385	F	F	F
0.5833328331482619	0.3750006497613256	0.0952907679801385	F	F	F
0.0833339335554157	0.8750032488066068	0.0952907679801385	F	F	F
0.5833328331482619	0.8750032488066068	0.0952907679801385	F	F	F
0.3333323329631952	0.5000017326968518	0.0952907679801385	F	F	F
0.8333313325930618	0.5000017326968518	0.0952907679801385	F	F	F
0.3333323329631952	0.0000000000000000	0.0952907679801385	F	F	F
0.8333313325930618	0.0000000000000000	0.0952907679801385	F	F	F
0.1666666666666643	0.0000000000000000	0.0000000000000000	F	F	F
0.6666656662965309	0.0000000000000000	0.0000000000000000	F	F	F
0.1666666666666643	0.5000017326968518	0.0000000000000000	F	F	F
0.6666656662965309	0.5000017326968518	0.0000000000000000	F	F	F
0.4166661664815976	0.1250010829355332	0.0000000000000000	F	F	F
0.9166651661114642	0.1250010829355332	0.0000000000000000	F	F	F
0.4166661664815976	0.6250010829355332	0.0000000000000000	F	F	F
0.9166651661114642	0.6250010829355332	0.0000000000000000	F	F	F
0.1666666666666643	0.2500012995226442	0.0000000000000000	F	F	F
0.6666656662965309	0.2500012995226442	0.0000000000000000	F	F	F
0.1666666666666643	0.7500012995226371	0.0000000000000000	F	F	F
0.6666656662965309	0.7500012995226371	0.0000000000000000	F	F	F
0.4166661664815976	0.3750006497613256	0.0000000000000000	F	F	F
0.9166651661114642	0.3750006497613256	0.0000000000000000	F	F	F
0.4166661664815976	0.8750032488066068	0.0000000000000000	F	F	F
0.9166651661114642	0.8750032488066068	0.0000000000000000	F	F	F

---

*KPOINTS file example*

```

K-Points
0
Monkhorst-Pack
9 9 1
0. 0. 0.

```

---

*Job script example*

```

#!/bin/sh
#
#SBATCH --job-name=BFAB_Bridge_FCC
#SBATCH -p normal
#SBATCH -n 80
#SBATCH --exclusive
#SBATCH --tasks-per-node=20
#SBATCH --time=01:30:00
#SBATCH --mail-type=end
#SBATCH --mail-user=bhattacharya@ou.edu

module purge
module load intel/2018a
mpirun -np $SLURM_NTASKS ~/labumm/VASP_544/vasp.5.4.4.pl2/bin/vasp_std

```

---

## Appendix D: MATLAB Script to Generate 109 Unique Tilt

### Direction and Twist Combinations

The script is developed using MATLAB R2021a version and it starts here.

```
clear; clc;
tic

%%%%%%%%%%%%%%%%%%%%%%%%%%%%%%%%%%%%%%%%%%%%%%%%%%%%%%%%%%%%%%%%%%%%%%%%Arrangement of the basis molecules%%%%%%%%%%%%%%%%%%%%%%%%%%%%%%%%%%%%%%%%%%%%%%%%%%%%%%%%%%%%%%%%%%%%%%%%
%
%                               (4)
%                               (3)
%-----Horizontal Mirror Plane-----
%                               (2)
%                               (1)
%%%%%%%%%%%%%%%%%%%%%%%%%%%%%%%%%%%%%%%%%%%%%%%%%%%%%%%%%%%%%%%%%%%%%%%%

A = 50;
B = 132;
C = 228;
D = 310;
N_sym_op = 16; % number of symmetry operations
N_comb = 4^4*6; % number of twist combinations

% index1: 4 basis types and tilt direction
% index2: 1,536 twist structures
TwistMatrix = zeros(5, N_comb);

id = 1;
for i0 = 1:6 % tilt directions
    for i1 = 1:4 % twist 1
        for i2 = 1:4 % twist 2
            for i3 = 1:4 % twist 3
                for i4 = 1:4 % twist 4
                    if i1 == 1
                        Basis1 = A;
                    end
                    if i1 == 2
                        Basis1 = B;
                    end
                    if i1 == 3
                        Basis1 = C;
                    end
                    if i1 == 4
                        Basis1 = D;
                    end
                    if i2 == 1
                        Basis2 = A;
                    end
                    if i2 == 2
                        Basis2 = B;
                    end
                    if i2 == 3
                        Basis2 = C;
                    end
                    if i2 == 4
                        Basis2 = D;
                    end
                    if i3 == 1
                        Basis3 = A;
                    end
                    if i3 == 2
```

```

        Basis3 = B;
    end
    if i3 == 3
        Basis3 = C;
    end
    if i3 == 4
        Basis3 = D;
    end
    if i4 == 1
        Basis4 = A;
    end
    if i4 == 2
        Basis4 = B;
    end
    if i4 == 3
        Basis4 = C;
    end
    if i4 == 4
        Basis4 = D;
    end
    if i0 == 1
        TiltDirection = 0;
    end
    if i0 == 2
        TiltDirection = 60;
    end
    if i0 == 3
        TiltDirection = 120;
    end
    if i0 == 4
        TiltDirection = 180;
    end
    if i0 == 5
        TiltDirection = 240;
    end
    if i0 == 6
        TiltDirection = 300;
    end

    TwistMatrix(:,id) = [Basis1, Basis2, Basis3, Basis4,...
                        TiltDirection];
    id = id + 1;
end
end
end
end
end
clear i0; clear i1; clear i2; clear i3; clear i4; clear id;
clear TiltDirection; clear Basis1; clear Basis2; clear Basis3; clear Basis4;
clear A; clear B; clear C; clear D;

Twist_symmetry = zeros(size(TwistMatrix,1), N_comb, N_sym_op);
Number_of_fixed_points_per_operation = zeros(1, N_sym_op);
for i = 1:N_sym_op % For each combination of symmetries

    ref_data_comp = TwistMatrix; % Copy the data to apply symmetries to it

    if mod(i, 2) == 1 % Rotation Symmetry
        ref_data_comp(5, :) = mod(ref_data_comp(5, :) + 180, 360);
        ref_data_comp([1, 3], :) = ref_data_comp([3, 1], :);
    end

    if mod(floor(i / 2), 2) == 1 % Mirror Symmetry w.r.t. horizontal mirror plane
        ref_data_comp(:, :) = mod(360 - ref_data_comp(:, :), 360);
        ref_data_comp([1, 3], :) = ref_data_comp([3, 1], :);
    end

    if mod(floor(i / 4), 4) == 1 % Translation Symmetry (along a)
        ref_data_comp(1:4, :) = ref_data_comp([4, 1, 2, 3], :);
    end

    if mod(floor(i / 4), 4) == 2 % Translation Symmetry (along c)

```

```

    ref_data_comp(1:4, :) = ref_data_comp([3, 4, 1, 2], :);
end

if mod(floor(i / 4), 4) == 3 % Translation Symmetry (along b)
    ref_data_comp(1:4, :) = ref_data_comp([2, 3, 4, 1], :);
end

Twist_symmetry(:, :, i) = ref_data_comp;

compare = (ref_data_comp - TwistMatrix).'; % Columns where all of the differences
                                           % are 0 are fixed points.
idx = ismember(compare, [0, 0, 0, 0, 0], 'rows'); % Count the fixed points.
Number_of_fixed_points_per_operation(1,i) = sum(idx);

clear ref_data_comp;
end
Number_of_orbits_predicted_from_fixed_points =
sum(Number_of_fixed_points_per_operation)/N_sym_op;

Boolean_array = ones(N_comb, N_sym_op, N_comb);
for i = 1:N_comb
    ref_structure = TwistMatrix(:, i);
    for j = 1:N_comb
        for k = 1:N_sym_op
            Boolean_array(j,k,i) = isequal(ref_structure, Twist_symmetry(:, j, k));
        end
    end
clear ref_structure;
end

Symmetry_indices = cell(1, N_comb);
for i = 1:N_comb % index for the TwistMatrix array
    temp_array = [];
    for j = 1:N_comb % gathering corresponding indices for the array Twist_symmetry
        if any(Boolean_array(j, :, i)) == 1
            temp_array = [temp_array, j];
        end
    end
    Symmetry_indices{1,i} = temp_array;
end
clear temp_array;

temp_index_array = Symmetry_indices;
Orbit_ids = {};
id = 1;
for i = 1:length(temp_index_array)

    % We begin with checking if the orbit has already been considered or
    % not. The way to do it is to check if the index of the first structure
    % in the orbit is zero or not. If the first index is zero that means
    % the orbit has been included.
    if temp_index_array{1,i}(1,1) ~= 0 % ~=0 means we have not included this orbit yet

        % Take the first structure from the orbit that represent the rest
        % of the structures (index if the structure)
        index(1,id) = temp_index_array{1,i}(1,1);

        Orbit_ids{id} = temp_index_array{1,i};

        % Go to rest of the structures in that orbit and make the index of
        % the first structure 0 so that we don't include it later
        for j = 2:length(temp_index_array{1,i})
            temp_index_array{1,temp_index_array{1,i}(1,j)}(1,1) = 0;
        end

        id = id + 1;
    end
end

Number_of_Orbits = id - 1; clear id;

% Verifying that there is no repeating structure

```

```

count = 0;
for i = 1:size(Orbit_ids,2)
    for j = 1:size(Orbit_ids{1,i},2)
        structure_id = Orbit_ids{1,i}(1,j); % structure to be compared with the rest
                                           % of the structures in the Orbit

        for k = 1:size(Orbit_ids,2)
            for m = 1:size(Orbit_ids{1,k},2)
                if Orbit_ids{1,k}(1,m) == structure_id && i ~= k && j ~= m
                    count = count + 1;
                end
            end
        end
    end
end
clear i; clear j; clear k; clear m;
if count == 0
    disp(' ')
    disp('No repeated structure detected')
else
    disp(' ')
    disp('Repeated structure detected')
end

UniqueTwists = zeros(size(TwistMatrix,1), length(index));
for i = 1:length(index)
    UniqueTwists(:,i) = TwistMatrix(:,index(1,i));
end

disp(' ')
toc

```

The script ends here.

## Appendix E: CDD Plots for Azimuthal Angles at High Symmetry Sites and Along Transition Paths

The crystal directions are given in Figure 6.8. The iso-surfaces values are  $+0.00105091 \text{ e}/\text{\AA}^3$  (red) and  $-0.00105091 \text{ e}/\text{\AA}^3$  (blue) for all the CDD analysis.

### 1. Bridge site with 12 azimuthal angles of the S-C bond

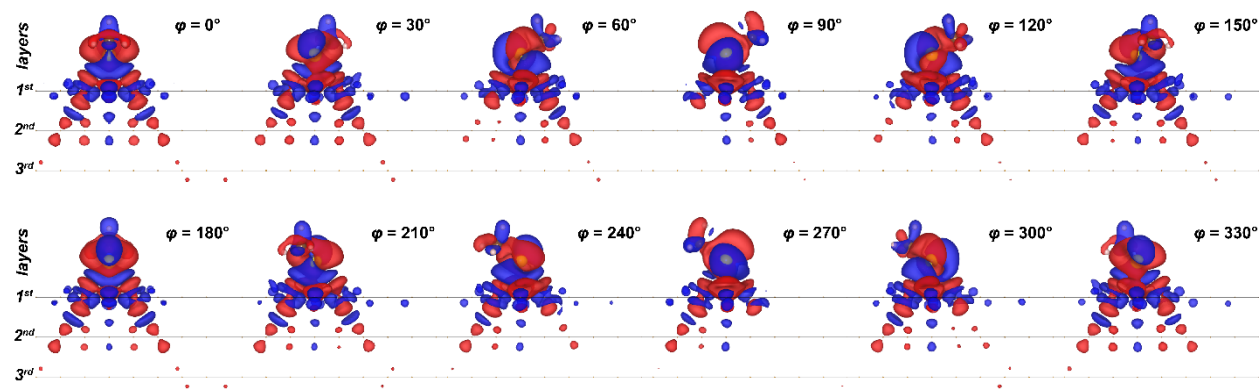


Figure E.1 CDD Side-View Looking along  $[\bar{1}\bar{1}2]$  of the Bridge Site for 12 Azimuthal Angles of the S-C Bond. The spatial distribution of the positive and the negative charge is indicated by red and blue colors, respectively.

### 2. fcc site with 3 unique azimuthal angles of the S-C bond

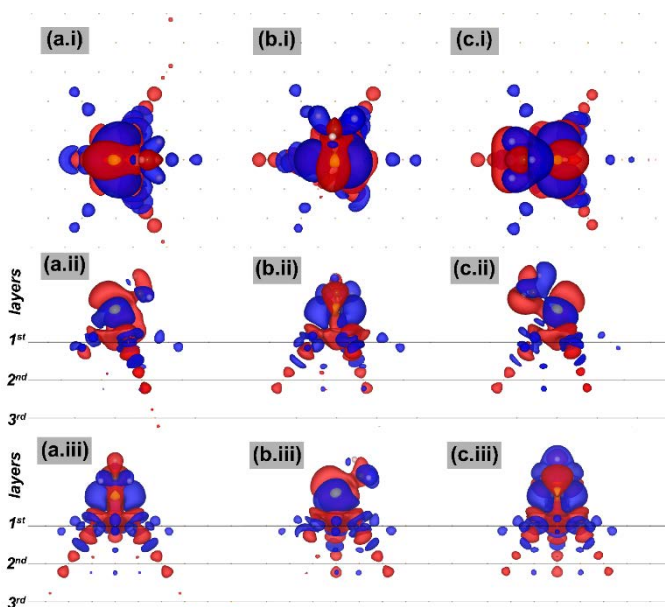


Figure E.2. CDD at the fcc Hollow Site for Three Azimuthal Angles of the S-C Bond. (a)  $\phi = 0^\circ$ ; (b)  $\phi = 90^\circ$ ; and (c),  $\phi = 180^\circ$ . Views of the CDD along the  $[\bar{1}\bar{1}\bar{1}]$ ,  $[\bar{1}\bar{1}0]$ , and  $[\bar{1}\bar{1}2]$  are shown in first (i), second (ii), and third (iii) rows, respectively.



3. hcp site with 3 unique azimuthal angles of the S-C bond

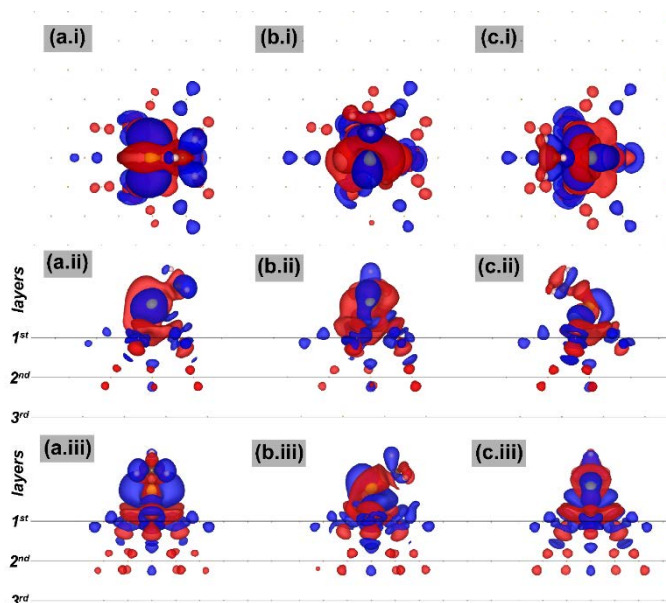


Figure E.3. CDD at the hcp Hollow Site for Three Azimuthal Angles of the S-C Bond. (a)  $\phi = 0^\circ$ ; (b)  $\phi = 90^\circ$ ; and (c),  $\phi = 180^\circ$ . Views of the CDD along the  $[\bar{1}\bar{1}\bar{1}]$ ,  $[\bar{1}\bar{1}0]$ , and  $[\bar{1}\bar{1}2]$  are shown in first (i), second (ii), and third (iii) rows, respectively.

4. Atop site with 2 unique azimuthal angles of the S-C bond

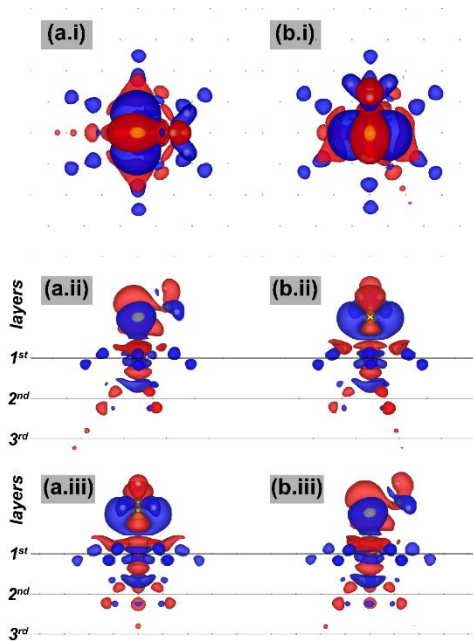


Figure E.4. CDD at the Atop Site for Two Azimuthal Angles of the S-C bond. (a)  $\phi = 0^\circ$ ; (b)  $\phi = 90^\circ$ . Views of the CDD along the  $[\bar{1}\bar{1}\bar{1}]$ ,  $[\bar{1}\bar{1}0]$ , and  $[\bar{1}\bar{1}2]$  are shown in first (i), second (ii), and third (iii) rows, respectively.

## 5. Bridge to Atop path

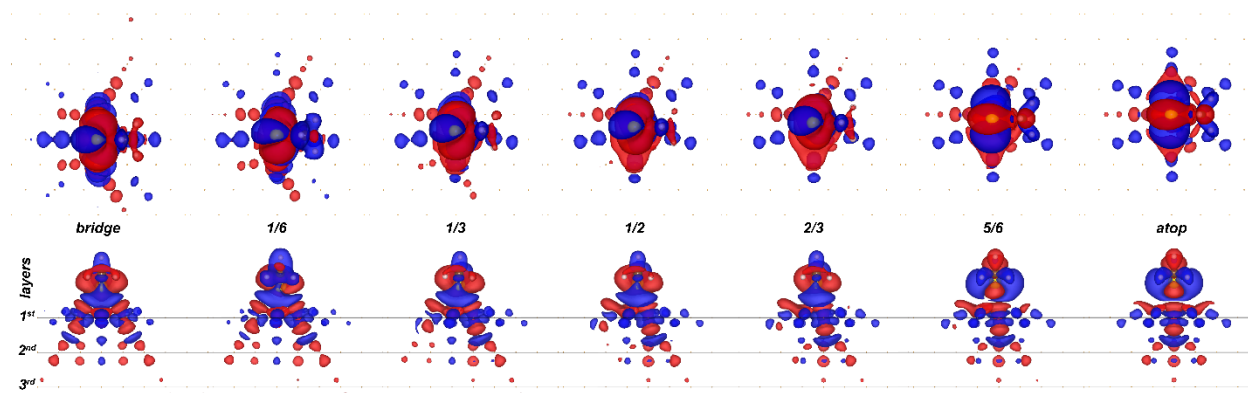


Figure E.5. CDD for Seven Sites on the Bridge to Atop Path with  $\phi = 0^\circ$ . Views of the CDD along the  $[\bar{1}\bar{1}\bar{1}]$ , and  $[\bar{1}\bar{1}2]$  are shown in first (i) and second (ii) rows, respectively.

## 6. fcc Hollow to hcp Hollow path via Bridge site

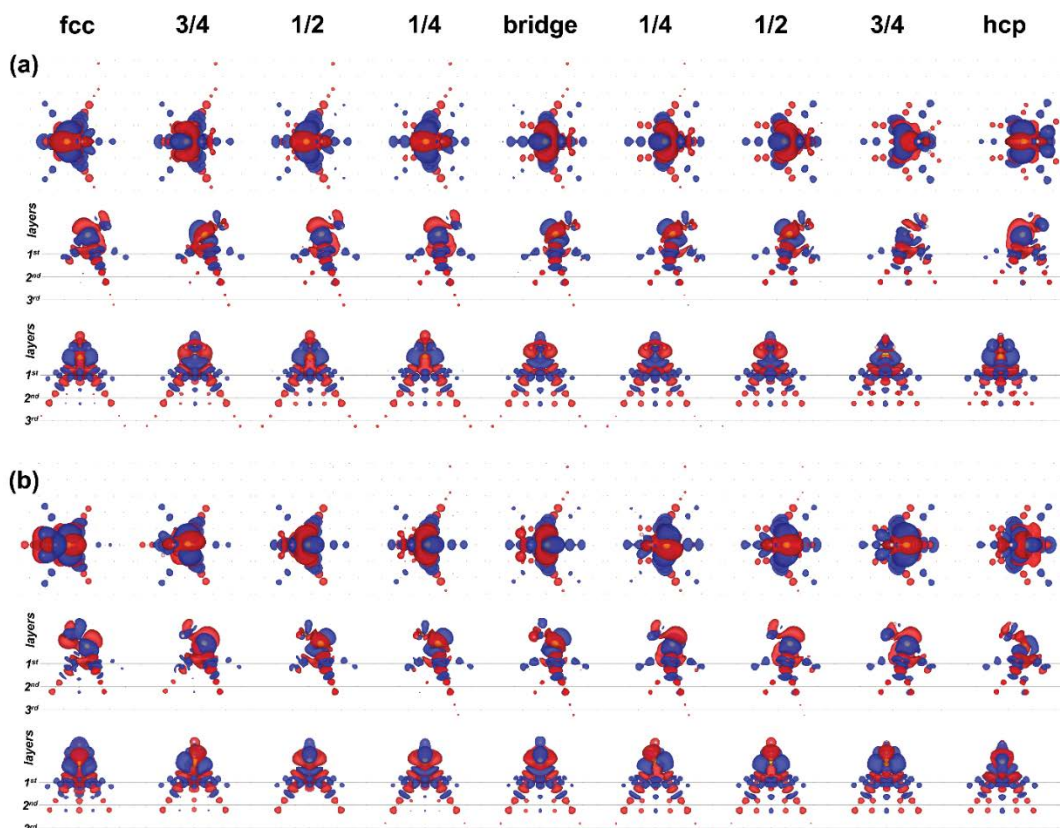


Figure E.6. CDD for Nine Sites on the fcc to hcp Path via the Bridge Site for Two Azimuthal Angles of the S-C Bond. (a)  $\phi = 0^\circ$ ; (b)  $\phi = 90^\circ$ . Views of the CDD along the  $[\bar{1}\bar{1}\bar{1}]$ ,  $[\bar{1}\bar{1}0]$ , and  $[\bar{1}\bar{1}2]$  are shown in first (i), second (ii), and third (iii) rows, respectively.

7. fcc hollow site to atop and hcp hollow site to atop paths

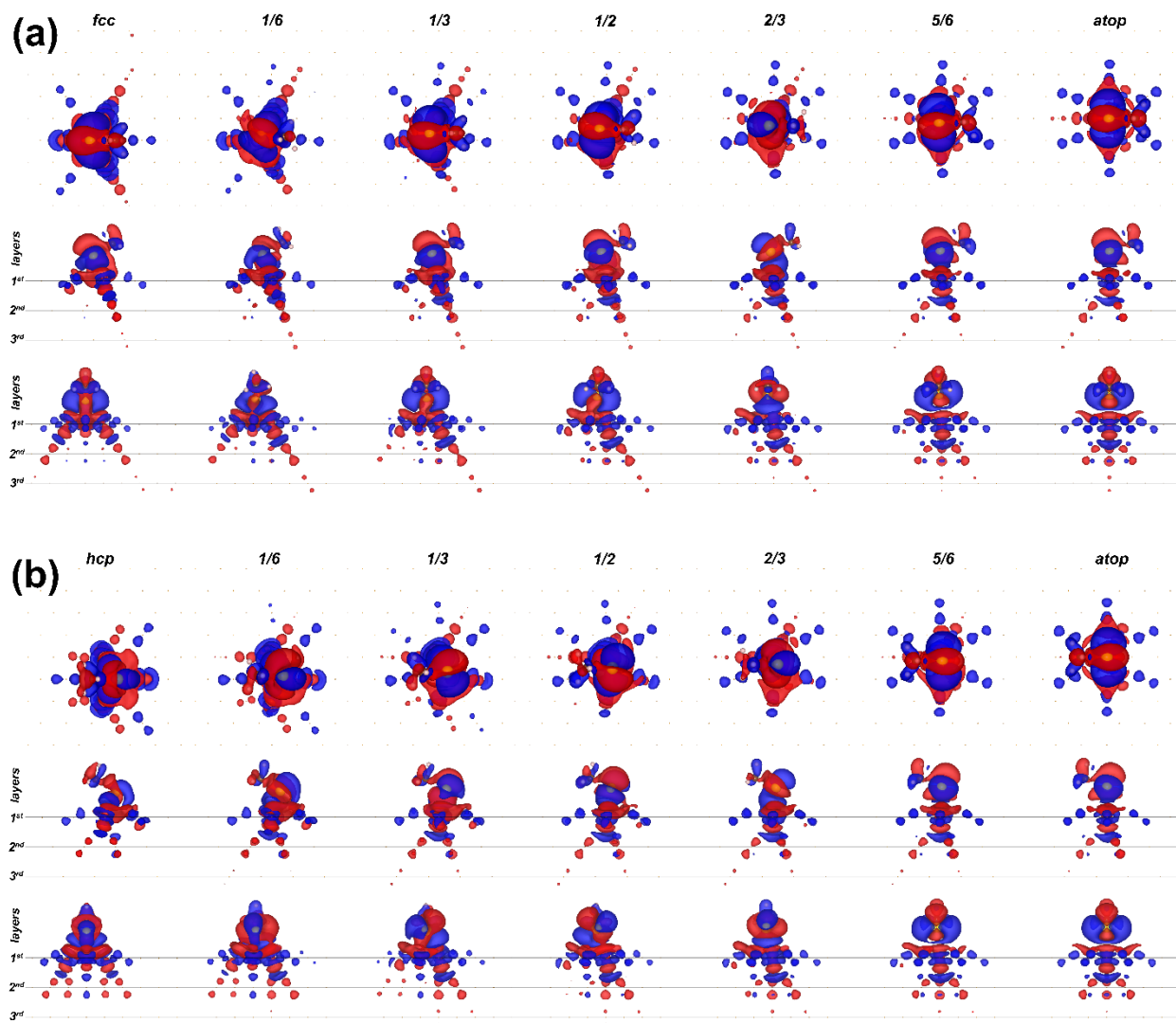


Figure E.7. CDD for Seven Sites along the Paths from a Hollow Site to the Atop Site. (a) fcc-atop  $\phi = 0^\circ$  and (b) hcp to atop  $\phi = 180^\circ$ . Views of the CDD along the  $[\bar{1}\bar{1}\bar{1}]$ ,  $[\bar{1}\bar{1}0]$ , and  $[\bar{1}\bar{1}2]$  are shown in first (i), second (ii), and third (iii) rows, respectively.

## Appendix F: STM Image Simulation from Molecular Dynamics

We use a two-layer tunnel junction model to simulate the topographic STM images of alkanethiol SAM from the molecular dynamics data to compare with experimental observations. Molecular dynamics predicts the physical height of the alkanethiol molecules, whereas the experimental STM image is a convolution of the molecular height, its electronic properties, and the details of the STM tip itself. As a result, a molecule with a shorter physical height, but a higher

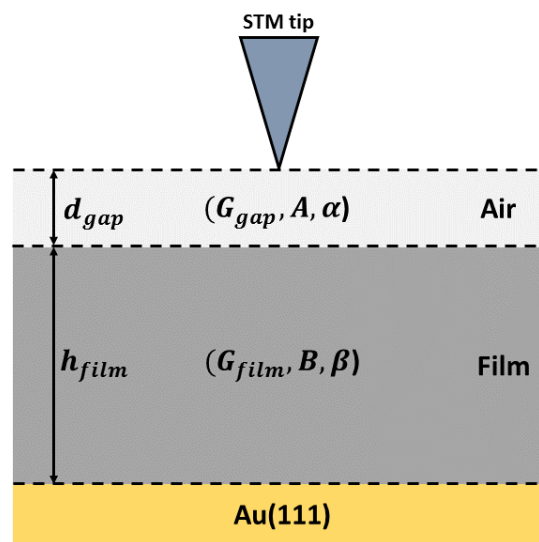


Figure F.1. Schematic Diagram of the Two-Layer Tunnel Junction Model. Layer 1 is the vacuum gap between the tip and the film. Layer 2 is the film itself.

conductivity would appear topographically higher on STM image. The conductivity of a molecule is determined by the alignment of the molecular orbitals with the Fermi level of the substrate Au atoms which is influenced by the bonding at the Au-S interface.<sup>1-3</sup>

The surface bonding depends on the adsorption sites as demonstrated in Chapter 6. Molecules within the  $(2\sqrt{3}\times 3)$ rect. unit cell will have different conductivities depending on their bonding to the substrate. In order to compare simulated STM images

with experiments, we need to include this site-dependent molecular conductivity in the STM model. Unfortunately, the dependency of the substrate bonding on the molecular conductivity is yet to be understood. For now, we have adopted a simple two-layer tunnel junction model,<sup>5</sup> where all the molecules have the same conductivity, to transform the molecular height from our simulated data into a constant current topographic STM image in comparison with the available experimental evidence.

The two-layer tunnel junction model divides the observed STM height ( $h_{STM}$ ) into two components, the height of the film ( $h_{film}$ ) and the distance between the STM tip (represented as a point) and the top of the film ( $d_{gap}$ ), shown in Figure F.1. Since the conductance of a layer exponentially decays with the thickness of the layer, the total conductance is given as

$$G_{total} = G_{gap} G_{film} \quad (G.1)$$

where  $G_{gap} = Ae^{-\alpha d_{gap}}$  and  $G_{film} = Be^{-\beta d_{film}}$ . A and B are the respective contact conductance, and  $\alpha$  ( $2.3 \text{ \AA}^{-1}$ ) and  $\beta$  ( $1.2 \text{ \AA}^{-1}$ ) are the respective decay constants. The time average constant current STM images were simulated using the contribution from both the  $\text{CH}_3$  and the last  $\text{CH}_2$  of the 50 nearest neighbor molecules for each pixel. To compare the simulated STM image from the molecular dynamics data with the experiment, we have considered the time average of the tunneling current rather than the time average of the molecular position. We have excluded the contribution of the H atoms to the tunneling current because the electron density of the H atom is 12 times smaller

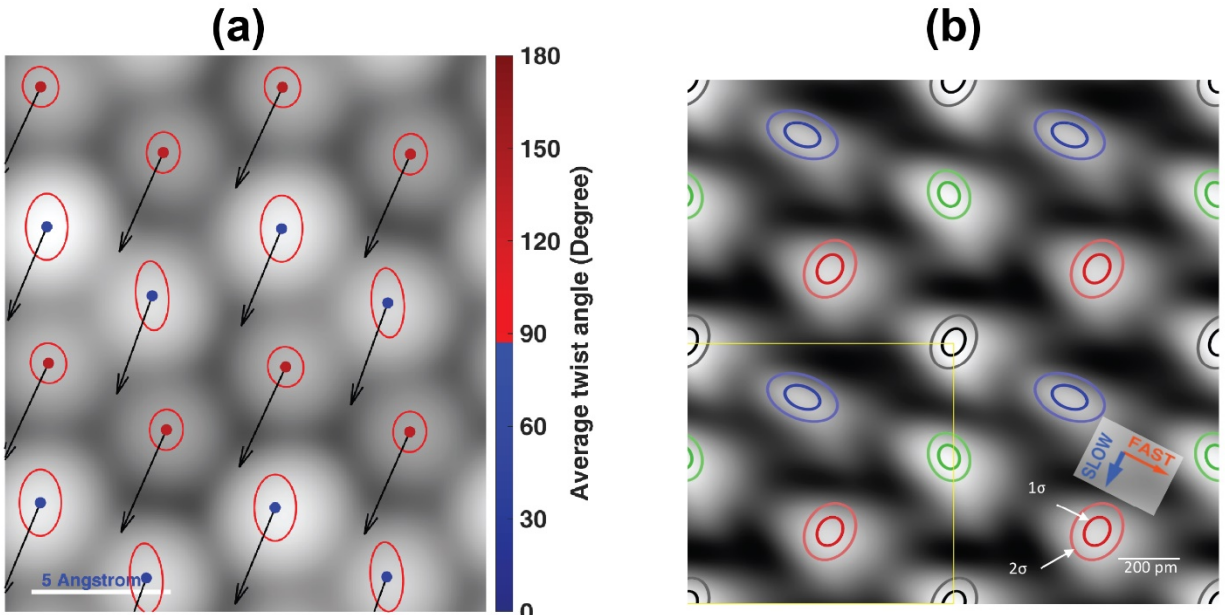


Figure F.2. Comparing Simulated and Experimental STM Images. Simulated STM image of Model A at 200 K (a) with the experimental STM image of decanethiol SAM (b).<sup>4</sup> The black arrows and ellipses in (a) represent the tilt direction, and the  $1\sigma$  position confidence of the termini, respectively. Molecular twists are given by the red and the blue dots.

than that of the C atom. Therefore, we assumed that the influence of the H atoms to the electron transport would be negligible compared to the contribution from the carbon atoms.

We demonstrate an example of comparing simulated STM image for the Model A at 200 K with the experimental observation in Figure F.2. Since all the molecules have the same conductivity, the STM image represents a weighted average of the molecular height at each pixel. By comparing the topographic features, we can predict the internal monolayer structures like tilt direction, twist angles, and the atomic description at the Au-S interface. Ab initio based techniques, such as non-equilibrium DFT, can be used to determine the adsorption site dependent molecular conductivity which can be easily incorporated in our current model to improve it.

## References

1. Romaner, L.; Heimel, G.; Zojer, E., Electronic Structure of Thiol-bonded Self-assembled Monolayers: Impact of Coverage. *Phys. Rev. B Condens. Matter* **2008**, *77* (4), 045113.
2. Heimel, G.; Romaner, L.; Brédas, J.-L.; Zojer, E., Interface Energetics and Level Alignment at Covalent Metal-Molecule Junctions:  $\pi$ -Conjugated Thiols on Gold. *Phys. Rev. Lett.* **2006**, *96* (19), 196806.
3. Heimel, G.; Romaner, L.; Brédas, J.-L.; Zojer, E., Organic/metal Interfaces in Self-assembled Monolayers of Conjugated Thiols: A First-principles Benchmark Study. *Surf. Sci.* **2006**, *600* (19), 4548-4562.
4. Yothers, M. P.; Browder, A. E.; Bumm, L. A., Real-space Post-processing Correction of Thermal Drift and Piezoelectric Actuator Nonlinearities in Scanning Tunneling Microscope Images. *Rev. Sci. Instrum.* **2017**, *88* (1), 013708.
5. Bumm, L. A.; Arnold, J. J.; Dunbar, T. D.; Allara, D. L.; Weiss, P. S., Electron Transfer through Organic Molecules. *J. Phys. Chem. B* **1999**, *103* (38), 8122-8127.



## Appendix G: IRRAS Simulation from Molecular Dynamics

We use our IRRAS model to compare the molecular geometry from the molecular dynamics simulation with the experimental measurement. In the experiment, a reference phase of randomly oriented alkanethiol molecules is used in a matrix of KBr to obtain the isotropic intensities and

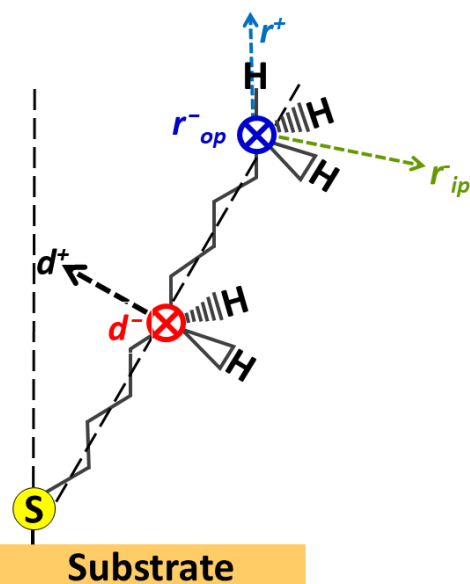


Figure G.1. The Vibrational Modes for Methyl and Methylene.  $\nu_s(\text{CH}_2)$ . The perpendicular component of the modes are enhanced, but the parallel component of the modes are suppressed by the image charge due to the presence of the metallic substrate.

line profiles of the bond stretching modes. Alkanethiol SAMs, on the other hand, have a particular orientation in the crystal. We can undo the orientational average of the reference phase to obtain the anisotropic intensities that corresponds to the orientation of the alkanethiol SAM. The hypothesis is that the presence of the metallic Au(111) substrate enhances the perpendicular component of the stretching modes, but the parallel components are suppressed by its image. Each methylene has a symmetric ( $d^+$ ) and an antisymmetric ( $d^-$ ) mode, shown in Figure H.1. The orientation of the molecular backbone is determined by comparing the ratio of these modes

between the reference phase and the SAM. The geometry of the alkanethiol molecules are already known in the molecular dynamics simulation. We use this known geometry and the reference spectra to simulate the corresponding IRRAS of the SAM to compare with experiments.

We begin our model by identifying the normal vibrational modes in the C-H stretching region, taken from Laibinis, et al. and listed in Table G.1.<sup>1</sup> The line shapes of each mode in the reference phase are modeled as a linear combination of the Gaussian and the Lorentzian line shapes. Those

values were not tabulated by the authors. We have extracted the shapes from Figure 3 of the supporting information (Laibinis, et al.) and tabulate them for each mode. The percent Gaussian and Lorentzian sum to 100%, thus only the former is given in the table.

Table G.1: The Vibrational Modes of Alkyl Chains in the C-H Stretching Region.

<b>Vibrational mode</b>	<b>Mode Description</b>	<b>Peak wavenumber (cm<sup>-1</sup>)</b>	<b>Gaussian Fraction (%)</b>
<i>CH<sub>2</sub> symmetric stretching, d<sup>+</sup></i>	ip with C-C-C backbone, ip with H-C-H	2850	10.25
<i>α - CH<sub>2</sub> symmetric stretching, d<sub>α</sub><sup>+</sup></i>	ip with C-C-C backbone, ip with H-C-H	2853	9.032
<i>CH<sub>3</sub> symmetric stretching, r<sup>+</sup></i>	to C-C-C backbone	2879	15.46
<i>FR of CH<sub>2</sub> symmetric stretching, FR-d<sup>+</sup></i>	ip with C-C-C backbone, ip with H-C-H	2895	0.362
<i>FR of CH<sub>2</sub> symmetric stretching, FR-d<sup>+</sup></i>	ip with C-C-C backbone, ip with H-C-H	2907	15.46
<i>CH<sub>2</sub> antisymmetric stretching, d<sup>-</sup></i>	⊥ to C-C-C backbone	2918	19.61
<i>α - CH<sub>2</sub> antisymmetric stretching, d<sub>α</sub><sup>-</sup></i>	⊥ to C-C-C backbone	2925	15.36
<i>FR of CH<sub>3</sub> symmetric stretching, FR-r<sup>+</sup></i>	to C-C-C backbone	2935	1.000
<i>CH<sub>3</sub> antisymmetric stretching(op), r<sub>op</sub><sup>-</sup></i>	⊥ to C-C-C backbone	2954	18.37
<i>CH<sub>3</sub> antisymmetric stretching(ip), r<sub>ip</sub><sup>-</sup></i>	ip of C-C-C backbone, ⊥ to C-CH <sub>3</sub>	2964	3.173



The intensity of these isotropic modes is then scaled using the known molecular geometry to obtain the corresponding anisotropic intensities. Finally, we add their intensities to get the full simulated IRRAS spectra for the alkanethiol SAM.

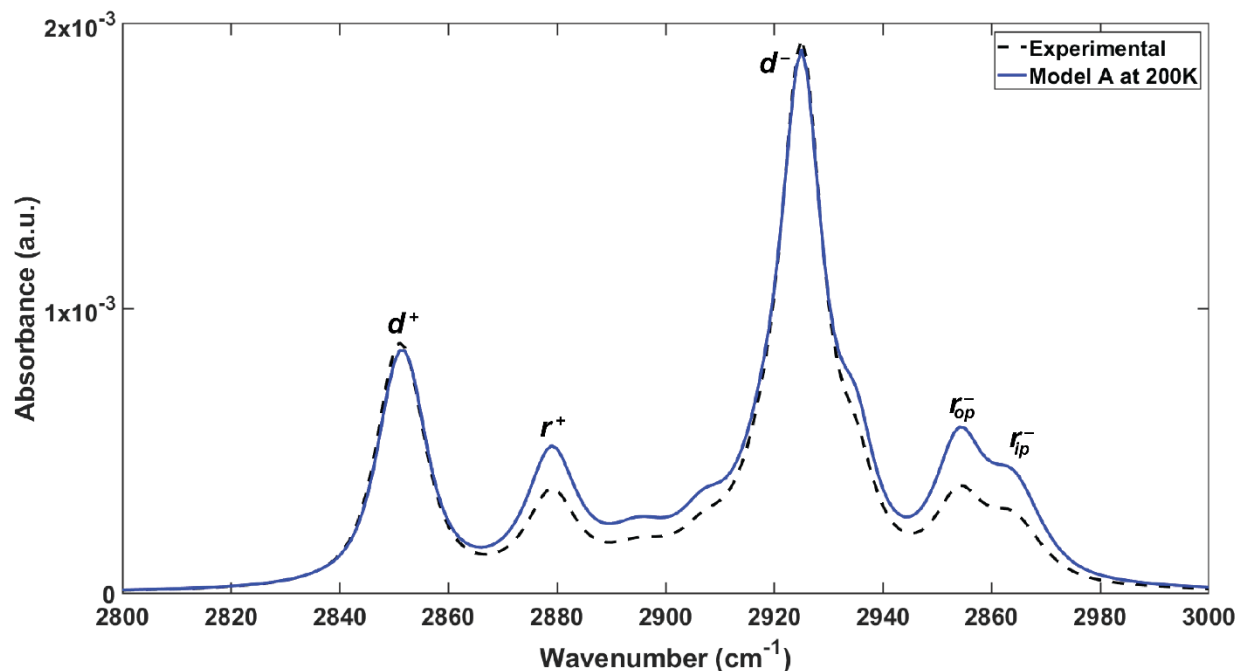


Figure G.2 Simulated and Experimental IRRAS Spectra. The simulated spectrum is for Model A at 200 K. The experimental spectrum is for a C18 SAM with tilt angle  $26^\circ$  and two nearly orthogonal twists ( $-48^\circ$  and  $50^\circ$ ). We linearly scaled the intensity of the experimental spectra to compare with the simulated spectra of a C10 SAM. Primary normal modes are identified in the figure.

It is useful to present the model in a mathematical framework. We use the adsorption spectra from the experiment ( $k_{isotropic}$ ). The perpendicular component of the vibrational mode with wavenumber ( $\nu$ ) is obtained from the molecular dynamics simulation by projecting the mode along the surface normal ( $\sim \cos^2\theta$ , where  $\theta$  is the angle between the normal mode and the surface normal). The anisotropic absorbance ( $A_{anisotropic}$ ) of a monolayer with thickness  $t$  (cm) can be obtained as follows

$$A_{anisotropic} = 12\pi k_{isotropic} (\cos^2 \theta) \nu t . \quad (\text{H.1})$$

The frequency of the bond vibration depends on its environment. We distinguish the methylene bonded to the headgroup ( $\alpha$ -CH<sub>2</sub>, shown in Table G.1 and 2) from the rest of the methylene along the backbone to improve our model.

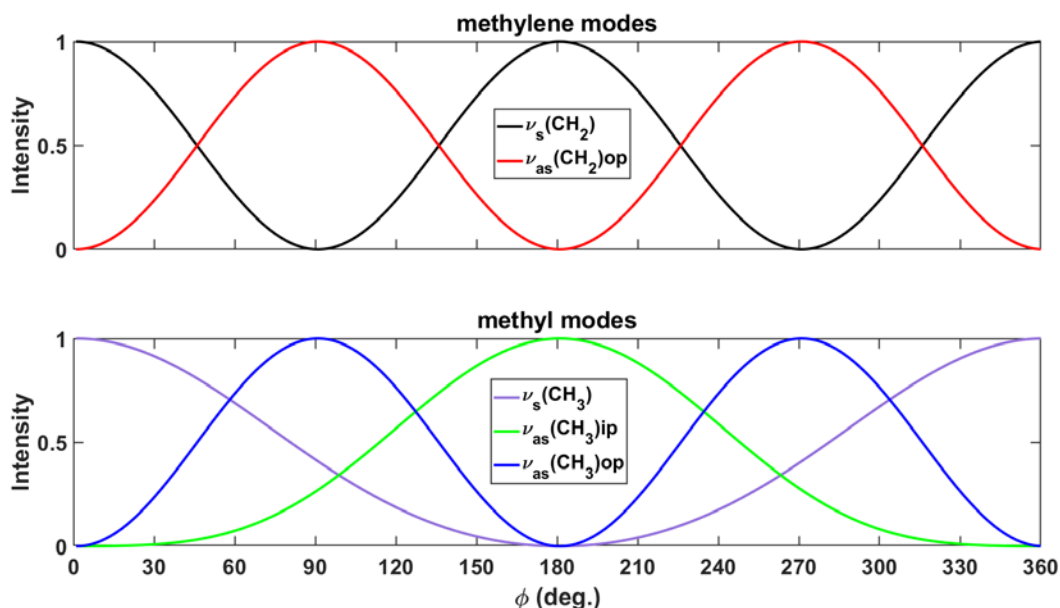


Figure G.3. Chain Twist Angle Dependence of the IRRAS Intensities of the C-H Modes. Symmetry of the normal modes are shown with normalized intensities.  $\nu_s(\text{CH}_2)$ ,  $\nu_{as}(\text{CH}_2)_{op}$ , and  $\nu_{as}(\text{CH}_3)_{op}$  have  $C_2$  symmetry.

A comparison between the simulated IRRAS of Model A at 200 K and the experiment is shown in Figure G.2. It shows that the methylene modes agree better with the experiment than the methyl modes. This is because the methyl modes are weak in the reference phase and are complicated by the Fermi resonances, and therefore we need a better calibration for the methyl modes. This is important because methyl modes can be used to distinguish twists related by mirror symmetry about the tilt plane provided that the gauche defect at the termini is negligible. The current model predicts the molecular twists by fitting the methylene modes. Since methylene modes have  $C_2$  symmetry (Figure G.3), they cannot be used to distinguish mirror twists. However, we can distinguish the mirror twists about the tilt plane with a better calibration of the methyl modes ( $\nu_s(\text{CH}_3)$  and  $\nu_{as}(\text{CH}_3)_{ip}$ ). It is important to note that the simulated spectra are calculated for a

single SAM domain, whereas the experimental IRRAS spectra is obtained over multiple domains with different possibilities of tilt direction. The simplified model presented here does not include changes in the real part of the refractive index, which plays a significant role in the IRRAS spectrum at grazing incidence where IRRAS is most sensitive. For a detailed discussion and methods to develop a full anisotropic model to simulate IRRAS spectra from MD data, see the MS thesis of Nafisa Amin.<sup>2</sup>

## Reference

1. Laibinis, P. E.; Whitesides, G. M.; Allara, D. L.; Tao, Y. T.; Parikh, A. N.; Nuzzo, R. G., Comparison of the Structures and Wetting Properties of Self-Assembled Monolayers of *n*-Alkanethiols on the Coinage Metal Surfaces, Copper, Silver, and Gold. *J. Am. Chem. Soc.* **1991**, *113* (19), 7152-7167.
2. Amin, N. Full Anisotropic Model for Simulating the Infrared Reflection Absorption Spectra (IRRAS) of Self-Assembled Monolayers (SAMS) from All-Atom Molecular Dynamics Simulations. MS Dissertation, University of Oklahoma, Norman, Ok, 2020.